# Collective quantum dynamics of molecular ensembles coupled to a Cavity

David Wellnitz

▶ **To cite this version:**

David Wellnitz. Collective quantum dynamics of molecular ensembles coupled to a Cavity. Quantum Physics [quant-ph]. Université de Strasbourg, 2022. English. NNT : 2022STRAF001 . tel-03688431

**HAL Id: tel-03688431**
**https://theses.hal.science/tel-03688431**

Submitted on 4 Jun 2022

**HAL** is a multi-disciplinary open access archive for the deposit and dissemination of scientific research documents, whether they are published or not. The documents may come from teaching and research institutions in France or abroad, or from public or private research centers.

L'archive ouverte pluridisciplinaire **HAL**, est destinée au dépôt et à la diffusion de documents scientifiques de niveau recherche, publiés ou non, émanant des établissements d'enseignement et de recherche français ou étrangers, des laboratoires publics ou privés.

**Université de Strasbourg**

École Doctorale de Sciences Chimiques – ED222

Institut de Science et d'Ingénierie Supramoléculaires (ISIS) – UMR 7006


# Thèse


présentée par David WELLNITZ



soutenue le 11 février 2022

pour obtenir le grade de: **Docteur de l'Université de Strasbourg**
Discipline/Spécialité: **Physique**


# Collective Quantum Dynamics of Molecular Ensembles coupled to a Cavity


THÈSE dirigée par:

**Pr. PUPILLO Guido** — Professeur, Université de Strasbourg
**Dr. SCHACHENMAYER Johannes** — Chargé de recherche, CNRS

RAPPORTEURS:

**Pr. OSPELKAUS Silke** — Professeur, Universität Hannover
**Pr. GENES Claudiu** — Professeur, MPL Erlangen

Université de Strasbourg

David Wellnitz

**Collective Quantum Dynamics of Molecular Ensembles coupled to a Cavity**

EDSC École Doctorale des Sciences Chimiques

**Résumé** Il a été démontré que le couplage collectif d'ensembles moléculaires à une cavité modifie les réactions chimiques, à la manière d'une catalyse. Cette observation suprenante a donné naissance au domaine de la chimie polaritonique, mais les principes sous-jacents ne sont pas encore bien établis. En particulier, le rôle des effets collectifs, dissipatifs et quantiques reste une question ouverte.

L'objectif central de cette thèse est de développer une compréhension théorique plus approfondie de la dynamique quantique collective et dissipative d'ensembles moléculaires couplés à des cavités. L'étude de cette dynamique est decomposé en trois parties : Dans la première partie, nous utilisons une cavité pour améliorer l'efficacité de formation de molécules ultra-froides dans leur état fondamental en exploitant la dissipation et les effets collectifs. En utilisant la symétrie de permutation et l'élimination adiabatique, nous avons développé une methode de simulation permettant de calculer efficacement de très grands ensembles ($> 10^6$ molécules). Dans la deuxième partie, l'analyse est étendue à la chimie polaritonique à température ambiante. Les différents régimes de dynamique de réaction sont ici identifiés dans le cas d'une réaction simple de transfert d'électrons photo-induite en présence de pompage dissipatif. Le rôle des effets quantiques est ensuite étudié à travers la création d'intrication entre les degrés de liberté vibrationnels, électroniques et photoniques. En utilisant des simulations de réseaux de tenseurs à grande échelle, nous démontrons que l'intrication peut être significativement augmentée en introduisant du désordre dans le système. Pour le régime sans désordre, nous avons développé d'autres méthodes d'approximation efficaces. Dans la troisième partie plus récente, nous étudions l'intrication des opérateurs dans une chaîne de spin ouverte avec déphasage, et démontrons que le déphasage conduit à une croissance logarithmique de l'intrication des opérateurs. Plus généralement, les deux premières parties démontrent l'importance et l'utilité des effets collectifs, dissipatifs et quantiques dans les ensembles couplés en cavité, tandis que la troisième partie aborde des sujets plus fondamentaux pour les systèmes quantiques ouverts.

**Mots clés**: QED en cavité, dynamique quantique à $N$ corps, chimie polaritonique, molécules ultra-froides, états de produits matriciels, systèmes quantiques ouverts, intrication.

**Abstract** Collectively coupling molecular ensembles to a cavity has been demonstrated to modify chemical reactions akin to catalysis. This intriguing observation has given rise to the field of polaritonic chemistry, however, the underlying principles are not yet well established. In particular, the role of collective, dissipative, and quantum effects remains an open question.

The central aim of this thesis is to develop a deeper theoretical understanding of the collective, dissipative quantum dynamics of cavity-coupled molecular ensembles. This dynamics is studied in three parts: In the first part, a cavity is used in a novel scheme for dissipative formation of ultra-cold ground state molecules with collectively enhanced efficiency. Using permutation symmetry and adiabatic elimination, a simulation is developed that can efficiently compute very large ($> 10^6$ molecules) ensembles. In the second part, the analysis is extended to room-temperature polaritonic chemistry. Here, regimes for modified reaction dynamics are identified for a simple photo-induced electron transfer reaction under dissipative pumping. Then, the role of quantum effects is investigated through the build-up of entanglement between vibrational and electro-photonic degrees of freedom. Using large scale matrix product state simulations, it is shown that entanglement can be significantly enhanced by introducing disorder into the system. For the disorder-less regime, further efficient approximations methods are developed. In the third part, a recent project, the build-up of operator entanglement is studied in an open spin-chain with dephasing. Here, it is found that dephasing leads to a logarithmic growth of operator entanglement. More generally, the first two parts demonstrate the importance and usefulness of collective, dissipative and quantum effects in cavity coupled ensembles, while the third part discusses more fundamental topics of open quantum systems.
**Keywords**: Cavity QED, Many-body Quantum Dynamics, Polaritonic Chemistry, Ultra-cold Molecules, Matrix Product States, Open Quantum Systems, Entanglement

*"Disorder, disorder, disorder"*

— System of a down, Toxicity

To my family and friends,
who always supported me

# Acknowledgements

Here, I want to thank everyone who contributed to the creation of this thesis, who helped to improve it, and everyone whom I met along the way. You gave me motivation, you supported me, you gave me ideas, discussed with me, or gave me respite. Of all those people, who are too many to list them all, some deserve special credit.

First of all, I want to thank Johannes Schachenmayer. You were my supervisor during the last three years, and it was from you that I learned most. You taught me how to think numerically, you taught me a lot of physics, and I also learned a lot from you beyond that. You were always ready to give advice when I needed it, and I consider myself lucky to have worked with you. We had a lot of fruitful discussions, and you never fail to lighten the mood at the right time. I want to also thank you for all the opportunities you provided me with to go to conferences, especially for the opportunity to go to an in-person conference despite the COVID pandemic.

Together with Johannes, I also need to thank Guido Pupillo. Together with Johannes, you supervised my research. During the last three years, you were always there to offer me advice and guidance when I asked for it, and your door was always open. I want to thank you for all the support you offered me, and for the many inspiring and insightful discussions.

Both of you, Guido and Johannes, have my deepest gratitude for giving me the opportunity to do a PhD in such an amazing environment, and for all the freedom you gave me during this time. I hope our paths will cross many times in the future, both inside and outside physics.

I also want to thank all the former and current members of the group. You were always available to talk about your or my research, to explain me concepts I didn't understand, and to give me feedback for my ideas. All of you taught me a lot. Thank you Guido, David, Stefan, Guillermo, Vineesha, Thomas, Sven, Francesco, and Jérôme!

I want to particularly acknowledge all those who collaborated with me on the different projects. Your input shaped these projects. You brought in new ideas, did part of the work, and gave helpful feedback. Thank you to Stefan Schütz, Guillermo Preisser, Shannon Whitlock, Felipe Herrera, Jérôme Dubail, and Vincenzo Alba. It was a pleasure to work with you, and will continue to be so in the future.

I also want to acknowledge all of my friends here in Strasbourg and back at home, who offered me supported me outside the office and showed me that life is not all about physics. Thank you for all the good times Guido, Rogéria, Filipa, Sayali, Renata, and Lukas. You are amazing friends, and I could always count on you. I want to especially thank Rogéria and Guido. Rogéria, you have always supported me during my PhD. All the wonderful time we have spend together have given me the strength and concentration to pursue my PhD with full focus. You came to Strasbourg during the height of the

pandemic, and kept me sane during that time. Guido, you have become my best friend during my time here in Strasbourg. You have been with me through all my ups and downs. And our time together has given me much needed respite from the hard work.

Last, but not least, I want to give special thanks my parents and my sister. You always stood behind me in whatever I decided to do, and encouraged me to pursue this path. To my parents, since your unconditional support is what made this work possible. You not only brought me into the position to write this thesis, but also helped me through it. Through the last three years you were always there for me when I needed you. Especially during the pandemic, you made sure I always had a place to stay. And to Johanna, who always brightens my mood and makes me laugh. Your support means most to me.

# Résumé de la Thèse en Français

## Introduction

La compréhension et le contrôle des réactions chimiques constituent un défi majeur des sciences physiques. Ce défi est principalement abordé en modifiant l'environnement chimique de la réaction, par exemple en choisissant méticuleusement le solvant ou en introduisant des matériaux capables de contrôler la réaction, appelés catalyseurs. Trouver de nouveaux moyens de contrôler la chimie est une tâche importante, qui présente un grand potentiel pour le progrès de la science et de la technologie.

Dans une expérience séminale en 2012, Hutchison *et al.* ont découverts une suppression d'une réaction de photo-isomérisation sous un couplage collectif d'une transition moléculaire électronique à une cavité [1]. Depuis ça, des diverses expériences ont montré des modifications des réactions chimiques induites par couplage à un mode de cavité. Les plus importantes de ces expériences ont démontrés que le couplage fort des transitions vibrationnelles d'une molécule peut modifier les taux de réaction pour les réactions thermiquement activées [2], et même orienter les réactions vers un produit désiré [3] par Thomas *et al.* Ces découvertes démontrent la possibilité de modifier les propriétés chimiques des molécules par couplage à des champs lumineux, lançant ainsi les bases de ce que l'on appelle désormais la chimie polaritonique [4–9]. Malgré ces résultats expérimentaux impressionnants, les principes sous-jacents ne sont pas encore bien établis. L'objectif principale de cette thèse est de développer une compréhension théorique plus profonde des processus sous-jacents, en particulier concernant le rôle des effets collectifs et dissipatifs.

La théorie décrivant les interactions lumière-matière est unifiée dans le cadre de l'électrodynamique quantique (EDQ), décrivant de nombreux phénomènes fondamentaux, tels que le spectre du corps noir, la structure fine des atomes et molécules, l'émission spontanée de la lumière et les interactions électro-magnétiques [10]. En plus, le couplage de nombreux émetteurs à un champ électromagnétique commun peut donner lieu à des effets dissipatifs collectifs [11, 12]. Pour leurs travaux sur cette théorie, Tomonaga, Schwinger et Feynman ont reçu le prix Nobel en 1965.

Si les modes de lumière sont confinés dans un volume fini par la présence d'une cavité, la théorie qui en résulte est appelée EDQ des cavités [10, 13, 14]. En physique atomique, moléculaire et optique (AMO), les configurations EDQ des cavités ont longtemps été étudiées comme un système quantique prototypique où les effets EDQ sont renforcés par rapport à un scénario sans cavité. En 2012, Serge Haroche a reçu un prix Nobel pour avoir démontré le contrôle et l'intrication de systèmes quantiques individuels en utilisant les interactions entre des atomes uniques et des champs lumineux quantiques. Afin

d'exploiter ce contrôle, différents types de « cavités » ont été développés pour confiner les modes de lumière [15–18]. Ces cavités sont généralement optimisées pour combiner de faibles taux de pertes et des intensités de champ locales élevées, afin de maximiser l'échange d'énergie cohérente avec un émetteur. Si le taux d'échange cohérent entre le champ et l'émetteur est plus rapide que les pertes de les deux, leurs degrés de liberté s'hybrident et forment ce que l'on appelle des polaritons, donnant lieu à des phénomènes physiques fondamentalement différents qui ne peux généralement pas être observés sans présence d'une cavité [13]. L'étude des conséquences des interactions lumière-matière renforcées par les cavités est un domaine de recherche dynamique, qui inclut le travail de cette thèse. Dans ce qui suit, je vais donner un bref aperçu des sujets spécifiques abordés dans cette thèse.

## Électrodynamique quantique des cavités

Les interactions lumière-matière sont l'une des pierres angulaires de la physique moderne, en particulier de la physique de l'AMO. Ces interactions déterminent non seulement (littéralement) tout ce que nous pouvons voir, mais leurs applications vont bien au-delà. Elles sont au cœur de la photochimie, des technologies solaires, de la photosynthèse et de la spectroscopie, et sont donc également essentielles aux mesures scientifiques. Par conséquent, elles sont fondamentales pour notre compréhension de toutes les sciences physiques.

Sans cavité, les interactions entre le champ électromagnétique du vide et la matière sont généralement faibles et peuvent être traitées de manière perturbative, comme le détermine la petite constante de structure fine $\alpha \sim 1/137$. Ceci est une conséquence du petit champ électrique du vide, qui est dilué dans un grand volume. À l'intérieur d'un volume confiné, c'est-à-dire une cavité, les modes électromagnétiques qui s'intègrent parfaitement dans ce volume sont considérablement renforcés, tandis que tous les autres modes sont supprimés par rapport au scénario du champ libre. Si le couplage est perturbatif, cela conduit à une augmentation des effets mentionnés ci-dessus. Plus particulièrement, par le confinement des modes lumineux, l'émission spontanée peut être modifiée de façon drastique, appelée l'effet Purcell [19]. Si le champ du vide est suffisamment renforcé, le couplage devient non-perturbatif, et les degrés de liberté de la lumière et de la matière s'hybrident et forment des états hybrides lumière-matière appelés polaritons [13]. Afin d'améliorer encore le couplage, des ensembles d'émetteurs peuvent être couplés au même mode de cavité [13]. Dans le régime perturbatif, cela conduit à une superradiance [11], tandis que dans le régime de couplage fort, cela conduit à un fractionnement accru des polaritons. Ces effets sont présentés en détail dans le chapitre 3.

L'exemple classique de confinement des modes lumineux consiste à placer deux miroirs métalliques l'un en face de l'autre. Par consequence, seuls les modes dont la longueur d'onde se situe entre les deux miroirs puissent exister à l'intérieur de la cavité. De telles cavités Fabri-Perot sont utilisées dans de nombreux montages, y compris dans certaines des expériences mentionnées ci-dessus [2, 3]. Différents matériaux ont été également adaptés pour servir de surfaces réfléchissantes, comme les fibres optiques pour les cavités

dites Fabri-Perot de fibre [15]. Les réflecteurs distribué de Bragg (« Distributed Bragg Reflectors », DBR) offrent une autre façon de confiner les modes lumineux [16]. Ces adaptations ont été réalisées pour atteindre de faibles pertes dans la cavité, qui entrent en compétition avec l'échange d'énergie cohérente. Cependant, en raison de la limite de réfraction, toutes ces cavités ont en commun que la lumière ne peut être confinée dans des volumes inférieurs à $\sim \lambda^3$ quand $\lambda$ est la longueur d'onde. Des méthodes permettant de confiner la lumière dans des volumes plus petits à proximité des émetteurs ont été développées dans le domaine de la plasmonique [17, 20]. Les plasmons sont eux-mêmes des excitations hybrides lumière-matière, qui conduisent à de grandes augmentations de champ à proximité d'une surface. Sur les surfaces structurées, ces plasmons se déplacent généralement sur la surface, mais en utilisant des nanoparticules métalliques, ils peuvent être fixes en place. Cependant, en raison de leur composante matérielle, les plasmons sont généralement affectés par un grand taux de perte. Tout au long de cette thèse, le champ est traité comme un champ quantique monomode générique, néanmoins, pour des estimations de paramètres réalistes, des cavités de type Fabri-Perot ou des DBRs sont considérés. En raison de leur plus grand volume, les effets collectifs sont plus importants dans ces cavités.

La EDQ des cavités a également été étudiée avec différents types d'émetteurs. De nombreuses expériences de couplage fort ont été réalisées en utilisant des excitons de Wannier-Mott dans des semi-conducteurs [21] et avec des atomes froids en physique AMO [22]. Ces deux systèmes présentent des excitations fondamentales généralement très bien contrôlées. Dans la physique AMO, cela est dû à un excellent contrôle des systèmes quantiques individuels à l'aide de lasers, et dans les semi-conducteurs, à des températures typiquement cryogéniques dans les expériences et à la grande extension des excitons de Wannier-Mott. Cette extension entraîne une moyannage sur le désordre local. Les semi-conducteurs organiques et les molécules organiques sont devenus une nouvelle alternative en raison de leurs grandes forces de couplage, bien qu'au prix d'une diminution de la qualité des excitons individuels [23, 24]. Naturellement, de nombreux autres types d'émetteurs ont été utilisés dans des expériences de couplage fort, comme les points quantiques [25], les qubits supraconducteurs [26], les centres de couleur (NV) [27], les matériaux 2D [28–30], et même les molécules ultra-froides [31]. Dans cette thèse, les excitations sont toujours considérées comme localisées, ce qui est le scénario typique des systèmes AMO ou des matériaux organiques.

## Chimie des polaritons

Le domaine de la chimie polaritonique a été établi sur la base de l'observation surprenante de la possibilité de modifier des réactions chimiques par un couplage fort de transitions moléculaires à un mode de cavité dans le groupe de Thomas Ebbesen à Strasbourg [1–3]. Dans une expérience révolutionnaire [1], Hutchison *et al.* ont couplé une transition électronique du produit d'une réaction de photo-isomérisation à une cavité, où ils ont observé une suppression du taux de réaction dans le régime de couplage fort collectif. Cela a conduit à un déplacement des concentrations d'équilibre des réactifs

et des produits sous irradiation ultra-violette. En 2016 [2], Thomas *et al.* ont montré que le couplage fort collectif d'une transition vibratoire peut conduire à une suppression d'une réaction thermiquement activée. Ils ont étudié la réaction de dissociation d'une molécule, qui a été ralentie par le couplage fort de la liaison dissociante à une cavité. Ce phénomène est particulièrement intriguant puisque la lumière n'est pas directement impliquée dans la réaction. En 2019 [3], Thomas *et al.* ont démontré que cet effet peut être utilisé pour modifier quel produit est favorisé dans une réaction de dissociation avec deux produits possibles. En détail, la cavité induit un ralentissement de l'une des vitesses de réaction, ce qui change le produit favorisé dans la réaction globale.

L'observation de la chimie modifiée a été confirmée dans une série d'expériences de suivi, qui peuvent être classées en deux régimes. Dans le régime de couplage électronique fort (ESC), une transition entre l'état fondamental de la molécule et un état électroniquement excité est couplée à la cavité, tandis que dans le régime de couplage vibrationnel fort (VSC), deux niveaux vibrationnels au sein de l'état fondamental électronique sont couplés. La différence d'énergie de transition entre les deux régimes ($\gtrsim 1\,\mathrm{eV}$ pour ESC et 100 meV pour VSC) conduit à des différences significatives à la fois dans la configuration et la chimie. De plus, en raison de l'énergie thermique de $\sim 25\,\mathrm{meV}$ à température ambiante, l'excitation thermique et les réactions activées thermiquement sont beaucoup plus importantes pour le VSC que pour l'ESC.

Afin de démontrer la chimie modifiée par cavité, jusqu'à présent, le mode principal de la cavité a généralement été couplé. Par conséquent, les énergies d'excitation $\gtrsim 1\,\mathrm{eV}$ se traduisent par des tailles de cavité $\lesssim 1\,\mu\mathrm{m}$ [32]. En raison de la petite taille des cavités, les matériaux couplés doivent généralement être en phase solide [4], et les réactions n'impliquent que des molécules individuelles. Les réactions de photo-isomérisation entre deux états fondamentaux d'une molécule ont été modifiées [1, 33–35]. Les implications pour la thermodynamique ont été analysées [33], et comment on peut utiliser ces effets pour le stockage d'énergie [34]. Une autre classe de réactions qui a été étudiée est celle des transitions singlet-triplet entre deux états électroniquement excités [36–43]. Ici, grâce au couplage de l'état singlet excité électroniquement à une cavité, les énergies des états singlets peuvent être modifiées, et même l'ordre énergétique des états singlet et triplet peuvent être modifié, ce qui conduit à une amélioration des taux de prélevation de triplet et d'annihilation triplet-triplet. Ces réactions sont particulièrement utiles pour des applications pratiques, comme les lasers ou les cellules solaires. Enfin, par un couplage fort des agrégats $J$ aux nanoparticules plasmoniques, la suppression des taux de photo-oxydation a été démontrée [44].

Au contraire, pour le VSC, les énergies plus faibles signifient que les cavités peuvent être suffisamment grandes pour être remplies de fluides, permettant ainsi une classe de réactions beaucoup plus large. En outre, les faibles échelles d'énergie signifient que des réactions thermiquement activées peuvent être observées. Ici, il a été démontré que le couplage du réactif, du produit et du solvant modifie la vitesse de réaction [2, 3, 45–47]. Dans cette thèse, je me concentre exclusivement sur les réactions dans le régime ESC.

Malgré ces résultats impressionnants, la compréhension théorique des processus impliqués n'en est encore qu'à ses débuts. Le problème sous-jacent est de calculer la dynamique de réaction d'un grand nombre de molécules, chacune avec de multiples degrés de liberté

électroniques et vibratoires, et toutes couplées indirectement via la cavité [5]. Divers outils numériques et analytiques ont été utilisés pour aborder ce défi. Analytiquement, des molécules simplifiées de modèle-jouet sont traitées, et les modifications génériques sont analysés [48–53]. Numériquement, on étudie généralement des molécules spécifiques de complexité variable allant des molécules simples diatomiques comme NaI [54] à des molécules organiques complexes comme la rhodamine [55]. Toutefois, afin de traiter de grands ensembles, la dynamique (au lieu du modèle moléculaire) doit être approximée. Dans le cadre de l'approximation de Born-Oppenheimer en cavité, l'état électrophotonique est approximé de ne changer qu'adiabatiquement avec la dynamique classique des degrés de liberté nucléaires [56]. En utilisant des extensions simples de cette approche telles que la dynamique de saut de surface ou le champ moyen d'Ehrenfest, la dynamique de l'état excité de grands ensembles moléculaires a été calculée [55, 57–60]. En revanche, pour calculer la dynamique quantique exacte, des méthodes plus sophistiquées sont nécessaires, et seul un petit nombré de molécules peut être traitées [54, 61–64]. Dans ce cas, les effets collectifs sont pris en compte en faisant correspondre le fractionnement de Rabi collectif à des valeurs expérimentales réalistes, car il a été déterminé que le fractionnement de Rabi est une quantité importante pour la chimie modifiée [2]. Cependant, le rôle précis des effets collectifs devient difficile ou même impossible à étudier. Nous donnons un aperçu des méthodes analytiques et numériques dominantes dans les chapitres 7 et 8, respectivement.

## Molécules et Chimie Ultrafroides

Les molécules ultrafroides sont des molécules à des températures au dessous de 1 µK. Ces molécules promettent d'avoir des applications dans les simulations quantiques, le calcul, la métrologie et l'étude des réactions chimiques dans le régime de l'ultrafroid [65–70]. En particulier, les dipôles permanents des molécules polaires offrent des implémentations de modèles plus riches avec différentes phases de la matière par rapport aux atomes ultrafroids [71, 72]. Les interactions dipolaires ont également été proposées pour être utilisées dans le calcul quantique [73, 74]. Cependant, de telles applications nécessitent encore des avancées dans le contrôle des molécules ultrafroides. À ce jour, les molécules ultrafroides ont été utilisées pour mesurer des constantes fondamentales [75], par exemple le moment dipolaire des électrons [76, 77] ou la constante de structure fine [78]. Les molécules ultrafroides ont également été utilisées pour étudier la chimie avec le contrôle des états quantiques internes [79–85].

Pour refroidir les molécules, différentes techniques ont été utilisées, comme le refroidissement direct par laser [86, 87], le refroidissement par gaz tampon [88], la décélération de Stark [89], le refroidissement de Sisyphe [90], et le refroidissement par évaporation [91]. De ces méthodes, uniquement le refroidissement par évaporation a permis d'atteindre le régime d'ultra-froid, mais même dans ce cas pas pour les molécules dans leur état fondamental total.

Il est également possible d'assembler directement des molécules ultrafroides à partir d'atomes ultrafroids. Dans ce cas, les techniques standard de refroidissement des

atomes peuvent être utilisées pour amener les atomes dans le régime d'ultrafroid [92, 93]. L'une des façons de créer des molécules à partir de ces atomes ultrafroids est la photo-association [94]. Dans la photo-association, des paires d'atomes sont amenées dans un état moléculaire électroniquement excité à l'aide d'un laser. L'état excité se désintègre ensuite dans l'état électronique de base de la molécule, laissant les molécules avec des degrés de liberté externes ultra-froids. Cependant, l'état interne ro-vibronique après la désintégration ne peut pas être contrôlé et est distribué de manière probabiliste selon les facteurs de Franck-Condon. Des schémas de repompage ont été développés avec quelque succès [95], mais à ce jour, aucun gaz moléculaire avec une densité d'espace de phase élevée n'a été créé.

L'association magnétique de molécules ultra-froides offre une alternative qui produit des molécules dans un état final bien défini [96]. En balayant un champ magnétique sur une résonance de Feshbach, les paires d'atomes sont déplacées adiabatiquement d'un état libre à un état moléculaire, qui est dans l'état électronique fondamental, mais fortement excité par les vibrations.

Afin de créer des ensembles à haute densité de molécules dans leur état fondamental, ces états peuvent ensuite être ramenés à l'état fondamental à l'aide d'un schéma de passage adiabatique Raman stimulé (STIRAP, « Stimulated Raman Adiabatic Passage ») [97–103]. Ce schéma implique l'état de Feshbach, l'état fondamental moléculaire et un état électroniquement excité supplémentaire. Deux impulsions laser sont montées et descendues en fonction du temps, changeant adiabatiquement l'état sombre du système de l'état initial à l'état fondamental moléculaire. L'état moléculaire suit alors ce changement adiabatique, transférant la population dans l'état fondamental. Cette méthode a été jusqu'à présent la seule méthode réussie pour produire des ensembles moléculaires ultrafroids dans l'état fondamental total. Dans le chapitre 5, nous proposons un schéma d'association alternatif utilisant les effets collectifs et dissipatifs dans une cavité.

## Systemes Quantiques Ouvertes

Dans de nombreux scénarios réalistes, les systèmes quantiques ne sont pas complètement isolés, mais interagissent avec leur environnement. Alors, en principe, un système ne peut pas être décrit seulement par lui-même, mais l'environnement doit être inclus dans la description, ce qui augmente considérablement sa complexité.

De tels systèmes quantiques ouverts sont omniprésents dans la nature. Par exemple, les atomes ou les molécules excités électroniquement se couplent au champ électromagnétique du vide, ce qui entraîne de petits déplacements de niveaux d'énergie et une émission spontanée [104]. Dans les molécules organiques, l'état électronique est également couplé aux vibrations moléculaires, ce qui entraîne un déphasage ou une relaxation des états excités [105]. Dans la chimie polaritonique, tous les degrés de liberté électroniques, photoniques et vibrationnels sont généralement couplés à l'environnement, de sorte qu'il faut l'analyser dans un cadre de système ouvert [32].

L'inclusion d'une description complète de l'environnement rendrait les calculs de la dynamique irréalisables dans la plupart des cas. Cependant, dans de nombreux scénarios, notamment en optique quantique, des approximations de l'environnement sont justifiées.

La plus importante d'entre elles est l'approximation de Markov, qui suppose que l'environnement est sans mémoire, tandis que l'évolution temporelle d'un système peut être décrite en termes de ses coordonnées actuelles uniquement, par une équation maîtresse de Markov [104, 106, 107]. Ceci est typiquement bien justifié dans les systèmes de type AMO [104], et sera utilisé tout au long de cette thèse.

Un grand nombre de méthodes ont été développées pour traiter les systèmes quantiques ouverts, en particulier dans l'approximation de Markov. L'élimination adiabatique est un traitement perturbatif qui élimine les degrés de liberté qui évoluent beaucoup plus rapidement que l'évolution du système [106]. Les trajectoires quantiques décrivent un système comme un mélange d'états qui évoluent selon une équation de mouvement probabiliste [108]. De plus, diverses méthodes ont été développées pour traiter les systèmes ouverts avec des états de réseaux tensorielles [109]. Le chapitre 2 présente les méthodes les plus importantes utilisées dans cette thèse.

## Intrication et Réseaux de Tenseurs

La simulation de l'évolution temporelle de systèmes quantiques à $N$ corps est une tâche importante, qui permet de mieux comprendre la physique important pour le système simulé. Cependant, cette tâche est rendue difficile par une croissance généralement exponentielle de l'espace de Hilbert avec la taille du système. Ceci est en contraste avec les systèmes classiques, où l'espace des phases croît généralement de façon linéaire avec le nombre de particules impliquées.

Cette complexité supplémentaire trouve son origine dans l'intrication entre différents objets quantiques [110–114]. L'intrication décrit le phénomène selon lequel l'état d'un objet quantique individuel peut être dans une mixture, bien que l'état de l'ensemble du système quantique soit unique, ce qui entraîne de grandes corrélations entre eux. Cela contraste avec les états classiques, qui ne peuvent être corrélés sans être dans un mélange statistique. Comme Bell a montré théoriquement et était confirmé par des expériences après, de telles corrélations quantiques peuvent également être plus fortes que toute corrélation classique possible, même en tenant compte des mélanges statistiques [115]. Dans un sens informatique, l'intrication peut donc mesurer la complexité de la dynamique quantique [116, 117].

Pour de nombreux états intéressants, l'intrication est locale dans le sens où la quantité d'intrication entre deux sous-systèmes ne depend qu'à la taille de leur frontière, et pas à leur volume totale [114]. Les exemples incluent les états fondamentaux des Hamiltoniens locaux, et plus généralement les états contribuant à la dynamique dans les systèmes désordonnés ou bruyants. Ceci peut être utilisé pour simuler efficacement des systèmes à plusieurs corps dans le formalisme des états de réseaux de tenseurs [116, 118]. En particulier, en une dimension (1D), la frontière d'un sous-système est indépendante de la taille du système, ce qui rend cette approche très prometteuse.

Sur cette base, les « Matrix Product States » (MPS) sont devenus l'outil par défaut pour les simulations numériques de systèmes quantiques 1D [119]. Ici, chaque sous-système est décrit par un tenseur, et l'intrication entre les sous-systèmes est capturée en

introduisant des « dimensions de liaison » (« bond dimension ») supplémentaires pour ces tenseurs. La dynamique de ces systèmes peut alors être simulée en effectuant des mises à jour locales des tenseurs, en augmentant la dimension de lien si nécessaire [116].

Dans le chapitre 4, les états de reseaux de tenseurs sont présentés en plus détail. Aux Chapitres 9 et 10, l'intrication entre les degrés de liberté vibrationelles, électronique, et photoniques est analysée à l'aide de MPS, et au Chapitre 11, l'évolution temporelle de l'intrication des opérateurs dans une chaîne de spin XXZ ouverte avec déphasage est discutée.

## Formation Collective et Dissipative de Molécules Ultra-froides

Dans le chapitre 5, nous avons dévelopés deux schémas pour réaliser la formation de molécules dans leur état fondamental à haut taux à partir d'atomes ultra-froids. Des paires d'atomes ultra-froids sont excitées en continu par un laser, et une décroissance collective vers l'état fondamental moléculaire est induite par un couplage à un mode de cavité avec pertes (voir figure 1). Cette décroissance vers la cavité peut être beaucoup plus importante que la décroissance vers n'importe quel autre état moléculaire. Ça conduit à un rendement moléculaire dans l'état fondamental augmenté, qui peut dépasser les efficacités des schémas d'association les plus modernes. En utilisant un laser continu, le rendement moléculaire peut être amélioré en augmentant simplement le nombre d'atomes, mais au prix d'un ralentissement collectif dû à la formation de polaritons qui déplacent l'état excité hors de la résonance. L'utilisation d'une impulsion laser chirpée pour rester en résonance avec l'énergie d'un polariton peut contourner ce ralentissement. Nous utilisons une combinaison d'outils analytiques et numériques pour simuler de grands systèmes en tirant parti de symétrie de permutation, et nous dérivons des estimations analytiques simples pour les rendements de l'état fondamental et les temps de transfert. Nous discutons de montages expérimentaux réalistes pour des molécules diatomiques polaires et non polaires, ouvrant ainsi la voie aux interactions matière-lumière collectives pour être utiliser dans l'ingénierie des états quantiques, la formation de molécules améliorées, la dynamique collective et la chimie par cavité.

Nous considérons $N$ paires d'atomes piégées dans un réseau optique à l'interieur d'une cavité. Chaque molécule est décrite par quatre états, comme le montre la figure 1. Initialement, toutes les molécules sont dans leur état initial $|i\rangle$, qui peut désigner une molécule de Feshbach pré-associée ou un état de paire d'atomes. Cet état est couplé à un état moléculaire excité $|e\rangle$ par un laser externe (fréquence de Rabi $\Omega$). L'état excité est ensuite couplé à l'état fondamental moléculaire $|g\rangle$ par une cavité (fractionnement de Rabi à vide d'une molécule $2g$, taux de désintégration $2\kappa$). En outre, l'état excité $|e\rangle$ peut se désintégrer par émission spontanée dans l'état initial $|i\rangle$ au taux $\gamma_i$, dans l'état fondamental $|g\rangle$ au taux $\gamma_g$, ou dans d'autres états moléculaires collectivement appelés $|x\rangle$ au taux $\gamma_x$. La dynamique de la matrice de densité $\hat{\rho}$ est décrite par une équation maîtresse

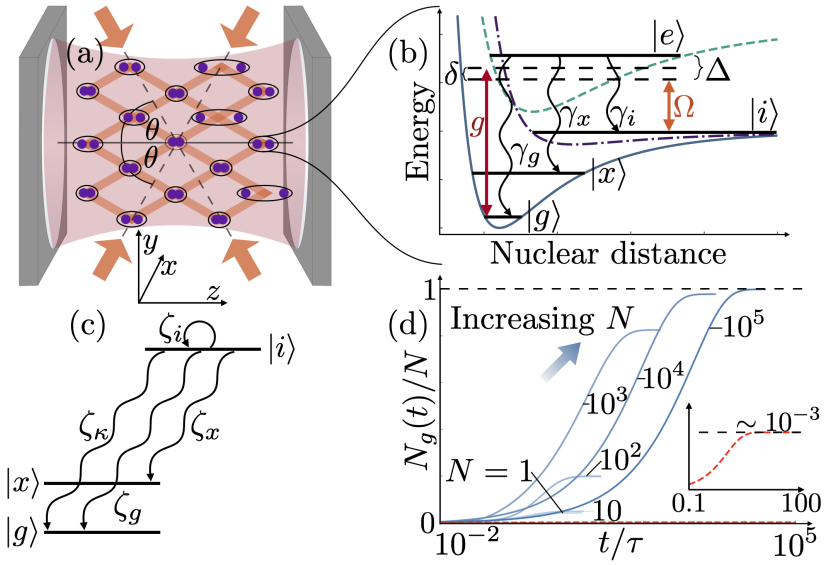


FIGURE 1. – Configuration pour la formation collective de molécules dissipatives. (a) Des molécules de Feshbach sont piégées dans un réseau optique à l'intérieur d'une cavité et amenées dans des états profondément liés par photoassociation. Un angle $\theta$ entre les faisceaux laser du réseau et l'axe de la cavité ($z$) assure la correspondance des modes. (b) Schéma des niveaux d'énergie et de leur couplage pour une seule molécule. Pour RbCs, les courbes d'énergie potentielle peuvent être identifiées avec le potentiel de l'état fondamental $X^1\Sigma^+$ (ligne continue ; se dissocie en $5s + 6s$), le potentiel de l'état fondamental triplet $a^3\Sigma^+$ (ligne en traits mixtes ; se dissocie en $5s + 6s$) et le potentiel de l'état excité $(A^1\Sigma^+ - b^3\Pi)0^+$ (ligne tiretée ; se dissocie en $5s + 6p$). Une molécule préparée dans un état de Feshbach $|i\rangle$ est excitée par laser (force de couplage $\Omega$, désaccord $\Delta$) dans l'état excité $|e\rangle$, qui peut retourner à $|i\rangle$, à l'état fondamental rovibrationnel $|g\rangle$ ou à tout autre état (lié ou non), appelé ici collectivement $|x\rangle$. (c) Niveaux d'énergie d'une seule molécule après élimination adiabatique de la cavité et de l'état excité avec des taux de décroissance $\zeta_\alpha$ ($\alpha$=$\kappa$, $i$, $x$, $g$). (d) Évolution de la fraction moléculaire de l'état fondamental de la cible $N_g/N$ en fonction du temps $t$ (voir le texte), pour différents $1 \leq N \leq 10^5$ (échelle logarithmique). La ligne tiretée rouge dans l'encadré indique les résultats sans cavité.

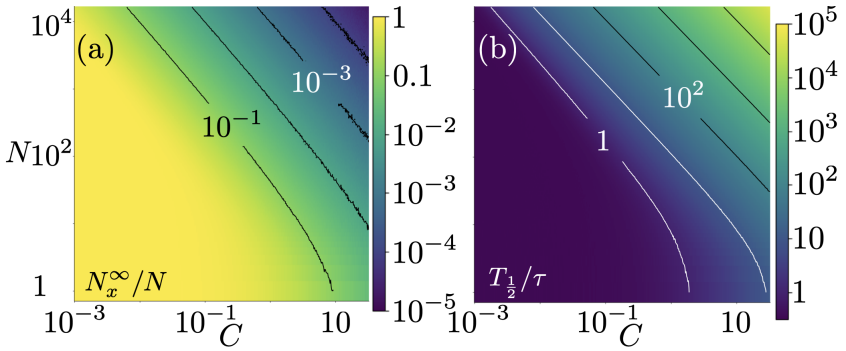


FIGURE 2. – Schéma 1 : (a) Courbe de niveau de la fraction de population finale dans l'état de perte $|x\rangle$, $N_x^\infty/N$, en fonction du nombre $N$ de molécules dans la cavité et de la coopérativité de la molécule unique $C$. (b) Courbe de niveau du temps $T_{\frac{1}{2}}$ nécessaire pour transférer la moitié de la population de l'état $|i\rangle$ en $\tau = \Gamma\Omega^{-2}$. Tous les axes sont logarithmiques.

de Lindblad

$$\partial_t\hat{\rho} = -\mathrm{i}\Big[\hat{H},\hat{\rho}\Big] - \sum_k \mathcal{D}\Big[\hat{L}_k\Big]\hat{\rho} \tag{1}$$

où les termes dissipatifs sont décrits par le dissipateur $\mathcal{D}[\hat{L}]\hat{\rho} = 2\hat{L}\hat{\rho}\hat{L}^\dagger - \hat{L}^\dagger\hat{L}\hat{\rho} - \hat{\rho}\hat{L}^\dagger\hat{L}$.

Dans un cadre en rotation (voir le chapitre 5 pour plus de détails), le Hamiltonien est donné par

$$\hat{H} = \Omega\sqrt{N}\Big(\hat{S}_{ie} + \hat{S}_{ei}\Big) + g\sqrt{N}\Big(\hat{S}_{eg}\hat{a} + \hat{S}_{ge}\hat{a}^\dagger\Big) + \Delta\hat{N}_e + \delta\hat{a}^\dagger\hat{a}, \tag{2}$$

avec les opérateurs collectifs $\hat{S}_{ab} = \sum_n(|a\rangle\langle b|_n)/\sqrt{N}$, $\hat{N}_a = \sum_n |a\rangle\langle a|$, et l'opérateur d'annihilation des photons de la cavité $\hat{a}$ (voir figure 1 pour les autres paramètres). Les opérateurs de Lindblad sont

$$\hat{L}_\kappa = \sqrt{\kappa}\hat{a}\,,\ \hat{L}_g^{(n)} = \sqrt{\gamma_g}\hat{\sigma}_{ge}^{(n)}\,,\ \hat{L}_i^{(n)} = \sqrt{\gamma_i}\hat{\sigma}_{ie}^{(n)}\,,\ \hat{L}_x^{(n)} = \sqrt{\gamma_x}\hat{\sigma}_{xe}^{(n)}\,, \tag{3}$$

avec $\hat{\sigma}_{ab}^{(n)} = |a\rangle\langle b|_n$.

En raison de la dimension de la croissance exponentielles de l'espace de Hilbert $\sim 4^N$ pour $N$ molécules, les simulations exactes sont intraitables pour $N \gtrsim 10$. Afin d'effectuer des simulations à grande échelle, nous avons éliminé de manière adiabatique les états excités de la molécule et de la cavité dans le régime de la petite population d'états excités $\langle\hat{N}_e + \hat{a}^\dagger\hat{a}\rangle \ll 1$. Nous avons trouvé un nouvel Hamiltonien effectif et des opérateurs de Lindblad (voir chapitre 5). De plus, en traitant le transfert de population vers l'état $|x\rangle$ comme un canal de perte, le système est réduit à un ensemble de systèmes à deux niveaux invariants par permutation, qui ont été efficacement simulés en utilisant une simulation de trajectoires quantiques [122].

Au fil du temps, les molécules sont transférées de l'état initial vers les états $|g\rangle$ ou $|x\rangle$. Cette dynamique est illustrée sur la figure 1 pour un laser avec une fréquence constant.

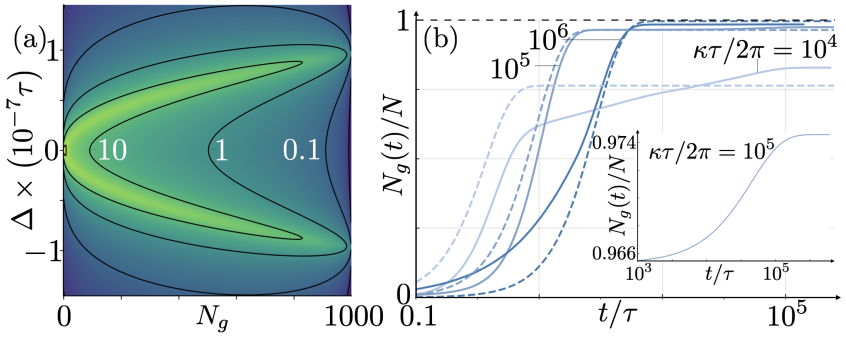


FIGURE 3. – Schéma 2 : (a) Courbe de niveau du taux de décroissance des molécules de Feshbach $\dot{N}_i$ (en unités $\tau^{-1}$, pour les états de Dicke symétriques), en fonction du désaccord du laser et du nombre de molécules de l'état fondamental. La cavité est maintenue en résonance avec l'énergie de transition ($\delta = \Delta$). (b) Evolution temporelle simulée de la population de l'état fondamental pour différents taux de décroissance de la cavité $\kappa$. Les paramètres sont choisis pour $10^3$ molécules de $Rb_2$ à l'intérieur d'une cavité [120, 121]. Lignes tiretées : ajustements analytiques.

Nous pouvons voir que le rendement moléculaire de l'état fondamental, ainsi que le temps de transfert, augmentent avec le nombre de molécules. Le rendement moléculaire dans l'état fondamental devient essentiellement unité pour une grande nombre des molécules $N$. Pour comprendre quantitativement ce comportement, nous avons dérivé des estimations analytiques simples à la fois pour la fraction finale de la population moléculaire dans l'état $|x\rangle$ $N_x^\infty/N = 1 - N_g^\infty/N$ et le temps auquel la moitié de la population a été transférée $T_{1/2}$, comme suit

$$N_x^\infty/N \approx \frac{f_x \ln(N)}{NC}\,, \quad T_{1/2} \sim NC\tau\,, \tag{4}$$

où $f_x = \gamma_x/\Gamma$ avec $\Gamma = \gamma_x + \gamma_g + \gamma_i$ est le facteur de Franck-Condon pour l'état $|x\rangle$ et $C = g^2/(\kappa\Gamma)$ est la coopérativité de la cavité (pour une seule particule). En plus, $\tau = \Omega^2/\gamma$ signifie l'échelle de temps naturelle de la dynamique effective. La figure 2 montre les résultats des simulations numériques en bon accord qualitatif avec les formules ci-dessus.

Nous avons identifié que le ralentissement de la dynamique de transfert peut être attribué à la formation de polaritons dans l'état excité, conduisant à un désaccord effectif entre le laser et l'état excité. Lorsque la population est transférée dans l'état fondamental, l'énergie du polariton se déplace en fonction du temps selon la division de Rabi du vide collectif comme $\sqrt{N_g + 1}g$ [voir figure 3(a)]. Nous pouvons supprimer le ralentissement en suivant cette résonance de polariton dépendante du temps, bien qu'au prix d'une sélectivité d'état plus faible. Dans ce cas, nous trouvons des estimations analytiques

$$N_x^\infty/N \sim \frac{\gamma_x}{\kappa}\,, \quad T_{1/2} \sim \Omega^2/\kappa\,. \tag{5}$$

La figure 3(b) montre une comparaison de la dynamique exacte et de l'estimation analytique, montrant à nouveau un bon accord qualitatif. Surprenant, l'augmentation du taux de perte de cavité $\kappa$ conduit à une plus grande sélectivité d'état.

Enfin, pour des configurations réalistes, nous avons trouvé que pour $10^4$ molécules de RbCs, une fraction d'état fondamental de $\sim 92\%$ après 47ms peut être atteinte avec le première scheme. Pour $10^3$ molécules de $Rb_2$, nous avons trouvé des fractions encore plus élevées, soit $\sim 98\%$ après 5ms, avec une impulsion chirpée. Dans les deux cas, ces résultats sont bien meilleurs que la photo-association sans cavité, et peuvent même dépasser les schémas STIRAP avec des efficacités de l'ordre de $\sim 90\%$.

## Réactions de Transfert d'Électrons Photo-induites Améliorées par une Cavité

Dans le chaiptre 6, nous avons étudié un modèle simple pour les réactions de transfert d'électrons photo-induites dans le cas de nombreuses paires donneur-accepteur qui sont couplées collectivement et de manière homogène à une seule mode d'une cavité [figure 4(a)]. Nous avons analysé les effets collectifs cohérents et dissipatifs résultant de ce couplage avec une équation maîtresse de Lindblad dans le cadre d'optique quantique. Nous avons dérivé une équation de taux effective pour le transfert d'électrons, en éliminant adiabatiquement les états donneur et accepteur et le mode de la cavité. L'équation de taux résultante est valable à la fois pour un couplage au mode de la cavité si faible si fort, et décrit le transfert électronique à travers des états couplés à la cavité et à travers des états sombres non couplés. Le taux de transfert instantané d'électrons dépend de manière non-triviale du nombre de paires dans l'état fondamental qui varie dans le temps. Nous constatons que dans des conditions de résonance appropriées, et en présence d'une pompage incohérente, les taux de réaction peuvent être améliorés par la cavité. Ceci est dû au fait que la cavité est beaucoup plus efficace pour absorber l'énergie de la pompage incohérente que les molécules individuelles.

Nous considérons $N$ molécules couplées à une cavité. Chaque molécule est décrite par quatre niveaux [voir la figure 4(b)]. Initialement, toutes les molécules sont dans leur état fondamental $|G\rangle$. À partir de là, les molécules sont entraînées de manière incohérente vers un état donneur excité $|D\rangle$ à un taux $\Gamma_+$, qui se désintègre pour revenir à l'état fondamental à un taux $\Gamma$. La transition $|G\rangle \leftrightarrow |D\rangle$ est également couplée à une cavité (séparation de Rabi dans le vide d'une seule molécule $2g$), qui est entraînée de manière incohérente à la vitesse $\kappa_+$ et se désintègre à la vitesse $\kappa$. La réaction de transfert d'électrons est décrite par un couplage cohérent $V$ entre l'état donneur excité $|D\rangle$ et un état accepteur excité $|A\rangle$, qui se relaxe ensuite de manière incohérente en un état final $|F\rangle$ au taux $\eta$. La dynamique résultante est décrite par une équation maîtresse de Lindblad (voir ci-dessus) avec un Hamiltonien

$$\hat{H} = g\sqrt{N}\left(\hat{S}_{GD}\hat{a}^\dagger + \hat{S}_{DG}\hat{a}\right) + V\sqrt{N}\left(\hat{S}_{DA} + \hat{S}_{AD}\right), \tag{6}$$

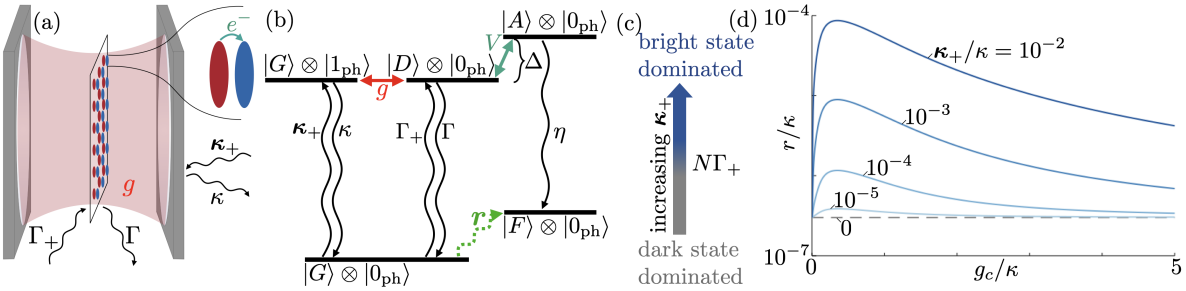


FIGURE 4. – (a) Modèle schématique. $N$ paires donneur (rouge) - accepteur (bleu) sont couplées de manière homogène à une cavité avec une constante de couplage $g$. Chaque paire et la cavité sont pompées de manière incohérente au taux $\Gamma_+$ et $\kappa_+$, et se désintègrent au taux $\Gamma$ et $\kappa$, respectivement. (b) Schéma de niveau d'une molécule unique couplée à la cavité : Chaque paire est décrite comme un système à 4 niveaux avec un état fondamental $|G\rangle$, des états excités donneur ($|D\rangle$) et accepteur ($|A\rangle$), et un état final $|F\rangle$, correspondant au produit de la réaction. Les états à zéro et un photon de la cavité sont désignés respectivement par $|0_{\rm ph}\rangle$ et $|1_{\rm ph}\rangle$. La cavité couple de manière cohérente les états $|G\rangle \otimes |1_{\rm ph}\rangle$ et $|D\rangle \otimes |0_{\rm ph}\rangle$ avec la force $g$, tandis que le couplage cohérent entre $|D\rangle \otimes |0_{\rm ph}\rangle$ et $|A\rangle \otimes |0_{\rm ph}\rangle$ avec la force $V$ et le désaccord $\Delta$ induit le transfert d'électrons. Après l'élimination adiabatique, toute la dynamique cohérente et dissipative peut être capturée par un taux de transfert effectif $r$ de la population de $|G\rangle$ à $|F\rangle$ (flèche verte pointillée). (c) Pour une augmentation de $\kappa_+$, la dynamique passe d'une dominance d'états sombres à une dominance d'états polaritoniques au-dessus de $\kappa_+ \gtrsim N\Gamma_+$. (d) Taux de transfert $r$ sur une échelle logarithmique en fonction du couplage collectif de la cavité $g_c = \sqrt{N}g$ pour différents taux de pompage de la cavité $0 \leq \kappa_+ \leq 10^{-2}\kappa$ avec $N = 10^4$, $\Gamma = 3 \times 10^{-7}\kappa$, $\Gamma_+ = 10^{-4}\Gamma$, $\Delta = 0.2\kappa$, $V = 0.1\kappa$, et $\eta = 10^{-2}\kappa$.

et des opérateurs de Lindblad

$$\hat{L}_\kappa = \sqrt{\kappa}\hat{a}\,,\ \hat{L}_{\kappa_+} = \sqrt{\kappa_+}\hat{a}^\dagger\,, \tag{7}$$

$$\hat{L}_\Gamma^{(n)} = \sqrt{\Gamma}\hat{\sigma}_{GD}^{(n)}\,,\ \hat{L}_{\Gamma_+}^{(n)} = \sqrt{\Gamma_+}\hat{\sigma}_{DG}^{(n)}\,,\ \hat{L}_\eta^{(n)} = \sqrt{\eta}\hat{\sigma}_{FA}^{(n)}\,. \tag{8}$$

Nous avons ensuite procédé à l'élimination des deux états excités $|D\rangle$ et $|A\rangle$ et de la cavité pour trouver un taux de transfert effectif $r$, qui décrit le transfert de population unidirectionnel incohérent de l'état fondamental $|G\rangle$ à l'état final $|F\rangle$. Ce taux de transfert a deux contributions $r = r_{\text{cav}} + r_{\text{ind}}$. Une contribution décrit le pompage direct des molécules individuelles par $\hat{L}_{\Gamma_+}$, qui est à peine modifié par la cavité, et l'autre contribution décrit le transfert à travers la cavité induit par $\hat{L}_{\kappa_+}$. Le contribution de la cavité peut dominer si $\kappa_+ \gg N\Gamma_+$, comme l'indique la figure 4(c). Dans ce cas, le taux de transfert peut être multiplié par plusieurs. Il est important de noter que nous trouvons une force de couplage de cavité optimale proche de la limite du couplage fort [figure 4(d)].

La dépendance des paramètres de la contribution de la cavité $r_{\text{cav}}$ est illustrée à la figure 5. Le panneau (a) montre à nouveau que le taux de transfert est le plus élevé pour un équilibre optimal entre le taux de décroissance de la cavité $\kappa$ et la force de couplage collectif de la cavité $g_c$, et qu'il est supérieur au taux de transfert sans cavité sur un grand régime de paramètres. Le panneau (b) montre une condition de résonance, c'est-à-dire que le taux de transfert est le plus élevé lorsque le désaccord des états donneur et accepteur est égal à la moitié de la division de Rabi $V = g_c$. Les panneaux (c) et (d) montrent la dépendance du couplage de la cavité $g$ et du nombre de molécules dans l'état fondamental $N$. Dans le panneau (c), la force de couplage de la cavité pour une seule molécule est maintenue constante, de sorte que les lignes pour un $N$ constant peuvent être considérées comme le taux de transfert variant dans le temps $r_{\text{cav}}$ lorsque les molécules sont transférées à partir de l'état initial. Nous pouvons voir que pour une diminution de $N$ et une augmentation de $g$, le taux de transfert augmente généralement. Le panneau (d) montre ce qui se passe si, au lieu de $g$, on fait varier $g_c = \sqrt{N}g$. Dans ce cas, une résonance claire est visible pour les petits $N$ qui disparaît pour les grands $N$ car pour $N\Gamma_+ > \kappa_+$ le canal sans cavité domine. Les panneaux (e) et (f) sont des coupes à travers les panneaux (c) et (d), respectivement, montrant en détail la dépendance de $N$ pour un $g$ ou un $g_c$ fixes.

## Intrication vibratoire améliorée par le désordre

Dans le chaiptre 9, nous avons étudié l'importance des effets quantiques dans la dynamique vibratoire en étudiant l'intrication entre les degrés de liberté nucléaires et électroniques. Un tel intrication est souvent négligé, par exemple en calculant la dynamique de champ moyenne d'Ehrenfest. Nous avons découvert que le désordre peut fortement augmenter l'accumulation de ce intrication sur de courtes échelles de temps après une photo-excitation incohérente. Nous avons constaté que cela peut avoir des conséquences directes sur la dynamique des coordonnées de réaction. Nous avons analysé ce phénomène dans un modèle désordonné de Holstein-Tavis-Cummings (HTC), un modèle jouet

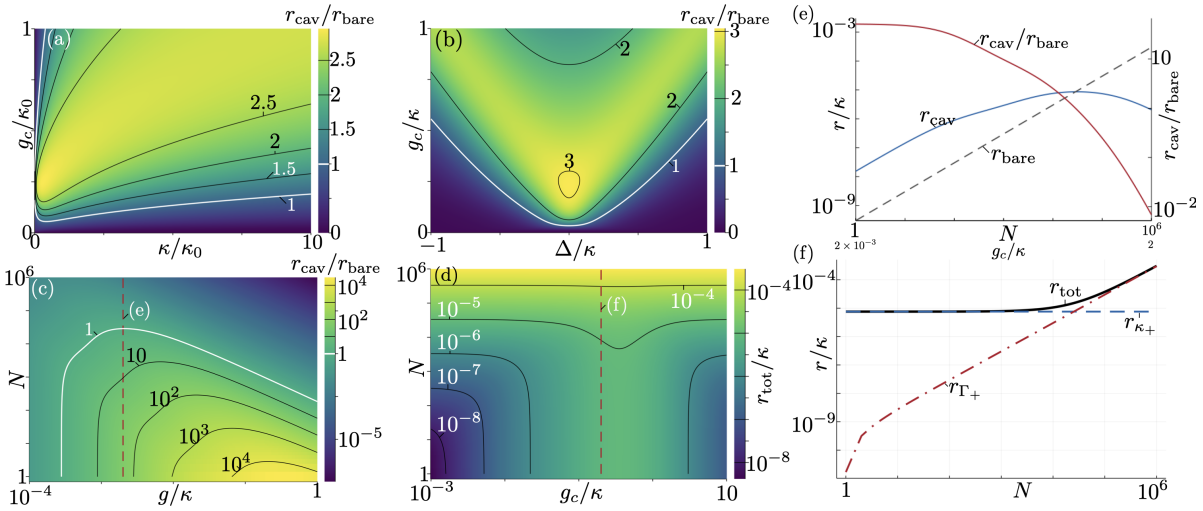


FIGURE 5. – Modification du taux de transfert par la cavité. Courbes de niveau du taux de transfert $r_{\mathrm{cav}}/r_{\mathrm{bare}}$ (a, b, c) et $r_{\mathrm{tot}}/\kappa$ (d). On obtient $r_{\mathrm{cav}}$ en définissant $\kappa_+ = 10^{-3}\kappa$ et $\Gamma_+ = 0$ ; on obtient $r_{\mathrm{bare}}$ en définissant $\kappa_+ = 0$, $\Gamma_+ = 10^{-3}\Gamma$ et $g = 0$ ; on obtient $r_{\mathrm{tot}}$ en définissant $\kappa_+ = 10^{-3}\kappa$, $\Gamma_+ = 10^{-3}\Gamma$. Nous définissons des unités normalisées $\kappa_0$ (par exemple $\kappa_0 = 1\,\mathrm{eV}$) et fixons : $V = 0{,}1\kappa_0$, $\Gamma = 3 \times 10^{-7}\kappa_0$, et $\eta = 10^{-2}\kappa_0$. Les lignes noires et blanches sont les contours du renforcement constant de la cavité comme indiqué dans la barre de couleur, les lignes blanches correspondent à $r_{\mathrm{cav}} = r_{\mathrm{bare}}$. (a) $r_{\mathrm{cav}}/r_{\mathrm{bare}}$ en fonction de $g_c$ et $\kappa$ pour $N = 10^4$ et $\Delta = 0{,}2\kappa_0$. (b) $r_{\mathrm{cav}}/r_{\mathrm{bare}}$ en fonction de $g_c$ et $\Delta$ pour $N = 10^4$ et $\kappa = \kappa_0$. (c) $r_{\mathrm{cav}}/r_{\mathrm{bare}}$ en fonction de $N$ et $g$ pour $\Delta = 0{,}2\kappa_0$ et $\kappa = \kappa_0$ (échelle logarithmique pour tous les axes et barre de couleur). (d) $r_{\mathrm{tot}}/\kappa$ en fonction de $N$ et $g_c$ pour $\Delta = 0{,}2\kappa_0$ et $\kappa = \kappa_0$. (e) $r_{\mathrm{cav}}$ (bleu plein, axe de gauche) et $r_{\mathrm{bare}}$ (gris tiretée, axe de gauche) et $r_{\mathrm{cav}}/r_{\mathrm{bare}}$ (rouge plein, axe de droite) en fonction de $N$, correspondant à une coupe (ligne en traits mixtes rouge) dans (c) avec $g = 2 \times 10^{-3}\kappa_0$. L'axe horizontal indique $g_c = g\sqrt{N}$ comme deuxième échelle (échelle logarithmique sur tous les axes). (f) Coupe à travers (d) équivalent à (e). On maintient $g_c$ constant en choisissant $g = g_c/\sqrt{N}$.

minimal qui inclut tous les degrés de liberté fondamentaux. À l'aide d'une technique numérique basée sur les états de reseaux tensoriels, nous avons simulé la dynamique quantique exacte de plus de 100 molécules. Nos résultats soulignent l'importance d'aller au-delà des théories de Born-Oppenheimer dans la chimie polaritonique.

Le modèle HTC décrit $N$ molécules avec deux niveaux électroniques $|g\rangle$ et $|e\rangle$, qui sont couplés à une seule coordonnée vibrationnelle (opérateur de destruction $\hat{b}$). De plus, la transition entre les deux niveaux électroniques est couplée à une cavité monomodale (opérateur d'annihilation $\hat{a}$). En résonance et dans un cadre rotatif, l'Hamiltonien du modèle HTC désordonné est (voir chapitre 7 pour plus des détails)

$$\hat{H} = \sum_n \left[ g\hat{a}\hat{\sigma}_{eg}^{(n)} + g\hat{a}^\dagger\hat{\sigma}_{ge}^{(n)} + \nu\hat{b}_n^\dagger\hat{b}_n - \lambda\nu\hat{\sigma}_{ee}^{(n)}\left(\hat{b}_n^\dagger + \hat{b}_n\right) + \epsilon_n\hat{\sigma}_{ee}^{(n)}\right]. \tag{9}$$

Ici, $g$ est la force de couplage de la cavité de la molécule unique, $\nu$ est la fréquence vibratoire, $\lambda$ est la force de couplage vibronique, et $\epsilon_n$ sont des énergies distribuées de manière gaussienne avec une moyenne de 0 et un écart type de $W$ [voir la figure 6(a) pour le modèle moléculaire].

Nous étudions la dynamique cohérente à temps courts après une excitation initiale de la cavité (état initial $\hat{a}^\dagger|G\rangle$) ou d'une seule molécule (état initial $\hat{\sigma}_{eg}^{(1)}|G\rangle$), où $|G\rangle$ est l'état fondamental total.

Conformément aux études précédentes [123, 124], nous constatons que le désordre améliore le transfert de l'excitation de la molécule ou de la cavité initialement excitée vers le collecteur de l'état sombre, comme l'indique schématiquement dans la figure 6(b). La figure 6(c) montre la moyenne de la probabilité de transfert à partir de l'état initial sur une période d'oscillation vibratoire, qui augmente avec le désordre $W$. Comme nous le verrons plus loin, ce transfert d'excitation a un impact significatif à la fois sur la dynamique vibratoire et sur l'intrication vibratoire, qui est indiqué schématiquement dans la figure 6(d).

Dans un état pur, l'intrication peut être mesurée par l'entropie d'intrication, qui est nulle dans un état de produit, et maximale dans un état d'intrication maximale. Pour $d$ degrés de liberté, l'entropie d'intrication prend des valeurs entre 0 et $\log_2(d)$. Ici, nous étudions l'entropie d'intrication entre les degrés de liberté collectifs électronique et photonique d'un côté et vibrationnel de l'autre.

La figure 7 montre la dynamique de transfert de vibrations et d'excitation pour les deux états initiaux différents. Si une molécule est initialement excitée, nous constatons que toutes les autres molécules subissent une petite dynamique vibrationnelle. Cette dynamique vibratoire est considérablement accrue par rapport au scénario sans désordre et est la plus importante pour les molécules en résonance énergétique avec la molécule initialement excitée. De manière analogue, le transfert d'excitation est le plus important vers les molécules en proximité énergétique avec la molécule initialement excitée [voir panneau (b)]. Si la cavité est initialement excitée [voir panneaux (c) et (d)], toutes les molécules subissent une dynamique vibratoire beaucoup plus importante, qui est considérablement renforcée par rapport au scénario sans désordre. Une fois encore, la dynamique vibratoire est plus importante sur les molécules auxquelles une plus grande

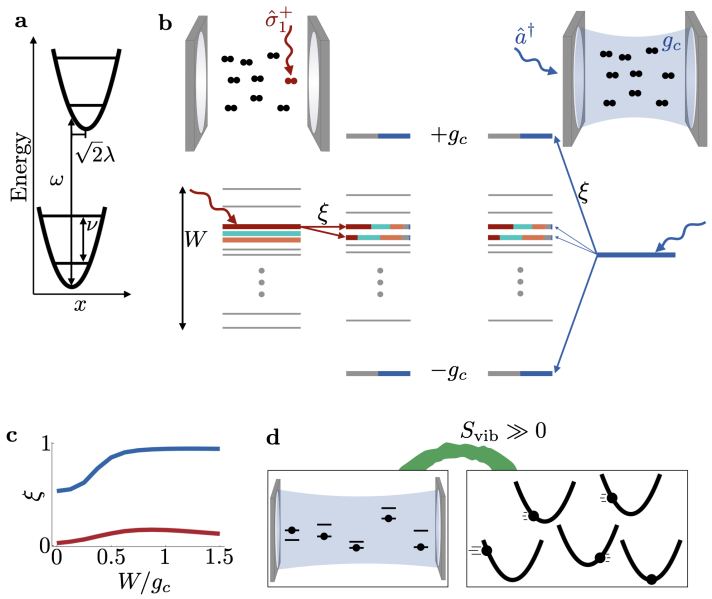


FIGURE 6. – **a** Nous considérons des molécules de modèle-jouet avec deux surfaces d'énergie potentielle harmoniques (espacement des niveaux vibrationnels $\nu$). Les deux surfaces sont séparées énergiquement par l'espacement de niveau électronique $\omega$ et déplacées de $\sqrt{2}\lambda$ le long de la coordonnée de réaction $x$. **b** Un ensemble de molécules est couplé à une cavité avec une force collective $g_c$. Nous analysons la dynamique après photo-excitation incohérente d'une molécule individuelle (rouge, gauche) ou de la cavité (bleu, droite). Un schéma de niveaux d'énergie pour les excitations électroniques et photoniques est esquissé. Le désordre conduit à un élargissement inhomogène par $W$ (gauche). Le couplage de $N$ états d'excitation électronique (à gauche ; lignes grises, rouges, cyan, orange) et d'une excitation unique de la cavité (à droite ; ligne bleue) conduit à de nouveaux états propres (au centre) qui sont des superpositions avec des contributions indiquées par les différentes couleurs. Pour $g_c \gg W$, deux états polaritons aux énergies $\pm g_c$ sont formés (moitié gris, moitié bleu), ainsi que $N-1$ états sombres (autres lignes). En raison du désordre, les états sombres sont des superpositions de quelques excitations électroniques énergiquement résonantes. Tous les états sombres acquièrent un petit poids de photons (très petite contribution bleue). Après une excitation incohérente, l'énergie est transférée à travers les états propres couplés comme indiqué par les flèches droites (probabilité de transfert $\xi$). Pour une excitation de molécule, l'énergie est principalement transférée par les états sombres, pour une excitation de cavité par les états polaritons (épaisseur de la flèche). **c** Le désordre augmente le transfert à partir de l'état initialement excité après l'excitation de la molécule (rouge) ou de la cavité (bleu). Le graphique montre une probabilité de transfert moyenne dans le temps : $\xi = \nu/(2\pi) \int_0^{2\pi/\nu} dt\, [1 - \langle \hat{O}^\dagger \hat{O} \rangle(t)]$ où $\hat{O} = \hat{\sigma}_1^-, \hat{a}$ dans un système de 100 molécules. **d** Le transfert d'excitation conduit à une oscillation cohérente déphasée des différentes molécules et donc à une grande entropie d'intrication, $S_{\rm vib}$, entre les degrés de liberté électronique et photonique (à gauche) et vibrationnel (à droite).

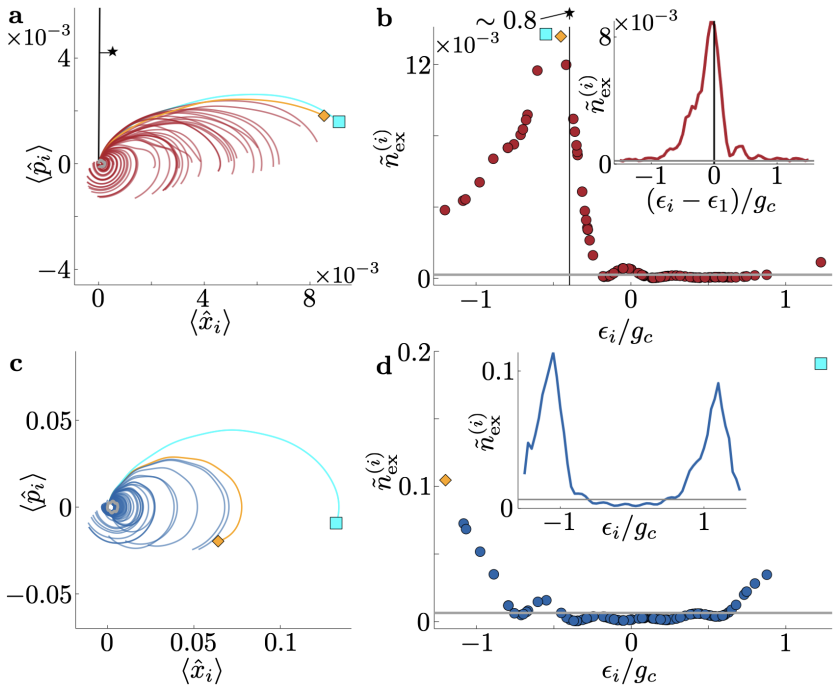


FIGURE 7. – **Dynamique de transfert d'excitation. a** Dynamique vibrationelle dans l'espace de phase microscopique de 100 oscillateurs moléculaires pour une réalisation de désordre unique avec $W = g_c/2$. L'étoile et la ligne noires correspondent à la molécule initialement excitée, les autres lignes aux 99 molécules initialement non excitées. La ligne grise (à peine visible autour de l'origine) représente la référence $W = 0$. Le carré cyan et le carreau orange sont deux exemples de molécules dont la dynamique vibratoire est la plus fortement modifiée, également identifiées dans **b**. **b** Probabilité d'excitation $\tilde{n}_{\rm ex}^{(i)} = \langle \hat{\sigma}_i^+ \hat{\sigma}_i^- \rangle (t = 2\pi/\nu)$ en fonction du décalage énergétique $\epsilon_i$ de la molécule respective. L'encart montre la probabilité d'excitation moyennée par le désordre en fonction de la différence d'énergie par rapport à l'état initialement excité. Les lignes horizontales grises représentent la référence $W = 0$. **c**,**d** tracés identiques pour une excitation de cavité. Paramètres : $N = 100$, $\nu = 0.3 g_c$, $\lambda = 0.4$, désordre tiré d'une distribution normale avec l'écart type $W$, 256 réalisations du désordre.

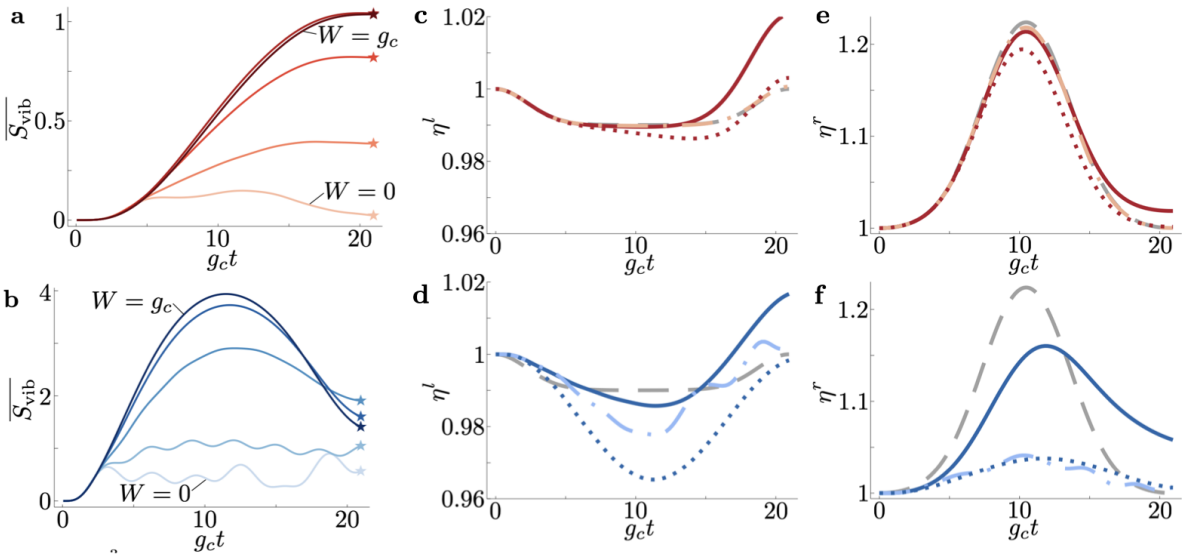


FIGURE 8. – **Dynamique de l'intrication et des queues integrées. a**,**b** Évolution temporelle de l'entropie d'intrication moyennée par le désordre $\overline{S_{\rm vib}}$ dans l'intervalle de temps $0 \leq t \leq 2\pi/\nu$ pour des valeurs de désordre $0 \leq W \leq g_c$ (de clair à sombre $W = 0$, $g_c/4$, $g_c/2$, $3g_c/4$, $g_c$). Les étoiles indiquent le temps final $t = 2\pi/\nu$. Les panneaux de hautes (lignes rouges) correspondent à l'état d'excitation initial de la molécule $|\psi_0^m\rangle$, les panneaux de bas (lignes bleues) à l'excitation initiale de la cavité $|\psi_0^c\rangle$. **c**,**d** Évolution temporelle de la queue gauche intégrée $\eta^l$. La ligne continue sombre représente l'évolution temporelle exacte moyennée par le désordre pour $W = g_c/2$, tandis que la ligne pointillée sombre montre les résultats équivalents calculés avec une approximation de champ moyen. La ligne en traits mixtes claire montre les résultats pour $W = 0$. La ligne tiretée grise correspond à la référence sans cavité.**e**,**f** Évolution temporelle de l'intégral la queue droite $\eta^r$ avec des styles de lignes analogues. Les paramètres sont $N = 100$, $\lambda = 0.4$, et $\nu = 0.3 g_c$. Moyenne sur 256 réalisations du désordre.

quantité d'excitation a été transférée. Or, ce transfert est plus important pour les molécules qui sont approximativement résonantes avec les états polaritoniques.

La figure 8 (a) et (b) montre la dynamique de l'intrication vibrationnelle pour différentes forces de désordre pour les deux états initiaux. Sans désordre, l'intrication reste faible à tout moment, mais pour un désordre croissant, l'intrication augmente de manière significative. Les panneaux (c) à (f) montrent les poids de queue gauche (c/d) et droite (e/f), définis comme suit

$$\eta^{l/r}(t) = \mp \sum_n \int_{x_{\rm thr}^{l/r}}^{\mp\infty} dx_n P_n(x_n, t)\,. \tag{10}$$

Ici, $x_{\rm thr}^{l/r} \approx \mp 1.6$ sont des coupures telles que le poids de la queue de l'état fondamental est de $N/100$. $P_n(x_n, t)$ est l'amplitude de probabilité de trouver la coordonnée vibration-

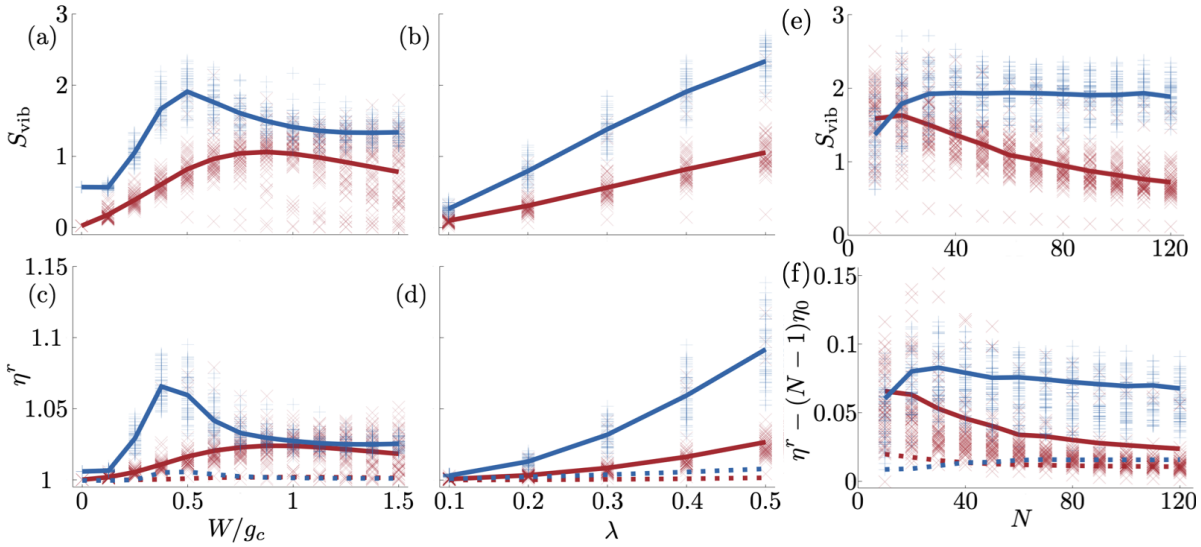


FIGURE 9. – Les panneaux supérieurs (a, b, e) montrent l'entropie d'intrication $S_{\mathrm{vib}}$, tandis que les panneaux inférieurs (c, d, f) montrent le poids de la queue de droite $\eta^r$ en fonction de la force de couplage vibronique $\lambda$ (a, c), de la largeur du désordre $W$ (b, d), et du nombre de molécules $N$ (e, f), évalué au temps $t = 2\pi/\nu$. Les symboles « × » rouges correspondent à une excitation moléculaire, les symboles « + » bleus correspondent à une excitation de la cavité. Les symboles représentent des réalisations individuelles de désordre. La ligne continue est un guide pour l'œil à travers les moyennes de toutes les 256 réalisations de désordre. Les lignes en pointillés dans les panneaux c, d et f représentent les résultats de champs moyenne moyenné par le désordre pour référence. $\eta_0 = 10^{-2}$ est le poids de la queue dans l'état fondamental. Les paramètres sont $N = 100$, $\nu = 0.3g_c$, $\lambda = 0.4$, et $W = g_c/2$ sauf indication contraire.

nelle à la position $x_n$ au temps $t$. Pour une molécule initialement excitée, sans désordre, la dynamique des queues est très similaire à la dynamique sans cavité [panneau (c)]. Cependant, en présence de désordre, la dynamique des queues change, et les deux queues sont augmenté après une période vibratoire. Pour une cavité initialement excitée, la dynamique de la queue droite est fortement supprimée. En présence de désordre, cependant, cette suppression ne subsiste pas, mais le pic sans cavité est élargi et décalé vers la droite. Il est important de noter qu'en présence de désordre, les prédictions d'un ansatz de champ moyen négligeant l'intrication sont fausses dans tous les scénarios.

La figure 9 est une image plus quantitative de ces résultats en montrant à la fois l'intrication et la queue droite après une période d'oscillation en fonction du couplage vibronique $\lambda$, du désordre $W$ et du nombre de molécules $N$. Nous avons trouvé une correspondance claire entre la queue droite et l'intrication vibratoire. Les deux quantités augmentent avec l'augmentation du couplage vibronique. Avec le désordre, les deux quantités ont un pic à une force de désordre intermédiaire $\sim g_c/2$, et un plateau pour

un grand désordre pour une cavité initialement excitée, alors que le pic n'existe pas pour une molécule initialement excitée. Pour une augmentation de $N$, les modifications de l'intrication et de la queue sont importantes si la cavité est initialement excitée, cependant, pour une molécule unique initialement excitée, les modifications disparaissent. Encore une fois, dans tous les cas, l'approximation du champ moyen est complètement fausse.

## Modèle HTC avec plusieurs excitations

Nous avons également étudié le modèle HTC sans désordre dans le scénario de multi-excitation. Nous avons étudié l'effet de la fraction d'excitation et du couplage vibronique sur la dynamique vibrationnelle et d'intrication, ainsi que l'approximabilité des systèmes par un ansatz de champ moyen vibrationnel. Nous avons trouvé que la dynamique vibratoire moyenne est bien décrite par un ansatz de champ moyen, tant que le couplage vibronique n'est pas trop grand. Nous avons utilisé l'ansatz de champ moyen pour estimer le transfert de l'excitation et de la dynamique vibratoire entre les molécules, et nous avons trouvé qu'il est le plus important si environ la moitié du système est initialement excité.

Nous avons étudié l'évolution temporelle du modèle HTC avec une nombre d'excitations $N_{\text{exc}}$ à partir de l'état initial $\prod_{n=1}^{N_{\text{exc}}} \hat{\sigma}_{eg}^{(n)} |G\rangle$, représenté schématiquement sur la figure 10(a). Nous avons analysé l'entropie de von Neumann entre les différents degrés de liberté, comme l'indique la figure 10(b).

Dans le chaiptre 8, nous avons calculé la dynamique en utilisant trois méthodes différentes : Une simulation MPS numériquement exacte comme référence exacte, une simulation de champ moyen (état produit, PS) négligeant tout intrication vibratoire, et une approximation de polariton rotatif (RPA) négligeant également la dynamique électrophotonique rapide. Cette hiérarchie est illustrée sur la figure 10 (c) et (d). Alors que les trois approximations reproduisent la réduction de la dynamique vibratoire par rapport au scénario sans cavité, seules la MPS et la PS reproduisent les détails de la dynamique vibratoire. Pour $N_{\text{exc}} = N$, la figure 10(e) montre la dynamique d'intrication, illustrant que l'intrication est la plus importante entre les degrés de liberté électroniques et photoniques, tandis que l'intrication vibrationnelle reste faible.

Cela change pour $N_{\text{exc}} < N$, comme le montre la figure 11. Dans ce cas, même pour de petits $\lambda\nu$, l'entropie d'intrication vibrationnelle est importante par rapport aux autres entropies [voir panneau (a)]. Pour une augmentation de $\lambda\nu$, $S_{\text{vib}}$ augmente davantage [voir les panneaux (b) à (d)]. Par conséquent, alors que pour un petit couplage vibronique, la dynamique moyenne est bien approximée par un ansatz de champ moyen, pour de grands $\lambda\nu$, cet ansatz échoue complètement [panneaux (e) à (h)]. De manière surprenante, pour $N_{\text{exc}} = N$, nous trouvons toujours un bon accord (non montré ici, voir Chapitre 8).

Pour les $\lambda\nu$ intermédiaires, nous avons également utilisé la simulation de champ moyen pour calculer le transfert d'excitation et les amplitudes vibrationnelles de la figure 12. Pour les petites fractions d'excitation, les excitations et la dynamique vibrationnelle res-

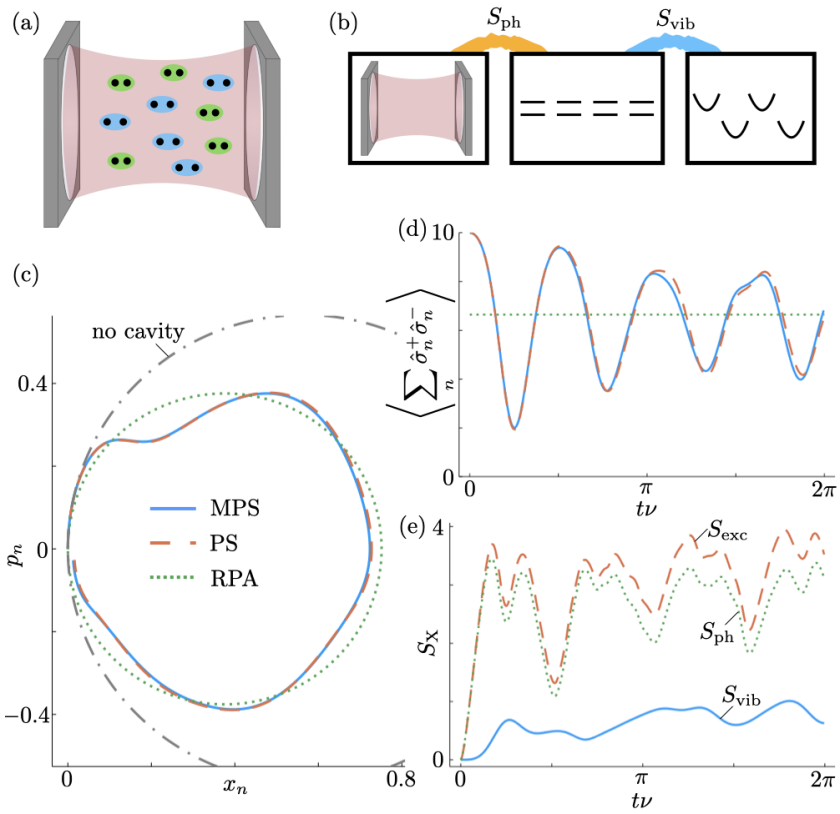


FIGURE 10. – Vue d'ensemble de la configuration. (a) Configuration schématique et état initial. (b) Illustration des degrés de liberté et des entropies d'intrication $S_{\mathrm{ph}}$ et $S_{\mathrm{vib}}$. (c) Évolution vibrationelle dans l'espace de phase dans les différents modèles, en unités du mouvement du point zéro. Pour comparaison, la ligne d'absence de cavité est également représentée (« no cavity ») (d) Nombre d'excitation dans les différents modèles. L'approximation du polariton rotatif traite l'excitation comme constante. (e) Évolution de l'entropie d'intrication de différentes partitions du système.

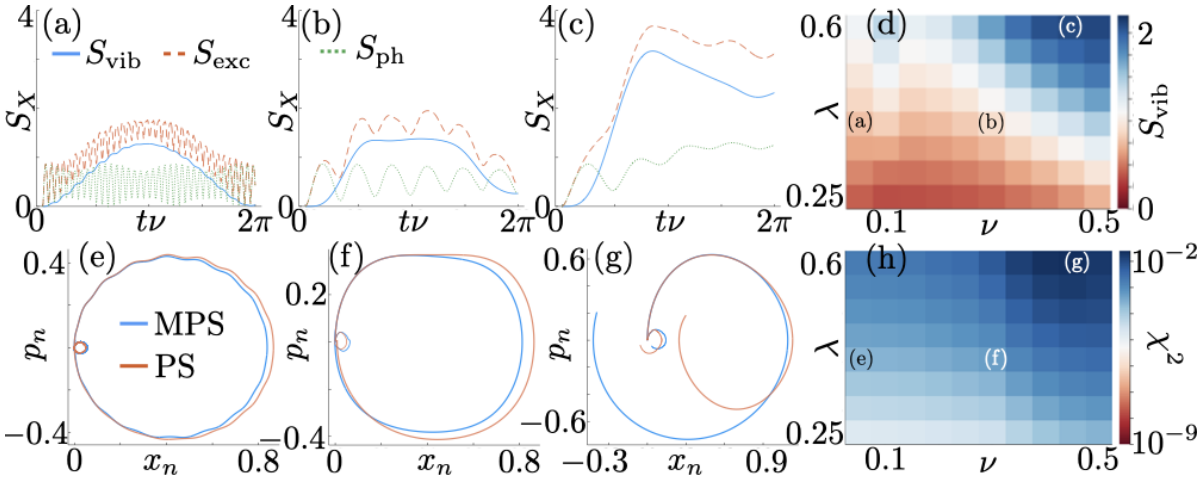


FIGURE 11. – Dynamique d'intrication et des vibration dans le modèle HTC. Nous considérons 10 molécules avec $N_{\text{exc}} = 2$, et fixons $g_c = 1$. (a) à (c) montrent l'évolution temporelle des entropies d'intrication $S_{\text{vib}}$ (bleu, continu), $S_{\text{exc}}$ (orange, tiretée), et $S_{\text{ph}}$ (verte, pointillée) pour différentes valeurs de $\lambda$ et $\nu$ indiquées en (d). (d) montre la dépendance de l'entropie vibrationnelle moyenne dans le temps $\overline{S_{\text{vib}}}$ par rapport à $\lambda$ et $\nu$ . (e) à (g) montrent les trajectoires dans l'espace de phase de la vibration d'une seule molécule calculées avec MPS (continu, bleu), PS (tiretée, orange), et RPA (pointillée, vert), pour différentes valeurs de $\lambda$ et $\nu$ . La figure (h) donne l'erreur de la dynamique vibratoire (détails dans le chapitre 8).

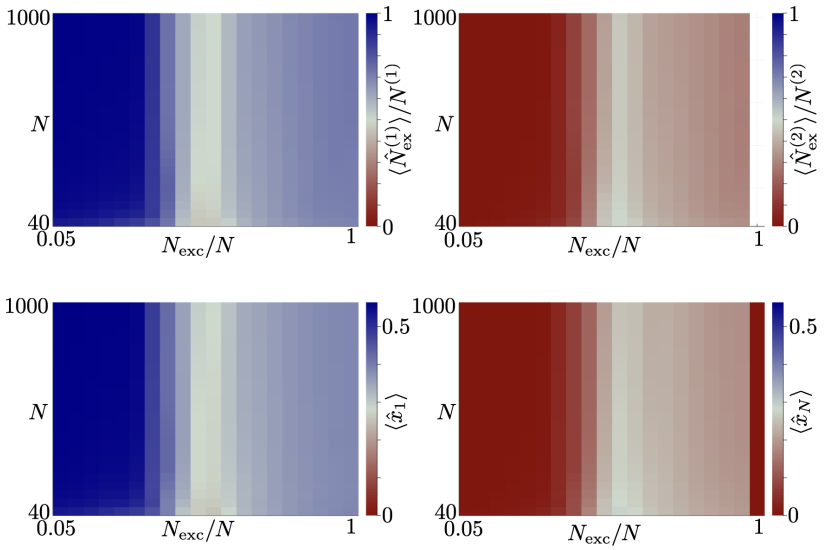


FIGURE 12. – Dépendance des fractions de déplacement et d'excitation du nombre de molécules et la fraction d'excitation initiale. $g_c = 1$, $\lambda = 0.4$, $\nu = 0.3$. $\hat{N}_{\text{exc}}^{(1)} = \sum_{n=1}^{N_{\text{exc}}} \hat{\sigma}_n^+ \hat{\sigma}_n^-$. $N^{(1)} = N_{\text{exc}}$, $N^{(2)} = N - N_{\text{exc}}$ Simulations de champs de moyenne.

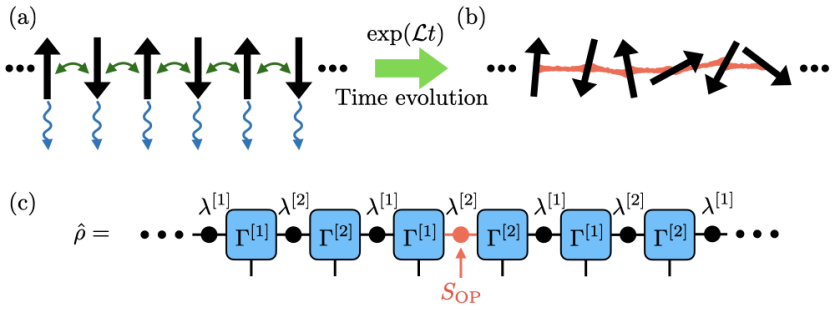


FIGURE 13. – Modèle schématique et simulation. (a) Nous considérons une chaîne de spins infinie avec des interactions entre voisins les plus proches (doubles flèches vertes) et un déphasage (flèches bleues), qui est initialement dans un état Néel. (b) Après quelques temps, le système évolue d'un état pur vers un état mixte avec des corrélations entre les spins, indiquées par les connexions rouges. (c) La chaîne de spins est simulée en utilisant un MPS infini comme décrit dans la section 4.5. L'intrication des opérateurs est déterminée par les tenseurs $\lambda$, comme indiqué en rouge.

tent localisées sur les états initialement excités, ce qui est cohérent avec la discussion de la section précédente sur le transfert d'excitation sans désordre. Lorsque environ la moitié des molécules sont initialement excitées $N_{\text{exc}}/N \sim 1/2$, le transfert de la dynamique vibratoire et des excitations est le plus important. Une augmentation supplémentaire de $N_{\text{exc}}/N$ réduit à nouveau le transfert d'excitation, mais ne le ramène pas à 0.

## Croissance logarithmique de l'intrication des opérateurs sous déphasage

Dans le chaiptre 11, nous avons commencé à étudier l'évolution temporelle de l'intrication des opérateurs dans les systèmes quantiques ouverts, en particulier sous déphasage. Nous avons découvert que si l'aimantation est conservée, après une hausse et une baisse initiales, l'intrication des opérateurs croît à nouveau de manière logarithmique. En particulier, dans le modèle XXZ, nous avons trouvé que cette croissance logarithmique a un préfacteur universel 1/4, indépendant des paramètres spécifiques.

Nous étudions un système ouvert qui évolue selon l'équation maîtresse. En particulier, nous avons examiné l'Hamiltonien

$$\hat{H} = \frac{1}{4}\sum_i \left(J_x \hat{\sigma}_i^x \hat{\sigma}_{i+1}^x + J_y \hat{\sigma}_i^y \hat{\sigma}_{i+1}^y + J_z \hat{\sigma}_i^z \hat{\sigma}_{i+1}^z\right) + \frac{h_z}{2}\sum_i \hat{\sigma}_i^z \,, \tag{11}$$

avec $\hat{\sigma}^{x/y/z}$ matrices de Pauli. Nous considérons le modèle XXZ $J_x = J_y$ et $h_z = 0$, le modèle XYZ $J_x \neq J_y$ et $h_z = 0$, et le modèle d'Ising à champ transverse avec $J_y = J_z = 0$. Nous appelons en outre $J = J_x$. Nous nous intéressons à un type particulier de

dissipation, le déphasage, qui apparaît lorsque le couplage avec l'environnement conserve l'aimantation

$$\hat{L}_i = \sqrt{\frac{\gamma}{2}}\hat{\sigma}_i^z \,. \tag{12}$$

Ce modèle décrit une chaîne de spins interagissant avec son environnement, comme l'indique schématiquement dans la figure 13(a) et (b). Nous étudions la dynamique d'une état initial Néel dans l'orientation $x$ ou $z$ [figure 13(b)].

Nous nous intéressons à la simulabilité du système à l'aide de réseaux tensoriels comme indiqué dans la figure 13(c). Dans ce cas, la simulabilité peut être quantifiée par l'intrication des opérateurs (OE), qui est essentiellement l'entropie de von Neumann des matrices de densité réinterprétées comme des états [voir la figure 13(c) ainsi que les Chapitres 4 et 11 pour plus de détails].

Dans le modèle XXZ pour une état initial Néel dans l'orientation $z$ et avec de petits taux de déphasage, nous constatons que initialement, l'OE croît rapidement, puis décroît et connaît une lente croissance logarithmique aux temps longs [figure 14(a)]. Cette croissance logarithmique est trouvée pour toutes différentes valeurs de $J_z$ et $\gamma$, mais le pic initial et le décalage dépendent de ces deux quantités. Cela contraste avec les modèles d'Ising avec champ transverse et XYZ qui ne conserve pas l'aimantation. Pour ces modèles, l'OE décroît jusqu'à une constante aux temps longs. Pour un état initial Néel dans l'orientation $x$ sans magnétisation bien définie, l'OE décroît jusqu'à zéro. De plus, nous constatons que sur une large gamme de paramètres, le préfacteur de la croissance logarithmique devient 1/4 aux temps longs [voir figure 14(c) et (d)]. Au Chapitre 11, nous expliquons l'origine de ce préfacteur.

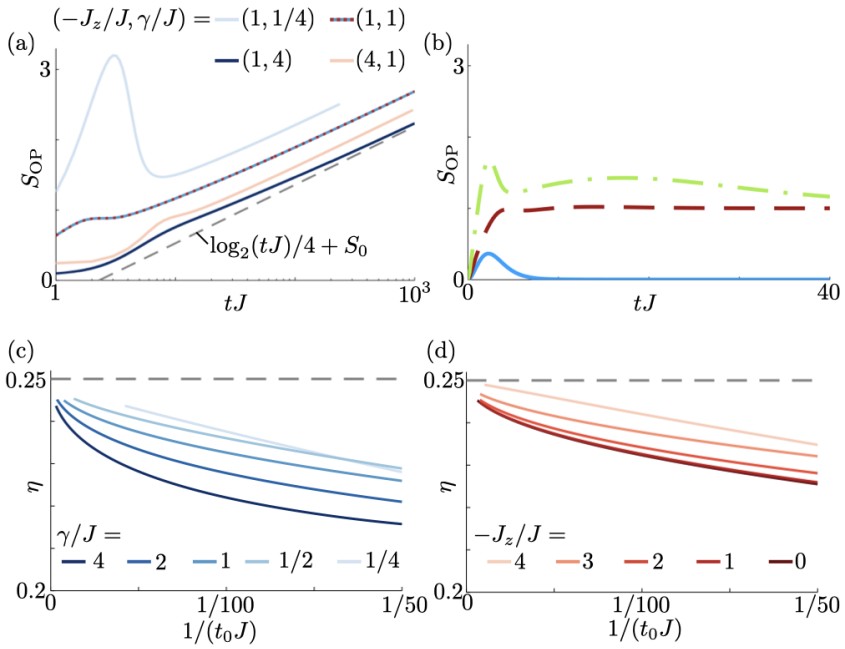


FIGURE 14. – Évolution temporelle de l'intrication des opérateurs $S_{\mathrm{OP}}$. (a) Évolution temporelle pour différents paramètres dans le modèle XXZ, avec un état initial de Néel dans la direction $z$ (axe de temps logarithmique). Aux temps longs, on trouve une croissance logarithmique avec le préfacteur 1/4. (b) Intrication des opérateurs pour différents scénarios. Ligne bleue pleine : Modèle XXZ avec l'état initial de Néel dans la direction $x$ ($J_z = -J/2$, $\gamma = J/2$) ; ligne tiretée rouge : modèle d'Ising à champ transverse avec l'état initial de Néel dans la direction $z$ ($h_z = J$, $\gamma = J/2$) ; ligne en traits mixtes verte : Modèle XYZ avec état initial de Néel dans la direction $z$ ($J_y = 0,8J$, $J_z = -J/2$, $\gamma = J/2$). (c),(d) Préfacteur de la croissance logarithmique aux temps longs. Les tangentes aux courbes d'intrication des opérateurs dans le panneau (a) $\eta \log_2(tJ) + S_0$ au temps $t_0$ sont calculées en fonction du temps inverse. Dans le panneau (c), $J_z = -J$ est fixé et $\gamma$ varie, tandis que dans le panneau (d), $\gamma = J$ est fixé et $J_z$ varie. Les lignes tiretée grises sont des estimations analytiques dans la limite d'un déphasage important et d'un temps long.

# Bibliographie


[1] J. A. Hutchison, T. Schwartz, C. Genet, E. Devaux, and T. W. Ebbesen, "Modifying Chemical Landscapes by Coupling to Vacuum Fields," *Angew. Chem. Int. Ed.*, vol. 51, pp. 1592–1596, Feb. 2012.

[2] A. Thomas, J. George, A. Shalabney, M. Dryzhakov, S. J. Varma, J. Moran, T. Chervy, X. Zhong, E. Devaux, C. Genet, J. A. Hutchison, and T. W. Ebbesen, "Ground-State Chemical Reactivity under Vibrational Coupling to the Vacuum Electromagnetic Field," *Angew. Chem. Int. Ed.*, vol. 55, no. 38, pp. 11462–11466, 2016.

[3] A. Thomas, L. Lethuillier-Karl, K. Nagarajan, R. M. A. Vergauwe, J. George, T. Chervy, A. Shalabney, E. Devaux, C. Genet, J. Moran, and T. W. Ebbesen, "Tilting a ground-state reactivity landscape by vibrational strong coupling," *Science*, vol. 363, pp. 615–619, Feb. 2019.

[4] F. J. Garcia-Vidal, C. Ciuti, and T. W. Ebbesen, "Manipulating matter by strong coupling to vacuum fields," *Science*, vol. 373, p. eabd0336, July 2021.

[5] F. Herrera and J. Owrutsky, "Molecular polaritons for controlling chemistry with quantum optics," *J. Chem. Phys.*, vol. 152, p. 100902, Mar. 2020.

[6] J. Feist, J. Galego, and F. J. Garcia-Vidal, "Polaritonic Chemistry with Organic Molecules," *ACS Photonics*, vol. 5, pp. 205–216, Jan. 2018.

[7] T. W. Ebbesen, "Hybrid Light–Matter States in a Molecular and Material Science Perspective," *Acc. Chem. Res.*, vol. 49, pp. 2403–2412, Nov. 2016.

[8] J. Yuen-Zhou and V. M. Menon, "Polariton chemistry : Thinking inside the (photon) box," *PNAS*, vol. 116, pp. 5214–5216, Mar. 2019.

[9] R. F. Ribeiro, L. A. Martínez-Martínez, M. Du, J. Campos-Gonzalez-Angulo, and J. Yuen-Zhou, "Polariton chemistry : Controlling molecular dynamics with optical cavities," *Chem. Sci.*, vol. 9, pp. 6325–6339, Aug. 2018.

[10] C. Cohen-Tannoudji, J. Dupont-Roc, and G. Grynberg, *Atom-Photon Interactions : Basic Processes and Applications*. New York : Wiley, 1992.

[11] R. H. Dicke, "Coherence in Spontaneous Radiation Processes," *Phys. Rev.*, vol. 93, pp. 99–110, Jan. 1954.

[12] M. Tavis and F. W. Cummings, "Exact solution for an $n$-molecule—radiation-field hamiltonian," *Phys. Rev.*, vol. 170, pp. 379–384, June 1968.

[13] S. Haroche and J.-M. Raimond, *Exploring the Quantum : Atoms, Cavities, and Photons*. OUP Oxford, Aug. 2006.

[14] C. W. Gardiner and P. Zoller, *The Quantum World of Ultracold Atoms and Light Book Ii : The Physics of Quantum Optical Devices*, vol. 4. World Scientific Publishing Company, 2015.

[15] D. Hunger, T. Steinmetz, Y. Colombe, C. Deutsch, T. W. Hänsch, and J. Reichel, "A fiber Fabry–Perot cavity with high finesse," *New J. Phys.*, vol. 12, p. 065038, June 2010.

[16] V. Savona, L. C. Andreani, P. Schwendimann, and A. Quattropani, "Quantum well excitons in semiconductor microcavities : Unified treatment of weak and strong coupling regimes," *Solid State Communications*, vol. 93, pp. 733–739, Mar. 1995.

[17] P. Törmä and W. L. Barnes, "Strong coupling between surface plasmon polaritons and emitters : A review," *Rep. Prog. Phys.*, vol. 78, p. 013901, Dec. 2014.

[18] A. Polman, "Plasmonics Applied," *Science*, vol. 322, pp. 868–869, Nov. 2008.

[19] E. M. Purcell, H. C. Torrey, and R. V. Pound, "Resonance Absorption by Nuclear Magnetic Moments in a Solid," *Phys. Rev.*, vol. 69, pp. 37–38, Jan. 1946.

[20] H. A. Atwater and A. Polman, "Plasmonics for improved photovoltaic devices," *Nature Mater*, vol. 9, pp. 205–213, Mar. 2010.

[21] T. B. Norris, J.-K. Rhee, C.-Y. Sung, Y. Arakawa, M. Nishioka, and C. Weisbuch, "Time-resolved vacuum Rabi oscillations in a semiconductor quantum microcavity," *Phys. Rev. B*, vol. 50, pp. 14663–14666, Nov. 1994.

[22] R. Miller, T. E. Northup, K. M. Birnbaum, A. Boca, A. D. Boozer, and H. J. Kimble, "Trapped atoms in cavity QED : Coupling quantized light and matter," *J. Phys. B : At. Mol. Opt. Phys.*, vol. 38, pp. S551–S565, Apr. 2005.

[23] P. Michetti, L. Mazza, and G. C. La Rocca, "Strongly Coupled Organic Microcavities," in *Organic Nanophotonics : Fundamentals and Applications* (Y. S. Zhao, ed.), Nano-Optics and Nanophotonics, pp. 39–68, Berlin, Heidelberg : Springer Berlin Heidelberg, 2015.

[24] D. G. Lidzey, D. D. C. Bradley, M. S. Skolnick, T. Virgili, S. Walker, and D. M. Whittaker, "Strong exciton–photon coupling in an organic semiconductor microcavity," *Nature*, vol. 395, pp. 53–55, Sept. 1998.

[25] J. P. Reithmaier, G. Sęk, A. Löffler, C. Hofmann, S. Kuhn, S. Reitzenstein, L. V. Keldysh, V. D. Kulakovskii, T. L. Reinecke, and A. Forchel, "Strong coupling in a single quantum dot–semiconductor microcavity system," *Nature*, vol. 432, pp. 197–200, Nov. 2004.

[26] A. Blais, R.-S. Huang, A. Wallraff, S. M. Girvin, and R. J. Schoelkopf, "Cavity quantum electrodynamics for superconducting electrical circuits : An architecture for quantum computation," *Phys. Rev. A*, vol. 69, p. 062320, June 2004.

[27] E. Janitz, M. K. Bhaskar, and L. Childress, "Cavity quantum electrodynamics with color centers in diamond," *Optica, OPTICA*, vol. 7, pp. 1232–1252, Oct. 2020.

[28] X. Liu, T. Galfsky, Z. Sun, F. Xia, E.-c. Lin, Y.-H. Lee, S. Kéna-Cohen, and V. M. Menon, "Strong light–matter coupling in two-dimensional atomic crystals," *Nature Photon*, vol. 9, pp. 30–34, Jan. 2015.

[29] W. Liu, B. Lee, C. H. Naylor, H.-S. Ee, J. Park, A. T. C. Johnson, and R. Agarwal, "Strong Exciton–Plasmon Coupling in MoS2 Coupled with Plasmonic Lattice," *Nano Lett.*, vol. 16, pp. 1262–1269, Feb. 2016.

[30] S. Wang, S. Li, T. Chervy, A. Shalabney, S. Azzini, E. Orgiu, J. A. Hutchison, C. Genet, P. Samorì, and T. W. Ebbesen, "Coherent Coupling of WS2 Monolayers with Metallic Photonic Nanostructures at Room Temperature," *Nano Lett.*, vol. 16, pp. 4368–4374, July 2016.

[31] H. Konishi, K. Roux, V. Helson, and J.-P. Brantut, "Universal pair polaritons in a strongly interacting Fermi gas," *Nature*, vol. 596, pp. 509–513, Aug. 2021.

[32] F. Herrera and F. C. Spano, "Theory of Nanoscale Organic Cavities : The Essential Role of Vibration-Photon Dressed States," *ACS Photonics*, vol. 5, pp. 65–79, Jan. 2018.

[33] A. Canaguier-Durand, E. Devaux, J. George, Y. Pang, J. A. Hutchison, T. Schwartz, C. Genet, N. Wilhelms, J.-M. Lehn, and T. W. Ebbesen, "Thermodynamics of Molecules Strongly Coupled to the Vacuum Field," *Angew. Chem. Int. Ed.*, vol. 52, pp. 10533–10536, Sept. 2013.

[34] J. Mony, C. Climent, A. U. Petersen, K. Moth-Poulsen, J. Feist, and K. Börjesson, "Photoisomerization Efficiency of a Solar Thermal Fuel in the Strong Coupling Regime," *Adv. Funct. Mater.*, vol. 31, p. 2010737, Mar. 2021.

[35] S. Satapathy, M. Khatoniar, D. K. Parappuram, B. Liu, G. John, J. Feist, F. J. Garcia-Vidal, and V. M. Menon, "Selective isomer emission via funneling of exciton polaritons," *Sci. Adv.*, vol. 7, no. 44, p. eabj0997, 2021.

[36] K. Stranius, M. Hertzog, and K. Börjesson, "Selective manipulation of electronically excited states through strong light–matter interactions," *Nat. Commun.*, vol. 9, p. 2273, June 2018.

[37] S. Takahashi, K. Watanabe, and Y. Matsumoto, "Singlet fission of amorphous rubrene modulated by polariton formation," *J. Chem. Phys.*, vol. 151, p. 074703, Aug. 2019.

[38] E. Eizner, L. A. Martínez-Martínez, J. Yuen-Zhou, and S. Kéna-Cohen, "Inverting singlet and triplet excited states using strong light-matter coupling," *Sci. Adv.*, vol. 5, p. eaax4482, Dec. 2019.

[39] D. Polak, R. Jayaprakash, T. P. Lyons, L. Á. Martínez-Martínez, A. Leventis, K. J. Fallon, H. Coulthard, D. G. Bossanyi, K. Georgiou, I. I. Anthony J. Petty, J. Anthony, H. Bronstein, J. Yuen-Zhou, A. I. Tartakovskii, J. Clark, and A. J. Musser, "Manipulating molecules with strong coupling : Harvesting triplet excitons in organic exciton microcavities," *Chem. Sci.*, vol. 11, pp. 343–354, Jan. 2020.

[40] Y. Yu, S. Mallick, M. Wang, and K. Börjesson, "Barrier-free reverse-intersystem crossing in organic molecules by strong light-matter coupling," *Nat Commun*, vol. 12, p. 3255, May 2021.

[41] C. Ye, S. Mallick, M. Hertzog, M. Kowalewski, and K. Börjesson, "Direct Transition from Triplet Excitons to Hybrid Light–Matter States via Triplet–Triplet Annihilation," *J. Am. Chem. Soc.*, vol. 143, pp. 7501–7508, May 2021.

[42] Q. Ou, Y. Shao, and Z. Shuai, "Enhanced Reverse Intersystem Crossing Promoted by Triplet Exciton–Photon Coupling," *J. Am. Chem. Soc.*, vol. 143, p. 17786, Oct. 2021.

[43] R. Puro, J. D. B. Van Schenck, R. Center, E. K. Holland, J. E. Anthony, and O. Ostroverkhova, "Exciton Polariton-Enhanced Photodimerization of Functionalized Tetracene," *J. Phys. Chem. C*, Dec. 2021.

[44] B. Munkhbat, M. Wersäll, D. G. Baranov, T. J. Antosiewicz, and T. Shegai, "Suppression of photo-oxidation of organic chromophores by strong coupling to plasmonic nanoantennas," *Sci. Adv.*, vol. 4, p. eaas9552, July 2018.

[45] J. Lather, P. Bhatt, A. Thomas, T. W. Ebbesen, and J. George, "Cavity Catalysis by Cooperative Vibrational Strong Coupling of Reactant and Solvent Molecules," *Angew. Chem. Int. Ed.*, vol. 58, no. 31, pp. 10635–10638, 2019.

[46] K. Hirai, R. Takeda, J. A. Hutchison, and H. Uji-i, "Modulation of Prins Cyclization by Vibrational Strong Coupling," *Angew. Chem. Int. Ed.*, vol. 59, no. 13, pp. 5332–5335, 2020.

[47] H. Hiura, A. Shalabney, and J. George, "Cavity Catalysis -Accelerating Reactions under Vibrational Strong Coupling- (preprint) chemrxiv.7234721.v3," Nov. 2018.

[48] F. Herrera and F. C. Spano, "Cavity-Controlled Chemistry in Molecular Ensembles," *Phys. Rev. Lett.*, vol. 116, p. 238301, June 2016.

[49] L. A. Martínez-Martínez, M. Du, R. F. Ribeiro, S. Kéna-Cohen, and J. Yuen-Zhou, "Polariton-Assisted Singlet Fission in Acene Aggregates," *J. Phys. Chem. Lett.*, vol. 9, pp. 1951–1957, Apr. 2018.

[50] M. Reitz, C. Sommer, and C. Genes, "Langevin Approach to Quantum Optics with Molecules," *Phys. Rev. Lett.*, vol. 122, p. 203602, May 2019.

[51] J. A. Campos-Gonzalez-Angulo, R. F. Ribeiro, and J. Yuen-Zhou, "Resonant catalysis of thermally activated chemical reactions with vibrational polaritons," *Nat Commun*, vol. 10, p. 4685, Oct. 2019.

[52] A. Mandal, T. D. Krauss, and P. Huo, "Polariton-Mediated Electron Transfer via Cavity Quantum Electrodynamics," *J. Phys. Chem. B*, vol. 124, pp. 6321–6340, July 2020.

[53] C. Sommer, M. Reitz, F. Mineo, and C. Genes, "Molecular polaritonics in dense mesoscopic disordered ensembles," *Phys. Rev. Research*, vol. 3, p. 033141, Aug. 2021.

[54] O. Vendrell, "Collective Jahn-Teller Interactions through Light-Matter Coupling in a Cavity," *Phys. Rev. Lett.*, vol. 121, p. 253001, Dec. 2018.

[55] G. Groenhof, C. Climent, J. Feist, D. Morozov, and J. J. Toppari, "Tracking Polariton Relaxation with Multiscale Molecular Dynamics Simulations," *J. Phys. Chem. Lett.*, vol. 10, pp. 5476–5483, Sept. 2019.

[56] J. Galego, F. J. Garcia-Vidal, and J. Feist, "Cavity-Induced Modifications of Molecular Structure in the Strong-Coupling Regime," *Phys. Rev. X*, vol. 5, p. 041022, Nov. 2015.

[57] Y. Zhang, T. Nelson, and S. Tretiak, "Non-adiabatic molecular dynamics of molecules in the presence of strong light-matter interactions," *J. Chem. Phys.*, vol. 151, p. 154109, Oct. 2019.

[58] J. Fregoni, G. Granucci, E. Coccia, M. Persico, and S. Corni, "Manipulating azobenzene photoisomerization through strong light–molecule coupling," *Nat. Commun.*, vol. 9, Dec. 2018.

[59] H. L. Luk, J. Feist, J. J. Toppari, and G. Groenhof, "Multiscale Molecular Dynamics Simulations of Polaritonic Chemistry," *J. Chem. Theory Comput.*, vol. 13, pp. 4324–4335, Sept. 2017.

[60] P. Antoniou, F. Suchanek, J. F. Varner, and J. J. Foley, "Role of Cavity Losses on Nonadiabatic Couplings and Dynamics in Polaritonic Chemistry," *J. Phys. Chem. Lett.*, vol. 11, pp. 9063–9069, Nov. 2020.

[61] E. Davidsson and M. Kowalewski, "Atom Assisted Photochemistry in Optical Cavities," *J. Phys. Chem. A*, vol. 124, pp. 4672–4677, June 2020.

[62] J. del Pino, F. A. Y. N. Schröder, A. W. Chin, J. Feist, and F. J. Garcia-Vidal, "Tensor network simulation of polaron-polaritons in organic microcavities," *Phys. Rev. B*, vol. 98, p. 165416, Oct. 2018.

[63] U. Mordovina, C. Bungey, H. Appel, P. J. Knowles, A. Rubio, and F. R. Manby, "Polaritonic coupled-cluster theory," *Phys. Rev. Research*, vol. 2, p. 023262, June 2020.

[64] D. S. Wang, T. Neuman, J. Flick, and P. Narang, "Light–matter interaction of a molecule in a dissipative cavity from first principles," *J. Chem. Phys.*, vol. 154, p. 104109, Mar. 2021.

[65] J. Doyle, B. Friedrich, R. V. Krems, and F. Masnou-Seeuws, "Editorial : Quo vadis, cold molecules ?," *Eur. Phys. J. D*, vol. 31, pp. 149–164, Nov. 2004.

[66] L. D. Carr, D. DeMille, R. V. Krems, and J. Ye, "Cold and ultracold molecules : Science, technology and applications," *New J. Phys.*, vol. 11, p. 055049, May 2009.

[67] G. Quéméner and P. S. Julienne, "Ultracold Molecules under Control !," *Chem. Rev.*, vol. 112, pp. 4949–5011, Sept. 2012.

[68] N. Balakrishnan, "Perspective : Ultracold molecules and the dawn of cold controlled chemistry," *J. Chem. Phys.*, vol. 145, p. 150901, Oct. 2016.

[69] S. A. Moses, J. P. Covey, M. T. Miecnikowski, D. S. Jin, and J. Ye, "New frontiers for quantum gases of polar molecules," *Nature Phys*, vol. 13, pp. 13–20, Jan. 2017.

[70] J. L. Bohn, A. M. Rey, and J. Ye, "Cold molecules : Progress in quantum engineering of chemistry and quantum matter," *Science*, vol. 357, pp. 1002–1010, Sept. 2017.

[71] M. A. Baranov, M. Dalmonte, G. Pupillo, and P. Zoller, "Condensed Matter Theory of Dipolar Quantum Gases," *Chem. Rev.*, vol. 112, pp. 5012–5061, Sept. 2012.

[72] N. Y. Yao, A. V. Gorshkov, C. R. Laumann, A. M. Läuchli, J. Ye, and M. D. Lukin, "Realizing Fractional Chern Insulators in Dipolar Spin Systems," *Phys. Rev. Lett.*, vol. 110, p. 185302, Apr. 2013.

[73] D. DeMille, "Quantum Computation with Trapped Polar Molecules," *Phys. Rev. Lett.*, vol. 88, p. 067901, Jan. 2002.

[74] P. Rabl, D. DeMille, J. M. Doyle, M. D. Lukin, R. J. Schoelkopf, and P. Zoller, "Hybrid Quantum Processors : Molecular Ensembles as Quantum Memory for Solid State Circuits," *Phys. Rev. Lett.*, vol. 97, p. 033003, July 2006.

[75] M. S. Safronova, D. Budker, D. DeMille, D. F. J. Kimball, A. Derevianko, and C. W. Clark, "Search for new physics with atoms and molecules," *Rev. Mod. Phys.*, vol. 90, p. 025008, June 2018.

[76] J. J. Hudson, D. M. Kara, I. J. Smallman, B. E. Sauer, M. R. Tarbutt, and E. A. Hinds, "Improved measurement of the shape of the electron," *Nature*, vol. 473, pp. 493–496, May 2011.

[77] W. B. Cairncross, D. N. Gresh, M. Grau, K. C. Cossel, T. S. Roussy, Y. Ni, Y. Zhou, J. Ye, and E. A. Cornell, "Precision Measurement of the Electron's Electric Dipole Moment Using Trapped Molecular Ions," *Phys. Rev. Lett.*, vol. 119, p. 153001, Oct. 2017.

[78] E. R. Hudson, H. J. Lewandowski, B. C. Sawyer, and J. Ye, "Cold Molecule Spectroscopy for Constraining the Evolution of the Fine Structure Constant," *Phys. Rev. Lett.*, vol. 96, p. 143004, Apr. 2006.

[79] S. Ospelkaus, K.-K. Ni, D. Wang, M. H. G. de Miranda, B. Neyenhuis, G. Quéméner, P. S. Julienne, J. L. Bohn, D. S. Jin, and J. Ye, "Quantum-State Controlled Chemical Reactions of Ultracold Potassium-Rubidium Molecules," *Science*, vol. 327, pp. 853–857, Feb. 2010.

[80] K.-K. Ni, S. Ospelkaus, D. Wang, G. Quéméner, B. Neyenhuis, M. H. G. de Miranda, J. L. Bohn, J. Ye, and D. S. Jin, "Dipolar collisions of polar molecules in the quantum regime," *Nature*, vol. 464, pp. 1324–1328, Apr. 2010.

[81] J. Rui, H. Yang, L. Liu, D.-C. Zhang, Y.-X. Liu, J. Nan, Y.-A. Chen, B. Zhao, and J.-W. Pan, "Controlled state-to-state atom-exchange reaction in an ultracold atom–dimer mixture," *Nature Phys*, vol. 13, pp. 699–703, July 2017.

[82] J. Wolf, M. Deiß, A. Krükow, E. Tiemann, B. P. Ruzic, Y. Wang, J. P. D'Incao, P. S. Julienne, and J. H. Denschlag, "State-to-state chemistry for three-body recombination in an ultracold rubidium gas," *Science*, Nov. 2017.

[83] J. Toscano, H. J. Lewandowski, and B. R. Heazlewood, "Cold and controlled chemical reaction dynamics," *Phys. Chem. Chem. Phys.*, vol. 22, no. 17, pp. 9180–9194, 2020.

[84] M.-G. Hu, Y. Liu, M. A. Nichols, L. Zhu, G. Quéméner, O. Dulieu, and K.-K. Ni, "Nuclear spin conservation enables state-to-state control of ultracold molecular reactions," *Nat. Chem.*, vol. 13, pp. 435–440, May 2021.

[85] Y. Liu, M.-G. Hu, M. A. Nichols, D. Yang, D. Xie, H. Guo, and K.-K. Ni, "Precision test of statistical dynamics with state-to-state ultracold chemistry," *Nature*, vol. 593, pp. 379–384, May 2021.

[86] E. B. Norrgard, D. J. McCarron, M. H. Steinecker, M. R. Tarbutt, and D. DeMille, "Submillikelvin Dipolar Molecules in a Radio-Frequency Magneto-Optical Trap," *Phys. Rev. Lett.*, vol. 116, p. 063004, Feb. 2016.

[87] L. Anderegg, B. L. Augenbraun, Y. Bao, S. Burchesky, L. W. Cheuk, W. Ketterle, and J. M. Doyle, "Laser cooling of optically trapped molecules," *Nature Phys*, vol. 14, pp. 890–893, Sept. 2018.

[88] N. R. Hutzler, H.-I. Lu, and J. M. Doyle, "The Buffer Gas Beam : An Intense, Cold, and Slow Source for Atoms and Molecules," *Chem. Rev.*, vol. 112, pp. 4803–4827, Sept. 2012.

[89] S. Y. T. van de Meerakker, H. L. Bethlem, and G. Meijer, "Taming molecular beams," *Nature Phys*, vol. 4, pp. 595–602, Aug. 2008.

[90] A. Prehn, M. Ibrügger, R. Glöckner, G. Rempe, and M. Zeppenfeld, "Optoelectrical Cooling of Polar Molecules to Submillikelvin Temperatures," *Phys. Rev. Lett.*, vol. 116, p. 063005, Feb. 2016.

[91] H. Son, J. J. Park, W. Ketterle, and A. O. Jamison, "Collisional cooling of ultracold molecules," *Nature*, vol. 580, pp. 197–200, Apr. 2020.

[92] H. J. Metcalf and P. van der Straten, "Laser Cooling and Trapping of Neutral Atoms," in *The Optics Encyclopedia*, John Wiley & Sons, Ltd, 2007.

[93] W. Ketterle and N. J. V. Druten, "Evaporative Cooling of Trapped Atoms," in *Advances In Atomic, Molecular, and Optical Physics* (B. Bederson and H. Walther, eds.), vol. 37, pp. 181–236, Academic Press, Jan. 1996.

[94] K. M. Jones, E. Tiesinga, P. D. Lett, and P. S. Julienne, "Ultracold photoassociation spectroscopy : Long-range molecules and atomic scattering," *Rev. Mod. Phys.*, vol. 78, pp. 483–535, May 2006.

[95] I. Manai, R. Horchani, H. Lignier, P. Pillet, D. Comparat, A. Fioretti, and M. Allegrini, "Rovibrational Cooling of Molecules by Optical Pumping," *Phys. Rev. Lett.*, vol. 109, p. 183001, Oct. 2012.

[96] T. Köhler, K. Góral, and P. S. Julienne, "Production of cold molecules via magnetically tunable Feshbach resonances," *Rev. Mod. Phys.*, vol. 78, pp. 1311–1361, Dec. 2006.

[97] J. G. Danzl, M. J. Mark, E. Haller, M. Gustavsson, R. Hart, J. Aldegunde, J. M. Hutson, and H.-C. Nägerl, "An ultracold high-density sample of rovibronic ground-state molecules in an optical lattice," *Nat. Phys.*, vol. 6, pp. 265–270, Apr. 2010.

[98] T. Takekoshi, L. Reichsöllner, A. Schindewolf, J. M. Hutson, C. R. Le Sueur, O. Dulieu, F. Ferlaino, R. Grimm, and H.-C. Nägerl, "Ultracold Dense Samples of Dipolar RbCs Molecules in the Rovibrational and Hyperfine Ground State," *Phys. Rev. Lett.*, vol. 113, p. 205301, Nov. 2014.

[99] F. Lang, K. Winkler, C. Strauss, R. Grimm, and J. H. Denschlag, "Ultracold Triplet Molecules in the Rovibrational Ground State," *Phys. Rev. Lett.*, vol. 101, p. 133005, Sept. 2008.

[100] S. A. Moses, J. P. Covey, M. T. Miecnikowski, B. Yan, B. Gadway, J. Ye, and D. S. Jin, "Creation of a low-entropy quantum gas of polar molecules in an optical lattice," *Science*, vol. 350, pp. 659–662, Nov. 2015.

[101] L. D. Marco, G. Valtolina, K. Matsuda, W. G. Tobias, J. P. Covey, and J. Ye, "A degenerate Fermi gas of polar molecules," *Science*, vol. 363, pp. 853–856, Feb. 2019.

[102] K. K. Voges, P. Gersema, M. Meyer zum Alten Borgloh, T. A. Schulze, T. Hartmann, A. Zenesini, and S. Ospelkaus, "Ultracold gas of bosonic $^{23}$Na$^{39}$K ground-state molecules," *Phys. Rev. Lett.*, vol. 125, p. 083401, Aug. 2020.

[103] K.-K. Ni, S. Ospelkaus, M. H. G. de Miranda, A. Pe'er, B. Neyenhuis, J. J. Zirbel, S. Kotochigova, P. S. Julienne, D. S. Jin, and J. Ye, "A High Phase-Space-Density Gas of Polar Molecules," *Science*, vol. 322, pp. 231–235, Oct. 2008.

[104] C. W. Gardiner and P. Zoller, *Quantum Noise*. Springer Series in Synergetics, Springer Berlin Heidelberg, 3rd ed., 2004.

[105] A. Nitzan, *Chemical Dynamics in Condensed Phases : Relaxation, Transfer and Reactions in Condensed Molecular Systems*. Oxford Graduate Texts, Oxford ; New York : Oxford University Press, 2006.

[106] C. W. Gardiner, *Stochastic Methods*. Springer Series in Synergetics, Springer Berlin Heidelberg, 2009.

[107] H.-P. Breuer and F. Petruccione, *The Theory of Open Quantum Systems*. Oxford ; New York : Oxford University Press, 2002.

[108] A. J. Daley, "Quantum trajectories and open many-body quantum systems," *Adv. Phys.*, vol. 63, pp. 77–149, Mar. 2014.

[109] H. Weimer, A. Kshetrimayum, and R. Orús, "Simulation methods for open quantum many-body systems," *Rev. Mod. Phys.*, vol. 93, p. 015008, Mar. 2021.

[110] A. Einstein, B. Podolsky, and N. Rosen, "Can Quantum-Mechanical Description of Physical Reality Be Considered Complete ?," *Phys. Rev.*, vol. 47, pp. 777–780, May 1935.

[111] E. Schrödinger, "Die gegenwärtige Situation in der Quantenmechanik," *Naturwissenschaften*, vol. 23, pp. 807–812, Nov. 1935.

[112] L. Amico, R. Fazio, A. Osterloh, and V. Vedral, "Entanglement in many-body systems," *Rev. Mod. Phys.*, vol. 80, pp. 517–576, May 2008.

[113] R. Horodecki, P. Horodecki, M. Horodecki, and K. Horodecki, "Quantum entanglement," *Rev. Mod. Phys.*, vol. 81, pp. 865–942, June 2009.

[114] J. Eisert, M. Cramer, and M. B. Plenio, "Colloquium : Area laws for the entanglement entropy," *Rev. Mod. Phys.*, vol. 82, pp. 277–306, Feb. 2010.

[115] J. S. Bell, "On the Einstein Podolsky Rosen paradox," *Physics Physique Fizika*, vol. 1, pp. 195–200, Nov. 1964.

[116] G. Vidal, "Efficient Simulation of One-Dimensional Quantum Many-Body Systems," *Phys. Rev. Lett.*, vol. 93, p. 040502, July 2004.

[117] M. A. Nielsen and I. Chuang, *Quantum Computation and Quantum Information*. Cambridge University Press, tenth ed., 2010.

[118] J. I. Cirac, D. Poilblanc, N. Schuch, and F. Verstraete, "Entanglement spectrum and boundary theories with projected entangled-pair states," *Phys. Rev. B*, vol. 83, p. 245134, June 2011.

[119] U. Schollwöck, "The density-matrix renormalization group in the age of matrix product states," *Annals of Physics*, vol. 326, pp. 96–192, Jan. 2011.

[120] T. Kampschulte and J. Hecker Denschlag, "Cavity-controlled formation of ultracold molecules," *New J. Phys.*, vol. 20, p. 123015, Dec. 2018.

[121] M. A. Bellos, D. Rahmlow, R. Carollo, J. Banerjee, O. Dulieu, A. Gerdes, E. E. Eyler, P. L. Gould, and W. C. Stwalley, "Formation of ultracold Rb2 molecules in the v′′ = 0 level of the a3Σ+u state via blue-detuned photoassociation to the 13Πg state," *Phys. Chem. Chem. Phys.*, vol. 13, no. 42, p. 18880, 2011.

[122] Y. Zhang, Y.-X. Zhang, and K. Mølmer, "Monte-Carlo Simulations of Superradiant Lasing," *New J. Phys.*, vol. 20, p. 112001, Nov. 2018.

[123] T. Botzung, D. Hagenmüller, S. Schütz, J. Dubail, G. Pupillo, and J. Schachenmayer, "Dark state semilocalization of quantum emitters in a cavity," *Phys. Rev. B*, vol. 102, p. 144202, Oct. 2020.

[124] N. C. Chávez, F. Mattiotti, J. A. Méndez-Bermúdez, F. Borgonovi, and G. L. Celardo, "Disorder-Enhanced and Disorder-Independent Transport with Long-Range Hopping : Application to Molecular Chains in Optical Cavities," *Phys. Rev. Lett.*, vol. 126, p. 153201, Apr. 2021.

# Contents

# 1. Introduction

Understanding and controlling chemical reactions is a major challenge in the physical sciences. So far, this challenge has mostly been approached by modifying the chemical environment of the reaction, e.g. by carefully choosing the solvent or introducing materials that can steer the reaction called catalysts. Finding novel ways to control chemistry is an important task and holds great potential for the advancement of science and technology.

In a seminal experiment in 2012, Hutchison *et al.* discovered the suppression of a photo-isomerization reaction under collective strong coupling of an electronic molecular transition to a cavity [1]. Since then, various experiments have shown modifications to chemical reactions induced by coupling to a cavity mode. One breakthrough was the finding that strong coupling of vibrational transitions of a molecule can modify reaction rates for thermally activated reactions [2], and even steer reactions to a desired product [3] by Thomas *et al.* These discoveries demonstrate the possibility to modify chemical properties of molecules solely by coupling to light fields, laying the foundation for what is now called polaritonic chemistry [4–9]. Despite these impressive experimental results, the theoretical understanding of the underlying processes is still in its infancy. Developing a deeper theoretical understanding of these processes, in particular concerning the role of collective and dissipative effects, is the general objective of this thesis.

The theory describing light-matter interactions is unified in the framework of quantum electrodynamics (QED), describing many fundamental phenomena, such as the black body spectrum, fine structure, spontaneous emission, and electro-magnetic interactions [10]. Furthermore, through the coupling of many emitters to a common electromagnetic field, collective dissipative effects can arise [11, 12]. For their work on this theory, Tomonaga, Schwinger and Feynman were awarded with the Nobel prize in 1965.

If the light-modes are confined to a finite volume by the presence of a cavity, the resulting theory is called cavity QED [10, 13, 14]. In atomic, molecular and optical (AMO) physics, cavity QED setups have long been studied as a prototypical quantum system where QED effects are enhanced compared to a free space scenario. In 2012, Serge Haroche was awarded a Nobel Prize for demonstrating the control and entanglement of individual quantum systems using interactions between single atoms and (quantized) light fields. In order to harness this control, various types of "cavities" have been developed to confine light modes [15–18]. These cavities are generally optimized to combine small loss rates and high local field intensities, in order to maximize the coherent energy exchange with an emitter. If the coherent exchange rate between field and emitter is faster than the losses of either of them, the two degrees of freedom hybridize and form so-called polaritons, giving rise to fundamentally different physical phenomena that are

generally not observed in free space [13]. Studying the consequences of cavity-enhanced light-matter interactions is a vibrant research field, which includes the work of this thesis.

In the remainder of this introduction, I will give a brief overview over the specific topics addressed in this thesis. The first section contains more details on cavity QED and polaritons, including systems in which systems they have been observed and their applications. Then, a more detailed overview of polaritonic chemistry is given. Following that, ultracold molecular setups are introduced, which are studied in the first part of this thesis. These three sections focus on the different setups considered in this thesis, while the following two sections will introduce the theoretical background of the methods used. Open quantum systems and dissipation are introduced, which will be in general part of the theoretical setup considered in this thesis. After that, entanglement and matrix product state are discussed, which are used for numerical studies throughout this thesis. Finally, the main results of this thesis are summarized.

## 1.1. Cavity Quantum Electrodynamics

Light-matter interactions are one of the corner-stones of modern physics, in particular of AMO physics. These interactions determine not only (quite literally) everything we can see, but their applications extend far beyond that. They are at the core of photochemistry, solar technologies, photosynthesis, and spectroscopy, thus being central also for scientific measurements. As a result, they are crucial for our understanding of all physical sciences.

In free space, interactions between the vacuum electromagnetic field and matter are typically weak and can be treated perturbatively, as determined by the small fine structure constant $\alpha \sim 1/137$. This is a consequence of the small vacuum electric field, which is diluted across a large volume. Within a confined volume, i.e. a cavity, the electromagnetic modes that fit neatly into this volume are significantly enhanced, whereas all other modes are suppressed compared to the free field scenario. If the coupling remains perturbative, this leads to an increase of the above mentioned effects. Most notably, through confinement of the light modes, spontaneous emission can be drastically modified, called the Purcell effect [19]. If the vacuum field is enhanced enough, the coupling becomes non-perturbative, and light and matter degrees of freedom hybridize and form hybrid light-matter states called polaritons [13]. In order to enhance the coupling further, ensembles of emitters can be coupled to the same cavity mode [13]. In the perturbative regime, this leads to superradiance [11], whereas in the strong coupling regime this leads to an enhanced polariton splitting. These effects are introduced in detail in Chapter 3.

The textbook example of confining light modes is by placing two metallic mirrors facing each other, such that inside the cavity only modes whose wavelength fits neatly in between both mirrors can exist. Such Fabri-Perot cavities are used in many setups, including some of the experiments mentioned above [2, 3]. Different materials have also been adapted to act as reflecting surfaces, such as optical Fibers for so called Fiber Fabri Perot cavities [15]. Dielectric Bragg reflectors (DBR) offer another way

to confine light modes [16]. These adaptations have been made to reach low cavity losses, which compete with coherent energy exchange. However, all these cavities have in common that, due to the refraction limit, light cannot be confined to volumes smaller than $\sim \lambda^3$ where $\lambda$ is the wavelength. Methods to confine light to smaller volumes in the proximity to emitters have been developed in the field of plasmonics [17, 20]. Plasmons are themselves hybrid light-matter excitations, that lead to large field enhancements close to a surface. On structured surfaces, these plasmons typically travel along the surface, but using metallic nanoparticles, they can be confined. However, due to their material component, plasmons are generally plagued by high loss rates. Throughout this thesis, the field is treated as a generic single mode quantum field, however, for realistic parameter estimates, Fabri-Perot type cavities or DBRs are considered. Due to their larger volume, in these cavities collective effects are more relevant.

Cavity QED has also been studied with different types of emitters. Many strong coupling experiments have been made using Wannier-Mott excitons in semi-conductors [21] and with cold atoms in AMO physics [22]. Both of these systems have typically very well-controlled fundamental excitations. In AMO physics this is due to excellent control of individual quantum systems using lasers, and in semi-conductors due to the large extension of Wannier-Mott excitons which leads to an effective averaging, in addition with typically cryogenic temperatures in experiments. Organic semi-conductors and organic molecules have become a staple alternative due to their large coupling strengths, albeit at the cost of a broadening (homogeneous and inhomogeneous) of the exciton resonance [23, 24]. Naturally, many other types of emitters have been used in strong coupling experiments, such as quantum dots [25], (superconducting) qubits [26], color (NV) centers [27], 2D materials [28–30], and ultracold molecules [31]. In this thesis, excitations are always considered to be localized, which are the typical scenario in AMO systems or organic materials.

Cold and ultracold atoms and molecules offer precise control over individual degrees of freedom, and strong coupling of individual atoms [32–34] or atomic ensembles [35] has been demonstrated. This makes cold atom cavity QED ideally suited for fundamental tests of quantum mechanics, such as preparing and measuring entangled states [36–38]. Similarly, the precise control allow to test fundamental physics in the setup of quantum metrology [39] and to create novel lasers using superradiance [40]. Furthermore, cold atom cavity QED has also been used for quantum simulation [41–47] and computing [48, 49], where precise control over individual degrees of freedom is needed. In Chapter 5, I consider strong coupling of ultracold molecules, which offer similar advantages as cold atoms [50–54], and for which strong coupling has been demonstrated [31].

The fundamental excitations in organic molecular materials are Frenkel excitons, which are localized on single molecules. As a result, their properties are strongly influenced by the local environment, leading to energetic disorder and fast decoherence. After the first observation of strong coupling with organic molecules in 1998 [24], the relaxation dynamics of excited states towards the lower polariton has been thoroughly investigated [55–66]. Under the right conditions, the relaxation can lead to Bose-Einstein condensation of polaritons and polariton lasing [67–78] (see e.g. Ref. [79] for a review).

Furthermore, the large dipoles of organic molecules enabled the study of the collective ultra-strong coupling regime, where the interaction strength becomes comparable to the bare excitation energy [80–83], as well as strong coupling of individual molecules [84–87]. The resulting collective hybrid states have been observed to be able to modify energy transport and conductivity [88–93]. Finally, and this is the topic of this thesis, modifications to chemistry have also been observed for strong coupling of electronic [1, 94–101] and vibrational [2, 3, 102, 103]. These modifications have been reviewed in different occasions [4, 5, 7, 104, 105] and will be discussed in the following section.

## 1.2. Polariton Chemistry

The field of polaritonic chemistry has been established based on the surprising observation of the possibility to modify chemical reactions by strong coupling of molecular transitions to a cavity mode in the group of Thomas Ebbesen in Strasbourg [1–3]. In a breakthrough experiment [1], Hutchison *et al.* have coupled an electronic transition of the product of a photo-isomerization reaction to a cavity, where they observed a suppression of the reaction rate in the collective strong coupling regime. This led to a shift in the equilibrium concentrations of reactants and products under ultra-violet irradiation. In 2016 [2], Thomas *et al.* have shown that collective strong coupling of a vibrational transition can lead to a suppression of a thermally activated reaction. In particular, they investigated the dissociation reaction of a molecule, which was slowed down by strong coupling of the dissociating bond to a cavity. This is particularly intriguing since light is not directly involved in the reaction. In 2019 [3], Thomas *et al.* demonstrated that this effect can be used to modify which product is favored in a dissociation reaction with two possible products. In detail, the cavity induces a slowdown of one of the reaction rates, which changes which product is favored in the overall reaction.

The observation of modified chemistry was confirmed in a series of follow-up experiments, which can be categorized into two regimes. In the electronic strong coupling (ESC) regime, a transition between the ground state and an electronically excited state is coupled to the cavity, whereas in the vibrational strong coupling (VSC) regime, two vibrational levels within the electronic ground state are coupled. The difference in transition energy between the two regimes ($\gtrsim 1\,\mathrm{eV}$ for ESC compared to $\sim 100\,\mathrm{meV}$ for VSC) leads to significant differences in both setup and chemistry. Furthermore, due to the thermal energy $\sim 25\,\mathrm{meV}$ at room temperature, thermal excitation and thermally activated reactions are much more important for VSC than for ESC.

In order to demonstrate cavity modified chemistry, so far, generally the principal mode of the cavity has been coupled. Therefore, the excitation energies $\gtrsim 1\,\mathrm{eV}$ translate to cavity sizes $\lesssim 1\,\mu\mathrm{m}$ [106]. Due to the small cavity sizes, coupled materials are typically in the solid phase [4], and reactions only involve individual molecules. Photo-isomerization reactions between two ground states of one molecules have been modified [1, 66, 101, 107]. The implications for thermodynamics have been analyzed [66], and how this may be useful for energy storage [101]. Another class of reactions that have been studied are singlet-triplet transitions between two electronically excited states [94–96, 99, 100, 108–

110]. Here, through coupling of the electronically excited singlet state to a cavity, the energies and even the energetic ordering of the singlet and triplet states can be modified, leading to enhanced triplet harvesting rates and triplet-triplet annihilation. These reactions are particularly useful for practical applications, such as lasers or solar cells. Lastly, by strong coupling of $J$-aggregates to plasmonic nano-particles, suppression of photo-oxidization rates has been demonstrated [97].

In contrast, for VSC, the smaller energies mean that cavities can be large enough to be filled with fluids, thus enabling a much wider class of reactions. In addition, the low energy scales mean that thermally activated reactions can be observed. Here, coupling of reactant, product, and solvent have been shown to modify the reaction rate [2, 3, 102, 111, 112]. In this thesis, I focus exclusively on reactions in the ESC regime.

Despite these impressive results, the theoretical understanding of the involved processes is still in its infancy. The underlying challenge is to compute the reaction dynamics of a large number of molecules, each with multiple electronic and vibrational degrees of freedom, and all indirectly coupled via the cavity [5]. Various numerical and analytical tools have been used to tackle this problem. Analytically, this challenge has been approached by considering generic toy-model molecules and analyzing how they are modified [113–118]. Numerically, generally specific molecules with varying complexity ranging from simple diatomic NaI [126] to complex organic molecules such as rhodamine [120] are studied. However, in order to treat large ensembles, the dynamics (instead of the molecular model) needs to be approximated. Within the cavity Born-Oppenheimer approximation, the electro-photonic state is assumed to change adiabatically with the classical dynamics of the nuclear degrees of freedom [119]. Using simple extensions of this approach such as surface hopping or mean-field Ehrenfest, the excited state dynamics of large molecular ensembles has been computed [120–124]. In contrast, in order to compute the exact quantum dynamics, more sophisticated methods are needed, and typically only a few molecules can be treated [125–129]. In this case, collective effects are accounted for by matching the collective Rabi splitting to realistic experimental values, since the Rabi splitting has been determined to be an important quantity for modified chemistry [2]. However, the precise role of collective effects becomes hard to investigate. We give an overview over the dominant analytical and numerical methods in Chapters 7 and 8, respectively.

## 1.3. Ultracold Molecules and Ultracold Chemistry

Ultracold molecules are molecules at sub-µK temperatures. These molecules promise to have applications in quantum simulations, computation, metrology, and the study of chemical reactions in the ultracold regime [50–54, 130]. In particular, the permanent dipoles of polar molecules offer implementations of richer models with different phases of matter compared to ultracold atoms [131, 132]. The dipole interactions have also been proposed to be used for quantum computation [133, 134]. However, such applications still

require advances in control of ultracold molecules. Ultracold molecules have been used for measurements of fundamental constants [135], e.g. the electron dipole moment [136, 137] or the fine structure constant [138]. Ultracold molecules have also been used to investigate chemistry with control of the internal quantum states [139–145].

In order to cool molecules, different techniques have been used, such as direct laser cooling [146, 147], buffer gas cooling [148], stark deceleration [149], Sisyphus cooling [150], and evaporative cooling [151]. Only evaporative cooling has so far reached the ultracold regime, however, not for molecules in the total ground state.

Alternatively, ultracold molecules can be directly assembled from ultracold atoms. In this case, standard atom cooling techniques can be used to bring atoms into the ultracold regime [152, 153]. One way to create molecules from these ultracold atoms is by photo-association [154]. Here, pairs of atoms are brought into an electronically excited molecular state with a laser. The excited state subsequently decays into the electronic molecular ground state, leaving molecules with ultracold external degrees of freedom. However, the internal ro-vibronic state after this decay cannot be controlled, and is instead probabilistically distributed according to Franck-Condon factors. Repumping schemes have been developed with limited success [155], but to date, no molecular gas with high phase space density has been created.

Magnetic association of ultracold molecules provides an alternative which produces molecules in a well defined final state [156]. By sweeping a magnetic field over a Feshbach resonance, atom pairs are adiabatically moved from a free scattering state to a molecular state, which is in the electronic ground state, but ro-vibrationally highly excited.

In order to create high density ensembles of ground state molecules, these states can be subsequently brought to the ground state using a stimulated Raman adiabatic passage (STIRAP) scheme [157–163]. This scheme involves the Feshbach state, the molecular ground state, and one additional electronically excited state. Two laser pulses are time-dependently ramped up and down, adiabatically changing the dark state of the system from the initial state to the molecular ground state. The molecular state then follows this adiabatic change, transferring population into the ground state. This method has so far been the only successful method to produce ultracold molecular ensembles in the total ground state. In Chapter 5, we propose an alternative association scheme using collective and dissipative effects in a cavity.

## 1.4. Open Quantum Systems

In many realistic scenarios, quantum systems are not closed, but interact with their environment. Then, in principle, a system cannot be described in isolation, but the environment needs to be included in the description, significantly increasing its complexity.

Such open quantum systems are omnipresent in nature. For example, electronically excited atoms or molecules couple to the electromagnetic vacuum field, leading to small energy level shifts and spontaneous emission [164]. In organic molecules, the electronic state is also coupled to molecular vibrations, resulting in dephasing or relaxation [165].

In polaritonic chemistry, typically all electronic, photonic, and vibrational degrees of freedom couple to the environment so that it needs to be analyzed in an open system framework [106].

Including a full description of the environment would make computations of the dynamics intractable in most cases. However, in many scenarios, especially in quantum optics, approximations of the environment are justified. The most important among these is the Markov approximation, which assumes that the environment is memoryless, and the time evolution of a system can be described in term of its current state, only, by a Markovian master equation [164, 166, 167]. This is typically well justified in AMO type systems [164], and will be used throughout this thesis.

There have been a large number of methods developed to treat open quantum systems, especially in the Markov approximation. Adiabatic elimination is a perturbative treatment that eliminates degrees of freedom that evolve much faster than the system's evolution [166]. Quantum trajectories describes a system as a mixture of states which evolve according to a probabilistic equation of motion [168]. In addition, various methods have been developed to treat open systems with Matrix Product states [169]. Chapter 2 introduces the most important methods used in this thesis.

## 1.5. Entanglement and Matrix Product States

Simulating the time evolution of quantum many body systems is an important task, which helps to gain a deeper insight into the underlying physics. However, this task is made challenging by a generally exponential growth of the Hilbert space with system size. This is in contrast to classical systems, where the phase space generally grows linearly with the number of involved particles.

This added complexity is rooted in entanglement between different quantum objects [170–174]. Entanglement describes the phenomenon that the state of an individual quantum object may be not well defined, although the state of the whole quantum system is well defined, leading to large correlations between them. This is in contrast to classical states, which cannot be correlated without being in a statistical mixture. As shown theoretically by Bell and confirmed in experiments, such quantum correlations can also be stronger than any possible classical correlation, even when allowing for statistical mixtures [175]. In a computational sense, entanglement thus measures the complexity of the quantum dynamics [176, 177].

For many interesting states, entanglement is local in the sense that the amount of entanglement between two subsystems scales with the size of their border [174]. Examples include ground states of local Hamiltonians, and more generally states contributing to the dynamics in disordered or noisy systems. This can be used to efficiently simulate many-body systems in the formalism of tensor network states [176, 178]. In particular in one dimension (1D), the border of a subsystem is independent of system size, making this approach very promising.

Based on this insight, matrix product states (MPS) have become the default tool for

numerical simulations of 1D quantum systems [179]. Here, each subsystem is described by a tensor, and entanglement between the subsystems is captured via introducing additional "bond dimensions" for these tensors. Dynamics of these systems can then be simulated by making local updates to the tensors, increasing the bond dimension if necessary [176].

In Chapter 4, matrix product states are introduced in more detail. In Chapters 9 and 10, the entanglement between vibrations and electro-photonic degrees of freedom is analyzed using MPS, and in Chapter 11, the time evolution of operator entanglement in a XXZ spin chain with dephasing is discussed.

## 1.6. Overview of Results

This thesis provides some insight into the role of collective and dissipative effects in polaritonic chemistry and where these effects may be useful. Concerning computations, it is demonstrated how to adapt methods from quantum optics to analyze the involved scenarios. In order to treat large ensembles, molecules are approximated by toy models for understanding fundamental aspects of the emergent dynamics in a bottom-up approach.

In the first part of this thesis, the theoretical background of the analytical and numerical methods is introduced. In Chapter 2, the concepts and methods of open quantum systems are illustrated. Then, quantum optics setups are introduced from an AMO perspective in Chapter 3. Finally, an overview over MPS with a focus on the methods used in this thesis is given in Chapter 4.

The methods introduced in Chapters 2 and 3 are then applied to study the formation of ground state molecules inside a cavity in Chapter 5. There, it is shown how the formation of ground state molecules from atom pairs can be collectively and dissipatively enhanced inside a cavity.

The third part is concerned with polaritonic chemistry. In Chapter 6, the methods used to analyze ground state formation in ultracold chemistry are adapted to photo-induced electron transfer reactions in a cavity. Here, conditions for modified reaction rates under incoherent pumping are discussed. Following that, an overview over previous analytical and numerical work on polaritonic chemistry is given in Chapters 7 and 8, respectively. In the final two chapters of this part, the entanglement between vibrational and electro-photonic degrees of freedom in simplified cavity coupled molecules is analyzed. In Chapter 9, it is shown that disorder of the electronic energies can surprisingly enhance this type of entanglement. This effect is related to a breaking of permutation symmetry, and ultimately leads to modified distributions along the vibrational coordinate. In Chapter 10 the influence of the excitation fraction on this entanglement is discussed, and a product state simulation for the regime with low entanglement is proposed.

In the final part of this thesis, operator entanglement as an open system adaptation of entanglement is discussed in Chapter 11. For an XXZ spin chain, it is shown that dephasing leads to a decrease followed by a logarithmic growth of operator entanglement.

This is in contrast to a strictly linear growth without dephasing. Finally, in Chapter 12, this thesis is concluded by summarizing the implications of the work presented in a general context and giving an outlook on future prospects.

# Bibliography


[1] J. A. Hutchison, T. Schwartz, C. Genet, E. Devaux, and T. W. Ebbesen, "Modifying Chemical Landscapes by Coupling to Vacuum Fields," *Angew. Chem. Int. Ed.*, vol. 51, pp. 1592–1596, Feb. 2012.

[2] A. Thomas, J. George, A. Shalabney, M. Dryzhakov, S. J. Varma, J. Moran, T. Chervy, X. Zhong, E. Devaux, C. Genet, J. A. Hutchison, and T. W. Ebbesen, "Ground-State Chemical Reactivity under Vibrational Coupling to the Vacuum Electromagnetic Field," *Angew. Chem. Int. Ed.*, vol. 55, no. 38, pp. 11462–11466, 2016.

[3] A. Thomas, L. Lethuillier-Karl, K. Nagarajan, R. M. A. Vergauwe, J. George, T. Chervy, A. Shalabney, E. Devaux, C. Genet, J. Moran, and T. W. Ebbesen, "Tilting a ground-state reactivity landscape by vibrational strong coupling," *Science*, vol. 363, pp. 615–619, Feb. 2019.

[4] F. J. Garcia-Vidal, C. Ciuti, and T. W. Ebbesen, "Manipulating matter by strong coupling to vacuum fields," *Science*, vol. 373, p. eabd0336, July 2021.

[5] F. Herrera and J. Owrutsky, "Molecular polaritons for controlling chemistry with quantum optics," *J. Chem. Phys.*, vol. 152, p. 100902, Mar. 2020.

[6] J. Feist, J. Galego, and F. J. Garcia-Vidal, "Polaritonic Chemistry with Organic Molecules," *ACS Photonics*, vol. 5, pp. 205–216, Jan. 2018.

[7] T. W. Ebbesen, "Hybrid Light–Matter States in a Molecular and Material Science Perspective," *Acc. Chem. Res.*, vol. 49, pp. 2403–2412, Nov. 2016.

[8] J. Yuen-Zhou and V. M. Menon, "Polariton chemistry: Thinking inside the (photon) box," *PNAS*, vol. 116, pp. 5214–5216, Mar. 2019.

[9] R. F. Ribeiro, L. A. Martínez-Martínez, M. Du, J. Campos-Gonzalez-Angulo, and J. Yuen-Zhou, "Polariton chemistry: Controlling molecular dynamics with optical cavities," *Chem. Sci.*, vol. 9, pp. 6325–6339, Aug. 2018.

[10] C. Cohen-Tannoudji, J. Dupont-Roc, and G. Grynberg, *Atom-Photon Interactions: Basic Processes and Applications*. New York: Wiley, 1992.

[11] R. H. Dicke, "Coherence in Spontaneous Radiation Processes," *Phys. Rev.*, vol. 93, pp. 99–110, Jan. 1954.

[12] M. Tavis and F. W. Cummings, "Exact solution for an $n$-molecule—radiation-field hamiltonian," *Phys. Rev.*, vol. 170, pp. 379–384, June 1968.

[13] S. Haroche and J.-M. Raimond, *Exploring the Quantum: Atoms, Cavities, and Photons*. OUP Oxford, Aug. 2006.

[14] C. W. Gardiner and P. Zoller, *The Quantum World of Ultracold Atoms and Light Book Ii: The Physics of Quantum Optical Devices*, vol. 4. World Scientific Publishing Company, 2015.

[15] D. Hunger, T. Steinmetz, Y. Colombe, C. Deutsch, T. W. Hänsch, and J. Reichel, "A fiber Fabry–Perot cavity with high finesse," *New J. Phys.*, vol. 12, p. 065038, June 2010.

[16] V. Savona, L. C. Andreani, P. Schwendimann, and A. Quattropani, "Quantum well excitons in semiconductor microcavities: Unified treatment of weak and strong coupling regimes," *Solid State Communications*, vol. 93, pp. 733–739, Mar. 1995.

[17] P. Törmä and W. L. Barnes, "Strong coupling between surface plasmon polaritons and emitters: A review," *Rep. Prog. Phys.*, vol. 78, p. 013901, Dec. 2014.

[18] A. Polman, "Plasmonics Applied," *Science*, vol. 322, pp. 868–869, Nov. 2008.

[19] E. M. Purcell, H. C. Torrey, and R. V. Pound, "Resonance Absorption by Nuclear Magnetic Moments in a Solid," *Phys. Rev.*, vol. 69, pp. 37–38, Jan. 1946.

[20] H. A. Atwater and A. Polman, "Plasmonics for improved photovoltaic devices," *Nature Mater*, vol. 9, pp. 205–213, Mar. 2010.

[21] T. B. Norris, J.-K. Rhee, C.-Y. Sung, Y. Arakawa, M. Nishioka, and C. Weisbuch, "Time-resolved vacuum Rabi oscillations in a semiconductor quantum microcavity," *Phys. Rev. B*, vol. 50, pp. 14663–14666, Nov. 1994.

[22] R. Miller, T. E. Northup, K. M. Birnbaum, A. Boca, A. D. Boozer, and H. J. Kimble, "Trapped atoms in cavity QED: Coupling quantized light and matter," *J. Phys. B: At. Mol. Opt. Phys.*, vol. 38, pp. S551–S565, Apr. 2005.

[23] P. Michetti, L. Mazza, and G. C. La Rocca, "Strongly Coupled Organic Microcavities," in *Organic Nanophotonics: Fundamentals and Applications* (Y. S. Zhao, ed.), Nano-Optics and Nanophotonics, pp. 39–68, Berlin, Heidelberg: Springer Berlin Heidelberg, 2015.

[24] D. G. Lidzey, D. D. C. Bradley, M. S. Skolnick, T. Virgili, S. Walker, and D. M. Whittaker, "Strong exciton–photon coupling in an organic semiconductor microcavity," *Nature*, vol. 395, pp. 53–55, Sept. 1998.

[25] J. P. Reithmaier, G. Sęk, A. Löffler, C. Hofmann, S. Kuhn, S. Reitzenstein, L. V. Keldysh, V. D. Kulakovskii, T. L. Reinecke, and A. Forchel, "Strong coupling in a single quantum dot–semiconductor microcavity system," *Nature*, vol. 432, pp. 197–200, Nov. 2004.

[26] A. Blais, R.-S. Huang, A. Wallraff, S. M. Girvin, and R. J. Schoelkopf, "Cavity quantum electrodynamics for superconducting electrical circuits: An architecture for quantum computation," *Phys. Rev. A*, vol. 69, p. 062320, June 2004.

[27] E. Janitz, M. K. Bhaskar, and L. Childress, "Cavity quantum electrodynamics with color centers in diamond," *Optica, OPTICA*, vol. 7, pp. 1232–1252, Oct. 2020.

[28] X. Liu, T. Galfsky, Z. Sun, F. Xia, E.-c. Lin, Y.-H. Lee, S. Kéna-Cohen, and V. M. Menon, "Strong light–matter coupling in two-dimensional atomic crystals," *Nature Photon*, vol. 9, pp. 30–34, Jan. 2015.

[29] W. Liu, B. Lee, C. H. Naylor, H.-S. Ee, J. Park, A. T. C. Johnson, and R. Agarwal, "Strong Exciton–Plasmon Coupling in MoS2 Coupled with Plasmonic Lattice," *Nano Lett.*, vol. 16, pp. 1262–1269, Feb. 2016.

[30] S. Wang, S. Li, T. Chervy, A. Shalabney, S. Azzini, E. Orgiu, J. A. Hutchison, C. Genet, P. Samorì, and T. W. Ebbesen, "Coherent Coupling of WS2 Monolayers with Metallic Photonic Nanostructures at Room Temperature," *Nano Lett.*, vol. 16, pp. 4368–4374, July 2016.

[31] H. Konishi, K. Roux, V. Helson, and J.-P. Brantut, "Universal pair polaritons in a strongly interacting Fermi gas," *Nature*, vol. 596, pp. 509–513, Aug. 2021.

[32] C. J. Hood, M. S. Chapman, T. W. Lynn, and H. J. Kimble, "Real-Time Cavity QED with Single Atoms," *Phys. Rev. Lett.*, vol. 80, pp. 4157–4160, May 1998.

[33] J. Ye, D. W. Vernooy, and H. J. Kimble, "Trapping of Single Atoms in Cavity QED," *Phys. Rev. Lett.*, vol. 83, pp. 4987–4990, Dec. 1999.

[34] H. J. Kimble, "Strong interactions of single atoms and photons in cavity QED," *Phys. Scr.*, vol. 1998, p. 127, Jan. 1998.

[35] F. Brennecke, T. Donner, S. Ritter, T. Bourdel, M. Köhl, and T. Esslinger, "Cavity QED with a Bose–Einstein condensate," *Nature*, vol. 450, pp. 268–271, Nov. 2007.

[36] E. Hagley, X. Maître, G. Nogues, C. Wunderlich, M. Brune, J. M. Raimond, and S. Haroche, "Generation of Einstein-Podolsky-Rosen Pairs of Atoms," *Phys. Rev. Lett.*, vol. 79, pp. 1–5, July 1997.

[37] J. M. Raimond, M. Brune, and S. Haroche, "Manipulating quantum entanglement with atoms and photons in a cavity," *Rev. Mod. Phys.*, vol. 73, pp. 565–582, Aug. 2001.

[38] H. Mabuchi and A. C. Doherty, "Cavity Quantum Electrodynamics: Coherence in Context," *Science*, vol. 298, pp. 1372–1377, Nov. 2002.

[39] J. A. Muniz, D. J. Young, J. R. K. Cline, and J. K. Thompson, "Cavity-qed measurements of the $^{87}$Sr millihertz optical clock transition and determination of its natural linewidth," *Phys. Rev. Research*, vol. 3, p. 023152, May 2021.

[40] J. G. Bohnet, Z. Chen, J. M. Weiner, D. Meiser, M. J. Holland, and J. K. Thompson, "A steady-state superradiant laser with less than one intracavity photon," *Nature*, vol. 484, pp. 78–81, Apr. 2012.

[41] K. Baumann, C. Guerlin, F. Brennecke, and T. Esslinger, "Dicke quantum phase transition with a superfluid gas in an optical cavity," *Nature*, vol. 464, pp. 1301–1306, Apr. 2010.

[42] H. Ritsch, P. Domokos, F. Brennecke, and T. Esslinger, "Cold atoms in cavity-generated dynamical optical potentials," *Rev. Mod. Phys.*, vol. 85, pp. 553–601, Apr. 2013.

[43] V. D. Vaidya, Y. Guo, R. M. Kroeze, K. E. Ballantine, A. J. Kollár, J. Keeling, and B. L. Lev, "Tunable-Range, Photon-Mediated Atomic Interactions in Multimode Cavity QED," *Phys. Rev. X*, vol. 8, p. 011002, Jan. 2018.

[44] M. A. Norcia, R. J. Lewis-Swan, J. R. K. Cline, B. Zhu, A. M. Rey, and J. K. Thompson, "Cavity-mediated collective spin-exchange interactions in a strontium superradiant laser," *Science*, July 2018.

[45] E. J. Davis, A. Periwal, E. S. Cooper, G. Bentsen, S. J. Evered, K. Van Kirk, and M. H. Schleier-Smith, "Protecting Spin Coherence in a Tunable Heisenberg Model," *Phys. Rev. Lett.*, vol. 125, p. 060402, Aug. 2020.

[46] J. A. Muniz, D. Barberena, R. J. Lewis-Swan, D. J. Young, J. R. K. Cline, A. M. Rey, and J. K. Thompson, "Exploring dynamical phase transitions with cold atoms in an optical cavity," *Nature*, vol. 580, pp. 602–607, Apr. 2020.

[47] R. J. Lewis-Swan, D. Barberena, J. R. K. Cline, D. J. Young, J. K. Thompson, and A. M. Rey, "Cavity-QED Quantum Simulator of Dynamical Phases of a Bardeen-Cooper-Schrieffer Superconductor," *Phys. Rev. Lett.*, vol. 126, p. 173601, Apr. 2021.

[48] S. J. van Enk, H. J. Kimble, and H. Mabuchi, "Quantum Information Processing in Cavity-QED," *Quantum Information Processing*, vol. 3, pp. 75–90, Oct. 2004.

[49] A. Imamoglu, D. D. Awschalom, G. Burkard, D. P. DiVincenzo, D. Loss, M. Sherwin, and A. Small, "Quantum Information Processing Using Quantum Dot Spins and Cavity QED," *Phys. Rev. Lett.*, vol. 83, pp. 4204–4207, Nov. 1999.

[50] J. Doyle, B. Friedrich, R. V. Krems, and F. Masnou-Seeuws, "Editorial: Quo vadis, cold molecules?," *Eur. Phys. J. D*, vol. 31, pp. 149–164, Nov. 2004.

[51] L. D. Carr, D. DeMille, R. V. Krems, and J. Ye, "Cold and ultracold molecules: Science, technology and applications," *New J. Phys.*, vol. 11, p. 055049, May 2009.

[52] G. Quéméner and P. S. Julienne, "Ultracold Molecules under Control!," *Chem. Rev.*, vol. 112, pp. 4949–5011, Sept. 2012.

[53] S. A. Moses, J. P. Covey, M. T. Miecnikowski, D. S. Jin, and J. Ye, "New frontiers for quantum gases of polar molecules," *Nature Phys*, vol. 13, pp. 13–20, Jan. 2017.

[54] J. L. Bohn, A. M. Rey, and J. Ye, "Cold molecules: Progress in quantum engineering of chemistry and quantum matter," *Science*, vol. 357, pp. 1002–1010, Sept. 2017.

[55] V. M. Agranovich, M. Litinskaia, and D. G. Lidzey, "Cavity polaritons in microcavities containing disordered organic semiconductors," *Phys. Rev. B*, vol. 67, Feb. 2003.

[56] T. Schwartz, J. A. Hutchison, J. Léonard, C. Genet, S. Haacke, and T. W. Ebbesen, "Polariton Dynamics under Strong Light-Molecule Coupling," *ChemPhysChem*, vol. 14, pp. 125–131, Jan. 2013.

[57] D. G. Lidzey, A. M. Fox, M. D. Rahn, M. S. Skolnick, V. M. Agranovich, and S. Walker, "Experimental study of light emission from strongly coupled organic

semiconductor microcavities following nonresonant laser excitation," *Phys. Rev. B*, vol. 65, p. 195312, May 2002.

[58] M. Litinskaya, P. Reineker, and V. M. Agranovich, "Fast polariton relaxation in strongly coupled organic microcavities," *Journal of Luminescence*, vol. 110, pp. 364–372, Dec. 2004.

[59] J.-H. Song, Y. He, A. V. Nurmikko, J. Tischler, and V. Bulovic, "Exciton-polariton dynamics in a transparent organic semiconductor microcavity," *Phys. Rev. B*, vol. 69, p. 235330, June 2004.

[60] P. G. Savvidis, L. G. Connolly, M. S. Skolnick, D. G. Lidzey, and J. J. Baumberg, "Ultrafast polariton dynamics in strongly coupled zinc porphyrin microcavities at room temperature," *Phys. Rev. B*, vol. 74, p. 113312, Sept. 2006.

[61] A. D. Dunkelberger, R. B. Davidson, W. Ahn, B. S. Simpkins, and J. C. Owrutsky, "Ultrafast Transmission Modulation and Recovery via Vibrational Strong Coupling," *J. Phys. Chem. A*, vol. 122, pp. 965–971, Feb. 2018.

[62] P. Saurabh and S. Mukamel, "Two-dimensional infrared spectroscopy of vibrational polaritons of molecules in an optical cavity," *J. Chem. Phys.*, vol. 144, p. 124115, Mar. 2016.

[63] B. Xiang, R. F. Ribeiro, A. D. Dunkelberger, J. Wang, Y. Li, B. S. Simpkins, J. C. Owrutsky, J. Yuen-Zhou, and W. Xiong, "Two-dimensional infrared spectroscopy of vibrational polaritons," *PNAS*, vol. 115, pp. 4845–4850, May 2018.

[64] A. D. Dunkelberger, B. T. Spann, K. P. Fears, B. S. Simpkins, and J. C. Owrutsky, "Modified relaxation dynamics and coherent energy exchange in coupled vibration-cavity polaritons," *Nat Commun*, vol. 7, p. 13504, Nov. 2016.

[65] D. M. Coles, Y. Yang, Y. Wang, R. T. Grant, R. A. Taylor, S. K. Saikin, A. Aspuru-Guzik, D. G. Lidzey, J. K.-H. Tang, and J. M. Smith, "Strong coupling between chlorosomes of photosynthetic bacteria and a confined optical cavity mode," *Nat Commun*, vol. 5, p. 5561, Nov. 2014.

[66] A. Canaguier-Durand, E. Devaux, J. George, Y. Pang, J. A. Hutchison, T. Schwartz, C. Genet, N. Wilhelms, J.-M. Lehn, and T. W. Ebbesen, "Thermodynamics of Molecules Strongly Coupled to the Vacuum Field," *Angew. Chem. Int. Ed.*, vol. 52, pp. 10533–10536, Sept. 2013.

[67] S. Kéna-Cohen and S. R. Forrest, "Room-temperature polariton lasing in an organic single-crystal microcavity," *Nat. Photonics*, vol. 4, pp. 371–375, June 2010.

[68] J. D. Plumhof, T. Stöferle, L. Mai, U. Scherf, and R. F. Mahrt, "Room-temperature Bose–Einstein condensation of cavity exciton–polaritons in a polymer," *Nature Mater*, vol. 13, pp. 247–252, Mar. 2014.

[69] K. S. Daskalakis, S. A. Maier, R. Murray, and S. Kéna-Cohen, "Nonlinear interactions in an organic polariton condensate," *Nature Mater*, vol. 13, pp. 271–278, Mar. 2014.

[70] C. P. Dietrich, A. Steude, L. Tropf, M. Schubert, N. M. Kronenberg, K. Ostermann, S. Höfling, and M. C. Gather, "An exciton-polariton laser based on biologically produced fluorescent protein," *Sci. Adv.*, vol. 2, no. 8, p. e1600666, 2016.

[71] T. Cookson, K. Georgiou, A. Zasedatelev, R. T. Grant, T. Virgili, M. Cavazzini, F. Galeotti, C. Clark, N. G. Berloff, D. G. Lidzey, and P. G. Lagoudakis, "A Yellow Polariton Condensate in a Dye Filled Microcavity," *Adv. Opt. Mater.*, vol. 5, no. 18, p. 1700203, 2017.

[72] G. Lerario, A. Fieramosca, F. Barachati, D. Ballarini, K. S. Daskalakis, L. Dominici, M. De Giorgi, S. A. Maier, G. Gigli, S. Kéna-Cohen, and D. Sanvitto, "Room-temperature superfluidity in a polariton condensate," *Nature Phys*, vol. 13, pp. 837–841, Sept. 2017.

[73] M. Ramezani, A. Halpin, A. I. Fernández-Domínguez, J. Feist, S. R.-K. Rodriguez, F. J. Garcia-Vidal, and J. G. Rivas, "Plasmon-exciton-polariton lasing," *Optica, OPTICA*, vol. 4, pp. 31–37, Jan. 2017.

[74] F. Scafirimuto, D. Urbonas, U. Scherf, R. F. Mahrt, and T. Stöferle, "Room-Temperature Exciton-Polariton Condensation in a Tunable Zero-Dimensional Microcavity," *ACS Photonics*, vol. 5, pp. 85–89, Jan. 2018.

[75] S. K. Rajendran, M. Wei, H. Ohadi, A. Ruseckas, G. A. Turnbull, and I. D. W. Samuel, "Low Threshold Polariton Lasing from a Solution-Processed Organic Semiconductor in a Planar Microcavity," *Adv. Opt. Mater.*, vol. 7, no. 12, p. 1801791, 2019.

[76] M. Wei, S. K. Rajendran, H. Ohadi, L. Tropf, M. C. Gather, G. A. Turnbull, and I. D. W. Samuel, "Low-threshold polariton lasing in a highly disordered conjugated polymer," *Optica, OPTICA*, vol. 6, pp. 1124–1129, Sept. 2019.

[77] A. I. Väkeväinen, A. J. Moilanen, M. Nečada, T. K. Hakala, K. S. Daskalakis, and P. Törmä, "Sub-picosecond thermalization dynamics in condensation of strongly coupled lattice plasmons," *Nat Commun*, vol. 11, p. 3139, June 2020.

[78] T. Yagafarov, D. Sannikov, A. Zasedatelev, K. Georgiou, A. Baranikov, O. Kyriienko, I. Shelykh, L. Gai, Z. Shen, D. Lidzey, and P. Lagoudakis, "Mechanisms of blueshifts in organic polariton condensates," *Commun Phys*, vol. 3, pp. 1–10, Jan. 2020.

[79] J. Keeling and S. Kéna-Cohen, "Bose–Einstein Condensation of Exciton-Polaritons in Organic Microcavities," *Annu. Rev. Phys. Chem.*, vol. 71, pp. 435–459, Apr. 2020.

[80] T. Schwartz, J. A. Hutchison, C. Genet, and T. W. Ebbesen, "Reversible Switching of Ultrastrong Light-Molecule Coupling," *Phys. Rev. Lett.*, vol. 106, May 2011.

[81] S. Kéna-Cohen, S. A. Maier, and D. D. C. Bradley, "Ultrastrongly Coupled Exciton–Polaritons in Metal-Clad Organic Semiconductor Microcavities," *Adv. Opt. Mater.*, vol. 1, no. 11, pp. 827–833, 2013.

[82] F. Barachati, J. Simon, Y. A. Getmanenko, S. Barlow, S. R. Marder, and S. Kéna-Cohen, "Tunable Third-Harmonic Generation from Polaritons in the Ultrastrong Coupling Regime," *ACS Photonics*, vol. 5, pp. 119–125, Jan. 2018.

[83] C. Bujalance, V. Esteso, L. Caliò, G. Lavarda, T. Torres, J. Feist, F. J. García-Vidal, G. Bottari, and H. Míguez, "Ultrastrong Exciton–Photon Coupling in

Broadband Solar Absorbers," *J. Phys. Chem. Lett.*, vol. 12, pp. 10706–10712, Nov. 2021.

[84] R. Chikkaraddy, B. de Nijs, F. Benz, S. J. Barrow, O. A. Scherman, E. Rosta, A. Demetriadou, P. Fox, O. Hess, and J. J. Baumberg, "Single-molecule strong coupling at room temperature in plasmonic nanocavities," *Nature*, vol. 535, pp. 127–130, July 2016.

[85] F. Benz, M. K. Schmidt, A. Dreismann, R. Chikkaraddy, Y. Zhang, A. Demetriadou, C. Carnegie, H. Ohadi, B. de Nijs, R. Esteban, J. Aizpurua, and J. J. Baumberg, "Single-molecule optomechanics in "picocavities"," *Science*, vol. 354, pp. 726–729, Nov. 2016.

[86] D. Wang, H. Kelkar, D. Martin-Cano, T. Utikal, S. Götzinger, and V. Sandoghdar, "Coherent Coupling of a Single Molecule to a Scanning Fabry-Perot Microcavity," *Phys. Rev. X*, vol. 7, p. 021014, Apr. 2017.

[87] O. S. Ojambati, R. Chikkaraddy, W. D. Deacon, M. Horton, D. Kos, V. A. Turek, U. F. Keyser, and J. J. Baumberg, "Quantum electrodynamics at room temperature coupling a single vibrating molecule with a plasmonic nanocavity," *Nat Commun*, vol. 10, p. 1049, Mar. 2019.

[88] D. M. Coles, N. Somaschi, P. Michetti, C. Clark, P. G. Lagoudakis, P. G. Savvidis, and D. G. Lidzey, "Polariton-mediated energy transfer between organic dyes in a strongly coupled optical microcavity," *Nature Mater*, vol. 13, pp. 712–719, July 2014.

[89] E. Orgiu, J. George, J. A. Hutchison, E. Devaux, J. F. Dayen, B. Doudin, F. Stellacci, C. Genet, J. Schachenmayer, C. Genes, G. Pupillo, P. Samorì, and T. W. Ebbesen, "Conductivity in organic semiconductors hybridized with the vacuum field," *Nat. Mater.*, vol. 14, pp. 1123–1129, Nov. 2015.

[90] X. Zhong, T. Chervy, S. Wang, J. George, A. Thomas, J. A. Hutchison, E. Devaux, C. Genet, and T. W. Ebbesen, "Non-Radiative Energy Transfer Mediated by Hybrid Light-Matter States," *Angew. Chem. Int. Ed.*, vol. 55, no. 21, pp. 6202–6206, 2016.

[91] X. Zhong, T. Chervy, L. Zhang, A. Thomas, J. George, C. Genet, J. A. Hutchison, and T. W. Ebbesen, "Energy Transfer between Spatially Separated Entangled Molecules," *Angew. Chem. Int. Ed.*, vol. 56, no. 31, pp. 9034–9038, 2017.

[92] K. Georgiou, P. Michetti, L. Gai, M. Cavazzini, Z. Shen, and D. G. Lidzey, "Control over Energy Transfer between Fluorescent BODIPY Dyes in a Strongly Coupled Microcavity," *ACS Photonics*, vol. 5, pp. 258–266, Jan. 2018.

[93] S. Hou, M. Khatoniar, K. Ding, Y. Qu, A. Napolov, V. M. Menon, and S. R. Forrest, "Ultralong-Range Energy Transport in a Disordered Organic Semiconductor at Room Temperature Via Coherent Exciton-Polariton Propagation," *Adv. Mater.*, vol. 32, no. 28, p. 2002127, 2020.

[94] E. Eizner, L. A. Martínez-Martínez, J. Yuen-Zhou, and S. Kéna-Cohen, "Inverting singlet and triplet excited states using strong light-matter coupling," *Sci. Adv.*, vol. 5, p. eaax4482, Dec. 2019.

[95] S. Takahashi, K. Watanabe, and Y. Matsumoto, "Singlet fission of amorphous rubrene modulated by polariton formation," *J. Chem. Phys.*, vol. 151, p. 074703, Aug. 2019.

[96] K. Stranius, M. Hertzog, and K. Börjesson, "Selective manipulation of electronically excited states through strong light–matter interactions," *Nat. Commun.*, vol. 9, p. 2273, June 2018.

[97] B. Munkhbat, M. Wersäll, D. G. Baranov, T. J. Antosiewicz, and T. Shegai, "Suppression of photo-oxidation of organic chromophores by strong coupling to plasmonic nanoantennas," *Sci. Adv.*, vol. 4, p. eaas9552, July 2018.

[98] V. N. Peters, M. O. Faruk, J. Asane, R. Alexander, D. A. Peters, S. Prayakarao, S. Rout, and M. A. Noginov, "Effect of strong coupling on photodegradation of the semiconducting polymer P3HT," *Optica, OPTICA*, vol. 6, pp. 318–325, Mar. 2019.

[99] D. Polak, R. Jayaprakash, T. P. Lyons, L. Á. Martínez-Martínez, A. Leventis, K. J. Fallon, H. Coulthard, D. G. Bossanyi, K. Georgiou, I. I. Anthony J. Petty, J. Anthony, H. Bronstein, J. Yuen-Zhou, A. I. Tartakovskii, J. Clark, and A. J. Musser, "Manipulating molecules with strong coupling: Harvesting triplet excitons in organic exciton microcavities," *Chem. Sci.*, vol. 11, pp. 343–354, Jan. 2020.

[100] Y. Yu, S. Mallick, M. Wang, and K. Börjesson, "Barrier-free reverse-intersystem crossing in organic molecules by strong light-matter coupling," *Nat Commun*, vol. 12, p. 3255, May 2021.

[101] J. Mony, C. Climent, A. U. Petersen, K. Moth-Poulsen, J. Feist, and K. Börjesson, "Photoisomerization Efficiency of a Solar Thermal Fuel in the Strong Coupling Regime," *Adv. Funct. Mater.*, vol. 31, p. 2010737, Mar. 2021.

[102] J. Lather, P. Bhatt, A. Thomas, T. W. Ebbesen, and J. George, "Cavity Catalysis by Cooperative Vibrational Strong Coupling of Reactant and Solvent Molecules," *Angew. Chem. Int. Ed.*, vol. 58, no. 31, pp. 10635–10638, 2019.

[103] R. M. A. Vergauwe, A. Thomas, K. Nagarajan, A. Shalabney, J. George, T. Chervy, M. Seidel, E. Devaux, V. Torbeev, and T. W. Ebbesen, "Modification of Enzyme Activity by Vibrational Strong Coupling of Water," *Angew. Chem. Int. Ed.*, vol. 58, no. 43, pp. 15324–15328, 2019.

[104] D. S. Dovzhenko, S. V. Ryabchuk, Y. P. Rakovich, and I. R. Nabiev, "Light–matter interaction in the strong coupling regime: Configurations, conditions, and applications," *Nanoscale*, vol. 10, pp. 3589–3605, Feb. 2018.

[105] M. Hertzog, M. Wang, J. Mony, and K. Börjesson, "Strong light–matter interactions: A new direction within chemistry," *Chem. Soc. Rev.*, vol. 48, pp. 937–961, Feb. 2019.

[106] F. Herrera and F. C. Spano, "Theory of Nanoscale Organic Cavities: The Essential Role of Vibration-Photon Dressed States," *ACS Photonics*, vol. 5, pp. 65–79, Jan. 2018.

[107] S. Satapathy, M. Khatoniar, D. K. Parappuram, B. Liu, G. John, J. Feist, F. J. Garcia-Vidal, and V. M. Menon, "Selective isomer emission via funneling of exciton polaritons," *Sci. Adv.*, vol. 7, no. 44, p. eabj0997, 2021.

[108] C. Ye, S. Mallick, M. Hertzog, M. Kowalewski, and K. Börjesson, "Direct Transition from Triplet Excitons to Hybrid Light–Matter States via Triplet–Triplet Annihilation," *J. Am. Chem. Soc.*, vol. 143, pp. 7501–7508, May 2021.

[109] Q. Ou, Y. Shao, and Z. Shuai, "Enhanced Reverse Intersystem Crossing Promoted by Triplet Exciton–Photon Coupling," *J. Am. Chem. Soc.*, vol. 143, p. 17786, Oct. 2021.

[110] R. Puro, J. D. B. Van Schenck, R. Center, E. K. Holland, J. E. Anthony, and O. Ostroverkhova, "Exciton Polariton-Enhanced Photodimerization of Functionalized Tetracene," *J. Phys. Chem. C*, Dec. 2021.

[111] K. Hirai, R. Takeda, J. A. Hutchison, and H. Uji-i, "Modulation of Prins Cyclization by Vibrational Strong Coupling," *Angew. Chem. Int. Ed.*, vol. 59, no. 13, pp. 5332–5335, 2020.

[112] H. Hiura, A. Shalabney, and J. George, "Cavity Catalysis -Accelerating Reactions under Vibrational Strong Coupling- (preprint) chemrxiv.7234721.v3," Nov. 2018.

[113] F. Herrera and F. C. Spano, "Cavity-Controlled Chemistry in Molecular Ensembles," *Phys. Rev. Lett.*, vol. 116, p. 238301, June 2016.

[114] L. A. Martínez-Martínez, M. Du, R. F. Ribeiro, S. Kéna-Cohen, and J. Yuen-Zhou, "Polariton-Assisted Singlet Fission in Acene Aggregates," *J. Phys. Chem. Lett.*, vol. 9, pp. 1951–1957, Apr. 2018.

[115] M. Reitz, C. Sommer, and C. Genes, "Langevin Approach to Quantum Optics with Molecules," *Phys. Rev. Lett.*, vol. 122, p. 203602, May 2019.

[116] J. A. Campos-Gonzalez-Angulo, R. F. Ribeiro, and J. Yuen-Zhou, "Resonant catalysis of thermally activated chemical reactions with vibrational polaritons," *Nat Commun*, vol. 10, p. 4685, Oct. 2019.

[117] A. Mandal, T. D. Krauss, and P. Huo, "Polariton-Mediated Electron Transfer via Cavity Quantum Electrodynamics," *J. Phys. Chem. B*, vol. 124, pp. 6321–6340, July 2020.

[118] C. Sommer, M. Reitz, F. Mineo, and C. Genes, "Molecular polaritonics in dense mesoscopic disordered ensembles," *Phys. Rev. Research*, vol. 3, p. 033141, Aug. 2021.

[119] J. Galego, F. J. Garcia-Vidal, and J. Feist, "Cavity-Induced Modifications of Molecular Structure in the Strong-Coupling Regime," *Phys. Rev. X*, vol. 5, p. 041022, Nov. 2015.

[120] G. Groenhof, C. Climent, J. Feist, D. Morozov, and J. J. Toppari, "Tracking Polariton Relaxation with Multiscale Molecular Dynamics Simulations," *J. Phys. Chem. Lett.*, vol. 10, pp. 5476–5483, Sept. 2019.

[121] Y. Zhang, T. Nelson, and S. Tretiak, "Non-adiabatic molecular dynamics of molecules in the presence of strong light-matter interactions," *J. Chem. Phys.*, vol. 151, p. 154109, Oct. 2019.

[122] J. Fregoni, G. Granucci, E. Coccia, M. Persico, and S. Corni, "Manipulating azobenzene photoisomerization through strong light–molecule coupling," *Nat. Commun.*, vol. 9, Dec. 2018.

[123] H. L. Luk, J. Feist, J. J. Toppari, and G. Groenhof, "Multiscale Molecular Dynamics Simulations of Polaritonic Chemistry," *J. Chem. Theory Comput.*, vol. 13, pp. 4324–4335, Sept. 2017.

[124] P. Antoniou, F. Suchanek, J. F. Varner, and J. J. Foley, "Role of Cavity Losses on Nonadiabatic Couplings and Dynamics in Polaritonic Chemistry," *J. Phys. Chem. Lett.*, vol. 11, pp. 9063–9069, Nov. 2020.

[125] E. Davidsson and M. Kowalewski, "Atom Assisted Photochemistry in Optical Cavities," *J. Phys. Chem. A*, vol. 124, pp. 4672–4677, June 2020.

[126] O. Vendrell, "Collective Jahn-Teller Interactions through Light-Matter Coupling in a Cavity," *Phys. Rev. Lett.*, vol. 121, p. 253001, Dec. 2018.

[127] J. del Pino, F. A. Y. N. Schröder, A. W. Chin, J. Feist, and F. J. Garcia-Vidal, "Tensor network simulation of polaron-polaritons in organic microcavities," *Phys. Rev. B*, vol. 98, p. 165416, Oct. 2018.

[128] U. Mordovina, C. Bungey, H. Appel, P. J. Knowles, A. Rubio, and F. R. Manby, "Polaritonic coupled-cluster theory," *Phys. Rev. Research*, vol. 2, p. 023262, June 2020.

[129] D. S. Wang, T. Neuman, J. Flick, and P. Narang, "Light–matter interaction of a molecule in a dissipative cavity from first principles," *J. Chem. Phys.*, vol. 154, p. 104109, Mar. 2021.

[130] N. Balakrishnan, "Perspective: Ultracold molecules and the dawn of cold controlled chemistry," *J. Chem. Phys.*, vol. 145, p. 150901, Oct. 2016.

[131] M. A. Baranov, M. Dalmonte, G. Pupillo, and P. Zoller, "Condensed Matter Theory of Dipolar Quantum Gases," *Chem. Rev.*, vol. 112, pp. 5012–5061, Sept. 2012.

[132] N. Y. Yao, A. V. Gorshkov, C. R. Laumann, A. M. Läuchli, J. Ye, and M. D. Lukin, "Realizing Fractional Chern Insulators in Dipolar Spin Systems," *Phys. Rev. Lett.*, vol. 110, p. 185302, Apr. 2013.

[133] D. DeMille, "Quantum Computation with Trapped Polar Molecules," *Phys. Rev. Lett.*, vol. 88, p. 067901, Jan. 2002.

[134] P. Rabl, D. DeMille, J. M. Doyle, M. D. Lukin, R. J. Schoelkopf, and P. Zoller, "Hybrid Quantum Processors: Molecular Ensembles as Quantum Memory for Solid State Circuits," *Phys. Rev. Lett.*, vol. 97, p. 033003, July 2006.

[135] M. S. Safronova, D. Budker, D. DeMille, D. F. J. Kimball, A. Derevianko, and C. W. Clark, "Search for new physics with atoms and molecules," *Rev. Mod. Phys.*, vol. 90, p. 025008, June 2018.

[136] J. J. Hudson, D. M. Kara, I. J. Smallman, B. E. Sauer, M. R. Tarbutt, and E. A. Hinds, "Improved measurement of the shape of the electron," *Nature*, vol. 473, pp. 493–496, May 2011.

[137] W. B. Cairncross, D. N. Gresh, M. Grau, K. C. Cossel, T. S. Roussy, Y. Ni, Y. Zhou, J. Ye, and E. A. Cornell, "Precision Measurement of the Electron's Electric Dipole Moment Using Trapped Molecular Ions," *Phys. Rev. Lett.*, vol. 119, p. 153001, Oct. 2017.

[138] E. R. Hudson, H. J. Lewandowski, B. C. Sawyer, and J. Ye, "Cold Molecule Spectroscopy for Constraining the Evolution of the Fine Structure Constant," *Phys. Rev. Lett.*, vol. 96, p. 143004, Apr. 2006.

[139] S. Ospelkaus, K.-K. Ni, D. Wang, M. H. G. de Miranda, B. Neyenhuis, G. Quéméner, P. S. Julienne, J. L. Bohn, D. S. Jin, and J. Ye, "Quantum-State Controlled Chemical Reactions of Ultracold Potassium-Rubidium Molecules," *Science*, vol. 327, pp. 853–857, Feb. 2010.

[140] K.-K. Ni, S. Ospelkaus, D. Wang, G. Quéméner, B. Neyenhuis, M. H. G. de Miranda, J. L. Bohn, J. Ye, and D. S. Jin, "Dipolar collisions of polar molecules in the quantum regime," *Nature*, vol. 464, pp. 1324–1328, Apr. 2010.

[141] J. Rui, H. Yang, L. Liu, D.-C. Zhang, Y.-X. Liu, J. Nan, Y.-A. Chen, B. Zhao, and J.-W. Pan, "Controlled state-to-state atom-exchange reaction in an ultracold atom–dimer mixture," *Nature Phys*, vol. 13, pp. 699–703, July 2017.

[142] J. Wolf, M. Deiß, A. Krükow, E. Tiemann, B. P. Ruzic, Y. Wang, J. P. D'Incao, P. S. Julienne, and J. H. Denschlag, "State-to-state chemistry for three-body recombination in an ultracold rubidium gas," *Science*, Nov. 2017.

[143] J. Toscano, H. J. Lewandowski, and B. R. Heazlewood, "Cold and controlled chemical reaction dynamics," *Phys. Chem. Chem. Phys.*, vol. 22, no. 17, pp. 9180–9194, 2020.

[144] M.-G. Hu, Y. Liu, M. A. Nichols, L. Zhu, G. Quéméner, O. Dulieu, and K.-K. Ni, "Nuclear spin conservation enables state-to-state control of ultracold molecular reactions," *Nat. Chem.*, vol. 13, pp. 435–440, May 2021.

[145] Y. Liu, M.-G. Hu, M. A. Nichols, D. Yang, D. Xie, H. Guo, and K.-K. Ni, "Precision test of statistical dynamics with state-to-state ultracold chemistry," *Nature*, vol. 593, pp. 379–384, May 2021.

[146] E. B. Norrgard, D. J. McCarron, M. H. Steinecker, M. R. Tarbutt, and D. DeMille, "Submillikelvin Dipolar Molecules in a Radio-Frequency Magneto-Optical Trap," *Phys. Rev. Lett.*, vol. 116, p. 063004, Feb. 2016.

[147] L. Anderegg, B. L. Augenbraun, Y. Bao, S. Burchesky, L. W. Cheuk, W. Ketterle, and J. M. Doyle, "Laser cooling of optically trapped molecules," *Nature Phys*, vol. 14, pp. 890–893, Sept. 2018.

[148] N. R. Hutzler, H.-I. Lu, and J. M. Doyle, "The Buffer Gas Beam: An Intense, Cold, and Slow Source for Atoms and Molecules," *Chem. Rev.*, vol. 112, pp. 4803–4827, Sept. 2012.

[149] S. Y. T. van de Meerakker, H. L. Bethlem, and G. Meijer, "Taming molecular beams," *Nature Phys*, vol. 4, pp. 595–602, Aug. 2008.

[150] A. Prehn, M. Ibrügger, R. Glöckner, G. Rempe, and M. Zeppenfeld, "Optoelectrical Cooling of Polar Molecules to Submillikelvin Temperatures," *Phys. Rev. Lett.*, vol. 116, p. 063005, Feb. 2016.

[151] H. Son, J. J. Park, W. Ketterle, and A. O. Jamison, "Collisional cooling of ultracold molecules," *Nature*, vol. 580, pp. 197–200, Apr. 2020.

[152] H. J. Metcalf and P. van der Straten, "Laser Cooling and Trapping of Neutral Atoms," in *The Optics Encyclopedia*, John Wiley & Sons, Ltd, 2007.

[153] W. Ketterle and N. J. V. Druten, "Evaporative Cooling of Trapped Atoms," in *Advances In Atomic, Molecular, and Optical Physics* (B. Bederson and H. Walther, eds.), vol. 37, pp. 181–236, Academic Press, Jan. 1996.

[154] K. M. Jones, E. Tiesinga, P. D. Lett, and P. S. Julienne, "Ultracold photoassociation spectroscopy: Long-range molecules and atomic scattering," *Rev. Mod. Phys.*, vol. 78, pp. 483–535, May 2006.

[155] I. Manai, R. Horchani, H. Lignier, P. Pillet, D. Comparat, A. Fioretti, and M. Allegrini, "Rovibrational Cooling of Molecules by Optical Pumping," *Phys. Rev. Lett.*, vol. 109, p. 183001, Oct. 2012.

[156] T. Köhler, K. Góral, and P. S. Julienne, "Production of cold molecules via magnetically tunable Feshbach resonances," *Rev. Mod. Phys.*, vol. 78, pp. 1311–1361, Dec. 2006.

[157] J. G. Danzl, M. J. Mark, E. Haller, M. Gustavsson, R. Hart, J. Aldegunde, J. M. Hutson, and H.-C. Nägerl, "An ultracold high-density sample of rovibronic ground-state molecules in an optical lattice," *Nat. Phys.*, vol. 6, pp. 265–270, Apr. 2010.

[158] T. Takekoshi, L. Reichsöllner, A. Schindewolf, J. M. Hutson, C. R. Le Sueur, O. Dulieu, F. Ferlaino, R. Grimm, and H.-C. Nägerl, "Ultracold Dense Samples of Dipolar RbCs Molecules in the Rovibrational and Hyperfine Ground State," *Phys. Rev. Lett.*, vol. 113, p. 205301, Nov. 2014.

[159] F. Lang, K. Winkler, C. Strauss, R. Grimm, and J. H. Denschlag, "Ultracold Triplet Molecules in the Rovibrational Ground State," *Phys. Rev. Lett.*, vol. 101, p. 133005, Sept. 2008.

[160] S. A. Moses, J. P. Covey, M. T. Miecnikowski, B. Yan, B. Gadway, J. Ye, and D. S. Jin, "Creation of a low-entropy quantum gas of polar molecules in an optical lattice," *Science*, vol. 350, pp. 659–662, Nov. 2015.

[161] L. D. Marco, G. Valtolina, K. Matsuda, W. G. Tobias, J. P. Covey, and J. Ye, "A degenerate Fermi gas of polar molecules," *Science*, vol. 363, pp. 853–856, Feb. 2019.

[162] K. K. Voges, P. Gersema, M. Meyer zum Alten Borgloh, T. A. Schulze, T. Hartmann, A. Zenesini, and S. Ospelkaus, "Ultracold gas of bosonic $^{23}$Na$^{39}$K ground-state molecules," *Phys. Rev. Lett.*, vol. 125, p. 083401, Aug. 2020.

[163] K.-K. Ni, S. Ospelkaus, M. H. G. de Miranda, A. Pe'er, B. Neyenhuis, J. J. Zirbel, S. Kotochigova, P. S. Julienne, D. S. Jin, and J. Ye, "A High Phase-Space-Density Gas of Polar Molecules," *Science*, vol. 322, pp. 231–235, Oct. 2008.

[164] C. W. Gardiner and P. Zoller, *Quantum Noise*. Springer Series in Synergetics, Springer Berlin Heidelberg, 3rd ed., 2004.

[165] A. Nitzan, *Chemical Dynamics in Condensed Phases: Relaxation, Transfer and Reactions in Condensed Molecular Systems*. Oxford Graduate Texts, Oxford ; New York: Oxford University Press, 2006.

[166] C. W. Gardiner, *Stochastic Methods*. Springer Series in Synergetics, Springer Berlin Heidelberg, 2009.

[167] H.-P. Breuer and F. Petruccione, *The Theory of Open Quantum Systems*. Oxford ; New York: Oxford University Press, 2002.

[168] A. J. Daley, "Quantum trajectories and open many-body quantum systems," *Adv. Phys.*, vol. 63, pp. 77–149, Mar. 2014.

[169] H. Weimer, A. Kshetrimayum, and R. Orús, "Simulation methods for open quantum many-body systems," *Rev. Mod. Phys.*, vol. 93, p. 015008, Mar. 2021.

[170] A. Einstein, B. Podolsky, and N. Rosen, "Can Quantum-Mechanical Description of Physical Reality Be Considered Complete?," *Phys. Rev.*, vol. 47, pp. 777–780, May 1935.

[171] E. Schrödinger, "Die gegenwärtige Situation in der Quantenmechanik," *Naturwissenschaften*, vol. 23, pp. 807–812, Nov. 1935.

[172] L. Amico, R. Fazio, A. Osterloh, and V. Vedral, "Entanglement in many-body systems," *Rev. Mod. Phys.*, vol. 80, pp. 517–576, May 2008.

[173] R. Horodecki, P. Horodecki, M. Horodecki, and K. Horodecki, "Quantum entanglement," *Rev. Mod. Phys.*, vol. 81, pp. 865–942, June 2009.

[174] J. Eisert, M. Cramer, and M. B. Plenio, "Colloquium: Area laws for the entanglement entropy," *Rev. Mod. Phys.*, vol. 82, pp. 277–306, Feb. 2010.

[175] J. S. Bell, "On the Einstein Podolsky Rosen paradox," *Physics Physique Fizika*, vol. 1, pp. 195–200, Nov. 1964.

[176] G. Vidal, "Efficient Simulation of One-Dimensional Quantum Many-Body Systems," *Phys. Rev. Lett.*, vol. 93, p. 040502, July 2004.

[177] M. A. Nielsen and I. Chuang, *Quantum Computation and Quantum Information*. Cambridge University Press, tenth ed., 2010.

[178] J. I. Cirac, D. Poilblanc, N. Schuch, and F. Verstraete, "Entanglement spectrum and boundary theories with projected entangled-pair states," *Phys. Rev. B*, vol. 83, p. 245134, June 2011.

[179] U. Schollwöck, "The density-matrix renormalization group in the age of matrix product states," *Annals of Physics*, vol. 326, pp. 96–192, Jan. 2011.

# Part I.

# Theory Background

# 2. Open Quantum Systems

Most naturally occurring quantum systems are not perfectly isolated from their environment, but instead interact with it. These quantum systems are called open quantum systems, in contrast to closed systems which do not interact with any environment. In fact, a perfectly isolated system could never be observed, as any observation presents an interaction with the environment (the observer) [1]. Interactions with the environment can have different consequences for the system. Energy can be lost to the environment, e.g. due to spontaneous emission of an atom or photon loss from a cavity. Alternatively, measurements (intentional or not) of the system by its environment will project the system into a specific state, leading to dephasing without loss of energy. In general, such interactions entangle the system with its environment, such that the two are not independent anymore [2].

The concept of open quantum systems is particularly important in quantum optics setups, where interactions with the free space electro-magnetic field are omnipresent, and the resulting dynamics has been studied in great detail [1–3]. In many situations, we are only interested in the system dynamics, and the environment acts as a bath that modifies the system dynamics without back-action on the bath [2]. In such cases, the bath can be treated as Markovian, i.e. memory-less [1, 2]. This approximation greatly simplifies the dynamics, as it means that the time evolution depends only on the current state of the system, and neither on the state of the bath (which is assumed to be at equilibrium) nor its prior evolution. Various methods have been developed to describe and simulate Markovian open quantum systems [1], including, but not limited to, Lindblad master equations [1, 2, 4], quantum Langevin equations [1, 5–7], and quantum trajectories [8–10].

The remainder of this chapter is organized as follows: In Section 2.1, the approximations needed to derive a Markovian master equation are discussed in detail, and the Lindblad master equation is introduced as the general form of a Markovian master equation. Section 2.2 shows how the Lindblad master equation can be unraveled into quantum trajectories, which can often be simulated more efficiently. This chapter is concluded with a discussion of adiabatic elimination in Section 2.3. Adiabatic eliminations is a technique for the perturbative treatment of the Lindblad master equation if the system can be separated into fast and slowly evolving coordinates. The Lindblad master equation, quantum trajectories, and adiabatic elimination are used to describe open quantum systems throughout this thesis, in particular in Chapters 5, 6, and 11.

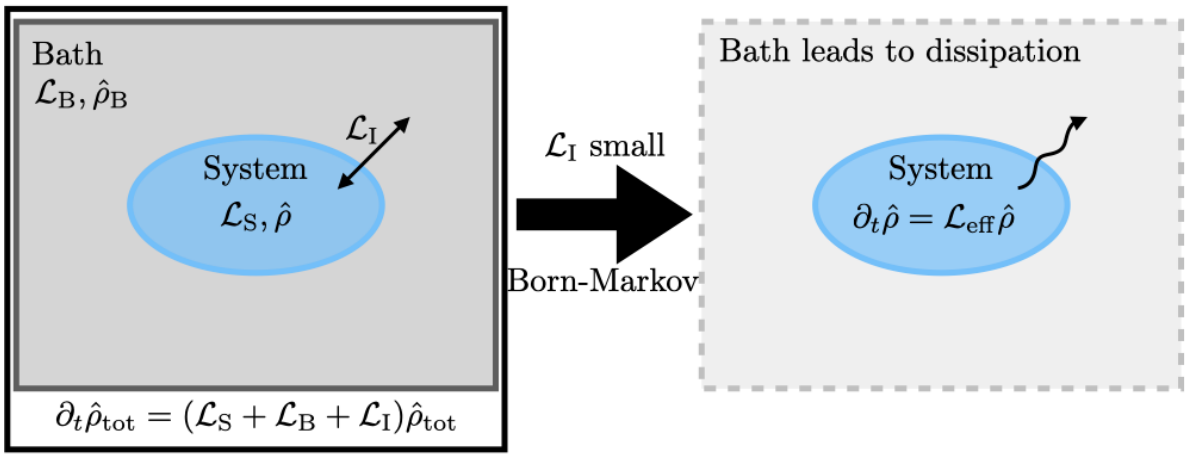


Figure 2.1. – Schematic illustration of the derivation of the master equation. The system (blue) is coupled to a bath (grey), such that the total evolution is a sum of system, bath, and interaction. Under some conditions, the bath can be eliminated, leading to a effective evolution of the system only, with the bath leading to dissipation.

## 2.1. The Markovian Master Equation in Lindblad Form

In this section, I will discuss the Lindblad master equation as a general Markovian master equation. I will further show how to derive a Markovian master equation from the coupled system-bath equation. This will provide some insight into the conditions which need to be fulfilled to describe a system as Markovian.

I consider a generic setup where the system of interest is weakly coupled to a much larger bath, as schematically illustrated in Figure 2.1(a). If the conditions detailed below are met, it is possible to derive an effective equation of motion for the system only, where the bath leads to qualitatively new, dissipative dynamics, including energy loss and decoherence. This is illustrated in Figure 2.1(b). The resulting equation describing the system's evolution, only, is generally known as a master equation.

The price to pay is that the system (in contrast to the combination system + bath) is not in a pure state, but instead in a mixed state, which is described by a density matrix [2]

$$\hat{\rho} = \sum_n p_n \left|\psi_n\right\rangle \left\langle\psi_n\right| . \tag{2.1}$$

Here, $|\psi_n\rangle$ are the different possible system states, and $p_n$ the probabilities that the system is in the respective state, such that $p_n \geq 0$ and $\sum_n p_n = 1$. The diagonal entries of the density matrix are called probabilities, since they correspond to the probabilities of the corresponding states; the off-diagonal entries are know as coherences, as they determine whether the density matrix describes a coherent or incoherent superposition of the two states. Notably, a density matrix contains quadratically more information

than a state, i.e. a state of dimension $D$ leads to a density matrix of dimension $D^2$. This can be seen as an added computational cost for eliminating the environment, even in the Markovian limit. The various properties and consequences of the density matrix have been discussed in great detail in many textbooks (see e.g. Reference [2]) and will not all be repeated here. Two important properties which will be used later are that (i) the diagonal entries are all $\geq 1$, and (ii) the trace is $\mathrm{Tr}\,\hat{\rho} = 1$, both trivial consequences from Equation (2.1).

Lindblad showed that under some reasonable conditions, a Markovian equation of motion that preserves the properties of a density matrix can always be written in the form of a so-called Lindblad master equation [4] (see also Section 3.2 of Reference [2])

$$\partial_t \hat{\rho} = -\mathrm{i}\left[\hat{H}, \hat{\rho}\right] + \sum_k \left(2\hat{L}_k \hat{\rho} \hat{L}_k^\dagger - \hat{L}_k^\dagger \hat{L}_k \hat{\rho} - \hat{\rho} \hat{L}_k^\dagger \hat{L}_k\right). \tag{2.2}$$

The first commutator on the right hand side describes coherent system dynamics, which can be either the system's Hamiltonian dynamics or induced by the bath. By itself, this term is known as the von Neumann equation and a direct generalization of the Schrödinger equation to density matrices. The sum over $k$ describes the incoherent processes. Each $k$ corresponds to a different process, whose properties are determined by the corresponding Lindblad operator $\hat{L}_k$. These terms are unique to open quantum systems and arise due to unidirectional transfer of information from the system to the bath.

The derivation of the Lindblad master equation, including the Lindblad operators, is generally tied to a specific system and bath [1]. Here, instead, I derive a Markovian master equation not in Lindblad form for an arbitrary system and bath, which is adapted from Crispin Gardiner and Peter Zoller's book "Quantum Noise" (Chapter 5, pages 135ff) [1]. The Lindblad form is then a consequence of the fact that it describes the most general possible Markovian master equation.

To start, I will introduce a vectorization of the density matrix and the Lindblad master equation (2.2). Conceptually, you may think of choosing a basis $\hat{\rho}_n$ for the density matrix (e.g. generalized Gell-Mann matrices), such that $\hat{\rho} = c_n \hat{\rho}_n$. The vectorized density matrix is then given as $\vec{\rho} = (c_n)_{n=1,\ldots,D^2-1}$. The vector space spanned by the density matrices has a well-defined scalar product given by the trace, i.e. $\vec{\rho}_1 \cdot \vec{\rho}_2 \equiv \mathrm{Tr}\{\hat{\rho}_1 \hat{\rho}_2\}$. With these definitions, we can rewrite the equation of motion as a matrix-vector equation

$$\partial_t \vec{\rho} = \mathcal{L}\vec{\rho}. \tag{2.3}$$

We call $\mathcal{L}$ the Liouvillian super-operator, since it is an operator acting on operators. Its elements are in principle computed by plugging the basis-elements $\hat{\rho}_n$ of the density matrix into Equation (2.2). With this definition, the master equation is formally solved by

$$\vec{\rho}(t) = e^{\mathcal{L}t}\vec{\rho}(0)\,. \tag{2.4}$$

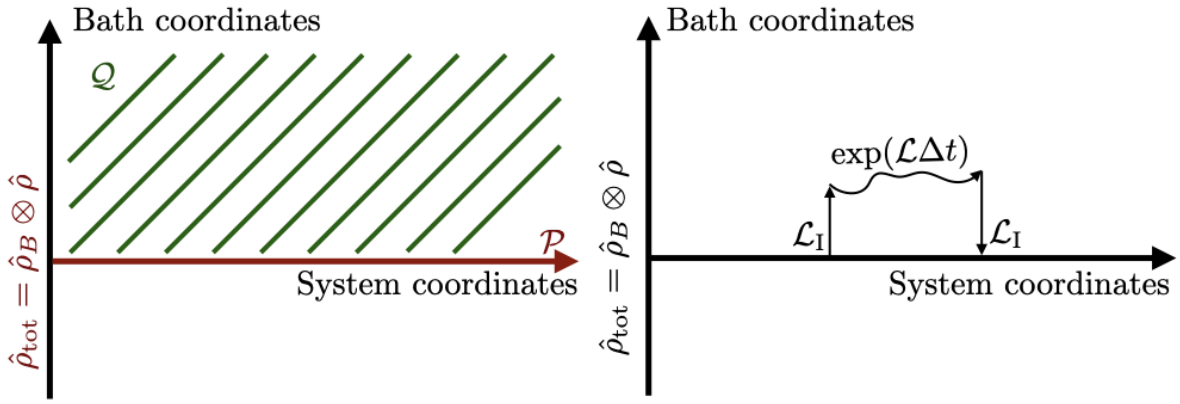


Figure 2.2. – Multi-dimensional "phase space" spanned by system (horizontal) and bath (vertical) coordinates. (a) Schematic representation of projectors $\mathcal{P}$ and $\mathcal{Q}$. The $\mathcal{P}$ manifold consists only of states with fixed bath density matrix, but arbitrary system. The $\mathcal{Q}$ manifold contains all other values of the bath density matrix as well as all possible correlations between system and bath. (b) Schematic representation of the allowed evolution.

Furthermore, projection super-operators $\mathcal{P}$ and $\mathcal{Q}$ are defined as illustrated in Figure 2.2(a) by

$$\mathcal{P}\hat{\rho}_{\text{tot}} = \hat{\rho}_B \otimes \text{Tr}_B\, \hat{\rho}_{\text{tot}}\,, \tag{2.5}$$

$$\mathcal{Q} = \mathcal{I} - \mathcal{P}\,. \tag{2.6}$$

Here, $\mathcal{I}$ is the super-operator identity. $\mathcal{P}$ projects the bath into its equilibrium state $\hat{\rho}_B$. Note that $\mathcal{Q}$ projects into all states whose bath density matrix is orthogonal to $\hat{\rho}_B$, including all states with system-bath entanglement.

Finding an effective equation for the system density matrix is then equivalent to finding an equation of motion for the density matrix restricted to the subspace $\mathcal{P}\hat{\rho}_{\text{tot}}$. This can be done by treating the system-bath interaction perturbatively, as illustrated in Figure 2.2(b). In particular, the evolution of the system is computed considering only terms that are fully restricted to the $\mathcal{P}$ manifold or bring the bath out of its equilibrium state and after some (short) evolution back into its equilibrium state.

Following is a list of conditions that are needed to derive the Markovian master equation in this way. These conditions should not be viewed as independent, but rather partially follow from each other. They are (with nomenclature from Figure 2.1):

1. Interaction between system and bath is weak $\mathcal{L}_{\text{I}} \ll \mathcal{L}_{\text{S}}, \mathcal{L}_{\text{B}}$
2. Factorization of the total density matrix $\hat{\rho}_{\text{tot}}(t) = \hat{\rho}_B \otimes \hat{\rho}(t)$ at $t = 0$ for a steady state of the bath $\hat{\rho}_B$: $\mathcal{L}_B \vec{\rho}_B = 0$
3. Factorization of the total density matrix $\hat{\rho}_{\text{tot}}(t) \approx \hat{\rho}_B \otimes \hat{\rho}(t)$ at $t > 0$
4. Statistical properties of the bath unaffected by coupling to the system ($\hat{\rho}_B$ does not change)

5. Markov approximation: Bath correlation functions decay (or oscillate) quickly
6. Choice of interaction such that $\mathcal{P}\mathcal{L}_I\mathcal{P} = 0$

Using the projection operators, the density operator can be rewritten as

$$\vec{\rho}_{\text{tot}}(t) = \mathcal{P}\vec{\rho}_{\text{tot}}(t) + \mathcal{Q}\vec{\rho}_{\text{tot}}(t) \equiv v(t) + w(t)\,. \tag{2.7}$$

We can write down the equations of motion for $v(t)$ and $w(t)$ as

$$\partial_t v(t) = \mathcal{P}(\mathcal{L}_{\text{S}} + \mathcal{L}_{\text{B}} + \mathcal{L}_{\text{I}})[v(t) + w(t)] = \mathcal{L}_{\text{sys}}v(t) + \mathcal{P}\mathcal{L}_{\text{I}}w(t)\,, \tag{2.8}$$

$$\partial_t w(t) = \mathcal{Q}(\mathcal{L}_{\text{S}} + \mathcal{L}_{\text{B}} + \mathcal{L}_{\text{I}})[v(t) + w(t)] = (\mathcal{L}_{\text{S}} + \mathcal{L}_{\text{B}} + \mathcal{Q}\mathcal{L}_{\text{I}})w(t) + \mathcal{Q}\mathcal{L}_{\text{I}}v(t)\,. \tag{2.9}$$

together with the initial condition $w(0) = 0$ (Condition 2). I have further used

1. $\mathcal{L}_{\text{S}}\mathcal{P} = \mathcal{P}\mathcal{L}_{\text{S}}$
   ($\mathcal{L}_S$ does not care for tracing out the bath)
2. $\mathcal{P}\mathcal{L}_{\text{B}} = 0$
   ($\mathcal{P}\mathcal{L}_{\text{B}} \sum_\alpha \vec{\rho}^{(\alpha)} \otimes \vec{\rho}_B^{(\alpha)} = \sum_\alpha \left[\vec{\rho}^{(\alpha)} \otimes \vec{\rho}_B\right] \left[\text{Tr}\left(\mathcal{L}_B \vec{\rho}_B^{(\alpha)}\right)\right] = 0$)
3. $\mathcal{L}_{\text{B}}\mathcal{P} = 0$
   (Condition 2)
4. $\mathcal{P}\mathcal{L}_{\text{I}}\mathcal{P} = 0$
   (Condition 6)

Equation (2.9) is formally solved by

$$w(t) = \int_0^t \mathrm{d}\tau \exp[(\mathcal{L}_{\text{S}} + \mathcal{L}_{\text{B}} + \mathcal{Q}\mathcal{L}_{\text{I}})(t-\tau)]\mathcal{Q}\mathcal{L}_{\text{I}}v(\tau)\,. \tag{2.10}$$

Plugging this solution into Equation (2.8), we find

$$\partial_t v(t) = \mathcal{L}_{\text{S}}v(t) + \mathcal{P}\mathcal{L}_{\text{I}} \int_0^t \mathrm{d}\tau \exp[(\mathcal{L}_{\text{S}} + \mathcal{L}_{\text{B}} + \mathcal{Q}\mathcal{L}_{\text{I}})(t-\tau)]\mathcal{Q}\mathcal{L}_{\text{I}}v(\tau)\,. \tag{2.11}$$

Since the interaction is assumed to be small (Condition 1), the $\mathcal{Q}\mathcal{L}_I$ in the exponent leads to higher order corrections and can be neglected. Now, the Markov approximation can be applied. The memory of the bath is here encoded in the decay or oscillation of the out-of-equilibrium bath $\exp[(\mathcal{L}_{\text{S}} + \mathcal{L}_{\text{B}})(t-\tau)]\mathcal{Q}$, which are assumed to decay or oscillate quickly. Then, only terms with $\tau \sim t$ contribute to the integral. Thus, we can replace $v(\tau) \approx v(t)$ and extend the lower integral bound to $-\infty$. For a precise discussion of the errors in the case of the quantum optics master equation, see e.g. Atom-Photon Interactions by Cohen-Tannoudji Chapter IV.D [3]. The result is

$$\partial_t v(t) = \mathcal{L}_{\text{S}}v(t) + \mathcal{P}\mathcal{L}_{\text{I}} \int_0^\infty \mathrm{d}\tau \exp[(\mathcal{L}_{\text{S}} + \mathcal{L}_{\text{B}})\tau]\mathcal{Q}\mathcal{L}_{\text{I}}v(t)\,. \tag{2.12}$$

Clearly, the right hand side only depends on time via $v(t)$, and not on $v(t')$ at earlier times $t' < t$ or explicitly on $t$.

One could now continue to derive a specific master equation by introducing a bath and a model, however, we will stop here with this general result.

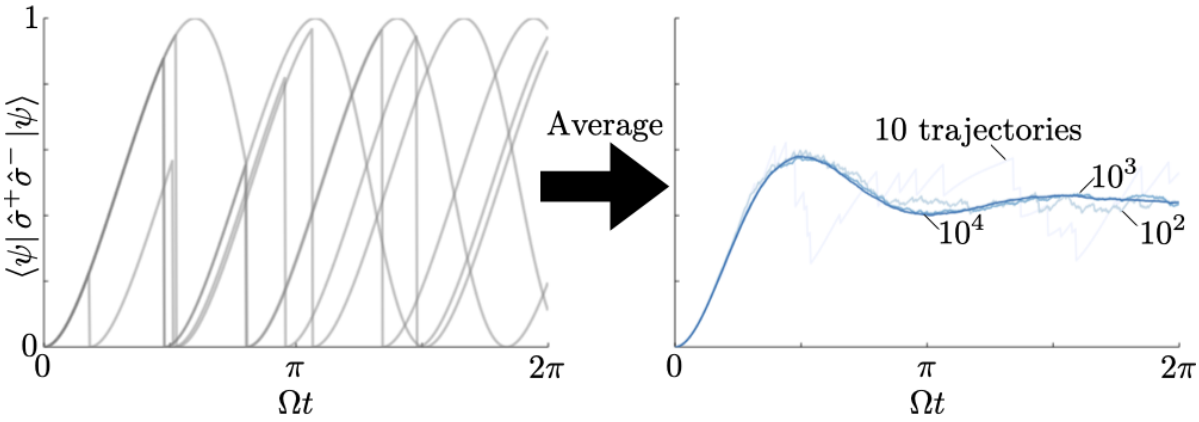


Figure 2.3. – Quantum trajectories for Rabi oscillations with spontaneous emission. $\gamma = \Omega$. (a) 5 example trajectories. (b) Average over an increasing number of up to $10^4$ trajectories.

## 2.2. Quantum Trajectories

The Lindblad master equation directly describes the time evolution of the system's density matrix. Depending on the context, however, alternative descriptions may be more appropriate. This can be due to computational cost, for subsequent analytical calculations, or for conceptual reasons. The most common alternative is the quantum trajectories algorithm, which describes an ensemble of states instead of the master equation [10]. This is in many situations more efficient to simulate.

The simulation of master equations in open quantum many-body systems is generally computationally expensive, due to a combination of the exponential scaling of the Hilbert space dimension combined with the quadratic scaling of the density matrix. Consider for example $N$ two level systems. Then, the Hilbert space has dimension $2^N$, whereas the density matrix has dimension $\sim (2^N)^2 = 4^N$. For $N = 20$, this leads to a Hilbert space dimension $\sim 10^6$, and to a density matrix dimension $\sim 10^{12}$, out of reach of any computation without further approximations. In the following, I will first explain the quantum trajectories algorithm and then show its equivalence to the Lindblad master equation.

In order to reduce the simulation complexity, the key idea behind the quantum trajectories algorithm is to decompose the density matrix into an ensemble of $M$ states $|\psi_n\rangle$, $n = 1, \ldots, M$, such that

$$\hat{\rho} = \frac{1}{M} \sum_{n=1}^{M} |\psi_n\rangle \langle\psi_n| \tag{2.13}$$

similar to Equation 2.1. The goal is then to write a (stochastic) equation of motion for the states $|\psi_n(t)\rangle$. This method is known under the names of *Monte Carlo wavefunctions*, *quantum jumps*, or *quantum trajectories* [8–10]. These states then follow a stochastic

evolution which sample the $p_n$s from Equation 2.1 in a Monte Carlo manner. Observables can be computed by averaging over different trajectories, as schematically illustrated in Figure 2.3.

In order to describe the quantum trajectories algorithm, we first define the non-hermitian Hamiltonian

$$\hat{H}_{\mathrm{NH}} = \hat{H} - \mathrm{i}\sum_k \hat{L}_k^\dagger \hat{L}_k \,. \tag{2.14}$$

The master equation then reads

$$\partial_t \hat{\rho} = -\mathrm{i}\hat{H}_{\mathrm{NH}}\hat{\rho} + \mathrm{i}\hat{\rho}\hat{H}_{\mathrm{NH}}^\dagger + 2\sum_k \hat{L}_\mathrm{k}\hat{\rho}\hat{L}_\mathrm{k}^\dagger \,. \tag{2.15}$$

The first two terms then describe some kind of generalized coherent dynamics, whereas the third term will lead to stochastic jumps.

To first order in $\delta t$, we can write the following algorithm [10]

1. Evolve the state according to

$$|\psi_n(t+\delta t)\rangle = \left(1 - \mathrm{i}\hat{H}_{\mathrm{NH}}\delta t\right)|\psi_n(t)\rangle \tag{2.16}$$

2. Compute the jump probability

$$\delta p = 1 - \langle\psi_n(t+\delta t)|\psi_n(t+\delta t)\rangle = \delta t \sum_k \langle\psi_n(t)|\,\hat{L}_k^\dagger \hat{L}_k\,|\psi_n(t)\rangle \tag{2.17}$$

3. Draw a random number $r \in [0,1]$. If $r < \delta p$, a jump happens, otherwise, renormalize $|\psi_n(t+\delta t)\rangle$ and restart from 1. for the next time step
4. Chose which jump operator $\hat{L}_k$ is applied with probabilities

$$p_k = \langle\psi_n(t)|\,\hat{L}_k^\dagger \hat{L}_k\,|\psi_n(t)\rangle\,/\delta p \times \delta t \tag{2.18}$$

5. Apply the jump

$$|\psi_n(t+\delta t)\rangle = L_k\,|\psi_n(t)\rangle\,/\sqrt{p_k \times \delta p/\delta t} \tag{2.19}$$

Starting from a pure density matrix $|\psi_n(t)\rangle\langle\psi_n(t)|$, the density matrix at time $t+\delta t$ is then given as a weighted sum of the density matrix if no jump happens and the different jump probabilities, each with their respective probability

$$\begin{aligned}\hat{\rho}(t+\delta t) = &\left(1 - \mathrm{i}\hat{H}_{\mathrm{NH}}\delta t\right)|\psi_n(t)\rangle\langle\psi_n(t)|\left(1 + \mathrm{i}\hat{H}_{\mathrm{NH}}\delta t\right) \\ &+ \delta p \sum_k p_k \hat{L}_k\,|\psi_n(t)\rangle\langle\psi_n(t)|\,\hat{L}_k^\dagger/(p_k \times \delta p/\delta t)\,.\end{aligned} \tag{2.20}$$

The first line gives the contribution if no jump happens, the second line gives the ensemble-averaged jump contributions. From here, the underlying equation of motion can be reconstructed as

$$\frac{\hat{\rho}(t+\delta t) - |\psi_n(t)\rangle\langle\psi_n(t)|}{\delta t} = -\mathrm{i}\hat{H}_{\mathrm{NH}}|\psi_n(t)\rangle\langle\psi_n(t)| + \mathrm{i}|\psi_n(t)\rangle\langle\psi_n(t)|\hat{H}_{\mathrm{NH}} + \sum_k \hat{L}_k|\psi_n(t)\rangle\langle\psi_n(t)|\hat{L}_k^\dagger + \mathcal{O}(\delta t^2)\,. \tag{2.21}$$

This result is exactly the first order approximation to the master equation Equation (2.15). If at time $t$ the density matrix does not describe a pure state, but instead given by a statistical mixture, the same arguments independently hold for all terms. Then, since the density matrix is a linear superposition of pure states and Equation 2.2 is linear in time and $\hat{\rho}$, the algorithm holds for arbitrary density matrices. Analogously, if the initial density matrix is not pure, it needs to be rewritten as in Equation (2.1) and the initial state needs to be sampled from the $|\psi_n\rangle$ with probabilities $p_n$, respectively [10].

This method is however still first order in time. In order to compute higher order methods, we use the following algorithm [10, 11]

1. Draw a random number $r \in [0,1]$
2. Solve the equation

$$\left\|\exp\left(-\mathrm{i}\hat{H}_{\mathrm{NH}}\Delta t\right)|\psi_n(t)\rangle\right\|^2 = r \tag{2.22}$$

   to compute the jump time $\Delta t$
3. Compute $|\psi_n(t')\rangle$ in the interval $t' \in [t, t+\Delta t]$ as

$$|\psi_n(t')\rangle = \frac{\exp\left[-\mathrm{i}\hat{H}_{\mathrm{NH}}(t'-t)\right]|\psi_n(t)\rangle}{\left\|\exp\left[-\mathrm{i}\hat{H}_{\mathrm{NH}}(t'-t)\right]|\psi_n(t)\rangle\right\|} \tag{2.23}$$

4. Choose a jump $k$ at random with probability

$$p_k = \frac{\langle\psi_n(t+\Delta t)|\hat{L}_k^\dagger\hat{L}_k|\psi_n(t+\Delta t)\rangle}{\sum_k \langle\psi_n(t+\Delta t)|\hat{L}_k^\dagger\hat{L}_k|\psi_n(t+\Delta t)\rangle} \tag{2.24}$$

5. Apply the jump

$$|\psi_n(t+\Delta t)\rangle = \frac{\hat{L}_k|\psi_n(t+\Delta t)\rangle}{\sqrt{p_k}} \tag{2.25}$$

6. Restart from step 1. with $t_{\mathrm{new}} = t + \Delta t$

It is straightforward to see that for an infinitesimal time step $dt$, this algorithm is equivalent to the first order algorithm above. That is, the evolution according to

$\exp\left(-\mathrm{i}\hat{H}_{\mathrm{NH}}t\right)$ is the proper generalization of the infinitesimal time step, and quantum jumps occur at the same rate.

The higher order method is particularly efficient if the jump time $\Delta t$ in Equation (2.22) can be computed analytically. This is e.g. the case if the dynamics due to $\hat{H}_{\mathrm{NH}}$ does not change the jump probabilities. In this case Equation (2.22) describes an exponential decay and an analytic solution is readily available. This is in particular the case in Chapters 5 and 6.

In order to compute expectation values of an operator $\hat{O}$ at time $t$, we need to compute $\mathrm{Tr}[\hat{\rho}(t)\hat{O}]$. With the decomposition of the density matrix Equation (2.13), one finds [10]

$$\mathrm{Tr}\left[\frac{1}{M}\sum_{n=1}^{M}|\psi_n(t)\rangle\langle\psi_n(t)|\hat{O}\right] = \frac{1}{M}\sum_{n=1}^{M}\langle\psi_n(t)|\hat{O}|\psi_n(t)\rangle \ . \tag{2.26}$$

Figure 2.3(a) shows the individual expectation values of the operator $\hat{\sigma}^+\hat{\sigma}^-$ in a driven dissipative two level system. Averaging many of these trajectories then slowly converges to the master equation, as shown in Figure 2.3(b).

In addition to standard numerical errors such as finite time steps, quantum trajectories also have a fundamental error source due to the finite number of trajectories $M$ [10]. This is fundamentally rooted in the fact that the ensemble averaged density matrix $\sum_n(|\psi_n\rangle\langle\psi_n|)/M$ only matches the true density matrix in the infinite sample limit.

For a finite sample size, expectation values are computed according to Equation (2.26) as the average over many trajectories. These trajectories are independent, and thus the central limit theorem ensures that the estimate of the expectation value will be Gaussian distributed with mean $\langle\hat{O}\rangle$ and variance $(\langle\hat{O}^2\rangle - \langle\hat{O}\rangle^2)/M$ [10]. The resulting statistical error is thus well-known, and can be controlled by increasing the sample size.

In addition to the computational equivalence, these algorithms are more fundamentally motivated by continuous measurement theory [12]. In quantum mechanics, a measurement projects the system into an eigenstate of the measurement operator. Analogously, incoherent interactions with the environment (such as spontaneous emission of a photon) can be thought of effective measurements of the system, potentially with a subsequent modification. For example, spontaneous emission of a photon can be thought of first measuring the atom in the excited state and subsequently transferring the atom into the ground state. Continuous measurement theory then describes a system under continuous monitoring by applying measurements *stochastically* at some average rate. This stochastic application directly leads to the above described algorithm [12].

## 2.3. Adiabatic Elimination

Adiabatic elimination provides a perturbative treatment of systems which can be separated into fast and slow evolving degrees of freedom with weak coupling between them. Then, excited states are only perturbatively populated due to far detuning or decay

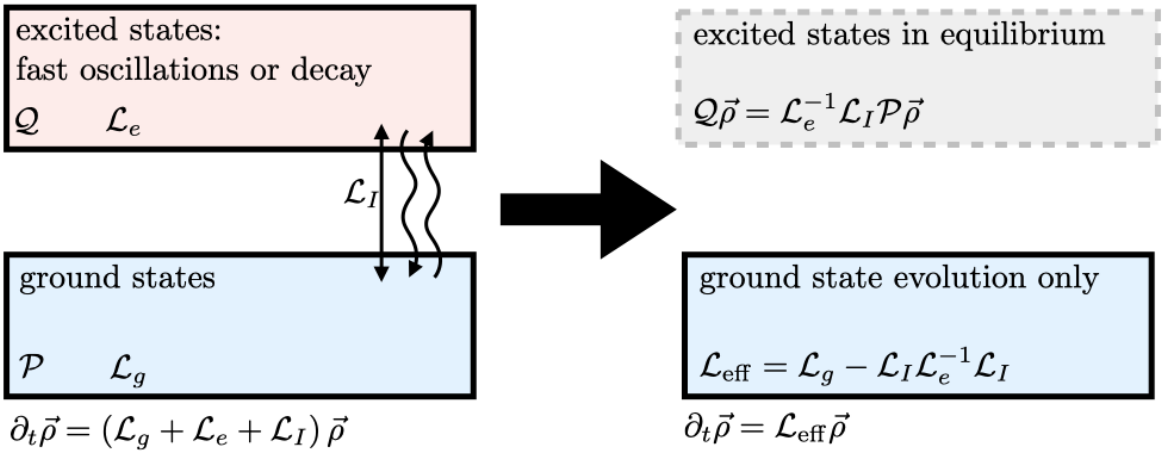


Figure 2.4. – Schematic illustration of the elimination procedure. The quantum system is split into ground states which evolve slowly according to $\mathcal{L}_g$; and excited states which quickly according to $\mathcal{L}_e$. Ground and excited state manifold are coupled by $\mathcal{L}_I$, such that the total density matrix evolves according to $\partial_t\vec{\rho} = (\mathcal{L}_g + \mathcal{L}_e + \mathcal{L}_I)\vec{\rho}$. Adiabatic elimination then gives an evolution for the ground states with excited states in equilibrium.

and can be adiabatically eliminated from the dynamics, leaving an effective equation for the ground states only. The book Stochastic Methods by Crispin Gardiner [13] provides a general introduction into adiabatic elimination in a way that can be applied to quantum or classical problems. Reiter and Sørensen derive explicit formulas for the effective Hamiltonian and Lindblad operators in the case that all dissipation brings excited states into the ground state manifold [14]. Adiabatic elimination has been used to describe many open quantum optics setups [3, 13, 14], for example cavity QED [15], dissipative preparation of entanglement [16], or effective descriptions of lasers [1].

The fundamental idea is shown in Figure 2.4: The system is split into excited states which decay quickly towards (or oscillate quickly around) their equilibrium. In order to adiabatically eliminate the excited states, one then assumes that they are well approximated by their equilibrium values, and derives a resulting equations for the ground states only. This is conceptionally very similar to the derivation of the Markovian master equation, where the bath's degrees of freedom quickly relax to their equilibrium, while the system evolves slowly (in the interaction picture). In contrast to that derivation, in this section we consider a direct separation into ground states and excited states split on the state level, instead of two distinct systems as used in Section 2.1. Mathematically that means the Hilbert space is a direct sum instead of a product of ground and excited states. The methods however are so similar that also the derivation of the master equation may be considered as an adiabatic elimination of the bath. Furthermore, both derivations rely on a vectorization of the density matrix, projection operators, and treating the fast evolving manifold as close to equilibrium.

In order to derive formulas for adiabatic elimination, the Hilbert space is split into

slowly evolving ground states $|g_n\rangle$ and fast evolving excited states $|e_m\rangle$. Then, projection operators can be defined as

$$\hat{P} = \sum_n |g_n\rangle \langle g_n| \,, \tag{2.27}$$

$$\hat{Q} = \sum_m |e_m\rangle \langle e_m| \,. \tag{2.28}$$

To more easily define super-operators, the following notation is used for super-operators

$$\left(\hat{A} \otimes \hat{B}\right)\hat{\rho} \equiv \hat{B}\hat{\rho}\hat{A}^T \,. \tag{2.29}$$

With this notation, for example, the Liouvillian super-operator $\mathcal{L}$ can be written as

$$\mathcal{L} = -\mathrm{i}\hat{I} \otimes \hat{H}_{\mathrm{NH}} + \mathrm{i}\hat{H}^*_{\mathrm{NH}} \otimes \hat{I} + 2\sum_k \hat{L}^*_k \otimes \hat{L}_k \,. \tag{2.30}$$

The projection super-operators are defined by

$$\mathcal{P} = \hat{P} \otimes \hat{P} \,, \tag{2.31}$$

$$\mathcal{Q} = \mathcal{I} - \mathcal{P} = \hat{Q} \otimes \hat{Q} + \hat{Q} \otimes \hat{P} + \hat{P} \otimes \hat{Q} \,. \tag{2.32}$$

These notation is analogously used in Reference [17] to derive lowest order estimates for the residual excited state population. The goal is now to proceed to derive an effective equation of motion for $\mathcal{P}\vec{\rho}$.

Following the Handbook of Stochastic Methods, we separate the Liouvillian $\mathcal{L} = \mathcal{L}_g + \mathcal{L}_e + \mathcal{L}_I$ according to

$$\mathcal{L}_g = \mathcal{P}\mathcal{L}\mathcal{P} \,, \tag{2.33}$$

$$\mathcal{L}_e = \mathcal{Q}\mathcal{L}\mathcal{Q} \,, \tag{2.34}$$

$$\mathcal{L}_I = \mathcal{P}\mathcal{L}\mathcal{Q} + \mathcal{Q}\mathcal{L}\mathcal{P} \,. \tag{2.35}$$

The following steps are now analogous to the derivation of the master equation in Section 2.1. First define

$$\vec{v}(t) \equiv \mathcal{P}\vec{\rho}(t) \,, \tag{2.36}$$

$$\vec{w}(t) \equiv \mathcal{Q}\vec{\rho}(t) \,. \tag{2.37}$$

The equations of motion for $\vec{v}$ and $\vec{w}$ then read

$$\partial_t \vec{v}(t) = \mathcal{L}_g \vec{v}(t) + \mathcal{L}_I \vec{w}(t) \,, \tag{2.38}$$

$$\partial_t \vec{w}(t) = \mathcal{L}_e \vec{w}(t) + \mathcal{L}_I \vec{v}(t) \,. \tag{2.39}$$

The equation for $\vec{w}(t)$ with $\vec{w}(0) = 0$ is then formally solved by

$$\vec{w}(t) = \int_0^t d\tau \exp[\mathcal{L}_e(t-\tau)]\mathcal{L}_I \vec{v}(\tau) \,. \tag{2.40}$$

The condition $\vec{w}(0) = 0$, i.e. no initial excited state population, is a reasonable assumption in most scenarios. If we had initial population in the excited state, it would quickly relax to the ground state. However, this relaxation dynamics can not be described by adiabatic elimination, since by definition during this dynamics the excited state population does not follow its equilibrium adiabatically.

Analogous to the derivation of the master equation, the excited states decay (or oscillate) fast, so that the only relevant contribution to the integral is at time $\tau \sim t$. Thus, the lower bound of the integral can be extended to $-\infty$ and $\vec{v}(\tau)$ can be replaced by $\vec{v}(t)$. Equation (2.40) then simplifies to

$$\vec{w}(t) = \int_0^\infty d\tau \exp(\mathcal{L}_e \tau) \mathcal{L}_I \vec{v}(t)\,, \tag{2.41}$$

which is solved by

$$\vec{w}(t) = -(\mathcal{L}_e)^{-1} \mathcal{L}_I \vec{v}(t)\,. \tag{2.42}$$

This is the dynamical equilibrium value of the excited state coordinates at time $t$ in first order perturbation theory.

Plugging this result back into Equation (2.38), we find [13, 17]

$$\partial_t \vec{v}(t) = \left[\mathcal{L}_g - \mathcal{L}_I (\mathcal{L}_e)^{-1} \mathcal{L}_I\right] \vec{v}(t) \equiv \mathcal{L}_{\text{eff}} \vec{v}(t)\,. \tag{2.43}$$

Thus, the effective evolution of the ground state has two contributions. The first term is the bare ground state evolution, and the second term is an effective excited state evolution due to excitation from the ground state, propagation in the excited state, and relaxation back to the ground state.

In the special case that all Lindblad operators describe relaxation processes from the excited state back to the ground state, i.e. $\hat{L}_k = \hat{P}\hat{L}_k\hat{Q}\ \forall k$, Reiter and Sørensen gave explicit formulas for the effective Hamiltonian and Lindblad operators [14]. They split the non-hermitian Hamiltonian $\hat{H}_{\text{NH}} = \hat{H}_g + \hat{H}_{\text{NH},e} + \hat{V}_+ + \hat{V}_-$ by projecting into the different subspaces

$$\hat{H}_g = \hat{P}\hat{H}\hat{P}\,, \tag{2.44}$$

$$\hat{H}_{\text{NH},e} = \hat{Q}\hat{H}_{\text{NH}}\hat{Q}\,, \tag{2.45}$$

$$\hat{V}_+ = \hat{Q}\hat{H}\hat{P}\,, \tag{2.46}$$

$$\hat{V}_- = \hat{P}\hat{H}\hat{Q}\,. \tag{2.47}$$

Note that due to the structure of the Lindblad operators, only the excited subspace Hamiltonian is non-hermitian. This situation is schematically illustrated on the left hand side of Figure 2.5.

Under this condition, $\mathcal{L}_{\text{eff}}$ can be written as a Lindblad master equation [14]

$$\partial_t \hat{\rho} = -\mathrm{i}\left[\hat{H}_{\text{eff}}, \hat{\rho}\right] + \sum_k 2\hat{L}_{\text{eff},k}\hat{\rho}\hat{L}_{\text{eff},k}^\dagger - \hat{L}_{\text{eff},k}^\dagger\hat{L}_{\text{eff},k}\hat{\rho} - \hat{\rho}\hat{L}_{\text{eff},k}^\dagger\hat{L}_{\text{eff},k} \tag{2.48}$$

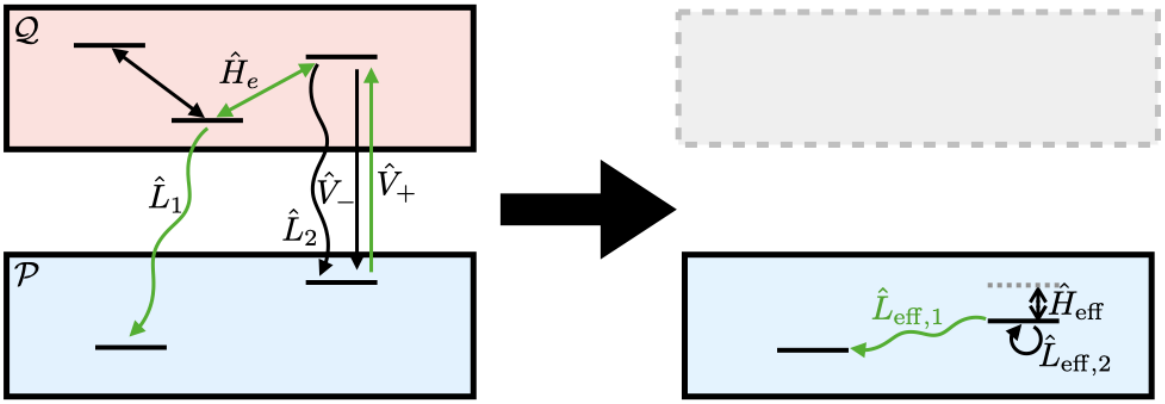


Figure 2.5. – Schematic illustration of the computation of the effective Hamiltonian and Lindblad operators according to Eqs. (2.49) and (2.50), respectively. The green arrows schematically indicate the path effectively taken by the dissipator $\hat{L}_{\mathrm{eff},1}$, which induces transfer between the ground states. In this example, $\hat{L}_{\mathrm{eff},2}$ leads to dephasing and $\hat{H}_{\mathrm{eff}}$ induces an energy shift.

with

$$\hat{H}_{\mathrm{eff}} = \hat{H}_g - \frac{1}{2}\hat{V}_- \left[\hat{H}_{\mathrm{NH},e}^{-1} + \left(\hat{H}_{\mathrm{NH},e}^{-1}\right)^\dagger\right]\hat{V}_+ \,, \tag{2.49}$$

$$\hat{L}_{\mathrm{eff},k} = \hat{L}_k \hat{H}_{\mathrm{NH},e}^{-1} \hat{V}_+ \,. \tag{2.50}$$

These terms are illustrated on the right hand side of Figure 2.5. In particular, the dissipators can be thought of virtually exciting an excited state, following the excited state evolution, and finally relaxing dissipatively to the ground state, as illustrated in green for $\hat{L}_{\mathrm{eff},1}$. Analogously, the Hamiltonian can be thought of as a virtual excitation process, followed by excited state evolution, and finally coherent transfer back to the ground state.

The Equations (2.49) and (2.50) are directly applied in Chapter 5 to compute the effective Hamiltonian and Lindblad operators for ultracold molecules coupled to a cavity. Here, a laser offers a weak coherent drive to excite electronically excited states, and cavity decay and spontaneous emission offer dissipative decay channels back to the ground state. In Chapter 6 we also consider incoherent pumping of the molecules. Then we need to use the more general formulation of Equation (2.43). There, in the absence of a coherent pump, we derive purely dissipative transfer rates between the ground states.

# Bibliography


[1] C. W. Gardiner and P. Zoller, *Quantum Noise*. Springer Series in Synergetics, Springer Berlin Heidelberg, 3rd ed., 2004.

[2] H.-P. Breuer and F. Petruccione, *The Theory of Open Quantum Systems*. Oxford ; New York: Oxford University Press, 2002.

[3] C. Cohen-Tannoudji, J. Dupont-Roc, and G. Grynberg, *Atom-Photon Interactions: Basic Processes and Applications*. New York: Wiley, 1992.

[4] G. Lindblad, "On the generators of quantum dynamical semigroups," *Commun.Math. Phys.*, vol. 48, pp. 119–130, June 1976.

[5] C. W. Gardiner and M. J. Collett, "Input and output in damped quantum systems: Quantum stochastic differential equations and the master equation," *Phys. Rev. A*, vol. 31, pp. 3761–3774, June 1985.

[6] C. W. Gardiner, A. S. Parkins, and M. J. Collett, "Input and output in damped quantum systems. II. Methods in non-white-noise situations and application to inhibition of atomic phase decays," *J. Opt. Soc. Am. B, JOSAB*, vol. 4, pp. 1683–1699, Oct. 1987.

[7] C. W. Gardiner, "Quantum noise and quantum Langevin equations," *IBM J. Res. Dev.*, vol. 32, pp. 127–136, Jan. 1988.

[8] K. Mølmer, Y. Castin, and J. Dalibard, "Monte Carlo wave-function method in quantum optics," *J. Opt. Soc. Am. B, JOSAB*, vol. 10, pp. 524–538, Mar. 1993.

[9] M. B. Plenio and P. L. Knight, "The quantum-jump approach to dissipative dynamics in quantum optics," *Rev. Mod. Phys.*, vol. 70, pp. 101–144, Jan. 1998.

[10] A. J. Daley, "Quantum trajectories and open many-body quantum systems," *Adv. Phys.*, vol. 63, pp. 77–149, Mar. 2014.

[11] R. Dum, A. S. Parkins, P. Zoller, and C. W. Gardiner, "Monte Carlo simulation of master equations in quantum optics for vacuum, thermal, and squeezed reservoirs," *Phys. Rev. A*, vol. 46, pp. 4382–4396, Oct. 1992.

[12] C. W. Gardiner, A. S. Parkins, and P. Zoller, "Wave-function quantum stochastic differential equations and quantum-jump simulation methods," *Phys. Rev. A*, vol. 46, pp. 4363–4381, Oct. 1992.

[13] C. W. Gardiner, *Stochastic Methods*. Springer Series in Synergetics, Springer Berlin Heidelberg, 2009.

[14] F. Reiter and A. S. Sørensen, "Effective operator formalism for open quantum systems," *Phys. Rev. A*, vol. 85, p. 032111, Mar. 2012.

[15] S. Schütz, J. Schachenmayer, D. Hagenmüller, G. K. Brennen, T. Volz, V. Sandoghdar, T. W. Ebbesen, C. Genes, and G. Pupillo, "Ensemble-Induced Strong Light-Matter Coupling of a Single Quantum Emitter," *Phys. Rev. Lett.*, vol. 124, p. 113602, Mar. 2020.

[16] M. J. Kastoryano, F. Reiter, and A. S. Sørensen, "Dissipative Preparation of Entanglement in Optical Cavities," *Phys. Rev. Lett.*, vol. 106, p. 090502, Feb. 2011.

[17] D. Finkelstein-Shapiro, D. Viennot, I. Saideh, T. Hansen, T. Pullerits, and A. Keller, "Adiabatic elimination and subspace evolution of open quantum systems," *Phys. Rev. A*, vol. 101, Apr. 2020.

# 3. Quantum Optics

In this chapter, some basic concepts of quantum optics are introduced. First, the Jaynes-Cummings model is derived in Section 3.1. This is the simplest model to describe quantum optics consisting of a single two-level emitter coupled to a single optical mode. The approximation made during the derivation of this model are discussed and some simple results are given. In Section 3.2, the Jaynes-Cummings model is generalized to many two-level emitters, i.e. the Tavis-Cummings model. In Section 3.3 the solution of the Tavis-Cummings model using generalized Dicke states is introduced. Dissipative effects and in particular collective dissipative effects are discussed in Section 3.4. Finally, the fate of Dicke states in setups with local dissipation and other symmetry breaking effects is considered in Sections 3.5 and 3.6, respectively.

## 3.1. The Jaynes-Cummings Model and the Rotating Wave Approximation

The simplest nontrivial setup in quantum optics consists of a single emitter coupled to a single electromagnetic mode. Such a setup may describe an atom in a cavity, where the discreteness of optical modes ensures that only one mode is coupled [1]. This setup is schematically indicated in Figure 3.1(a).

In this setup, the quantized electromagnetic mode has an annihilation operator $\hat{a}$, and the Hamiltonian of the mode only reads

$$\hat{H} = \hbar\omega_c \hat{a}^\dagger \hat{a}\,. \tag{3.1}$$

Here, we ignore the vacuum energy $\hbar\omega_c/2$, which just shifts the total energy. In the emitter, often only one transition between two energy levels called $|g\rangle$ and $|e\rangle$ is resonant with the optical mode. Thus, ignoring all other energy levels, the Hamiltonian of the free dipole reads

$$\hat{H} = \hbar\omega_g \left|g\right\rangle \left\langle g\right| + \hbar\omega_e \left|e\right\rangle \left\langle e\right|\,. \tag{3.2}$$

The coupling between an electromagnetic field $\vec{E}$ and an emitter is determined by the emitter's dipole $\vec{d}$ and given by $\vec{d}\vec{E}$. If the emitter is not a perfect dipole, other coupling terms may arise, but in practice this coupling is sufficient to describe most situations [1]. We assume that the charge distribution in the emitter differs for ground and excited states. In this case, there is generally a non-vanishing transition dipole $\vec{d}_{eg} = \langle g|\,\hat{\vec{d}}\,|e\rangle$ for $\hat{\vec{d}} = \int d^3\vec{r}\,q(\vec{r})\hat{\vec{r}}$ the dipole operator for a charge distribution $q(\vec{r})$. If

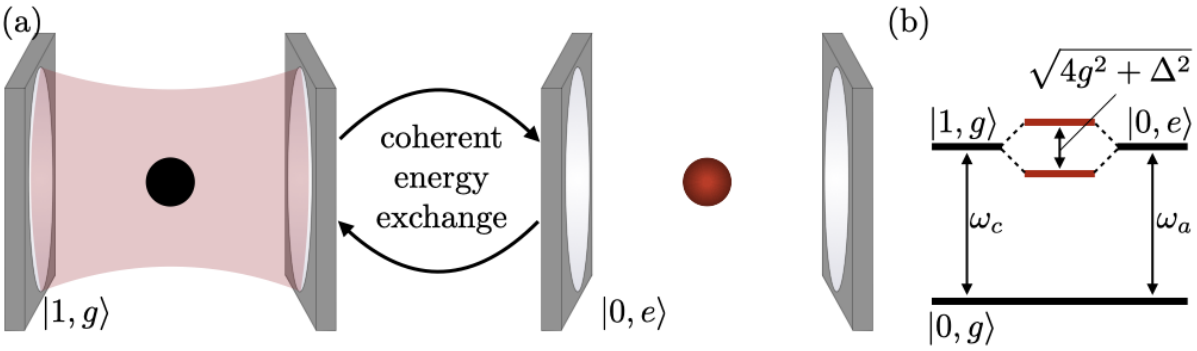


Figure 3.1. – Schematic illustration of the setup and the level scheme of the Jaynes-Cummings model. (a) The cavity and the atom coherently exchange energy. (b) The possible states in the single excitation regime are the total ground state $|0,g\rangle$, the single photon state $|1,g\rangle$ and the atomic excited state $|0,e\rangle$. Due to the coherent coupling, the excited states hybridize to form polaritons (red) with the Rabi splitting $\sqrt{4g^2+\Delta^2}$.

the emitter has no permanent dipole, i.e. $\langle g|\,\hat{\vec{d}}\,|g\rangle = \langle e|\,\hat{\vec{d}}\,|e\rangle = 0$, the dipole operator can be written as $\hat{d} = \vec{d}_{eg}(|e\rangle\langle g| + |g\rangle\langle e|)$. The electric field operator can be written in terms of creation and annihilation operator as $\hat{\vec{E}} = \vec{E}_0(\hat{a}^\dagger + \hat{a})$ [1]. In total, the coupling Hamiltonian reads

$$\hat{H} = \vec{d}_{eg}\vec{E}_0(|e\rangle\langle g| + |g\rangle\langle e|)(\hat{a}^\dagger + \hat{a})\,. \tag{3.3}$$

In order to simplify the notation, raising, lowering, and population operators are defined as $\hat{\sigma}^+ = |e\rangle\langle g|$, $\hat{\sigma}^- = |g\rangle\langle e|$, and $\hat{\sigma}^z = |e\rangle\langle e| - |g\rangle\langle g|$, respectively. The total Hamiltonian is then given by

$$\hat{H}_{\text{Rabi}} = \hbar\omega_a\hat{\sigma}^+\hat{\sigma}^- + \hbar\omega_c\hat{a}^\dagger\hat{a} + g\big(\hat{\sigma}^+ + \hat{\sigma}^-\big)\big(\hat{a}^\dagger + \hat{a}\big)\,, \tag{3.4}$$

with $\omega_a = \omega_e - \omega_g$ and $g = \vec{d}_{eg}\vec{E}_0$, and the Hamiltonian shifted by the energy $\omega_g$. This Hamiltonian is known as the quantum Rabi model. Note that, since the vacuum field strength $\vec{E}_0$ is inversely proportional to the square root of the cavity volume, so is the coupling constant $g$, motivating the search for small volume cavities mentioned in the discussion. Despite only having two degrees of freedom, this Hamiltonian still hosts rich physics and has only been solved recently [2].

The quantum Rabi Hamiltonian can be further simplified by the so-called rotating wave approximation (RWA). This approximation is most easily understood by transforming into the rotating frame with the time-dependent unitary transform

$$\mathcal{U} = \exp\big[\mathrm{i}t\big(\omega_a\hat{\sigma}^+\hat{\sigma}^- + \omega_c\hat{a}^\dagger\hat{a}\big)\big]\,. \tag{3.5}$$

The states are transformed according to $|\psi\rangle \to \mathcal{U}|\psi\rangle$, and the transformed Hamiltonian reads

$$\begin{aligned}\hat{H} &= \mathcal{U}\hat{H}\mathcal{U}^\dagger + \mathrm{i}\hbar(\partial_t\mathcal{U})\mathcal{U}^\dagger && (3.6)\\ &= g\left\{\hat{\sigma}^+\hat{a}^\dagger \exp[-\mathrm{i}t(\omega_a+\omega_c)] + \hat{\sigma}^+\hat{a}\exp[-\mathrm{i}t(\omega_a-\omega_c)] + \right.\\ &\qquad \left.\hat{\sigma}^-\hat{a}^\dagger\exp[\mathrm{i}t(\omega_a-\omega_c)] + \hat{\sigma}^-\hat{a}\exp[\mathrm{i}t(\omega_a+\omega_c)]\right\}. && (3.7)\end{aligned}$$

For $g, \Delta \ll \omega_a + \omega_c$ ($\Delta = \omega_a - \omega_c$), the terms proportional $\hat{\sigma}^+\hat{a}^\dagger$ and $\hat{\sigma}^-\hat{a}$ oscillate very fast compared to the system dynamics. In this case, these oscillations average out quickly. For typical cold atom experiments, $g$ and $\Delta$ are MHz or GHz, whereas $\omega_a + \omega_c \sim 10^{15}$Hz, 6 orders of magnitude larger. The RWA then consisits of neglecting these terms, and we can write the Jaynes-Cummings Hamiltonian [3]

$$\hat{H}_{\mathrm{JC}} = \hbar\omega_a\hat{\sigma}^+\hat{\sigma}^- + \hbar\omega_c\hat{a}^\dagger\hat{a} + \hbar g\left(\hat{\sigma}^+\hat{a} + \hat{\sigma}^-\hat{a}^\dagger\right). \tag{3.8}$$

This Hamiltonian provides an excellent approximation for most experimental setups. This approximation is in fact so good that trying to reach break this approximation has given rise to a field of its own. This challenge of reaching the so-called ultra-strong coupling regime $g \sim \omega_a + \omega_c$ has been achieved using organic molecules about a decade ago [4, 5].

In contrast to $\hat{H}_{\mathrm{Rabi}}$, $\hat{H}_{\mathrm{JC}}$ conserves the number of excitations $\hat{a}^\dagger\hat{a} + \hat{\sigma}^+\hat{\sigma}^-$. From another perspective, the terms that do not conserve excitation number and thus break energy conservation need to oscillate quickly due to Heisenberg's uncertainty principle. As a result, $\hat{H}_{\mathrm{JC}}$ only couples states with the same number of excitation. The manifold with $N_{\mathrm{ex}}$ excitations is spanned by the two states $|N_{\mathrm{ex}}, g\rangle$ and $|N_{\mathrm{ex}}-1, e\rangle$. The first number is the number of photons, whereas the second number is the state of the emitter. As a result, the spectrum of the Hamiltonian can be easily obtained by diagonalizing $2\times 2$ matrices [1, 6].

$$\begin{pmatrix} N_{\mathrm{ex}}\omega_c & \sqrt{N_{\mathrm{ex}}}g \\ \sqrt{N_{\mathrm{ex}}}g & (N_{\mathrm{ex}}-1)\omega_c + \omega_a \end{pmatrix} \tag{3.9}$$

The absolute ground state $|0, g\rangle$ is the only state with 0 excitations. The energies of the other states with $N_{\mathrm{ex}} > 0$ excitations are given by

$$E_{N_{\mathrm{ex}},\pm} = \hbar\left[\frac{\omega_a + (2N_{\mathrm{ex}}-1)\omega_c}{2} \pm \sqrt{\frac{\Delta^2}{4} + N_{\mathrm{ex}}g^2}\right]. \tag{3.10}$$

The corresponding eigenstates are $|\pm_{N_{\mathrm{ex}}}\rangle = \alpha_{N_{\mathrm{ex}},\pm}|N_{\mathrm{ex}}, g\rangle + \beta_{N_{\mathrm{ex}},\pm}|N_{\mathrm{ex}}-1, e\rangle$ with

$$\alpha_{N_{\mathrm{ex}},\pm} = \sqrt{\frac{2N_{\mathrm{ex}}g^2}{\Delta^2 + 4N_{\mathrm{ex}}g^2 \pm \Delta\sqrt{\Delta^2 + 4N_{\mathrm{ex}}g^2}}}, \tag{3.11}$$

$$\beta_{N_{\mathrm{ex}},\pm} = \sqrt{\frac{\Delta^2 + 2N_{\mathrm{ex}}g^2 \pm \Delta\sqrt{\Delta^2 + 4N_{\mathrm{ex}}g^2}}{\Delta^2 + 4N_{\mathrm{ex}}g^2 \pm \Delta\sqrt{\Delta^2 + 4N_{\mathrm{ex}}g^2}}}. \tag{3.12}$$

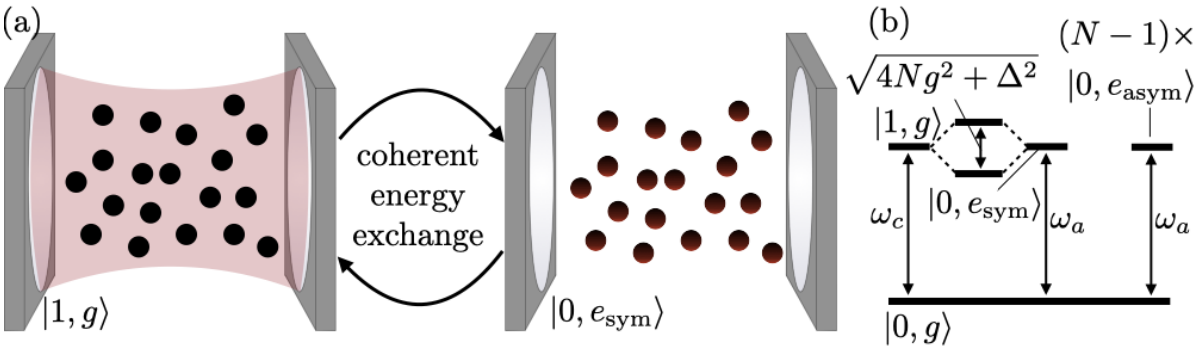


Figure 3.2. – Schematic illustration of the Tavis-Cummings model. (a) $N$ identical emitters are coupled to a cavity mode, leading to coherent energy exchange between the excited cavity state $|1,g\rangle$ and the symmetric emitter excited state $|0,e_{\mathrm{sym}}\rangle$. (b) Schematic level diagram. In the single excitation limit, the states $|1,g\rangle$ and $|0,e_{\mathrm{sym}}\rangle$ hybridize and for polaritons split by the energy $\sqrt{4Ng^2+\Delta^2}$. The $N-1$ orthogonal emitter states $|0,e_{\mathrm{asym}}\rangle$ remain unperturbed.

The energy difference $E_{1,+}-E_{1,-}$ on resonance ($\Delta=0$) for $M=1$ is known as the vacuum Rabi (or polariton) splitting and given by $2g$. This is schematically illustrated in Figure 3.1(b). The first excited states $|\pm_1\rangle$ are also known as polaritons (or polaritonic states).

## 3.2. The Tavis-Cummings Model

If, instead of a single emitter, $N$ identical emitters are coupled to the same electromagnetic mode, the Jaynes-Cummings model straightforwardly generalises to the Tavis-Cummings model with the Hamiltonian

$$\hat{H}_{\mathrm{TC}}=\hbar\omega_a\sum_{n=1}^{N}\hat{\sigma}_n^+\hat{\sigma}_n^-+\hbar\omega_c\hat{a}^\dagger\hat{a}+g\sum_{n=1}^{N}\hat{\sigma}_n^+\hat{a}+\hat{\sigma}_n^-\hat{a}^\dagger\,, \tag{3.13}$$

where the subscript $n$ indicates which emitter the corresponding operator is acting on [7]. The RWA can be made analogously to the single emitter case, and the Hamiltonian $\hat{H}_{\mathrm{TC}}$ conserves the total excitation number $\hat{N}_{\mathrm{ex}}=\sum_n\hat{\sigma}_n^+\hat{\sigma}_n^-+\hat{a}^\dagger\hat{a}$.

First, consider the single excitation limit $N_{\mathrm{ex}}\leq 1$. The unique ground state is given by $|G\rangle\equiv|0,g\cdots g\rangle$ with $N_{\mathrm{ex}}=0$. The manifold $N_{\mathrm{ex}}=1$ is spanned by the single photon state $|1,g\cdots g\rangle$ and the $N$ emitter excited states $\hat{\sigma}_n^+|0,g\cdots g\rangle$. In the manifold of emitter excited states, only the symmetric superposition $(1/\sqrt{N})\hat{S}^+|G\rangle$ with $\hat{S}^+=\sum_n\hat{\sigma}_n^+$ is coupled to the cavity with enhanced coupling strength $\sqrt{N}g$. The other states [e.g. $(\hat{\sigma}_1^+-\hat{\sigma}_2^+)/\sqrt{2}\,|0,g\cdots g\rangle$] decouple from the cavity and are commonly labeled "dark states." A simple basis for these dark states is given by $|k\rangle=\sum_n\exp(2\pi\mathrm{i}kn/N)\hat{\sigma}_n^+|G\rangle$

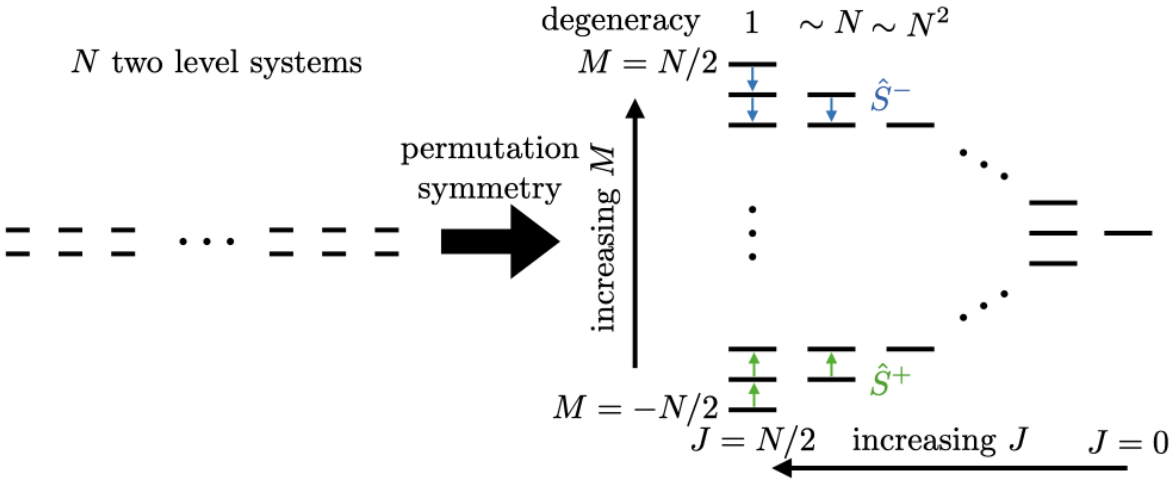


Figure 3.3. – Schematic illustration of the generalized Dicke states. Through the use of permutation symmetry, $N$ identical two level systems can be re-written in the Dicke basis. Each state is determined by its $J$ (left-right) and $M$ (up-down) quantum number, with $-J \leq M \leq J$. The $\hat{S}^+$ operator (green) keeps $J$ constant and *increases* $M$ by one, while the $\hat{S}^-$ operator (blue) keeps $J$ constant and *reduces* $M$ by one. States with $J < N/2$ are highly degenerate.

with $k = 1, \ldots, N-1$. The eigenenergies and eigenstates of $\hat{H}_{\mathrm{TC}}$ are then given analogous to Equations (3.10), (3.11) and (3.12), as well as the dark states with bare energies $\omega_a$.

## 3.3. Generalized Dicke States

In this section, the eigenstates of $\hat{H}_{\mathrm{TC}}$ with arbitrary $N_{\mathrm{ex}}$ are described. In this case, the permutation symmetry among the emitters can be used to classify the emitter excited states. In particular, the emitter states are described by so-called generalized Dicke states schematically shown in Figure 3.3 [6], where the states have been classified according the total spin symmetry

$$\hat{S}^2 = \left(\sum_n \hat{\sigma}_n^x\right)^2 + \left(\sum_n \hat{\sigma}_n^y\right)^2 + \left(\sum_n \hat{\sigma}_n^z\right)^2, \tag{3.14}$$

with $\hat{\sigma}^x = \hat{\sigma}^+ + \hat{\sigma}^-$ and $\hat{\sigma}^y = -\mathrm{i}(\hat{\sigma}^+ - \hat{\sigma}^-)$. Analogously to other spin operators, the operators $\hat{S}^+$, $\hat{S}^-$ and $\hat{S}^z$ commute with $\hat{S}^2$. As a consequence, $\hat{H}_{\mathrm{TC}}$ commutes with $\hat{S}^2$, and the total spin $J$ with $\hat{S}^2/4\,|\psi\rangle = J(J+1)\,|\psi\rangle$ is a conserved quantum number. In addition, emitter states are labeled by their spin-$z$ quantum number $M$: $\hat{S}^z/2\,|\psi\rangle = M\,|\psi\rangle$. The additional factors $1/4$ and $1/2$ are introduced to translate between Pauli matrices and spin operators.

The symmetry sectors with $J < N/2$ are highly degenerate. However, it is possible to further split the Hilbert space into a direct sum of sub-spaces which the Hamiltonian are

not mixed by the spin operators $\hat{S}^{\pm,z}$ [8, 9]. As a consequence, for an initial state with a given $J$, the relevant Hilbert space that this state can explore has size $2J$ and contains only states with equal $J$, but different $M$ (see Figure 3.3). The Hilbert space may be even further restricted due to the excitation number, that is for states with excitation number $N_{\mathrm{ex}}$, the condition $M \leq N_{\mathrm{ex}} - N/2$ has to be fulfilled. As a simple example, the $J = N/2$ manifold is given by $N+1$ states $|J = N/2, M = N_{\mathrm{ex}} - N/2\rangle \propto \left(\hat{S}^{+}\right)^{N_{\mathrm{ex}}} |0, g \cdots g\rangle$.

This separation into symmetry sectors can be concisely written as [8]

$$\left[\mathcal{D}^{1/2}(R)\right]^{\otimes N} \cong \bigoplus_{J=J_{\mathrm{min}}}^{J_{\mathrm{max}}} \bigoplus_{i=1}^{d_J^N} \mathcal{D}^{J,i}(R) \tag{3.15}$$

This formula essentially states that any rotation (which is the same as applications of global spin operations) of $N$ identical spin-1/2 particles is equivalent to a block-diagonal diagonal operation where an equivalent rotation is applied on a collective spin with size $J$ somewhere between $J_{\mathrm{min}} = 0, 1/2$ and $J_{\mathrm{max}} = N/2$.

The spin operators can be straightforwardly applied to the Dicke states using the standard spin algebra. We write the states as $|J, M\rangle$ (dropping the index $i$ which resolves the additional degeneracy for convenience) and find

$$\hat{S}^{\pm}/2\,|J, M\rangle = \sqrt{J(J+1) - M(M \pm 1)}\,|J, M \pm 1\rangle\ , \tag{3.16}$$

$$\hat{S}^{z}/2\,|J, M\rangle = M\,|J, M\rangle\ , \tag{3.17}$$

$$\hat{S}^{2}/4\,|J, M\rangle = J(J+1)\,|J, M\rangle\ . \tag{3.18}$$

Here, the additional degeneracy has been dropped, as it is irrelevant for this equation.

With these identities, the Tavis-Cummings model can be solved straightforwardly even for large atom numbers $N$. The dark states are then the states in the bottom diagonal of the Dicke ladder, which have finite excitation but cannot transfer energy to the cavity, i.e. $\hat{S}^{-}\,|J, M = -J\rangle = 0$. These results will be used when describing large ensembles of molecules coupled to a cavity in Chapter 5.

## 3.4. Weak Coupling, the Purcell Effect, and Superradiance

In realistic cavities, photons are not trapped indefinitely, but are instead lost over time. In this section, the consequences of photon-loss from the cavity are discussed, while the next section deals with spontaneous emission from the atoms. In the first part of this section, only a single emitter coupled to the cavity mode is considered, and in the second part, collective effects are taken into account.

Figure 3.4 illustrates the scenario where a single two level atom is coherently coupled to a cavity mode which decays at rate $\kappa$. Then, the time evolution is described by the master equation Eq. (2.2) with $\hat{H} = \hat{H}_{\mathrm{JC}}$ and $\hat{L} = \sqrt{\kappa/2}\hat{a}$

$$\partial_t \hat{\rho} = -\mathrm{i}\left[\hat{H}_{\mathrm{JC}}, \hat{\rho}\right] - \frac{\kappa}{2}\hat{a}^{\dagger}\hat{a}\hat{\rho} - \frac{\kappa}{2}\hat{\rho}\hat{a}^{\dagger}\hat{a} + \kappa\hat{a}\hat{\rho}\hat{a}^{\dagger}\,. \tag{3.19}$$

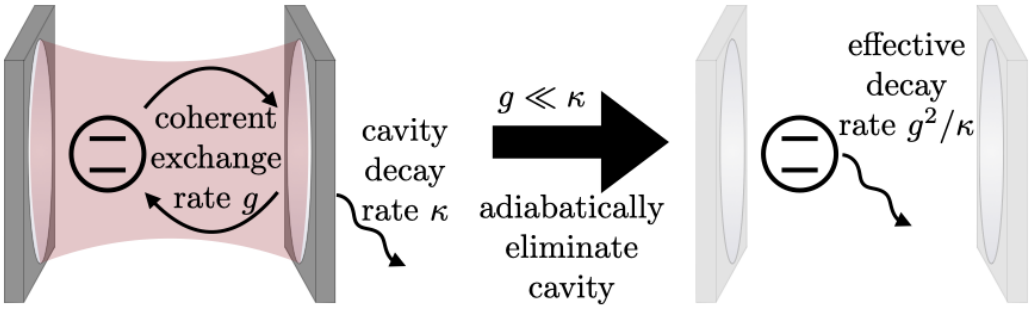


Figure 3.4. – Schematic illustration of the Purcell effect. Left side: a single two level emitter is coherently coupled (rate $g$) to a decaying cavity mode (rate $\kappa$). Right side: If the decay of the cavity is much faster than the coherent energy exchange, the cavity can be adiabatically eliminated, leading to an effective decay rate of the emitter $g^2/\kappa$.

For simplicity we assume $\Delta = 0$ in the following discussion and only consider the single excitation manifold $\hat{a}^\dagger\hat{a} + \hat{\sigma}^+\hat{\sigma}^- = 1$. The results can be straightforwardly extended. The eigenenergies and decay rates of the excited states can be found by diagonalizing

$$\hat{H}_{\mathrm{NH}} = \begin{pmatrix} -\mathrm{i}\kappa/2 & g \\ g & 0 \end{pmatrix} \tag{3.20}$$

The eigenvalues are

$$E_\pm = \frac{-\mathrm{i}\kappa}{4} \pm \sqrt{g^2 - \frac{\kappa^2}{16}}\,. \tag{3.21}$$

This result exhibits a bifurcation at $\kappa = 4g$. For $\kappa < 4g$ the root is real and the eigenenergies are shifted with respect to the bare eigenenergies. This is the so-called strong coupling regime, and the physics is determined by the polaritons discussed above in Section 3.1.

For $\kappa > 4g$ the root is imaginary, and dissipation is so fast that coherent exchange of energy between atom and cavity is suppressed. In this case, the eigenenergies are not shifted with respect to the bare ones, and we speak of the weak coupling regime. However, both eigenvalues are imaginary, showing that the cavity provides a decay channel for both excited states. For $\kappa \gg g$, the effect of the cavity on the excited emitter state $|0, e\rangle$ can be computed perturbatively and expanding the root yields a decay rate $g^2/(2\kappa)$. The same result can be obtained by adiabatic elimination of the $|1, g\rangle$ state [see Figure 3.4(b)]. This modified decay rate due to modifications of the vacuum electromagnetic field was predicted by Purcell 1946 and is accordingly called Purcell effect [10].

Now, consider the generalization of this effect to the case of many identical emitters coupled to a lossy cavity, as illustrated in Figure 3.5(a). As discussed in Section 3.2, without losses, the coupling of symmetric excited states to the cavity is collectively

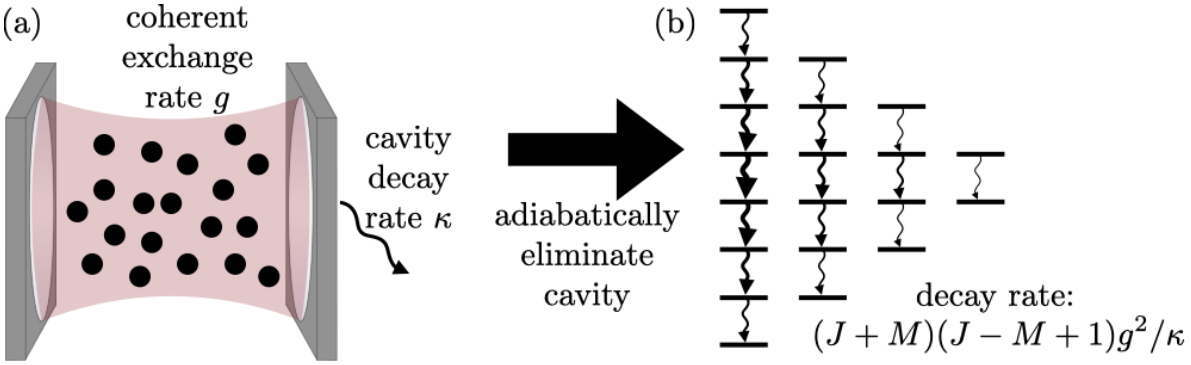


Figure 3.5. – Schematic Illustration of superradiance. (a) Many emitters are coupled to a lossy cavity with decay rate $\kappa$ larger than any coherent exchange rate. (b) Adiabatic elimination of the cavity leads to an effective model for the emitters only, which can be written using generalized Dicke states. The decay rate depends on the Dicke quantum numbers and is indicated by the thickness of the arrow.

enhanced. As a result, the condition for strong or weak coupling (defined for the single excitation limit) becomes $\kappa = 4\sqrt{N}g$.

In the case where the cavity decay is much faster than any coherent process, the cavity excited state can be adiabatically eliminated (see Section 2.3 in the previous chapter). In this case, the ground state manifold consists of all states without cavity photons, and the excited state manifold contains all states with exactly one cavity photon. States with more cavity photons are ignored and lead to higher order corrections. Then the terms for adiabatic elimination using the result derived by Reiter and Sørensen [11] can be written as

$$\hat{Q} = \hat{a}^\dagger \hat{a}\,, \tag{3.22}$$

$$\hat{H}_{e,\mathrm{NH}} = \left(-\Delta - \mathrm{i}\frac{\kappa}{2}\right)\hat{a}^\dagger \hat{a}\,, \tag{3.23}$$

$$\hat{H}_g = 0\,, \tag{3.24}$$

$$\hat{V}_+ = g\hat{a}^\dagger \hat{S}^-\,, \tag{3.25}$$

$$\hat{V}_- = g\hat{a}\hat{S}^+\,. \tag{3.26}$$

The effective operators read

$$\hat{H}_{\mathrm{eff}} = \frac{g^2\Delta}{\Delta^2 + \kappa^2/4}\hat{S}^+\hat{S}^- \tag{3.27}$$

$$\hat{L}_{\mathrm{eff}} = \frac{g\sqrt{\kappa}}{-\Delta - \mathrm{i}\kappa/2}\hat{S}^- \tag{3.28}$$

As a result, the effective (non-hermitian) Hamiltonian is diagonalized by the generalized Dicke states. Using Equation (3.16), both energy shifts and decay rates are collectively

enhanced and proportional to

$$\langle J, M| \hat{S}^+ \hat{S}^- |J, M\rangle = J(J+1) - M(M-1) = (J+M)(J-M+1)\,. \tag{3.29}$$

This is schematically illustrated in Figure 3.5(b) for $\Delta = 0$. The decay is strongest in the completely symmetric manifold, i.e. for $J = N/2$. Importantly the dark states $M = -J$ do not couple to the cavity, and clearly do not decay according to Equation (3.29). As a result, even inside a lossy cavity, some excited states cannot decay due to their symmetry.

This enhanced decay rate is known as super-radiance, whereas the suppression of decay in the dark states is called sub-radiance. The first prediction of super-radiance was made by Dicke in 1954 [12]. He considered an ensemble of emitters that are so close to each other that they all couple to the same light mode in free space. In particular, all emitters are within one wavelength. In this case, the same type of symmetric states become fundamental excitations of the system, and constructive interference of spontaneous emission leads to collectively enhanced decay.

## 3.5. Spontaneous Emission and the Fate of Dicke States

Above, I have shown how the Dicke basis can be used to efficiently simulate or even diagonalize permutation symmetric cavity problems. This discussion relied on the writing of the Hamiltonian and Lindblad operators in terms of total spin operators $\hat{S}^{\pm,z}$. As a result, the Hamiltonian commutes with $\hat{S}^2$, giving an additional symmetry to the problem. This result remained valid even under cavity decay, which does not break the permutation symmetry.

If, however, spontaneous emission of individual atoms is added to the problem, the Lindblad operators also depend on the individual Lindblad operators, even if the decay rate is identical for all atoms. In fact, it is not a priori obvious whether the Dicke states are a useful basis in this case. Several works have been published on how to use permutation symmetry also in this case [8, 9, 13–16].

In 2008, Chase and Geremia have shown that indeed identical dissipation of individual two-level emitters can be captured by the Dicke states [8]. In particular, they give formulas to compute the recycling terms in the Dicke basis. Importantly, these recycling terms can change the quantum number $J$. However, the full density matrix is determined by amplitudes for different $J$ and $M$, since the recycling terms do not couple different degenerate subspaces within the same $J$-manifold. Zhang *et al.* used this result to develop a quantum trajectories simulation in the Dicke basis [16], which we adapt in Chapter 5 for the simulation of ultracold molecules coupled to a cavity.

If more than two levels are involved, no mapping to the Dicke states is known. However, it is still possible to drastically reduce computational cost by taking advantage of permutation symmetry [9, 14]. The underlying insight is that density matrix elements that can be transformed into each other by permutation of emitters must be identical, leading to a drastic reduction in the number of independent density matrix elements.

## 3.6. Some Notes on Breaking Permutation Symmetry

The above simplifications for the many emitter scenario rely on the permutation symmetry of the emitters. It is thus important to consider what happens if this permutation symmetry is broken. In general, as long as the exchange between emitter and light mode happens on a faster time scale than any symmetry breaking effects, such effects should be perturbative. In this case, polariton formation should not be inhibited. Below, different types of "disorder" are discussed.

The least disruptive type of disorder is a local phase shift of the excited states. This might happen because the light arrives at different atoms at different times. A simple unitary transform into the so-called timed Dicke states can be used to transform back into a picture without phase shift, such that the physics is not changed [17].

This changes for disordered local coupling strengths to the cavity, e.g. due to its spacial mode profile. In this case, the permutation symmetry is irreversibly broken, and the symmetrically excited state is not the one coupling to the cavity. Instead, e.g. in the single excitation manifold, the state coupling to the cavity is given by

$$\sum_n \frac{g_n \hat{\sigma}_n^+}{\sqrt{\sum_n g_n^2}} |0, g \cdots g\rangle \ , \tag{3.30}$$

where $g_n$ are the local coupling strengths. The resulting Rabi splitting is simply $2\sqrt{\sum_n g_n^2}$. Similar to the symmetric case, all orthogonal excited emitter states remain dark. However, for multiple excitations, the state created by applying the same operator multiple times to the ground state is only approximately an eigenstate of the system, and the real eigenstates become more complex.

In the case of local energetic disorder, as is common for example in organic molecules coupled to cavities, the dark states acquire a photon contribution [18, 19]. In the case where $\sqrt{N}g$ is larger than the disorder, this photon contribution is perturbative, and polariton states with approximately the same properties as the bare polaritons can be defined [20]. However, even in this case the disorder can lead to interesting, qualitatively new effects such as enhanced transfer [18, 21]. This physics is the topic of Chapter 9.

Finally, also other local couplings such as dipole interactions between the emitters can break the permutation symmetry and lead to large modifications, especially in high density ensembles [22].

# Bibliography


[1] C. Cohen-Tannoudji, J. Dupont-Roc, and G. Grynberg, *Atom-Photon Interactions: Basic Processes and Applications*. New York: Wiley, 1992.

[2] D. Braak, "On the Integrability of the Rabi Model," *Phys. Rev. Lett.*, vol. 107, p. 100401, Aug. 2011.

[3] E. Jaynes and F. Cummings, "Comparison of quantum and semiclassical radiation theories with application to the beam maser," *Proc. IEEE*, vol. 51, pp. 89–109, Jan. 1963.

[4] A. A. Anappara, S. De Liberato, A. Tredicucci, C. Ciuti, G. Biasiol, L. Sorba, and F. Beltram, "Signatures of the ultrastrong light-matter coupling regime," *Phys. Rev. B*, vol. 79, p. 201303, May 2009.

[5] T. Schwartz, J. A. Hutchison, C. Genet, and T. W. Ebbesen, "Reversible Switching of Ultrastrong Light-Molecule Coupling," *Phys. Rev. Lett.*, vol. 106, May 2011.

[6] B. M. Garraway, "The Dicke model in quantum optics: Dicke model revisited," *Philos. Trans. R. Soc. Math. Phys. Eng. Sci.*, vol. 369, pp. 1137–1155, Mar. 2011.

[7] M. Tavis and F. W. Cummings, "Exact solution for an $n$-molecule—radiation-field hamiltonian," *Phys. Rev.*, vol. 170, pp. 379–384, June 1968.

[8] B. A. Chase and J. M. Geremia, "Collective processes of an ensemble of spin-12 particles," *Phys. Rev. A*, vol. 78, p. 052101, Nov. 2008.

[9] M. Bolaños and P. Barberis-Blostein, "Algebraic solution of the Lindblad equation for a collection of multilevel systems coupled to independent environments," *J. Phys. Math. Theor.*, vol. 48, p. 445301, Nov. 2015.

[10] E. M. Purcell, H. C. Torrey, and R. V. Pound, "Resonance Absorption by Nuclear Magnetic Moments in a Solid," *Phys. Rev.*, vol. 69, pp. 37–38, Jan. 1946.

[11] F. Reiter and A. S. Sørensen, "Effective operator formalism for open quantum systems," *Phys. Rev. A*, vol. 85, p. 032111, Mar. 2012.

[12] R. H. Dicke, "Coherence in Spontaneous Radiation Processes," *Phys. Rev.*, vol. 93, pp. 99–110, Jan. 1954.

[13] S. Hartmann, "Generalized Dicke states," *Quantum Info. Comput.*, vol. 16, pp. 1333–1348, Nov. 2016.

[14] M. Gegg and M. Richter, "Efficient and exact numerical approach for many multi-level systems in open system CQED," *New J. Phys.*, vol. 18, p. 043037, Apr. 2016.

[15] N. Shammah, S. Ahmed, N. Lambert, S. De Liberato, and F. Nori, "Open quantum systems with local and collective incoherent processes: Efficient numerical simulations using permutational invariance," *Phys. Rev. A*, vol. 98, p. 063815, Dec. 2018.

[16] Y. Zhang, Y.-X. Zhang, and K. Mølmer, "Monte-Carlo Simulations of Superradiant Lasing," *New J. Phys.*, vol. 20, p. 112001, Nov. 2018.

[17] A. A. Svidzinsky and M. O. Scully, "Evolution of collective N atom states in single photon superradiance: Effect of virtual Lamb shift processes," *Optics Communications*, vol. 282, pp. 2894–2897, July 2009.

[18] T. Botzung, D. Hagenmüller, S. Schütz, J. Dubail, G. Pupillo, and J. Schachenmayer, "Dark state semilocalization of quantum emitters in a cavity," *Phys. Rev. B*, vol. 102, p. 144202, Oct. 2020.

[19] J. Dubail, T. Botzung, J. Schachenmayer, G. Pupillo, and D. Hagenmüller, "Large Random Arrowhead Matrices: Multifractality, Semi-Localization, and Protected Transport in Disordered Quantum Spins Coupled to a Cavity," *ArXiv210508444 Quant-Ph*, May 2021.

[20] R. Houdré, R. P. Stanley, and M. Ilegems, "Vacuum-field Rabi splitting in the presence of inhomogeneous broadening: Resolution of a homogeneous linewidth in an inhomogeneously broadened system," *Phys. Rev. A*, vol. 53, pp. 2711–2715, Apr. 1996.

[21] N. C. Chávez, F. Mattiotti, J. A. Méndez-Bermúdez, F. Borgonovi, and G. L. Celardo, "Disorder-Enhanced and Disorder-Independent Transport with Long-Range Hopping: Application to Molecular Chains in Optical Cavities," *Phys. Rev. Lett.*, vol. 126, p. 153201, Apr. 2021.

[22] C. Sommer, M. Reitz, F. Mineo, and C. Genes, "Molecular polaritonics in dense mesoscopic disordered ensembles," *Phys. Rev. Research*, vol. 3, p. 033141, Aug. 2021.

# 4. Matrix Product States

Many body quantum systems are generally hard to simulate due to the exponential scaling of the Hilbert space with system size. That is, in order to describe an arbitrary state of $N$ $d$-level system, in principle $d^N$ parameters are needed, as opposed to $N \times d$ parameters for an equivalent classical system. This is due to entanglement between the different sub-systems [1–3]. Entanglement describes the phenomenon that in quantum mechanics, a quantum system can be in a well-defined (pure) state, while neither sub-system is in a well-defined state individually. Then, all information is stored in the correlation between the sub-systems. This is in contrast to classical systems, whose state must be well-defined on a fundamental level (i.e. each sub-system is in a well-defined state). The need to fully account for all possible correlations leads to the exponential scaling with system size.

In contrast, in real-world quantum systems entanglement is typically limited and local, meaning that entanglement of a sub-system with the rest scales as the surface of the subsystem, called "area-law" [1]. Based on this insight, tensor network states have been developed as a method to describe quantum systems [4, 5]. In these states, the Hilbert space is systematically truncated by limiting entanglement via a so-called bond-dimension. Tensor network methods have proven particularly successful for 1D systems, where the surface of a subsystem in 0-dimensional, i.e. constant. One-dimensional tensor network states are known as Matrix Product States (MPS) [4, 6]. In this case, the bond dimension can be interpreted as the maximum number of allowed correlations in any contiguous bi-partition of the system.

In this chapter, Matrix Product States are introduced with a focus on the methods used in this thesis. The underlying mathematical framework together with the common concise graphical notation is established in Section 4.1. In Section 4.2, the canonical form of the MPS is defined, followed by a brief interlude on how conserved quantities can increase the efficiency of an MPS simulation in Section 4.3. In Section 4.4, the time evolving block decimation algorithm is discussed to compute the time evolution of a state. This algorithm is used to compute the short time dynamics of the Holstein-Tavis-Cummings model in Chapters 9 and 10. To conclude this chapter, in Section 4.5 a specific implementation to simulate translation invariant infinite open systems is explained. This implementation is used to analyze the operator entanglement dynamics of an XXZ chain with dephasing in Chapter 11.

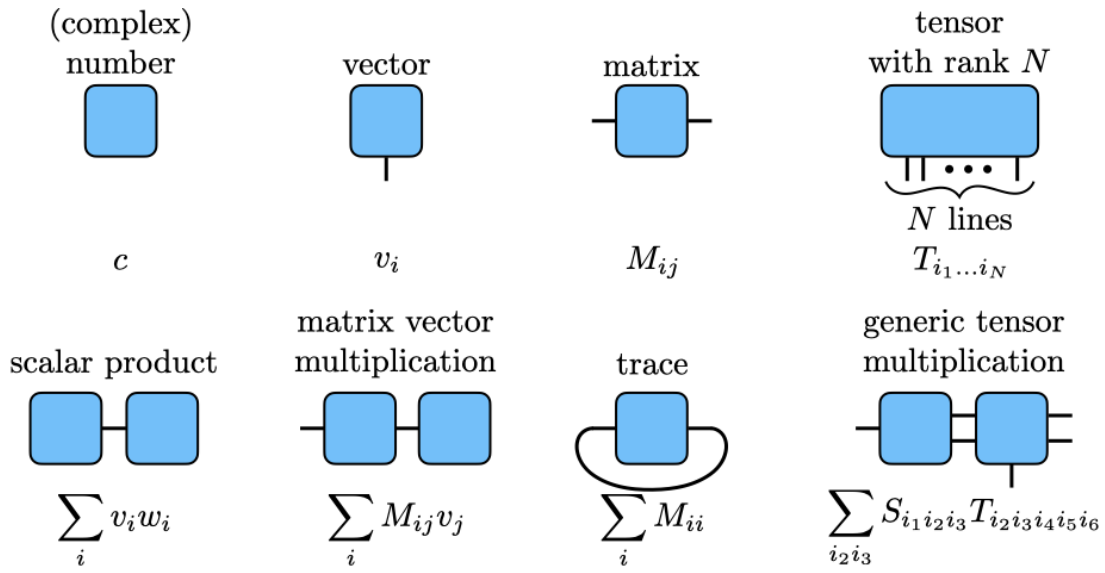


Figure 4.1. – Examples for the graphical representation of tensors and tensor products. Each box is a tensor, each leg is one index. A shared leg (index) signifies contraction of that index. The top row gives examples for tensors, the bottom row displays how to represent calculations.

## 4.1. Matrix Product State Representation

Almost as the name suggests, the Matrix Product State framework decomposes state vectors into products of tensors (of rank 2 and 3). Writing down the corresponding equations typically results in a clutter of indices that hides the underlying concepts. This motivates an easier visual representation of tensors introduced in Figure 4.1, which is standard in the field. Each blue box stands for a tensor, and the number of legs of each box is the rank of that tensor (its number of indices). Some examples are shown in the top row. Furthermore, if two tensors share the same leg, the corresponding index is contracted over. As a simple example, two boxes connected by one leg represent the scalar product of two vectors (bottom left). With this definition, generic tensor products can be displayed graphically (see bottom row for examples).

With this notation, we now proceed to discuss the MPS representation of a state. An arbitrary state of $N$ $d$-dimensional quantum objects [e.g. a spin $(d-1)/2$ chain of length $N$] is fully determined by a $d^N$ dimensional tensor $c_{i_1,\ldots,i_N}$ with

$$|\psi\rangle = \sum_{i_1=1}^{d} \cdots \sum_{i_N=1}^{d} c_{i_1,\ldots,i_N} |i_1, \ldots, i_N\rangle \ . \tag{4.1}$$

A MPS is a decomposition of the tensor $c_{i_1,\ldots,i_N}$ into a product of rank-3 $\Gamma$ tensors (rank-2 tensors at the edges) as shown in Figure 4.2. The indices connecting two adjacent $\Gamma$s (sites) are called internal indices, the open indices correspond to the physical dimension and are thus called physical indices. The dimension of the internal indices

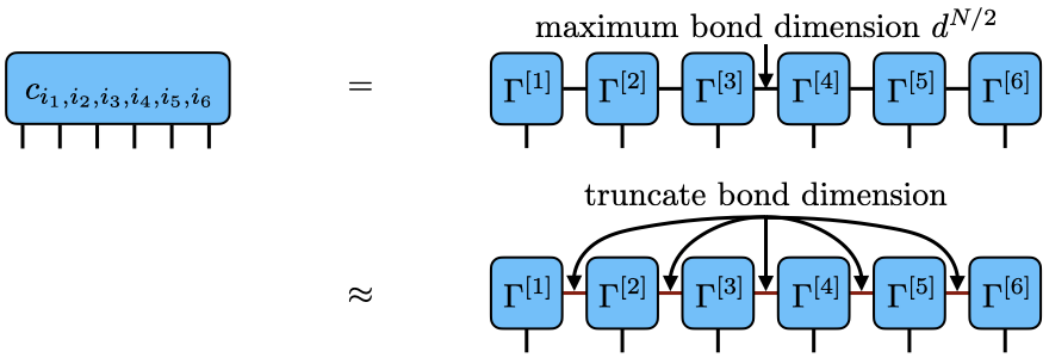


Figure 4.2. – The MPS approximation. An arbitrary tensor can be decomposed into a product of lower rank tensors, where the "bond dimension" is exponentially large and stores the information (top row). The MPS approximation then consists of systematically truncating of the bond dimension to compress the information with minimal loss.

is called the "bond dimension." Such a decomposition is in principle always possible, e.g. by a successive application of matrix decomposition algorithms [such as a singular value decomposition (SVD) [7]] with the combination of multiple indices into one matrix dimension. For a general tensor $c$, the maximum bond dimension in the center of the chain is $d^{N/2}$. Then, the total dimension of one of the central tensors ($\Gamma^{[3/4]}$ if Figure 4.2) is $d^N$, and the MPS representation does not lead to any compression of information. In contrast, a simple product state can be described by a decomposition with bond dimension 1, by identifying $\Gamma^{[n]}$ with the state vector on the $n$th site.

The central approximation is to systematically truncate the bond dimension to a maximum value $\chi$ by neglecting the least important correlations [4, 6]. This is schematically indicated in the second row of Figure 4.2. In practice, this can be done by computing a SVD of the two tensors to both sides of the bond in a physically meaningful basis as detailed below in Section 4.2. Then, the smallest singular values can be neglected, effectively reducing the bond dimension. As a result, the total number of elements in the truncated MPS is $\sim N\chi^2 d \ll d^N$, and it grows only linearly with $N$ for fixed bond dimension. In practice, larger systems often require larger bond dimension, however, the scaling is typically sub-exponential [4].

## 4.2. Canonical Form

As introduced above, the $\Gamma$ tensors are not uniquely defined. Given a certain MPS representation, other representations can be generated by multiplying tensor $\Gamma^{[n]}$ with a matrix $A$ from the right and tensor $\Gamma^{[n+1]}$ with the inverse $A^{-1}$ from the left, such that upon contraction $A$ and $A^{-1}$ cancel. However, in order to be able to truncate in a physically meaningful way, certain orthogonality conditions should be fulfilled, leading to the so-called canonical form [8]. In the canonical form, in addition to the $\Gamma$ tensors, diagonal $\chi \times \chi$ matrices $\lambda^{[n]}$ are introduced as indicated in Figure 4.3(a). The freedom

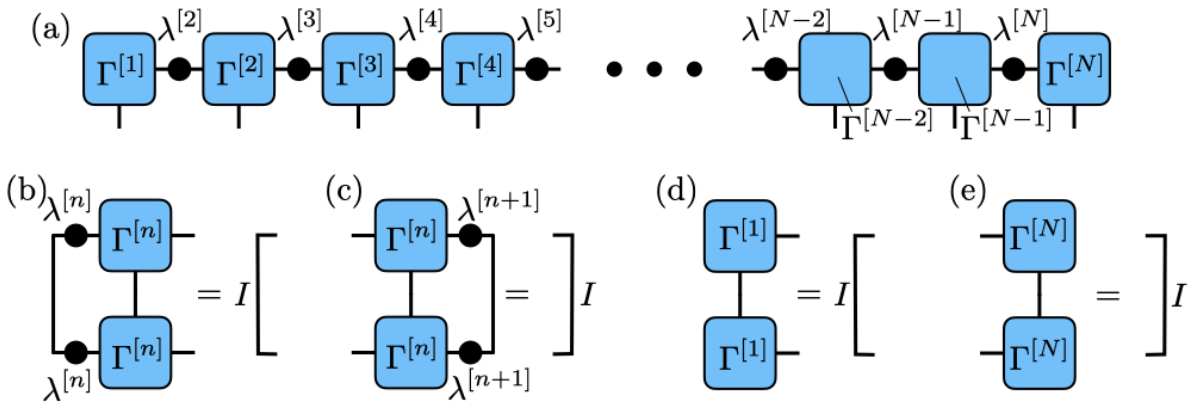


Figure 4.3. – Canonical form of the MPS. (a) In addition to the rank-3 $\Gamma$ tensors (blue squares), diagonal $\lambda$-tensors (black dots) are stored. (b)-(e) Orthogonality conditions: Appropriate contraction over a physical and bond index yields the identity ($I$). (d/e) At the edges of the chain, only the physical index is contracted.

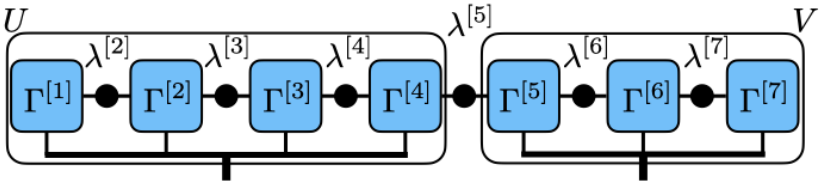


Figure 4.4. – Canonical form as a Schmidt decomposition. Due to the orthogonality conditions Figure 4.3(b) to (e), the matrices $U$ and $V$ are unitary. The entries of $\lambda^{[n]}$ are then the singular (or Schmidt) values for this decomposition.

of choice from the $\Gamma^{[n]}$s and the $\lambda^{[n]}$s is then used to fulfill the orthogonality conditions Figure 4.3(b) to (e).

Physically, this condition is related to writing the state $|\psi\rangle$ as a Schmidt decomposition in the following way [6, 8]: The matrices $U$ and $V$ to the left and right of a given $\lambda^{[n]}$ as defined in Figure 4.4 are semi-unitary, i.e. matrix multiplication with respect to the physical indices gives the identity. This can be easily confirmed by repeated application of conditions (b) and (d) [(c) and (e)] for $U$ [$V$], respectively. As a consequence, the states given by the columns of $U$ (rows of $V$) are orthogonal to each other and the entries of the diagonal matrix $\lambda^{[n]}$ are the *unique* Schmidt values of the decomposition of the

whole state according to [8]

$$|\psi\rangle = \sum_i \lambda_{ii}^{[n]} \left|\psi_i^L\right\rangle \otimes \left|\psi_i^R\right\rangle , \tag{4.2}$$

$$\left\langle \psi_i^{L/R} \middle| \psi_j^{L/R} \right\rangle = \delta_{ij} . \tag{4.3}$$

This orthogonality property ensures that setting the smallest entries $\lambda^{[n]}$ to zero during the truncation corresponds to throwing away the least important contributions [4].

Furthermore, the conditions Figure 4.3(b) to (e) give a straightforward recipe to compute the canonical form using SVDs. In particular, a SVD of the total tensor $c_{i_1,\ldots,i_N}$ with treating the indices $\{i_1,\ldots,i_{n-1}\}$ as a combined left and the indices $\{i_n,\ldots,i_N\}$ as a combined right index gives the desired unitarity of the matrices $U$ and $V$ in Figre 4.4. Successive application of the SVD then results in the correct conditions for the $\Gamma$s and $\lambda$s. Sections 4.4 and 4.5 discuss how to preserve these conditions during time evolution.

In addition to its fundamental role in ensuring the truncation accuracy, the canonical form is also practically useful when computing expectation values, as illustrated in Figure 4.5 [6]. In general, an expectation value of an operator is given by the tensor contraction shown in Figure 4.5(a). In many cases, local operators containing only a few indices are the most interesting. In these cases, the operator acting on the full state is a tensor product of the local operator with identities acting on all other physical dimensions, e.g. $\hat{I}_1 \otimes \hat{O}_{23} \otimes \hat{I}_{456}$ [see Figure 4.5(b)]. Then, the contraction over these indices becomes trivial, as illustrated in Figure 4.5(b). If the MPS is given in its canonical form, application of the conditions Figure 4.3(b) to (e) can be used to simplify the computation, and only local tensors $\Gamma$ and $\lambda$ are needed to compute the expectation values of local operators [Figure 4.5(c)].

Analogously, local density matrices can also be computed from local tensors, only. Local density matrices are computed by tracing out all other degrees of freedom

$$\hat{\rho}_n = \mathrm{Tr}_{1,\ldots,n-1,n+1,\ldots,N} |\psi\rangle \langle\psi| . \tag{4.4}$$

In graphical notation, this translates to contracting all but one index as shown in Figure 4.5(d). Again, the conditions Figure 4.3(b) to (e) can be applied to reduce the computation to only include local tensors.

Lastly, the Schmidt value interpretation of the $\lambda$ tensors results in a very easy method to compute entanglement or von Neumann entropies for bi-partitions of the system [6]. In particular, according to Equation (4.2), the reduced density matrix of the right hand side is given by

$$\hat{\rho}^R = \sum_i \left(\lambda_{ii}^{[n]}\right)^2 \left|\psi_i^R\right\rangle \left\langle\psi_i^R\right| . \tag{4.5}$$

As a result, the entanglement entropy is given by

$$S = \mathrm{Tr}\left[\hat{\rho}^R \log_2\left(\hat{\rho}^R\right)\right] = \sum_i \left(\lambda_{ii}^{[n]}\right)^2 \log_2\left[\left(\lambda_{ii}^{[n]}\right)^2\right] . \tag{4.6}$$

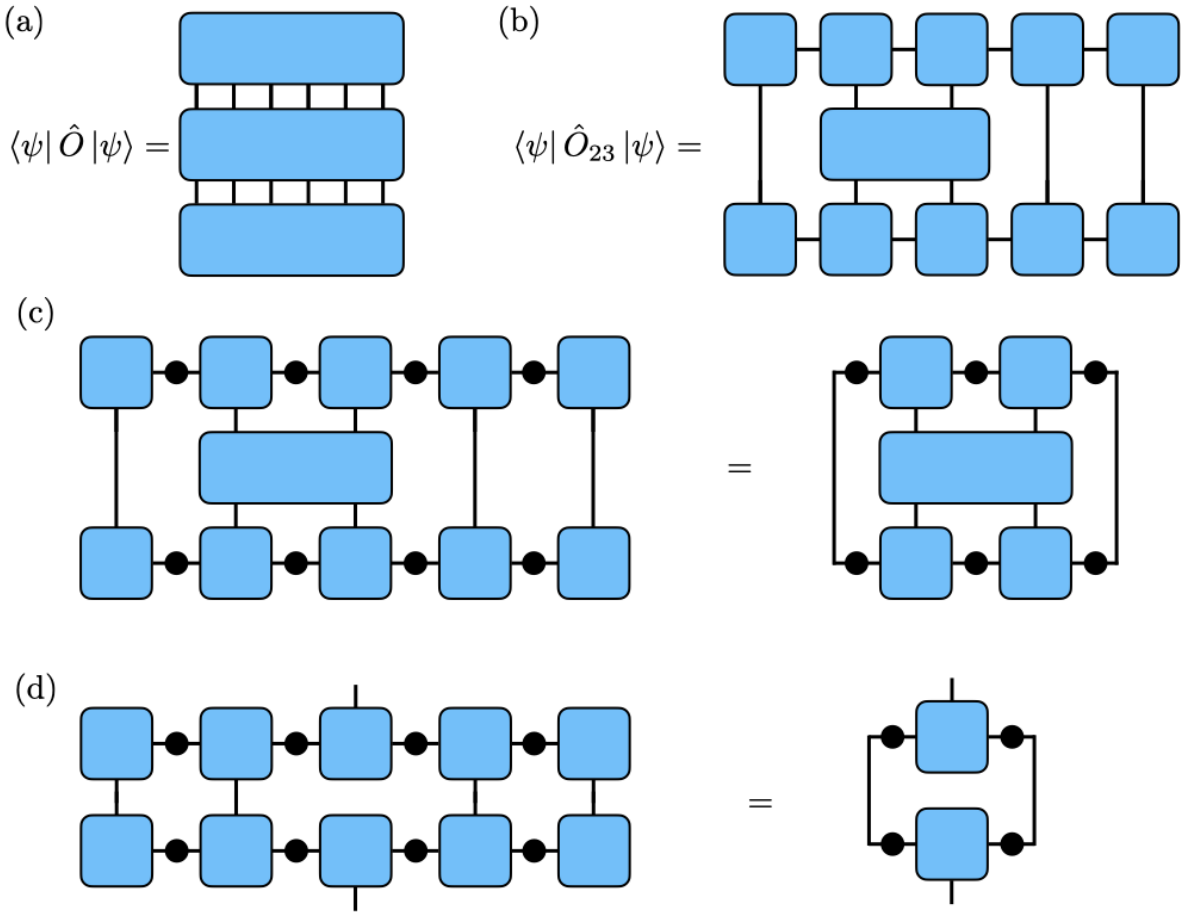


Figure 4.5. – Computation of local expectation values density matrices using MPS. (a) General expectation value using the graphical tensor notation. (b) Within the MPS framework, a local expectation value is computed by contracting all open indices. (c) Using the canonical form, the MPS can be contracted and local expectation values can be computed using local tensors, only. (d) Local density matrices are computed by contracting the all indices except for the local physical ones. Using orthogonality conditions in the canonical form, this computation can be reduced local tensors.

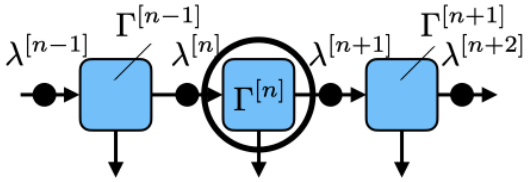


$$\Gamma^{[n]} = \begin{pmatrix} \begin{bmatrix} \chi_{\text{in}} = -3 \\ \chi_{\text{out}} = -2 \\ i_{\text{out}} = -1 \end{bmatrix} & 0 & \cdots & 0 \\ 0 & \begin{bmatrix} \chi_{\text{in}} = -2 \\ \chi_{\text{out}} = -1 \\ i_{\text{out}} = -1 \end{bmatrix} & \cdots & 0 \\ \vdots & \vdots & \ddots & \vdots \\ 0 & 0 & \cdots & \begin{bmatrix} \chi_{\text{in}} = 3 \\ \chi_{\text{out}} = 2 \\ i_{\text{out}} = 1 \end{bmatrix} \end{pmatrix}$$

Figure 4.6. – Quantum Number Conservation. The top indicates the "flow" of quantum numbers. Number conservation requires that incoming and outgoing indices add up to the same number. The matrix below indicates the resulting block-sparse structure of $\Gamma^{[n]}$.

This formula will be used to compute entanglement entropies and operator space entanglement entropies in Chapters 9 and 11, repsectively.

## 4.3. Conserved Quantities

This section contains a brief interlude on how to use conserved quantities to improve the efficiency of numerical simulations. More mathematical background can be e.g. found in References [6, 9], and a practical introduction in Reference [10]. In this thesis, conservation laws are used to make MPS simulations more efficient in Chapters 9, 10 and 11.

In this section, I only discuss conservation laws that can be written as a sum of single-site operators. Examples include the total magnetization of a spin chain $\hat{S}^z = \sum_n \hat{\sigma}^z_n$, the total particle number $\hat{n}_{\text{tot}} = \sum_n \hat{b}^\dagger_n \hat{b}_n$, or the number of excitations in a cavity problem $\hat{n}_{\text{exc}} = \hat{a}^\dagger \hat{a} + \sum_n \hat{\sigma}^+_n \hat{\sigma}^-_n$. Furthermore, the system is assumed to be in an eigenstate of the operator assigned to the conserved quantity. In this case, a quantum number flow can be assigned to each possible value of an index, as schematically indicated in Figure 4.6. As an example, consider a system with conserved magnetization $\hat{S}^z$. Here, the local physical index on one site $i_{\text{out}}$ can have two possible values for the conserved quantity, $+1$ or $-1$ in the spin up and spin down state, respectively. Quantum numbers can then also be assigned to the internal indices by enforcing that the flow through

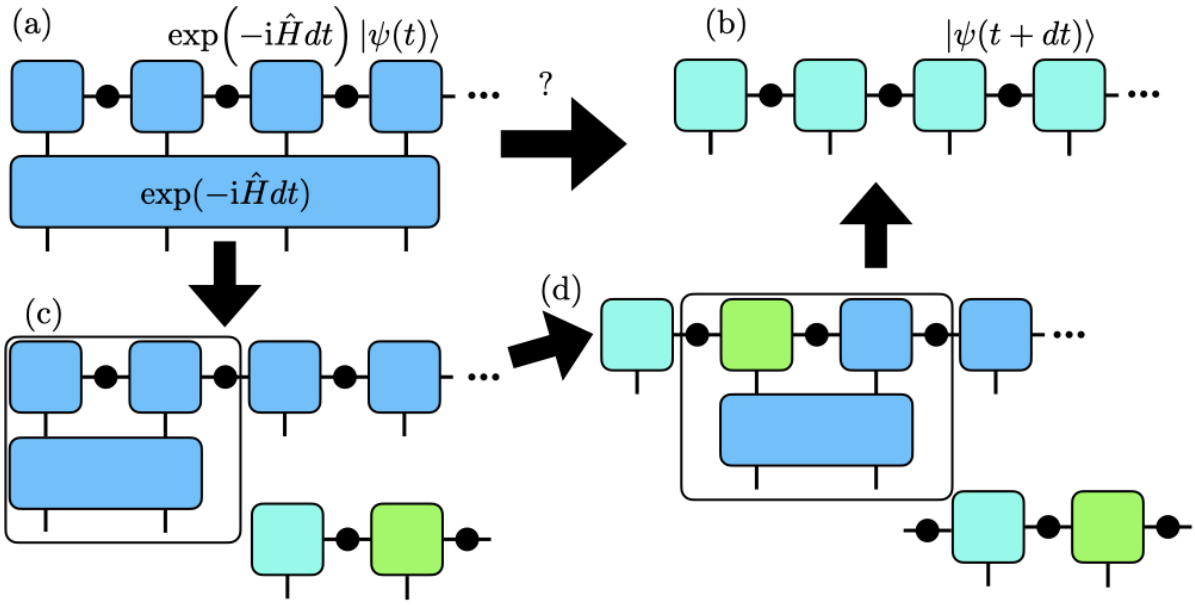


Figure 4.7. – Schematic illustration of the TEBD algorithm. (a) A time step is generally computed by multiplying a state with $\exp\left(-\mathrm{i}\hat{H}dt\right)$. (b) The goal is to find a MPS representation of the final state. (c)/(d) The TEBD algorithm decomposes the evolution operator into two site "gates." These are then applied locally together with a singular value decomposition, which yields the updated $\Gamma$ and $\lambda$ tensors.

each tensor balances $\chi_{\text{in}} = \chi_{\text{out}} + i_{\text{out}}$. As a consequence, the value of $\chi_{\text{in}}$ is equal to the inverse magnetization of the left part of the chain. Starting to build from the left, it is clear that such a decomposition is always possible. With these choices, the tensors $\Gamma^{[n]}$ become block-sparse with blocks associated to the different possible quantum numbers, as indicated in Figure 4.6. This block-sparse structure can lead to a significant speedup in matrix operations required for computing the time evolution, such as matrix multiplication of SVDs.

The different possible values of the conserved quantity can be identified as symmetry sectors, and are discussed in detail in Chapter 11.

## 4.4. Time Evolving Block Decimation

In order to simulate dynamics, we need to compute a MPS representation of the state $|\psi(t+dt)\rangle$ from the representation of $|\psi(t)\rangle$. This can be achieved by applying the time evolution operator $\exp\left(-\mathrm{i}\hat{H}dt\right)$ to the state $|\psi(t)\rangle$ as shown in Figure 4.7(a/b). However, in most cases of interest the time evolution operator is hard to compute exactly. In addition, even with an approximate representation of the time evolution operator, a direct application would increase the dimension of all internal bonds at once, making

the intermediate state expensive to store.

One way to circumvent this problem is given by the time evolving block decimation (TEBD) algorithm, which uses a Trotter decomposition of the time evolution operator into local two-site operators [4, 6]. In the context of classical simulation of quantum computation, methods to efficiently apply such one- and two-site gates have been developed [8]. Then, using a SVD, the resulting state can be truncated, as schematically indicated in Figure 4.7(c/d).

In detail, the total Hamiltonian $\hat{H}$ is decomposed into a sum of local two site Hamiltonians $\hat{H}_{nn+1}$ as

$$\hat{H} = \sum_n \hat{H}_{nn+1} \,. \tag{4.7}$$

Then, the time evolution operator can be approximately written as a product of two-site operators

$$\begin{aligned} \exp\Big(-\mathrm{i}\hat{H}dt\Big) &= \exp\left[-\mathrm{i}\left(\sum_n \hat{H}_{nn+1}\right)dt\right] \\ &= \prod_n \exp\Big[-\mathrm{i}\hat{H}_{nn+1}dt\Big] + \mathcal{O}(dt^2)\,, \end{aligned} \tag{4.8}$$

where the remainder $\sim \mathcal{O}(dt^2)$ is given by the Baker-Campbell-Hausdorff formula. The MPS can then be multiplied with this product by successively multiplying with every factor (gate), where each gate acts only on two sites. This successive application of gates is often called a sweep, and by sweeping through the system, the MPS at time $t+dt$ can be computed. The simple sweep given is Equation (4.8) is only accurate up to first order in the time step, and would thus require very small time steps. Higher order sweeps that reduce this error have also been developed [11]. In this thesis in particular, second order sweeps *LRRL* and fourth order sweeps *LRL(-2R)LLLLRLRRRR(-2L)RLR* [11] are used, where $L$ indicates a sweep from the left to the right, and $R$ indicates a sweep starting from the right and ending at the left. The -2 indicates that the gates should be applied for a negative timestep $-2dt$. Note that the definition left to right is arbitrary, and it is only important that the gates are applied in opposite order.

Figure 4.8 shows in detail how a two site gate is applied, including truncation, while keeping the MPS in canonical form [4, 6, 8]. The key idea lies in the SVD in (c), which allows for proper truncation, and the reintroduction of $\lambda^{[n]}$ and $\lambda^{[n+2]}$ in step (d), which restore the correct orthogonality conditions. Panels (g) and (h) show that indeed, the resulting MPS is orthogonal. Notably, the proof of orthogonality in condition (h) relies on the unitarity of the time evolution gate, which will become important in the next section when we consider non-unitary time evolution.

The TEBD algorithm as introduced above can only treat nearest neighbor interactions. However, by swapping two neighboring sites, this can be easily generalized to arbitrary interactions [8]. The respective SWAP gate is illustrated in Figure 4.9, and orthogonality can be proven exactly as in Figure 4.8(g/h). By iterative swapping of a single site

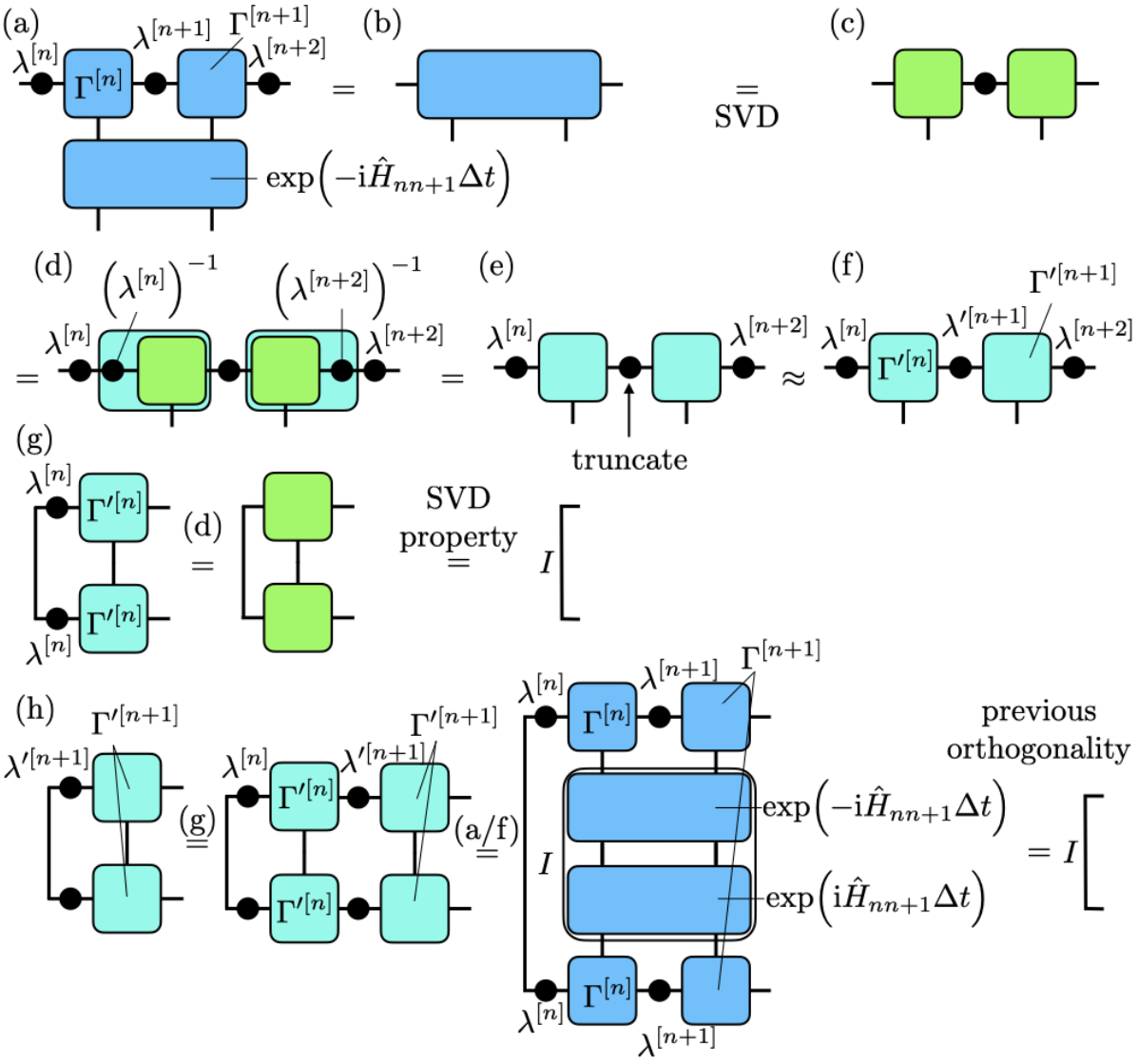


Figure 4.8. – Application of a two site gate. (a) The local time evolution operator is applied by contracting the tensor including three local $\lambda$s, two $\Gamma$s and the unitary operator (b). (c) A singular value decomposition is performed with the left physical and bond index as one – and the right physical and bond index as the other matrix dimension, resulting in two unitary tensors (green squares) and one diagonal tensor (black dot). (d) The unitary tensors are multiplied with the inverse of the outside $\lambda$ tensors (cyan rectangles). (e/f) If necessary, the central diagonal tensor is truncated to find the new $\lambda$s and $\Gamma$s. (g) Due to the unitarity of the singular value decomposition, the orthogonality condition at the $n$th side is fulfilled. (h) Due to the unitarity of the gate, the orthogonality condition at the $(n+1)$th side is fulfilled.

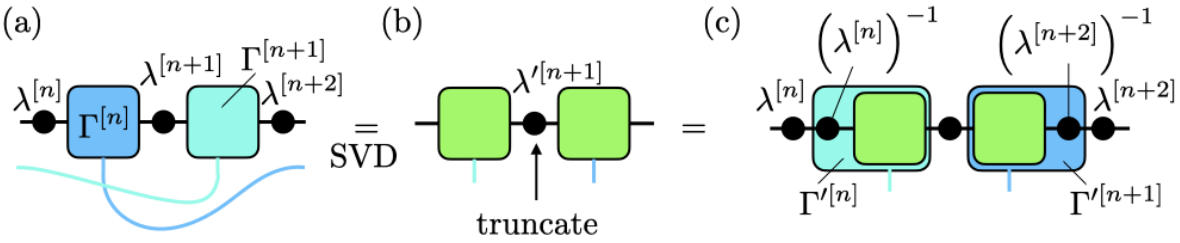


Figure 4.9. – Scheme for swapping two sites. A SVD is performed by identifying the left bond and right physical index with one matrix dimension, and the right bond and left physical index with the other.

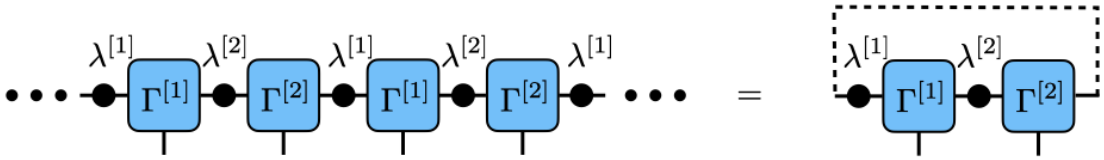

Figure 4.10. – Infinite MPS. Translation invariance of the state by $n$ sites can be used to reduce the MPS to $n$ sites. Here, $n = 2$.

through the system, a one-to-all coupling of spin-boson type models can be efficiently implemented [12], which we use to simulate cavity QED Hamiltonians in Chapters 9 and 10.

As a final note for this section, we have only discussed two-site Hamiltonians and two-site gates. The inclusion of single site Hamiltonians (such as random energy offsets) is possible either by including them into two site gates or by adding separate single site gates, which just modify the local tensor $\Gamma^{[n]}$, i.e. need no SVD or truncation [8].

## 4.5. Time Evolving Block Decimation for Infinite Open Systems

In the final section of the chapter the extension of MPS concepts to translation-invariant infinite open systems is discussed. This section is strongly based on works of Orús and Vidal [13, 14], who first discussed the underlying concepts in the late 2000s. First, infinite translation-invariant MPS are introduced, then an MPS description of open systems using density matrices. Finally, those concepts are combined into translation invariant open systems.

### Infinite MPS

If a state $|\psi\rangle$ is translation invariant, then the MPS representation of this state needs to be translation invariant as well. As a result, only one of the translation invariant

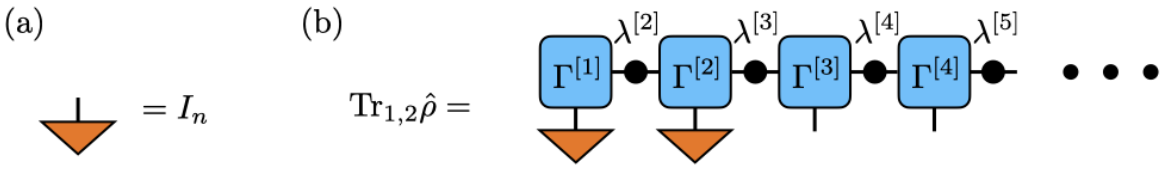


Figure 4.11. – Computing partial traces for an open system MPS. Locally, the trace is computed by multiplication with the trace-ket (orange triangle), which is the tensor corresponding to the identity matrix of local physical dimension $n$.

sub-systems needs to be stored, instead of an entire (infinitely long) chain. This is schematically illustrated in Figure 4.10 for translation invariance by two sites. In this case, only four distinct tensors $\Gamma^{[1/2]}$ and $\lambda^{[1/2]}$ exist, which are infinitely repeated. This is illustrated by connecting the right internal index of $\Gamma^{[2]}$ to $\lambda^{[1]}$.

Note that although the right part of the equality in Figure 4.10 looks similar to a finite periodic system, it in fact does not correspond to a periodic system. Indeed, for bond dimensions $\chi > 1$, non-trivial correlations between site $n$ and site $n+2$ are possible, which would not be the case for periodic systems. In contrast, in those systems, one of the internal indices could always be reduced to dimension 1, since there can be no entanglement between a system and itself.

## Open System MPS

The MPS concepts used to describe quantum states can be straightforwardly generalized to density matrices [6, 15, 16]. In fact, the basic idea introduced in Figure 4.2 describes the decomposition of an arbitrary tensor into a product of rank 3 and 2 tensors. By defining a basis set $\hat{\rho}_i^{[n]}$, $i = 1, \ldots, d^2$ for the density matrix, the global density matrix can be written in terms of a tensor $c_{i_1,\ldots,i_N}$ completely analogously to Equation (4.1) as

$$\hat{\rho} = \sum_{i_1,\ldots,i_N} c_{i_1,\ldots,i_N} \hat{\rho}_{i_1}^{[1]} \otimes \cdots \otimes \rho_{i_N}^{[N]} . \tag{4.9}$$

This tensor can then be written in terms of a matrix product state, with analogous definitions of the canonical form, implementation of conservation laws, and so on.

Importantly, we want to choose an orthonormal basis under the natural scalar product given by the trace, i.e. [15]

$$\mathrm{Tr}\left[\left(\hat{\rho}_i^{[n]}\right)^T \hat{\rho}_j^{[n]}\right] = \delta_{ij} . \tag{4.10}$$

This means that internal products of vectorized operators correspond to taking the trace of the matrix product, as is used e.g. when computing expectation values. The most

standard choice of basis is the so-called Choi isomorphism [15], i.e. interpreting both left and right indices of the density matrix as one joint index.

In order to compute a reduced density matrix from the full density matrix, the other degrees of freedom need to be traced over. Due to the definition of the scalar product and the orthonormal basis choice Equation (4.10), this translates to multiplication with the the vectorized identity matrix, which we call here "trace-ket", as illustrated in Figure 4.11. Analogously, local expectation values can be computed by contracting the respective physical index with the vectorized form of the corresponding operator.

The dynamics can be computed analogously to the dynamics of states by replacing the Hamiltonian with the Lindbladian $\exp(\mathcal{L}dt)$ [15]. The Trotter decomposition and the TEBD scheme from Section 4.4 work analogously for density matrices. However, since the evolution operator is in general non-unitary, the re-orthogonalization according to Figure 4.8(h) does not hold, and the MPS needs to be re-orthogonalized by hand (see Reference [6] for how that can be done for finite systems). For infinite systems, this re-orthogonalization is discussed below.

Alternatively, the vectorization process can be thought of as stacking two state representations on top of each other as $\hat{\rho} = |\psi\rangle\langle\psi|$ and then combining the two physical indices for each site [16]. This however leads to an increase in the bond dimension $\chi \to \chi^2$ and the physical dimension $d \to d^2$. Naïvely, this results in a quadratic increase in computational cost, however, the required bond dimension is often relatively small [15] (see also Chapter 11). At this point it is worth noting that also other approaches have been developed to simulate open systems [16], e.g. based on quantum trajectories [17].

## Infinite Open Systems

The concepts for translation invariant infinite and those for open systems can be directly combined to compute the time evolution of infinite open chains. However, a few technical problems arise when computing observables/reduced density matrices and trying keep the MPS in its canonical form. These problems are discussed in this section.

To restore the canonical form of the MPS after a non-unitary gate application, a re-orthogonalization scheme was introduced by Orús and Vidal [14]. The underlying insight to restore the orthogonality is the following: Instead of the identity, the tensors $T_L = (\lambda^{[n]}\Gamma^{[n]})^\dagger(\lambda^{[n]}\Gamma^{[n]})$ in Figure 4.3(b) will have generally different eigenvectors, the largest of which is labeled $V_L$, as shown in Figure 4.12(c). By finding this eigenvectors and multiplying the tensor $T$ from the left with the eigenvector and from the right with its inverse, the identity will clearly be an eigenvector of the modified tensor. An equivalent modification can be made for the condition in Figure 4.3(c). Both of these modifications can be done in parallel, as shown in Figure 4.12.

In order to compute local reduced density matrices (and expectation values) in an infinite open chain, we need to trace over all other infinitely many degrees of freedom, as schematically indicated in Figure 4.13(a). This corresponds to multiplying one "block" with $A^\infty$ from both sides, where the matrix $A$ is defined in Figure 4.13(b) as the trace over one of the infinitely repeating blocks. This infinite trace can be computed by first diagonalizing $A = W^{-1}DW$, and then computing $D^\infty$ as shown in Figure 4.13(c), which

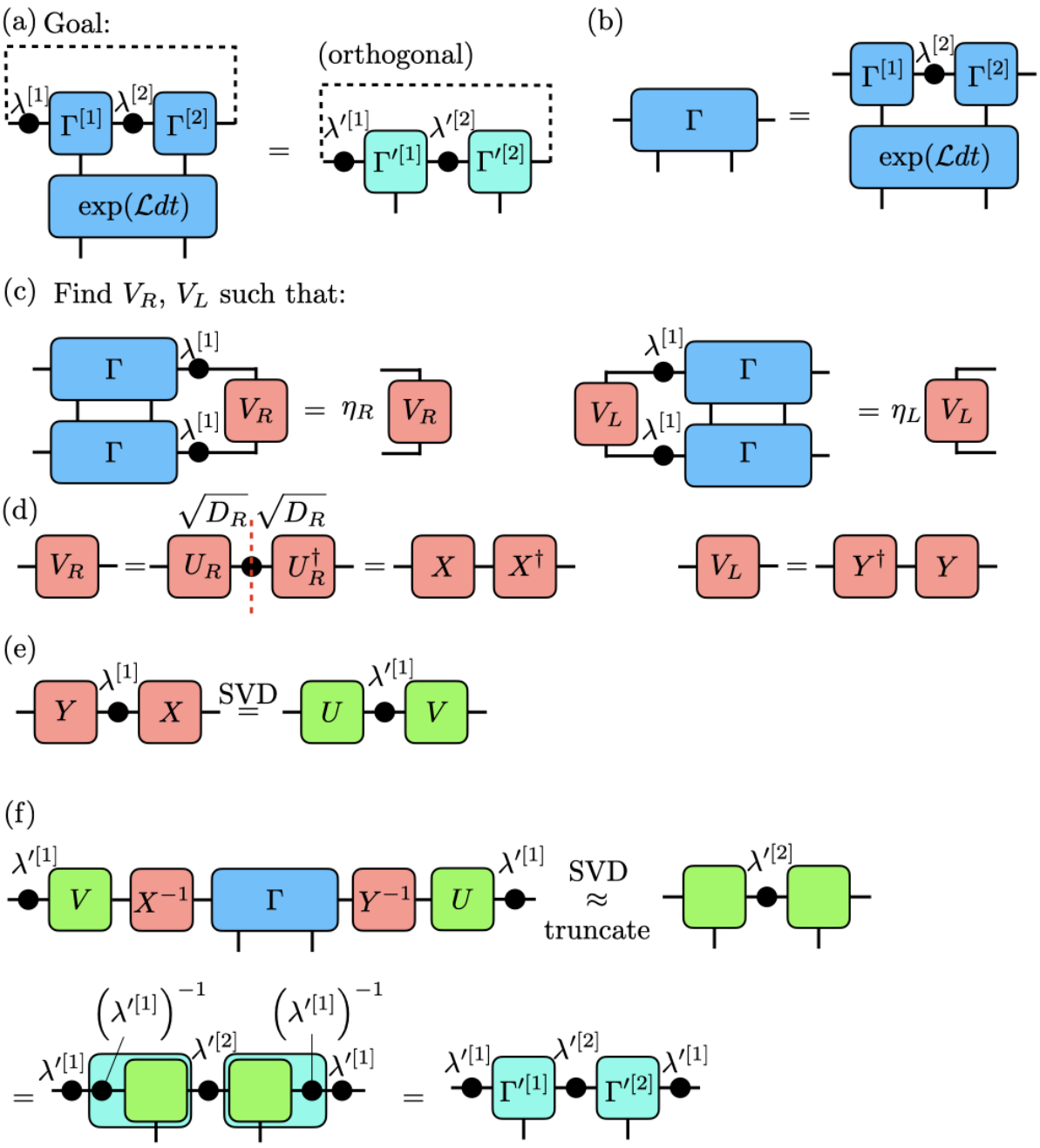


Figure 4.12. – Application of a non-unitary two site gate to an infinite MPS with re-orthogonalization. Details are given in the main text.

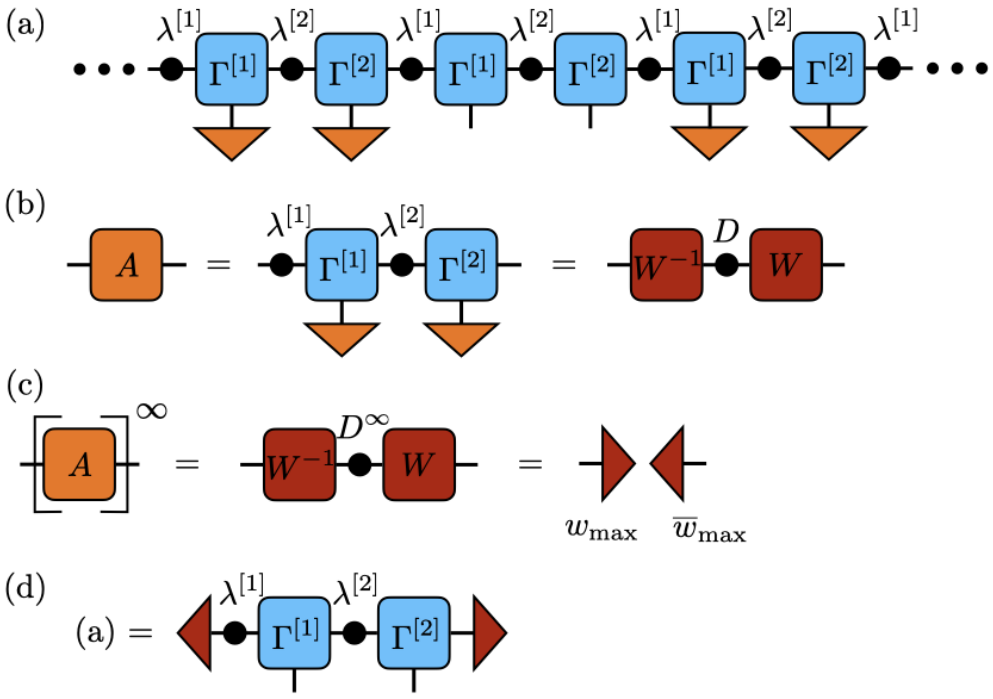


Figure 4.13. – Computation of the reduced density matrix for an infinite open system. Details are given in the text.

can be done element-wise. Importantly, this power is always well defined. To see this, consider that $\mathrm{Tr}(\hat{\rho}) = 1$ by definition, but also $\mathrm{Tr}(\hat{\rho}) = \mathrm{Tr}(A^\infty) = \mathrm{Tr}(D^\infty)$. This is only possible if $A$ has exactly one eigenvalue of 1 and all other eigenvalues are smaller than 1, so that they vanish when taken to power $\infty$. Then, $A^\infty$ becomes just the projector onto its largest eigenvector, which can be easily computed, as shown in Figure 4.13(c). Note that this computation of the largest eigenvector is stable even in the presence of numerical errors, when the eigenvalues are not identical 1. Finally, the local density matrix can be computed by contracting with the maximal left and right eigenvectors of $A$, as shown in Figure 4.13(d). To my knowledge, this is the first time a partial trace was computed in this way.

In order to use conservation laws in infinite systems, it is important that the blocks are initially truly translation invariant. That means that in the initial state, the "quantum number flow" through one block needs to add to 0. This is used in Chapter 11 to include the conservation of magnetization in an open XXZ chain with dephasing.

# Bibliography


[1] J. Eisert, M. Cramer, and M. B. Plenio. Colloquium: Area laws for the entanglement entropy. *Rev. Mod. Phys.*, 82(1):277–306, February 2010.

[2] Ryszard Horodecki, Paweł Horodecki, Michał Horodecki, and Karol Horodecki. Quantum entanglement. *Rev. Mod. Phys.*, 81(2):865–942, June 2009.

[3] Luigi Amico, Rosario Fazio, Andreas Osterloh, and Vlatko Vedral. Entanglement in many-body systems. *Rev. Mod. Phys.*, 80(2):517–576, May 2008.

[4] Guifré Vidal. Efficient Simulation of One-Dimensional Quantum Many-Body Systems. *Phys. Rev. Lett.*, 93(4):040502, July 2004.

[5] J. Ignacio Cirac, Didier Poilblanc, Norbert Schuch, and Frank Verstraete. Entanglement spectrum and boundary theories with projected entangled-pair states. *Phys. Rev. B*, 83(24):245134, June 2011.

[6] Ulrich Schollwöck. The density-matrix renormalization group in the age of matrix product states. *Annals of Physics*, 326(1):96–192, January 2011.

[7] Roger A. Horn and Charles R. Johnson. *Matrix Analysis*. Cambridge University Press, Cambridge ; New York, 2nd ed edition, 2012.

[8] Guifré Vidal. Efficient Classical Simulation of Slightly Entangled Quantum Computations. *Phys. Rev. Lett.*, 91(14):147902, October 2003.

[9] Ian P. McCulloch. From density-matrix renormalization group to matrix product states. *J. Stat. Mech.*, 2007(10):P10014–P10014, October 2007.

[10] Matthew Fishman, Steven R. White, and E. Miles Stoudenmire. The ITensor Software Library for Tensor Network Calculations. *ArXiv200714822 Cond-Mat Physicsphysics*, July 2020.

[11] A. T. Sornborger and E. D. Stewart. Higher-order methods for simulations on quantum computers. *Phys. Rev. A*, 60(3):1956–1965, September 1999.

[12] Michael L. Wall, Arghavan Safavi-Naini, and Ana Maria Rey. Simulating generic spin-boson models with matrix product states. *Phys. Rev. A*, 94(5):053637, November 2016.

[13] G. Vidal. Classical Simulation of Infinite-Size Quantum Lattice Systems in One Spatial Dimension. *Phys. Rev. Lett.*, 98(7):070201, February 2007.

[14] R. Orús and G. Vidal. Infinite time-evolving block decimation algorithm beyond unitary evolution. *Phys. Rev. B*, 78(15):155117, October 2008.

[15] Michael Zwolak and Guifré Vidal. Mixed-State Dynamics in One-Dimensional Quantum Lattice Systems: A Time-Dependent Superoperator Renormalization Algorithm. *Phys. Rev. Lett.*, 93(20):207205, November 2004.

[16] Hendrik Weimer, Augustine Kshetrimayum, and Román Orús. Simulation methods for open quantum many-body systems. *Rev. Mod. Phys.*, 93(1):015008, March 2021.

[17] Andrew J. Daley. Quantum trajectories and open many-body quantum systems. *Adv. Phys.*, 63(2):77–149, March 2014.

# Part II.

# Ultracold Chemistry

# 5. Publication: Collective Dissipative Formation of Ultracold Molecules in a Cavity

The following chapter is a reprint of a work proposing to use a cavity to enhance the formation of ultra-cold molecules, published in *Phys. Rev. Lett.* **125** 193201 (2020) [1]. In this work, we have studied a mechanism to realize high-yield molecular formation from ultra-cold atoms. We have considered a setup where atom pairs are continuously excited into a molecular state by a laser, and the subsequent decay is steered into the ground state by collective coupling of the molecules to a cavity mode. We have demonstrated that the ground state molecular yield can be improved by simply increasing the number of atoms and can overcome efficiencies of state-of-the-art association schemes. Two different implementations for our proposal setup were examined, and their advantages and disadvantages are discussed. Using a combination of analytical and numerical tools, we were able to simulate very large ($\sim 10^6$) molecular ensembles.

This chapter is organized as follows: In Section 5.1, we introduce ultra-cold molecules in general, together with our scheme to create them. In Section 5.2, we present the model that is used to describe said scheme, and in Section 5.3, the excited states are eliminated to derive an effective model. In Section 5.4, we discuss the first implementation, which leads to very high efficiencies, albeit at the cost of long creation times. In Section 5.5, we explain how to speed up the creation by introducing a chirped laser pulse. In Section 5.6, we estimate realistic numbers for the creation of RbCs and $Rb_2$ molecules that are competitive with or even better than STIRAP. Finally, Section 5.7 concludes this chapter.

## 5.1. Introduction

There is considerable interest in preparing and manipulating ultracold ensembles of molecules for quantum simulations, metrology and the study of chemical reactions in the ultracold regime [2–6]. Diatomic molecules in their electronic and rovibrational ground state are routinely produced using the coherent stimulated Raman adiabatic passage (STIRAP) technique [7–11]. Alternatively, continuous formation of ground state molecules can be realized by photoassociation via a weakly bound excited molecular state [12–17]. While more sophisticated methods such as photoassociation followed by pulsed population transfer [18] or re-pumping of vibrationally excited molecules [19, 20] have been experimentally demonstrated, efficiencies of ground state molecular formation

are usually lower than those achieved with STIRAP and without rotational state selectivity. It has recently been proposed that these efficiencies can be increased by strengthening light-molecule coupling rates to ground-state transitions using a cavity [21] or a photonic waveguide [22]. Common to all these schemes is the use of formation processes based on single molecules.

Here, we propose a mechanism to exploit collective effects to perform continuous high-yield molecular formation from ultracold atoms in a cavity. Our scheme is based on photoassociation to a collective excited bound-state followed by superradiant-type decay induced by the cavity to the molecular ground state. We consider the regime of large dissipation with negligible number of cavity photons and electronic excitations, and derive an effective master equation for the internal dynamics of $N$ atom pairs. We show that (i) a continuous laser gives rise to enhancement of the fraction of ground state molecules $N_g^\infty/N \sim [1 - \log(N)/(NC)]$ approaching 1, with $NC$ the collective cooperativity; and (ii) a chirped laser pulse that matches the time-varying excited molecular polariton energies can lead to a final molecular yield $N_g^\infty/N \sim 1 - \Gamma/\kappa$, with $\Gamma$ the excited state linewidth and $\kappa$ the cavity linewidth. The two schemes are most useful for weak and strong cavity couplings, respectively, for which we provide concrete examples. With scheme (i) collective effects always increase the molecular yields at the cost of decreased transfer rates. In contrast, scheme (ii) cannot be directly compared to the single particle scenario with a cavity, but always has higher yields than single-particle photo-association without a cavity. Both schemes can serve as alternatives to STIRAP that relax the requirement for expensive, narrow linewidth, phase-coherent lasers [23], and offer a natural way to continuously populate a molecular lattice coupled to a cavity. More broadly, this work exemplifies the opportunities for state engineering using collective effects in the presence of strong dissipation.

## 5.2. Model

We consider a setup consisting of $N$ identical pairs of atoms and a single mode cavity. The external dynamics of each pair is assumed to be frozen, e.g., by confining to an optical lattice potential. We model each atom pair as a four-level system with states $|i\rangle_n, |e\rangle_n, |g\rangle_n$ and $|x\rangle_n$, $1 \leq n \leq N$. The first three states correspond to a two-atom initial state (e.g., a low-energy scattering state or pre-formed Feshbach molecular bound state), a molecular excited state and the absolute electronic and rovibrational molecular ground state, respectively [see Fig. 5.1(b)]. The fourth level $|x\rangle_n$ represents a set of arbitrary excited molecular (e.g. vibrationally or rotationally excited) or free particle states, whose population we want to avoid. The dynamics of the system's density matrix $\hat{\rho}$ is governed by the master equation $\partial_t \hat{\rho} = -\mathrm{i}[\hat{H}, \hat{\rho}] + \mathcal{D}\hat{\rho}$, with $\hat{H} = \hat{H}_{LA} + \hat{H}_C + \hat{H}_0$ the system Hamiltonian and ($\hbar = 1$)

$$\hat{H}_{LA} = \Omega\sqrt{N}\left(\hat{S}_{ie} + \hat{S}_{ei}\right) \tag{5.1}$$

$$\hat{H}_C = g\sqrt{N}\left(\hat{a}^\dagger \hat{S}_{ge} + \hat{S}_{eg}\hat{a}\right). \tag{5.2}$$

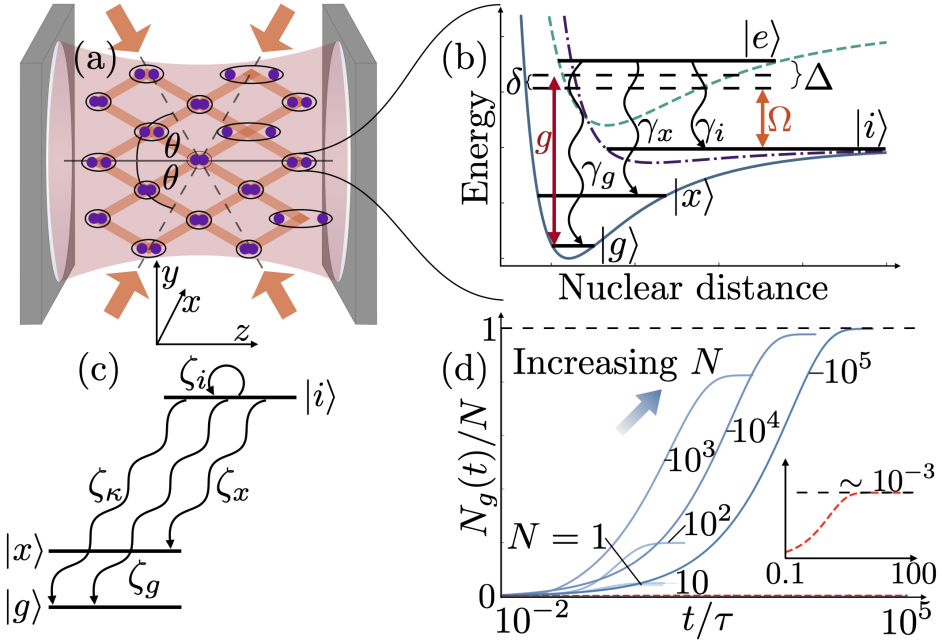


Figure 5.1. – Basic setup for collective dissipative molecule formation. (a) Feshbach molecules are trapped in a lattice inside a cavity and brought into deeply bound states by photoassociation. An angle $\theta$ between the lattice laser beams and the cavity ($z$) axis ensures mode matching. (b) Scheme of energy levels and their coupling for a single molecule. For RbCs the potential energy curves can be identified with the ground state potential $X^1\Sigma^+$ (continuous line; dissociates to $5s + 6s$), triplet ground state potential $a^3\Sigma^+$ (dash-dotted line; dissociates to $5s + 6s$) and excited state potential $(A^1\Sigma^+ - b^3\Pi)0^+$ (dashed line; dissociates to $5s+6p$). A molecule prepared in a Feshbach state $|i\rangle$ is laser excited (coupling strength $\Omega$, detuning $\Delta$) into the excited state $|e\rangle$, which can decay back into $|i\rangle$, the rovibrational ground state $|g\rangle$ or any other state (bound or not), here collectively called $|x\rangle$. (c) Energy levels of a single molecule after adiabatic elimination of the cavity and excited state with decay rates $\zeta_\alpha$ ($\alpha$=$\kappa$, $i$, $x$, $g$). (d) Evolution of the target ground state molecular fraction $N_g/N$ as a function of rescaled time $t$ (see text), for different $1 \leq N \leq 10^5$ (log-scale). The red dashed line in the Inset indicates the results without cavity.

Here, $\hat{H}_{LA}$ and $\hat{H}_C$ represent the coupling of the transition dipole moments of the transitions $|i\rangle_n \leftrightarrow |e\rangle_n$ and $|e\rangle_n \leftrightarrow |g\rangle_n$ to the laser and cavity fields with Rabi frequency $\Omega$ and vacuum Rabi frequency $g$, respectively. $\hat{S}_{\alpha\beta} = \sum_n \hat{\sigma}^{(n)}_{\alpha\beta}/\sqrt{N}$ are collective operators that couple the internal states of each pair $n$ via $\hat{\sigma}^{(n)}_{\alpha,\beta} = |\alpha\rangle\langle\beta|_n$ ($\alpha, \beta = i, e, g, x$). $\hat{H}$ is defined in a rotating frame (see Appendix) with the detunings of the laser and the cavity, $\Delta = \omega_{ie} - \omega_L$ and $\delta = \omega_C - \omega_L - \omega_{gi}$, respectively. These are included in $\hat{H}_0 = \Delta\hat{N}_e + \delta\hat{a}^\dagger\hat{a}$, where $\hat{N}_\alpha = \sum_n \hat{\sigma}^{(n)}_{\alpha\alpha}$ are total state populations, $\hat{a}$ is the cavity photon annihilation operator, and $\omega_L$, $\omega_C$ and $\omega_{\alpha\beta}$ are the frequencies of the laser, the cavity and the transitions, respectively.

Dissipative terms are described by the super-operator

$$\mathcal{D}\hat{\rho} = \mathcal{L}[\hat{L}_\kappa]\hat{\rho} + \sum_{n=1}^{N} \left(\mathcal{L}[\hat{L}^{(n)}_{\gamma_i}] + \mathcal{L}[\hat{L}^{(n)}_{\gamma_x}] + \mathcal{L}[\hat{L}^{(n)}_{\gamma_g}]\right)\hat{\rho} \tag{5.3}$$

with $3N + 1$ decay channels, each governed by a Lindblad term $\mathcal{L}[\hat{L}]\hat{\rho} = -\{\hat{L}^\dagger\hat{L}, \hat{\rho}\} + 2\hat{L}\hat{\rho}\hat{L}^\dagger$. Here we include cavity decay with rate $2\kappa$, $\hat{L}_\kappa = \sqrt{\kappa}\hat{a}$, and spontaneous emission from the excited state $|e\rangle_n$ for each pair $n$, $\hat{L}^{(n)}_{\gamma_\alpha} = \sqrt{\gamma_\alpha}\hat{\sigma}^{(n)}_{\alpha e}$ with rates $2\gamma_\alpha$ for $\alpha = i, g, x$. We define $\Gamma = \sum_\alpha \gamma_\alpha$ and the complex detunings $\tilde{\Delta} = \Delta - \mathrm{i}\Gamma$ and $\tilde{\delta} = \delta - \mathrm{i}\kappa$.

## 5.3. Adiabatic Elimination

In the regime of strong dissipation, both the excited states and the cavity mode are weakly populated $\langle\hat{N}_e + \hat{a}^\dagger\hat{a}\rangle \ll 1$ and can be adiabatically eliminated [24] (see Appendix). Then, the dynamics reduces to an effective master equation for the subsystems $\{|i\rangle_n, |g\rangle_n, |x\rangle_n\}$ [see Fig. 5.1(c)]. We find that the new effective Lindblad operators read

$$\hat{L}^{\kappa}_{\text{eff}} = \sqrt{\lambda_\kappa}\hat{\xi}\hat{S}_{gi} \quad \hat{L}^{\alpha,(n)}_{\text{eff}} = \sqrt{\lambda^\alpha_\gamma}\left(\hat{\sigma}^{(n)}_{\alpha i} - \hat{\sigma}^{(n)}_{\alpha g}\hat{\xi}\hat{S}_{gi}\right) \tag{5.4}$$

The terms $\hat{L}^{\kappa}_{\text{eff}}$ and $\hat{L}^{\alpha,(n)}_{\text{eff}}$ in Eq. (5.4) result from a virtual excitation of the states $|e\rangle_n$ being lost via the cavity or via spontaneous emission, respectively. Here, $\lambda_\kappa = \Omega^2\kappa/g^2$ and $\lambda^\alpha_\gamma = \Omega^2\gamma_\alpha/\tilde{\Delta}^2$ are the respective rates, while $\hat{\xi} = \sqrt{N}g^2(\hat{N}_g g^2 - \tilde{\Delta}\tilde{\delta})^{-1}$ is a collective dimensionless operator stemming from the excited state propagator, which captures the effects of virtually excited superradiant states [in the weak light-matter coupling regime $(N_g + 1)g^2 < (\kappa - \Gamma)^2/4$] or virtually excited polaritons [in the strong coupling regime $(N_g + 1)g^2 > (\kappa - \Gamma)^2/4$]. Thus, Eq. (5.4) gives rise to collective, dissipative, and unidirectional population transfer from the states $|i\rangle_n$ to the desired molecular bound states $|g\rangle_n$ and the loss states $|x\rangle_n$ [see Fig. 5.1(c)], with rates that depend on the many-body state via $\hat{\xi}\hat{S}_{gi}$.

We find a new effective Hamiltonian

$$\hat{H}_{\text{eff}} = -\frac{\Omega^2}{2\tilde{\Delta}}\left(\hat{N}_i + \sqrt{N}\hat{S}_{ig}\hat{\xi}\hat{S}_{gi}\right) + \text{h.c.} \tag{5.5}$$

The first term $-\Omega^2\hat{N}_i/(2\tilde{\Delta})$ in Eq. (5.5) corresponds to the usual AC Stark shift for a small coupling $\Omega$. The second term corresponds to the self energy due to a molecule being virtually excited by the laser and exchanging this excitation with the cavity. Since $[\hat{N}_\alpha, \hat{H}_{\text{eff}}] = 0$, $\hat{H}_{\text{eff}}$ cannot drive any coherent population transfer and thus we find that all interesting dynamics is driven by dissipation. In the following, we simulate the effective equations of motion first on bare resonance $\Delta = \delta = 0$, then on resonance with a (virtual) polariton.

Numerically, the master equation evolution with terms from Eqs. (5.4) and (5.5) can be efficiently simulated by exploiting the permutation symmetry among the $N$ three level systems, which allows for utilizing a collective spin basis [25]. In practice we furthermore employ a quantum trajectory method [25, 26] (see Appendix). In the numerical simulations, the initial state is the product $\bigotimes_n |i\rangle_n$.

For $\Delta = 0$, we choose typical parameters for RbCs as measured in Ref. [27] [see also Fig. 5.1(b) and Appendix]. We consider up to $N = 10^5$ molecules trapped in a three-dimensional optical lattice created by a laser with wavelength $\lambda_{\text{latt}} = 1064.5\,\text{nm}$. Two lattice beams are placed at angles $\pm\theta$ ($\theta = \arccos[\lambda_{\text{latt}}/(2\lambda_{\text{eg}})] = 57°$) with respect to the cavity axis in order to match a desired cavity mode [Fig. 5.1(a) and below]. The excited state has a half linewidth $\Gamma/2\pi = 2.65\,\text{MHz}$. The branching ratios $f_\alpha \equiv \gamma_\alpha/\Gamma$ for the decay from $|e\rangle$ into the states $|x\rangle$, $|g\rangle$, and $|i\rangle$ are $f_x \approx 0.999$, $f_g = 1.3 \times 10^{-3}$, and $f_i = 1.3 \times 10^{-4}$, respectively, such that photoassociation without a cavity leads to a maximal asymptotic value of $(\langle\hat{N}_g\rangle/N)(t \to \infty) \equiv (N_g/N)(t \to \infty) \equiv N_g^\infty/N = f_g/(f_g + f_x) \approx 1.3 \times 10^{-3}$. The photoassociation laser (wavelength of $\lambda_{\text{PA}} = 1557\,\text{nm}$) has a Rabi frequency $\Omega/2\pi = 70\,\text{kHz}$ in the weak coupling regime. We assume a cavity of length $L = 280\,\mu\text{m}$, free spectral range $c/2L = 535\,\text{GHz}$, mode waist $\omega_0 = 12\,\mu\text{m}$, and half linewidth $\kappa/2\pi = 5.4\,\text{MHz}$, which is tuned in resonance with the $\lambda_{\text{eg}} = 977\,\text{nm}$ transition $|e\rangle \leftrightarrow |g\rangle$, resulting in a peak vacuum Rabi frequency $g/2\pi = d_{\text{el}}\sqrt{f_g\omega_{ge}/2\hbar\varepsilon_0 V}/2\pi = 770\,\text{kHz}$ with the mode volume $V = \pi\omega_0^2 L/4$ and the electronic transition dipole moment $d_{\text{el}} = 0.1\,\text{a.u.}$ [27]. We assume the temperature to be small enough so that all molecules are in the lowest lattice band. For a typical lattice depth of $E_0 = 48E_R$ [8], with $E_R = (2\pi\hbar/\lambda_{\text{latt}})^2/(2m_{\text{RbCs}})$ the recoil energy, this implies $T \ll 400\,\text{nK}$, but even for higher temperatures the scheme may be beneficial (see Appendix).

## 5.4. On Bare Resonance

For $\Delta = \delta = 0$, we find $\hat{H}_{\text{eff}} = 0$ and the dynamics is governed by dissipative Lindblad terms *only*, with $\hat{\xi} = \sqrt{N}C(1 + \hat{N}_g C)^{-1}$. Figure 5.1(d) shows exemplary results for the time evolution of the molecular ground state fraction $N_g/N$ as a function of $N$, with $1 \le N \le 10^5$ in units of the characteristic time scale $\tau = \Gamma\Omega^{-2}$. For $N = 1$ the figure shows that the presence of a cavity (here $C \approx 0.04$) induces an enhancement of $N_g^\infty/N$ from $\sim 0.1\,\%$ (no cavity, dashed red line) to $\sim 4\,\%$, due to increased state-selectivity [21]. Strikingly, with increasing $N$, we observe an enhancement towards $N_g^\infty/N \to 1$, at the cost of an increased transfer time. Figure 5.2(a) is a contour plot of the long-time population fraction $N_x^\infty/N$ in the loss state $|x\rangle$ as a function of $N$ and $C$. The plot

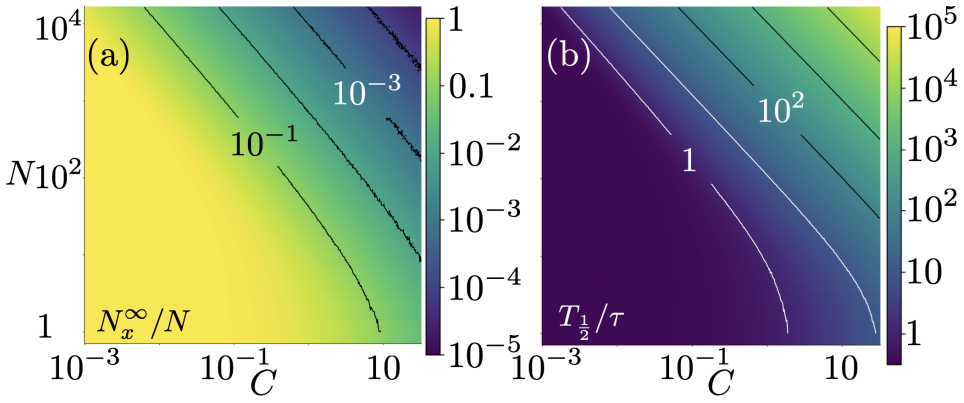


Figure 5.2. – On bare resonance: (a) Contour plot of the final population fraction in the loss state $|x\rangle$, $N_x^\infty/N$, as a function of the number $N$ of molecules in the cavity and the single molecule cooperativity $C$. (b) Contour plot of the time $T_{\frac{1}{2}}$ needed to transfer half of the population away from the state $|i\rangle$ in $\tau = \Gamma\Omega^{-2}$. All axes are logarithmic.

shows that, for increasing collective cooperativity $NC$, $N_x^\infty/N$ rapidly decreases from its bare (no-cavity) value $\sim 1$ towards 0 [upper right corner in Fig. 5.2(a)].

To gain further insight, we obtain an analytical solution of the dynamics in the limit of large collective cooperativity $NC \gg 1$ and large but finite molecule number $N_g \gg 1$. In the quantum trajectories picture, the decay rate of a state $|\psi\rangle$ is given by $\langle\psi| - 2\sum \hat{L}_{\text{eff}}^\dagger \hat{L}_{\text{eff}} |\psi\rangle$. With these assumptions, we can restrict the discussion to the symmetric Dicke states, assume $(N_g{+}1)C \gg 1$, and neglect fluctuations by approximating operators by their expectation values $N_\alpha \equiv \langle \hat{N}_\alpha \rangle$. We then obtain the following rates for the decays via the different channels (see Appendix)

$$2\left\langle \hat{L}_{\text{eff}}^{\kappa\dagger} \hat{L}_{\text{eff}}^{\kappa} \right\rangle \approx \frac{2}{\tau} \frac{N_i}{(N_g+1)C} \equiv \zeta_\kappa \,, \tag{5.6}$$

$$2\sum_n \left\langle \hat{L}_{\text{eff}}^{\alpha,(n)\dagger} \hat{L}_{\text{eff}}^{\alpha,(n)} \right\rangle \approx \frac{2f_\alpha}{\tau} \frac{N_i}{(N_g+1)^2 C^2} \equiv \zeta_\alpha \,. \tag{5.7}$$

For $(N_g+1)C \gg 1$, the cavity-decay dominates, $\zeta_\kappa \gg \zeta_\alpha$. Dynamics is then governed by the non-linear rate equations $\dot{N}_i = -\zeta_x - \zeta_g - \zeta_\kappa$, $\dot{N}_x = \zeta_x$, and $\dot{N}_g = \zeta_g + \zeta_\kappa$, for which we provide analytical solutions in the Appendix for the time-dependence of the populations, $N_\alpha(t)$. For large $N_g^\infty$, we find for the loss state fraction

$$\frac{N_x^\infty}{N} \approx \frac{f_x \ln(N)}{NC} \xrightarrow{NC\to\infty} 0, \tag{5.8}$$

demonstrating a collective improvement over the single molecule result $f_x/(C+1)$ of Ref. [21]. The half time $T_{\frac{1}{2}} = \int_{N_i=N}^{N/2} \mathrm{d}N_i/\dot{N}_i$ for population transfer out of state $|i\rangle$ is

well approximated by

$$T_{\frac{1}{2}} \sim NC\tau. \tag{5.9}$$

This scaling is observed as straight contours for large $NC$ in the numerical simulations of Fig. 5.2(b). The demonstration of increased molecular yield in the ground state due to collective dissipative effects, at the cost of decreased transfer rates, is one of the central results of this work.

## 5.5. Following the Polaritons

We find that the slowdown of $T_{\frac{1}{2}}$ in Eq. (5.9) is due to terms $\propto 1/[(N_g+1)C]$ in Eqs. (5.6) and (5.7), caused by Zeno blocking of the virtually excited superradiant states and detuning from the virtually excited polaritons. The latter usually dominates and is captured by Fig. 5.3(a), which is a contour plot of $\dot{N}_i$ as a function of $N_g$ and $\Delta$, with $\delta = \Delta$. For $\Delta = 0$, the figure shows that $\dot{N}_i$ decreases rapidly with increasing $N_g$. The rate $\dot{N}_i$ is instead maximized for an optimal choice of detuning

$$\Delta^{\pm}_{\text{opt}} = \pm\left[\max\left(0, (N_g+1)g^2 - \frac{\Gamma^2+\kappa^2}{2}\right)\right]^{1/2}. \tag{5.10}$$

This reflects the formation of two polaritons with energy $E^{\pm} \sim \Delta^{\pm}_{\text{opt}}$ for large enough $N_g \geq (\Gamma^2+\kappa^2)/2g^2$. To circumvent the slowdown, we propose to chirp the laser detuning to stay resonant with the polariton energy, which depends on the (time dependent) ground state population $N_g(t)$. This adjustment can be adiabatic since the dynamics of $N_g(t)$ is slow compared to $\Gamma$ $[\mathcal{O}(\Omega^2/\Gamma)]$, and thus it is sufficient to consider a time dependent $\Delta(t)$ and $\delta(t) = \Delta(t)$ in Eqs. (5.4) and (5.5).

For $g \ll \kappa + \Gamma \ll \sqrt{N_g+1}g$, the decay rates of the different channels assume the simple form (see Appendix) [1]

$$2\left\langle \hat{L}^{\kappa\dagger}_{\text{eff}} \hat{L}^{\kappa}_{\text{eff}} \right\rangle \approx \frac{2\Omega^2\kappa}{(\kappa+\Gamma)^2} N_i \equiv \zeta_\kappa \tag{5.11}$$

$$2\sum_n \left\langle \hat{L}^{\alpha,(n)\dagger}_{\text{eff}} \hat{L}^{\alpha,(n)}_{\text{eff}} \right\rangle \approx \frac{2\Omega^2\gamma_\alpha}{(\kappa+\Gamma)^2} N_i \equiv \zeta_\alpha. \tag{5.12}$$

and the rate equations $\dot{N}_{i,g,x}$ above are solved as

$$\frac{N_i(t)}{N} = \exp\left[-\frac{2\Omega^2(\kappa+\gamma_g+\gamma_x)t}{(\kappa+\Gamma)^2}\right] \tag{5.13}$$

$$\frac{N_g(t)}{N} = \frac{\kappa+\gamma_g}{\kappa+\gamma_g+\gamma_x}\left\{1 - \exp\left[-\frac{2\Omega^2(\kappa+\gamma_g+\gamma_x)t}{(\kappa+\Gamma)^2}\right]\right\}. \tag{5.14}$$

1. We note that the inequality $g \ll \kappa+\Gamma$ ensures that staying in resonance with the polariton is possible, as for $g \gtrsim \kappa+\Gamma$ this is prevented by fluctuations of $N_g$. For small $N_g$ we have $\kappa+\Gamma \gtrsim \sqrt{N_g+1}g$ and no polariton splitting is present.

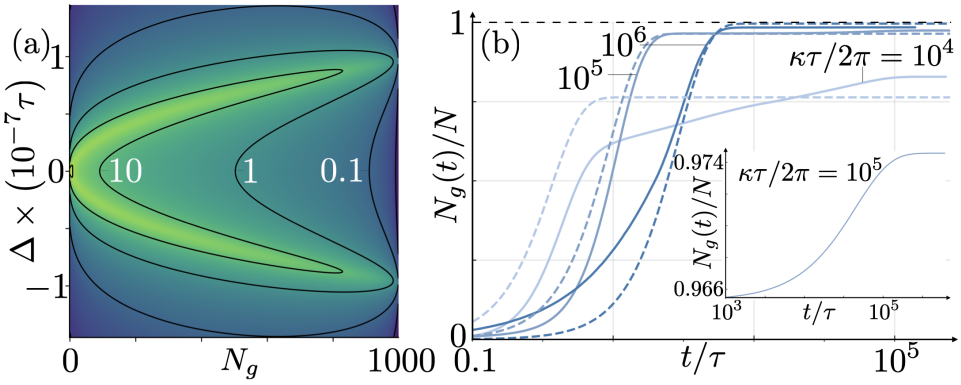


Figure 5.3. – Chirped pulse: (a) Contour plot of the decay rate of Feshbach molecules $\dot{N}_i$ (in units $\tau^{-1}$, for symmetric Dicke states), as a function of the laser detuning and the number of ground state molecules. The cavity is kept at resonance with the transition energy ($\delta = \Delta$). (b) Simulated time evolution of the ground state population for different cavity decay rates $\kappa$. The parameters are chosen for $10^3$ $Rb_2$ molecules inside a cavity [14, 21], i. e. $\Gamma/2\pi = 6\,\mathrm{MHz}$ and $g/2\pi \approx 50\,\mathrm{MHz}$. Dashed lines: analytical fits of Eqs. (5.13) and (5.14).

These results are formally similar to those of Ref. [22] for a single molecule coupled to a photon wave-guide, however, here the cavity decay rate $\kappa$ is fully tuneable. We note that while collective effects are present in the polariton formation, the final rate is independent of $N$ [2]. For $\kappa \gg \gamma_x$, the ground state population approaches $N$ as $N_g^\infty/N \simeq 1 - \gamma_x/\kappa$, at the cost of an increasing time-scale $\sim \kappa/\Omega^2$, due to the continuous Zeno effect [28].

Figure 5.3(b) shows a comparison of numerical and analytical results (continuous and dashed lines, respectively) for the increase of $N_g/N$ as a function of time $t$, for different values of $\kappa$. We find good agreement for large values of $t/\tau$ and $\kappa\tau$ in the regime of validity of Eqs. (5.13) and (5.14), as expected. In addition to this dynamics, a few molecules are trapped in so-called "dark states" $|d\rangle$ that cannot decay via the cavity ($\hat{L}_{\mathrm{eff}}^{\kappa}|d\rangle = 0$). This minor effect is caused by the breaking of permutation symmetry through spontaneous emission [29, 30] (see also Appendix), and responsible for a time delay in reaching the asymptotic $N_g^\infty$, as magnified in the inset of Fig. 5.3(b).

## 5.6. Experimental Considerations

Whether higher molecular yields are reached by staying on bare resonance or chirping the laser depends on what limits state selectivity. If transfer times are not a concern, staying on bare resonance is usually best, as we estimate $N_x^\infty(\mathrm{chirp}) > N_x^\infty(\mathrm{bare})$ for $Ng^2/[\kappa^2 \ln(N)] > 1$ (see Appendix). If instead transfer times are a concern, due, e.g., to background gas collisions, then the chirped scheme may be better, as for a given

2. This is in contrast to the scheme of Ref. [22], for which collective effects decrease the efficiency due to dark state population caused by individual laser excitations.

$T_{\frac{1}{2}}$ we find $N_x^{\infty}(\text{bare}) \sim \ln(N) N_x^{\infty}(\text{chirp})$ (see Appendix). These behaviors, derived for identical cavity coupling strengths $g_n$, hold also approximately for moderately varying $g_n$ due to, e.g, in-homogeneity of the cavity mode, lattice geometry or thermal motion (see Appendix).

For $N = 10^4$ RbCs Feshbach molecules (see parameters above), the system is closer to the first scenario and we find that staying on bare resonance ($\Delta = 0$) provides the highest yield. For a reasonable lattice lifetime of 1 s, we obtain a peak ground state population $N_g/N \approx 92\,\%$ after 55 ms with a transfer half time $T_{\frac{1}{2}} \approx 3.2$ ms (98 % for infinite lattice lifetime). These results are essentially unchanged by considering locally different coupling constants $g_n = g(\vec{x}_n) = g \exp[-(x_n^2 + y_n^2)/\omega_0^2] \cos(2\pi z_n/\lambda_{\text{eg}})$, due to the finite cavity mode waist $\omega_0$ and the different lattice positions, with $z_n$ ($x_n$, $y_n$) oriented along the cavity axis (in the perpendicular planes) [see Fig. 5.1(a)]. For example, for a $20 \times 20 \times 25$ lattice at angle $\theta = 57°$ and assuming perfect matching of lattice and cavity modes with $\cos(2\pi z_n/\lambda_{\text{eg}}) = 1$ [3], we find a peak $N_g/N \sim 92\,\%$, a transfer time 48 ms and $T_{\frac{1}{2}} \sim 2.7$ ms, with infinite lattice lifetime final fraction 97 %. Thus, ground state populations comparable to STIRAP ($\sim 90\,\%$) [8, 9] can be achieved without the need of time-dependent laser pulses. These results are robust against reasonable lattice mismatches. Even in a worst case scenario of complete positional disorder [i.e., uniform and Gaussian ($\sigma_{xy} = 5\,\mu$m) distributions in the $z$ and $x - y$ directions, respectively] we find a peak $N_g/N \sim 71\,\%$ (73 % for infinite lattice lifetime) after 21 ms and $T_{\frac{1}{2}} \sim 0.4$ ms.

For a scenario with $10^3$ $Rb_2$ Feshbach molecules (see Fig. 5.3, parameters as in Ref. [14, 21]) we are in the regime where the chirped pulse results in a higher yield. For example, choosing a vacuum Rabi frequency $g/2\pi \approx 50$ MHz, a laser Rabi frequency $\Omega/2\pi = 200$ kHz, and a cavity half linewidth $\kappa/2\pi = 300$ MHz, we obtain a ground state population of $N_g/N \approx 98\,\%$ after 5 ms ($T_{\frac{1}{2}} \sim 0.5$ ms). Even for a spatially disordered worst case scenario (uniform position distribution along $z$, $\sigma_{xy} = 2.5\,\mu$m, mode waist of 5 µm), we reach a ground state fraction of 89 % after 5 ms ($T_{\frac{1}{2}} \sim 0.3$ ms). In both cases this is a significant increase from 54 % without cavity, and can overcome typical STIRAP efficiencies [9].

Similar to STIRAP [8, 23], the presence of additional excited states in proximity to the $|e\rangle$ state might decrease the transfer efficiency of our schemes. This can be avoided by choosing an excited state with sufficiently large hyperfine and Zeeman splitting [8]. Once the rovibrational ground state is reached, population transfer between the hyperfine sublevels can be achieved with high fidelity [31].

## 5.7. Conclusion

In summary, we proposed two novel methods for high-yield state selective preparation of ultracold molecules in a cavity that exploit collective and dissipative effects. It is an exciting prospect to investigate how similar collective effects could be used to

3. Lattice positions are defined as $x_n = (m + 1/2)\lambda_{\text{latt}}/2$, and $y_n = (m' + 1/2)\Delta y$ with $\Delta y = \lambda_{\text{latt}}/[4\sin(\theta)] \approx 317$ nm, with $-10 \leq (m, m') < 10$ integers.

engineer generic state-transfer schemes and even chemical reactions outside of the ultracold regime [32–36], such as room-temperature cavity-modified electron transfer reactions [37, 38]. The experimental setups proposed here – molecules trapped on a lattice potential and embedded in a cavity – offer unique opportunities to explore collective dynamics for measurements [39], non-equilibrium quantum phase transitions [40, 41], or quantum information applications using long-lived molecular states [42] and cavity-controlled gates [43, 44], while also allowing for a non-destructive detection of the molecules [45, 46].

## Acknowledgements

We thank Claudiu Genes for helpful discussions. This work is supported by ANR 5 "ERA-NET QuantERA" - Projet "RouTe" (ANR-18-QUAN-0005-01), LabEx ("Nanostructures in Interaction with their Environment," NIE) under contract ANR-11-LABX-0058 NIE within the Investissement d'Avenir program ANR-10-IDEX-0002-02, and IdEx Unistra project STEMQuS. D. W. acknowledges financial support from Agence Nationale de la Recherche (Grant ANR-17-EURE-0024 EUR QMat). G. P. acknowledges support from the Institut Universitaire de France (IUF) and the University of Strasbourg Institute of Advanced Studies (USIAS).

# Appendix

In Sec. 5.A we define the rotating frame. In Sec. 5.B, we give details for the adiabatic elimination. In Sec. 5.C, we discuss how the permutation symmetry can be used for an efficient simulation and display the resulting equations that are used for the simulation. In Sec. 5.D we give the states used for the RbCs simulations. In Sec. 5.E we derive the rate equations on bare resonance, and their solution is presented in Sec. 5.F. The rate equations on polariton resonance and the function to match the polariton resonance are provided in Sec. 5.G. In Sec. 5.H we give some details on the dark states. In Sec. 5.I we compare the schemes on bare resonance and on polariton resonance, and in Sec. 5.J we display the threshold and effective cooperativity used to describe the local cavity coupling constants. In Sec. 5.K we discuss the effects of finite temperature.

## 5.A. Rotating Frame

Setting the initial state energy to zero, the full Hamiltonian reads in a non-rotating frame of reference

$$\begin{aligned}\hat{H} = &\sum_n \omega_{ie}\hat{\sigma}_{ee}^{(n)} + \omega_{ix}\hat{\sigma}_{xx}^{(n)} - \omega_{gi}\hat{\sigma}_{gg}^{(n)} + \omega_C\hat{a}^\dagger\hat{a} \\ &+ \Omega\Big\{\hat{\sigma}_{ie}^{(n)}\exp\Big[\mathrm{i}(\omega_L t - \vec{k}\vec{x}_n)\Big] + \mathrm{h.c.}\Big\} + g(\hat{\sigma}_{ge}^{(n)}\hat{a}^\dagger + \mathrm{h.c.})\end{aligned} \tag{5.15}$$

We arrive at the given Hamiltonian by applying the unitary transform

$$\mathcal{U} = \exp\left[\mathrm{i}\left(\sum_n \omega_L t\hat{\sigma}_{ee}^{(n)} + \omega_{ix}t\hat{\sigma}_{xx}^{(n)} - \omega_{gi}t\hat{\sigma}_{gg}^{(n)} + (\omega_L+\omega_{gi})t\hat{a}^\dagger\hat{a} + \vec{k}\vec{x}_n\hat{\sigma}_{ee}^{(n)}\right)\right] \tag{5.16}$$

according to the rules

$$\hat{H} \to \hat{H}' = \mathcal{U}\hat{H}\mathcal{U}^\dagger + \mathrm{i}(\partial_t\mathcal{U})\mathcal{U}^\dagger \tag{5.17}$$

$$|\psi\rangle \to |\psi'\rangle = \mathcal{U}|\psi\rangle \tag{5.18}$$

$$\hat{O} \to \hat{O}' = \mathcal{U}\hat{O}\mathcal{U}^\dagger \tag{5.19}$$

with $\hat{O}$ an arbitrary observable. In the paper the further definitions $\Delta = \omega_{ie} - \omega_L$ and $\delta = \omega_C - \omega_L - \omega_{gi}$ were used.

## 5.B. Adiabatic Elimination

In order to adiabatically eliminate the cavity and the excited states, we follow the formalism of *Reiter and Sørensen* [24]. First, we split the system into an excited state manifold with fast dynamics and a ground state manifold with slow dynamics, both of which are weakly coupled. We define the ground state manifold by $\hat{N}_e + \hat{a}^\dagger\hat{a} = 0$, so that there are neither molecular excitations nor photons. The excited state manifold contains

all remaining states ($\hat{N}_e + \hat{a}^\dagger\hat{a} \geq 1$), but as we use the interaction as a perturbation, it is sufficient to restrict the analysis to the single excitation limit $\hat{N}_e + \hat{a}^\dagger\hat{a} = 1$. The condition for the adiabatic elimination to be valid is that the interaction is much slower than the excited state dynamics, e. g. because $\sqrt{N}\Omega \ll \Gamma$ or $\sqrt{N}\Omega \ll \sqrt{N_g}g$. Following the notation of *Reiter and Sørensen*, we arrive at:

$$\begin{aligned}\hat{H}_e &= \hat{H}_0 + \hat{H}_C \\ &= \Delta\hat{N}_e + \delta\hat{a}^\dagger\hat{a} + g\sqrt{N}\left(\hat{a}^\dagger\hat{S}_{ge} + \hat{S}_{eg}\hat{a}\right) \qquad (5.20)\\ \hat{H}_g &= 0 \qquad (5.21)\\ \hat{V}^+ &= \sqrt{N}\Omega\hat{S}_{ei} \qquad (5.22)\\ \hat{V}^- &= \sqrt{N}\Omega\hat{S}_{ie} \qquad (5.23)\end{aligned}$$

The Lindblad operators $\hat{L}_k$ are defined in the main paper.

Next, we calculate the non-hermitian Hamiltonian $\hat{H}_{\mathrm{NH}} \equiv \hat{H}_e - \mathrm{i}\sum \hat{L}_k^\dagger\hat{L}_k$. Note that the factor 2 compared to *Reiter and Sørensen* [24] arises due to a different definition of the Lindblad operators:

$$\hat{H}_{\mathrm{NH}} = \tilde{\Delta}\hat{N}_e + \tilde{\delta}\hat{a}^\dagger\hat{a} + g\sqrt{N}\left(\hat{a}^\dagger\hat{S}_{ge} + \hat{S}_{eg}\hat{a}\right) \qquad (5.24)$$

with $\tilde{\Delta} \equiv \Delta - \mathrm{i}\Gamma$ and $\tilde{\delta} \equiv \delta - \mathrm{i}\kappa$. In the single excitation limit $\hat{H}_{\mathrm{NH}}$ can be inverted. It is straightforward to confirm that:

$$\begin{aligned}\hat{H}_{\mathrm{NH}}^{-1} = &\left[\tilde{\Delta}^2\tilde{\delta} - \tilde{\Delta}(\hat{N}_g + \hat{N}_e)g^2\right]^{-1}\times \\ &\left\{\tilde{\Delta}^2\hat{a}^\dagger\hat{a} - g\sqrt{N}\tilde{\Delta}\left(\hat{S}_{eg}\hat{a} + \hat{S}_{ge}\hat{a}^\dagger\right) + \left[\tilde{\Delta}\tilde{\delta} - \left(\hat{N}_g + 1\right)g^2\right]\hat{N}_e + Ng^2\hat{S}_{eg}\hat{S}_{ge}\right\} \qquad (5.25)\end{aligned}$$

The effective operators are now given by:

$$\begin{aligned}\hat{H}_{\mathrm{eff}} &= -\frac{1}{2}\hat{V}^-\left[\hat{H}_{\mathrm{NH}}^{-1} + \left(\hat{H}_{\mathrm{NH}}^{-1}\right)^\dagger\right]\hat{V}^+ + \hat{H}_g \qquad (5.26)\\ \hat{L}_{\mathrm{eff}}^k &= \hat{L}_k\hat{H}_{\mathrm{NH}}^{-1}\hat{V}^+ \qquad (5.27)\end{aligned}$$

We find:

$$\begin{aligned}\hat{H}_{\mathrm{eff}} &= -\frac{\Omega^2}{2\tilde{\Delta}}\left(\hat{N}_i + \sqrt{N}\hat{S}_{ig}\hat{\xi}\hat{S}_{gi}\right) + \mathrm{h.c.} \qquad (5.28)\\ \hat{L}_{\mathrm{eff}}^{\kappa} &= \frac{\Omega\sqrt{\kappa}}{g}\hat{\xi}\hat{S}_{gi} \qquad (5.29)\\ \hat{L}_{\mathrm{eff}}^{\alpha,(n)} &= \frac{\Omega\sqrt{\gamma_\alpha}}{\tilde{\Delta}}\left(\hat{\sigma}_{\alpha i}^{(n)} - \hat{\sigma}_{\alpha g}^{(n)}\hat{\xi}\hat{S}_{gi}\right) \qquad (5.30)\end{aligned}$$

with $\hat{\xi} = \sqrt{N}g^2\left(\hat{N}_g g^2 - \tilde{\Delta}\tilde{\delta}\right)^{-1}$.

The adiabatic elimination as discussed above is valid in the single excitation limit, which can be assumed if $\langle \hat{N}_e + \hat{a}^\dagger \hat{a} \rangle \ll 1$. The number of excitation $\langle \hat{N}_e + \hat{a}^\dagger \hat{a} \rangle$ can be estimated by comparing the pumping rate $\sqrt{N_i}\Omega$ to the total excitation decay $\Gamma_{\text{tot}}$ and the total detuning $\Delta_{\text{tot}}$:

$$\langle \hat{N}_e + \hat{a}^\dagger \hat{a} \rangle \approx \frac{N_i \Omega^2}{\Gamma_{\text{tot}}^2 + \Delta_{\text{tot}}^2} \overset{!}{\ll} 1 \,. \tag{5.31}$$

We first consider the scheme on bare resonance. The short times dynamics is best described in terms of bare excitons so that $N_i \approx N$, $\Gamma_{\text{tot}} = \Gamma$, and $\Delta_{\text{tot}} = 0$. In this case we can rewrite Eq. (5.31) to find $N \overset{!}{\ll} \Gamma^2/\Omega^2 \approx 1400$ for the RbCs parameters. In contrast, the long time dynamics is best described by polaritons and dark states. As the latter are populated only very slowly, we restrict the analysis of the long time dynamics to polaritons. We find $\Gamma_{\text{tot}} = (\kappa + \Gamma)/2$ and $\Delta_{\text{tot}}^2 = N_g g^2 - (\Gamma - \kappa)^2/2$. For $g \gg \Gamma + \kappa$ and $N_g > 0$ the condition Eq. (5.31) simplifies to $N_g/N \ll g^2/\Omega^2 \approx 8 \times 10^{-3}$. We conclude for the RbCs parameters in the paper, although the initial dynamics is not described correctly by adiabatic elimination, after a population fraction of around 1 % is transferred to the ground state, the adiabatic elimination is valid.

Using the chirped pulse the initial dynamics is still described by bare excitons as above and we find $N \overset{!}{\ll} \Gamma^2/\Omega^2 \approx 1000$ for the $Rb_2$ parameters. For later times, again ignoring dark states, we find $\Gamma_{\text{tot}} = (\kappa + \Gamma)/2$ and $\Delta_{\text{tot}}^2 = 0$. This leads to the condition $(\kappa^2/2 + \Gamma^2/2)/\Omega^2 \approx 1.4 \times 10^5 \overset{!}{\gg} N$. Thus for the $Rb_2$, the initial dynamics is not fully captured by the adiabatic elimination, but as soon as polaritons form, which happens after a short time, the elimination condition is clearly fulfilled.

Note that for the theoretical part of the paper the results are fully independent of the choice of $\Omega$, which only enters into the definition of $\tau$. Hence, for the theory the adiabatic elimination condition is fulfilled if $\Omega$ is kept small enough to fulfill condition Eq. (5.31).

## 5.C. Numerical Simulations

In order to develop an efficient algorithm, we use two steps: In a first step we go from $N$ three level molecules (with states $|i\rangle$, $|g\rangle$, and $|x\rangle$) to two level molecules (with states $|i\rangle$ and $|g\rangle$) with variable molecule number. In a second step we take advantage of the permutation symmetry of the system to reduce $N$ spin-1/2 (two level) systems (dimension $\sim 2^N$) to one spin-$N/2$ system (dimension $\sim N^2$) [25, 47–51]. Note that both steps are exact.

For the first step we use that molecules that enter state $|x\rangle$ have no coherence with the rest of the system (decay only via local dissipation) and have no influence on the dynamics of the system. This allows us to treat decay into state $|x\rangle$ as molecule loss and we only need to treat the dynamics of the remaining two level systems.

In order to simulate $N$ identical two level systems with particle loss, we employ a quantum trajectories algorithm analogous to the one used by *Zhang et al.* [25]. We

| Term | Value |
|---|---|
| $-\mathrm{i}\left[\hat{H}_{\mathrm{eff}}, \overline{\lvert N,J,M\rangle\langle N,J,M\rvert}\right]$ | $0$ |
| $-\left\{\sum_k \hat{L}^{k\dagger}_{\mathrm{eff}} L^{k}_{\mathrm{eff}}, \overline{\lvert N,J,M\rangle\langle N,J,M\rvert}\right\}$ | $-\frac{2\Omega^2\kappa}{g^2}\overline{\lvert N,J,M\rangle\langle N,J,M\rvert}(J+M)(J-M+1)\lvert\xi\rvert^2$<br>$-\frac{2\Omega^2\Gamma}{\lvert\tilde{\Delta}\rvert^2}\overline{\lvert N,J,M\rangle\langle N,J,M\rvert}$<br>$\times\left[\frac{N}{2}+M-2(J+M)(J-M+1)\,\mathrm{Re}\,(\xi)+(J+M)(J-M+1)\left(\frac{N}{2}-M+1\right)\lvert\xi\rvert^2\right]$ |
| $\hat{L}^{\kappa}_{\mathrm{eff}}\overline{\lvert N,J,M\rangle\langle N,J,M\rvert}\hat{L}^{\kappa\dagger}_{\mathrm{eff}}$ | $\frac{\Omega^2\kappa}{g^2}\overline{\lvert N,J,M-1\rangle\langle N,J,M-1\rvert}(J+M)(J-M+1)\lvert\xi\rvert^2$ |
| $\sum_n \hat{L}^{i,(n)}_{\mathrm{eff}}\overline{\lvert N,J,M\rangle\langle N,J,M\rvert}\hat{L}^{i,(n)\dagger}_{\mathrm{eff}}$ | $\frac{\Omega^2\gamma_i}{\lvert\tilde{\Delta}\rvert^2}\overline{\lvert N,J-1,M\rangle\langle N,J-1,M\rvert}\beta^J_N(J-M)$<br>$+\frac{\Omega^2\gamma_i}{\lvert\tilde{\Delta}\rvert^2}\overline{\lvert N,J,M\rangle\langle N,J,M\rvert}\left[\frac{N}{4}+M-(J+M)(J-M+1)\,\mathrm{Re}\,(\xi)\right]$<br>$+\frac{\Omega^2\gamma_i}{\lvert\tilde{\Delta}\rvert^2}\overline{\lvert N,J,M\rangle\langle N,J,M\rvert}\alpha^J_N\lvert M-(J+M)(J-M+1)\xi\rvert^2$<br>$+\frac{\Omega^2\gamma_i}{\lvert\tilde{\Delta}\rvert^2}\overline{\lvert N,J+1,M\rangle\langle N,J+1,M\rvert}\delta^J_N(J+M+1)$ |
| $\sum_n \hat{L}^{g,(n)}_{\mathrm{eff}}\overline{\lvert N,J,M\rangle\langle N,J,M\rvert}\hat{L}^{g,(n)\dagger}_{\mathrm{eff}}$ | $\frac{\Omega^2\gamma_g}{\lvert\tilde{\Delta}\rvert^2}\overline{\lvert N,J-1,M-1\rangle\langle N,J-1,M-1\rvert}\beta^J_N(J+M-1)$<br>$+\frac{\Omega^2\gamma_g}{\lvert\tilde{\Delta}\rvert^2}\overline{\lvert N,J,M-1\rangle\langle N,J,M-1\rvert}(J+M)(J-M+1)\left[-\,\mathrm{Re}\,(\xi)+\frac{1}{4}\lvert\xi\rvert^2\right]$<br>$+\frac{\Omega^2\gamma_g}{\lvert\tilde{\Delta}\rvert^2}\overline{\lvert N,J,M-1\rangle\langle N,J,M-1\rvert}\alpha^J_N(J+M)(J-M+1)\lvert1+(M-1)\xi\rvert^2$<br>$+\frac{\Omega^2\gamma_g}{\lvert\tilde{\Delta}\rvert^2}\overline{\lvert N,J+1,M-1\rangle\langle N,J+1,M-1\rvert}\delta^J_N(J-M+2)$ |
| $\sum_n \hat{L}^{x,(n)}_{\mathrm{eff}}\overline{\lvert N,J,M\rangle\langle N,J,M\rvert}\hat{L}^{x,(n)\dagger}_{\mathrm{eff}}$ | $\frac{\Omega^2\gamma_x}{\lvert\tilde{\Delta}\rvert^2}\overline{\left\lvert N-1,J-\frac{1}{2},M-\frac{1}{2}\right\rangle\left\langle N-1,J-\frac{1}{2},M-\frac{1}{2}\right\rvert}4J\beta^J_N$<br>$+\frac{\Omega^2\gamma_x}{\lvert\tilde{\Delta}\rvert^2}\overline{\left\lvert N-1,J+\frac{1}{2},M-\frac{1}{2}\right\rangle\left\langle N-1,J+\frac{1}{2},M-\frac{1}{2}\right\rvert}4(J+1)\delta^J_N$ |

Table 5.1. – Different contributions to the time evolution of density matrix element $\overline{|N,J,M\rangle\langle N,J,M|}$. Notation: $\xi = g^2/[(N/2-M+1)g^2-\tilde{\Delta}\tilde{\delta}]$ (a factor of $\sqrt{N}$ different from the operator $\hat{\xi}$). $\alpha^J_N = (N+2)/(4J(J+1))$, $\beta^J_N = (N+2J+2)(J+M)|1-(J-M+1)\xi|^2/(4J(2J+1))$, $\delta^J_N = (N-2J)(J-M+1)|1+(J+M)\xi|^2/[4(J+1)(2J+1)]$.

describe the dynamics of the two level systems in the Dicke basis $|J,M\rangle$ [47], while keeping track of the molecule number $N$ [25]. The result are equations for a matrix of the form $\overline{|N,J,M\rangle\langle N,J,M'|}$. The contributions to the equations of motion for the diagonal matrix elements $\overline{|N,J,M\rangle\langle N,J,M|}$ are given in Tab. 5.1.

As there are no off-diagonal elements generated in the equations in Tab. 5.1 and the initial state is given by the diagonal element $\overline{|N,N/2,N/2\rangle\langle N,N/2,N/2|}$, the diagonal elements are sufficient to describe the system dynamics. This motivates the description using a quantum trajectory algorithm, which becomes a simple Monte Carlo Markov chain of jumps between the matrix elements, due to the trivial Hamiltonian contribution.

## 5.D. Molecular States

We choose the states proposed in Ref. [27] for STIRAP association of ultracold molecules. The initial state $|i\rangle$ is given by a Feshbach molecule in the sixth vibrational level below dissociation threshold, characterized by the atomic quantum numbers $f_{\mathrm{Rb}} = 2$; $m_{f_{\mathrm{Rb}}} = 2$; $f_{\mathrm{Cs}} = 4$; $m_{f_{\mathrm{Cs}}} = 2$; $m_f = 4$, and the quantum numbers for the atomic motion $l = 2$; $m_l = 0$, which couple to $M_F = 4$. For the excited state we choose $|e\rangle = (A^1\Sigma^+ - b^3\Pi)0^+$ ($v' = 38$), which has favorable transition dipole moments to both

the initial Feshbach molecule and to the absolute ground state $|g\rangle = X^1\Sigma^+\,(v=0)$.

## 5.E. Derivation of Rate Equations

In order to consider the effects of the different decay channels, we need to separate the decay rates given in the second row of Tab. 5.1 into the different decay channels. For no detuning $\Delta = \delta = 0$, this yields:

$$\begin{aligned}
&-\left\{\hat{L}_{\text{eff}}^{\kappa\dagger}L_{\text{eff}}^{\kappa}, \overline{|N,J,M\rangle\langle N,J,M|}\right\} \\
&\quad = -\frac{2\Omega^2}{C\Gamma}\frac{(J+M)(J-M+1)}{\left(\frac{N}{2}-M+1+\frac{1}{C}\right)^2}\overline{|N,J,M\rangle\langle N,J,M|} \qquad (5.32)\\
&-\left\{\sum_n \hat{L}_{\text{eff}}^{\alpha,(n)\dagger}L_{\text{eff}}^{\alpha,(n)}, \overline{|N,J,M\rangle\langle N,J,M|}\right\} \\
&\quad = -\frac{2\Omega^2\gamma_\alpha}{\Gamma^2}\overline{|N,J,M\rangle\langle N,J,M|}\times \\
&\qquad \left[\frac{N}{2}+M-2\frac{(J+M)(J-M+1)}{\frac{N}{2}-M+1+\frac{1}{C}}+\frac{(J+M)(J-M+1)\left(\frac{N}{2}-M+1\right)}{\left(\frac{N}{2}-M+1+\frac{1}{C}\right)^2}\right] \qquad (5.33)
\end{aligned}$$

where $\alpha = i, g, x$.

To simplify these equations, we make two assumptions: (i) We assume that the dynamics is taking place in the completely symmetric state, for which $J = N/2$, and (ii) we assume $N_g C \gg 1$. The first assumption is justified further below. The second assumption is justified for large collective cooperativity $NC$ and not too small $C$ (e. g. $C \sim 10^{-3}$ is fine for $N \sim 10^5$, but not thermodynamic limit with $N \to \infty$ and $C \to 0$). In this way, only the initial dynamics with $N_g \ll N$ is ignored, which we empirically find to be a good approximation. Using $N_g = N/2 - M$ and $N_i = N/2 + M$, we simplify:

$$\begin{aligned}
&-\left\{\hat{L}_{\text{eff}}^{\kappa\dagger}\hat{L}_{\text{eff}}^{\kappa}, \overline{|N,J,M\rangle\langle N,J,M|}\right\} \\
&\quad \overset{(i)}{\approx} -\frac{2\Omega^2}{C\Gamma}\frac{N_i(N_g+1)}{\left(N_g+1+\frac{1}{C}\right)^2} \\
&\quad \overset{(ii)}{\approx} -\frac{2\Omega^2}{\Gamma}\frac{N_i}{(N_g+1)C} \qquad (5.34)\\
&-\left\{\sum_n \hat{L}_{\text{eff}}^{\alpha,(n)\dagger}\hat{L}_{\text{eff}}^{\alpha,(n)}, \overline{|N,J,M\rangle\langle N,J,M|}\right\} \\
&\quad \overset{(i)}{\approx} -\frac{2\Omega^2\gamma_\alpha}{\Gamma^2}\left[N_i - 2\frac{N_i(N_g+1)}{N_g+1+\frac{1}{C}}+\frac{N_i(N_g+1)(N_g+1)}{\left(N_g+1+\frac{1}{C}\right)^2}\right] \\
&\quad \overset{(ii)}{\approx} \frac{2\Omega^2\gamma_\alpha}{\Gamma^2}\frac{N_i}{(N_g+1)^2C^2}\,. \qquad (5.35)
\end{aligned}$$

Now we can justify assumption (i): For $N_g C \gg 1$ the cavity decay channel is dominant, for which $J$ does not change. As $J = N/2$ for the initial state, we can thus expect $J$ to remain close to this value. In fact, the dominant spontaneous emission rate $\gamma_x$ can only decrease $N - 2J$, pushing the system back into the superradiant state $J = N/2$ if it moves out of that state during the initial dynamics. This corresponds to the results of numerical simulation, where initially $N - 2J$ grows, but then quickly decays back towards zero.

Note that the Eqs. (5.34) to (5.35) are still state dependent. In order to get rate equations we need to take the expectation value of the right hand side. For $N \gg 1$, the fluctuations of the particle numbers $N_i$ and $N_g$ around their mean values are typically small compared to their expectation values. Therefore, the expectation values of the right hand side are well approximated by taking the expectation value of $N_g$ directly in the denominator, recovering the rate equations given in the paper. Note that by comparing simulations of the rate equations to simulations of the full master equation, we find that up to a prefactor for the loss state population $N_x$ they give a good approximation to the dynamics.

## 5.F. Solution of Rate Equations

For large $N_g C$, we note that $N_x \ll N$, as $\dot{N}_x \ll \dot{N}_g$. Thus, to first order $N_g = N - N_i$. For large $N$, we can thus write down a differential equation for the initial state population:

$$\dot{n}_i \equiv \dot{N}_i/N \approx -\frac{2}{NC\tau}\frac{n_i}{1-n_i} \tag{5.36}$$

with $\tau = \Gamma/\Omega^2$ This equation can be integrated to find for the time $T$ to reach a population fraction $n_i$ in the initial state:

$$T(n_i) = \int_1^{n_i} \frac{\mathrm{d}n_i'}{\dot{n}_i'} = \frac{NC\tau}{2}\ln\left(\frac{e^{n_i-1}}{n_i}\right) \tag{5.37}$$

or inverted to get the time evolution of $n_i$

$$n_i(t) = -W\left[-\exp\left(-1-\frac{2t}{NC\tau}\right)\right] \tag{5.38}$$

where $W(x)$ is the product logarithm or Lambert $W$ function, which is defined as the inverse of $x = we^w$.

## 5.G. Rate Equations with Detuning

In order to compute rate equations for the chirped pulse, we replace $\Delta = \delta = \Delta_{\mathrm{opt}}$ with

$$\Delta_{\mathrm{opt}} = \left\{\max\left[0, (N_g+1)g^2 - \frac{\Gamma^2+\kappa^2}{2}\right]\right\}^{1/2}. \tag{5.39}$$

If we assume $(N_g+1)g^2 > (\kappa^2+\Gamma^2)/2$, the cavity decay dominates and we can restrict the analysis to the completely symmetric Dicke state, for which one can replace $\hat{S}_{ig}\hat{S}_{gi} = \hat{N}_i(\hat{N}_g+1)/N$. This leads to:

$$\begin{aligned}
\hat{L}_{\text{eff}}^{\kappa\dagger}\hat{L}_{\text{eff}}^{\kappa} &= \Omega^2 g^2 \kappa \frac{\hat{N}_i\Big(\hat{N}_g+1\Big)}{\Big[\Big(\hat{N}_g-N_g\Big)g^2-\frac{(\kappa-\Gamma)^2}{2}\Big]^2+(\kappa+\Gamma)^2\big[(N_g+1)g^2-\frac{\Gamma^2+\kappa^2}{2}\big]} \\
&\approx \frac{\Omega^2\kappa}{(\Gamma+\kappa)^2}\hat{N}_i \qquad (5.40)\\
\hat{L}_{\text{eff}}^{\alpha\dagger}\hat{L}_{\text{eff}}^{\alpha} &= \frac{\Omega^2\gamma_\alpha}{\Gamma^2+(N_g+1)g^2} \\
&\quad\times\left\{\hat{N}_i-\frac{2\hat{N}_i\Big(\hat{N}_g+1\Big)g^2\kappa\Gamma+\hat{N}_i\Big(\hat{N}_g+1\Big)^2g^4}{\Big[\Big(\hat{N}_g-N_g\Big)g^2-\frac{(\kappa-\Gamma)^2}{2}\Big]^2+(\kappa+\Gamma)^2\big[(N_g+1)g^2-\frac{\Gamma^2+\kappa^2}{2}\big]}\right\} \\
&\approx \frac{\Omega^2\gamma_\alpha}{(\Gamma+\kappa)^2}\hat{N}_i \qquad (5.41)
\end{aligned}$$

where we approximated by replacing operators with their expectation values and neglecting higher order terms in $(\Gamma+\kappa)/\sqrt{N_g+1}g$.

However, in numerical simulations the noise term $\hat{N}_g - N_g$ turns out to be important as well. Firstly, for $\Delta N_g \sim \sqrt{N_g}$, we find that the noise term looks like $N_g g^4$. This is only negligible if $N^{1/4}g \ll \kappa+\Gamma$. Secondly, we can end up in a negative feedback loop, running out of resonance: Consider a state for which $\langle\hat{N}_g\rangle(t_1) < N_g(t_1)$. In this case $\partial_t\langle\hat{N}_g\rangle \sim \langle\hat{L}_{\text{eff}}^{\kappa\dagger}\hat{L}_{\text{eff}}^{\kappa}\rangle < \partial_t N_g \sim \langle\hat{L}_{\text{eff}}^{\kappa\dagger}\hat{L}_{\text{eff}}^{\kappa}\rangle\Big|_{\hat{N}_g=N_g}$. This leads to $(\langle\hat{N}_g\rangle - N_g)(t_2) < (\langle\hat{N}_g\rangle - N_g)(t_1)$ for $t_2 > t_1$, running further out of resonance. In practice this can be solved by keeping $\Delta$ a bit smaller than $\Delta_{\text{opt}}$. We choose

$$\Delta = \left\{\max\left[0, N\left(\frac{N_g(t)}{N}\right)^{1.5}g^2-\frac{\Gamma^2+\kappa^2}{2}\right]\right\}^{1/2} \qquad (5.42)$$

with $N_g(t)/N$ plugged in according to an empiric estimate

$$\begin{aligned}
\frac{N_g(t)}{N} &= \frac{(\kappa+\gamma_g)(\kappa+\gamma_x)}{(\kappa+\gamma_g+\gamma_x)^2}\left\{1-\exp\left[-\frac{2\Omega^2(\kappa+\gamma_g+\gamma_x)t}{(\kappa+\Gamma)^2}\right]\right\} \\
&\quad+\frac{\gamma_g^2}{(\kappa+\gamma_g+\gamma_x)(\gamma_g+\gamma_x)}\left\{1-\exp\left[\frac{2\Omega^2(\gamma_g+\gamma_x)t}{Ng^2-\frac{\Gamma^2}{2}+\frac{\kappa^2}{2}}\right]\right\} \qquad (5.43)
\end{aligned}$$

This choice yields very good results, and a further optimization is beyond the scope of this paper.

## 5.H. Dark States

As discussed above and shown in Tab. 5.1, only spontaneous emission towards $|i\rangle$ and $|g\rangle$ can decrease $J - N/2$. This effect corresponds to a symmetry breaking, as only the $J = N/2$ states are completely symmetric at the state level. The resulting states with lowered $J$ can still decay via the cavity until $M = -J$, or reformulated $N_i = N/2 - J$. This however leaves $N/2 - J$ molecules trapped in the initial state, as $\hat{L}_\kappa^{\text{eff}} |N/2, J, M = -J\rangle = 0$. The remaining states are dark states and will decay with a lower rate. Note that the dark states do not have shifted energies with respect to the bare excited states. Thus the laser is detuned with respect to the initial state – dark state transition by about $\Delta^2 \sim Ng^2$. This leads to a further lowered decay rate.

We can estimate the number of molecules that are trapped in these dark states by assuming that every spontaneous emission towards $|g\rangle$ reduces $J$, whereas spontaneous emission towards $|i\rangle$ leaves $J$ unchanged. This rough approximation is empirically justified for $J \approx N/2$, and is consistent with the finding of Ref. [30] that spontaneous emission is more relevant for dark states than dephasing. With this assumption the dark state fraction becomes $\gamma_g/(\kappa + \gamma_g + \gamma_x)$. The decay rate of this dark states is given by $2\Omega^2(\gamma_g + \gamma_x)/(\Delta^2 + \Gamma^2) \approx 2\Omega^2(\gamma_g + \gamma_x)/(Ng^2 - \kappa^2/2 + \Gamma^2/2)$.

## 5.I. Comparison between both Schemes

For given $g$, we find that the chirped pulse scheme gives a loss state population of:

$$\frac{N_x^\infty}{N}(\text{chirp}) \approx \frac{\gamma_x}{\kappa} \gg \frac{\gamma_x}{\sqrt{N}g} \gg \frac{\gamma_x}{\sqrt{N}g}\frac{\kappa}{\sqrt{N}g} = \frac{f_x}{NC} \approx \frac{N_x^\infty}{N\ln(N)}(\text{no chirp}) \tag{5.44}$$

Thus for $\ln(N) < Ng^2/\kappa^2$ the scheme without a chirp yields higher state selectivity.

In contrast, for given half time we find:

$$\frac{N_x^\infty}{N}(\text{no chirp}) \approx \frac{f_x \tau \ln(N)}{5T_{\frac{1}{2}}} \tag{5.45}$$

$$T_{\frac{1}{2}}(\text{chirp}) \approx \frac{\ln(2)\kappa}{\Omega^2} \approx \frac{\ln(2)\tau\kappa}{\Gamma} \tag{5.46}$$

$$\frac{N_x^\infty}{N}(\text{chirp}) \approx \frac{f_x \tau \ln(2)}{T_{\frac{1}{2}}} \tag{5.47}$$

Thus, for $N \gtrsim 30$, the state selectivity with the second scheme is higher. For a typical number of $N \sim 1000$ molecules we find that the state selectivity with the chirped pulse is higher by a factor of 2. Note also that the first scheme does not decay exponentially, but the long time dynamics exhibits a stronger collective slowdown so that considering the total transfer time instead of the half time favors the chirped scheme even more.

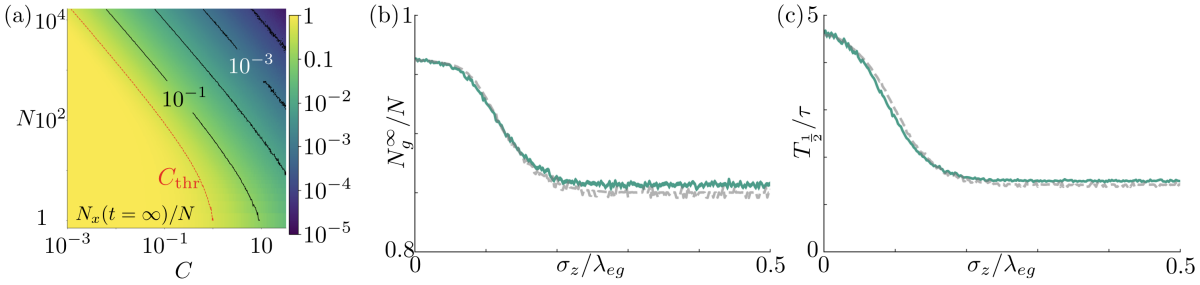


Figure 5.4. – (a) Contour plot of $N_x^\infty/N$ with indicated choice of $C_{\rm thr}$ for the disorder model according to the red dashed line. This corresponds to $N_x^\infty$ being half of its no cavity value. (b, c) Comparison of (b) the final ground state population and (c) the halftime calculated with the full simulation (continuous line) and the effective model (dashed line). We choose $N = 10$ and $C_0 \equiv g_0^2/(\kappa\Gamma) \approx 4$. The local coupling strength is given by $g(z) = g_0 \cos(2\pi z/\lambda_{eg})$ and $z$ is randomly distributed with probability density function $p(z) = \exp[-z^2/(2\sigma_z^2)]$.

## 5.J. Influence of Local Cavity Coupling Constant

In order to model local cavity coupling constants for large molecule numbers, we use an effective model. We define a threshold cooperativity $C_{\rm thr}$, and assume that molecules with local coupling $C_n = g_n^2/(\kappa\Gamma) < C_{\rm thr}$ do not couple to the cavity $g_n \to 0$, whereas molecules with $C_n > C_{\rm thr}$ couple with average cooperativity $C_n \to C_{\rm eff} = (\sum C_n)/N'$. By employing this binary decision model, we arrive at a situation with particle permutation symmetry, which can be simulated as described above. $C_{\rm thr} = C_{\rm thr}(N)$ is chosen such that, if $N$ molecules couple with $C_{\rm thr}$ to a cavity, the $|x\rangle$ state fraction is half of its no cavity value [red dashed line in Fig. 5.4(a)]. Errors are given by or smaller than the linewidth.

In order to derive an expression for $C_{\rm eff}$, we analyze the limit for which the cavity decay is dominant. We first derive an expression for the states after $k$ decay processes via the cavity. Then, we calculate the cavity decay rate and the spontaneous emission rates for these states. Comparing the rates of decay for the different decay channels we can estimate the final ground state population and the half time.

For a local cavity coupling constant, we find effective operators for the master equation after adiabatic elimination

$$\hat{H}_{\rm eff} = 0 \tag{5.48}$$

$$\hat{L}_{\rm eff}^{\kappa} = \sqrt{\lambda_\kappa}\hat{\xi}\hat{S}_{gi} \tag{5.49}$$

$$\hat{L}_{\rm eff}^{\alpha,(n)} = \sqrt{\lambda_\gamma^\alpha}\left(\hat{\sigma}_{\alpha i}^{(n)} - \frac{\hat{\sigma}_{\alpha g}^{(n)} g_n}{g_0}\hat{\xi}\hat{S}_{gi}\right) \tag{5.50}$$

with $\hat{S}_{gi} = \sum_n g_n\hat{\sigma}_{gi}^{(n)}/(\sqrt{N}g_0)$ and $\hat{\xi} = \sqrt{N}g_0^2(\sum_n g_n^2\hat{\sigma}_{gg}^{(n)} + \kappa\Gamma)^{-1}$, where $g_0$ is the peak cavity coupling constant, $\bar{C}$ is the average cooperativity and $C$ is the peak cooperativity.

Taking the initial state as $\left|\psi^{(0)}\right\rangle = \bigotimes_n |i\rangle_n$, the state after $k$ decay processes via the cavity decay channel $\hat{L}^{\kappa}_{\text{eff}}$ is given by

$$\left|\psi^{(k)}\right\rangle = \frac{1}{\mathcal{N}_k}\left(\hat{L}^{\kappa}_{\text{eff}}\right)^k \left|\psi^{(0)}\right\rangle = \frac{1}{\mathcal{N}'_k}\sum_{I,G}\bigotimes_{l\in I} g_l\,|i\rangle_l \otimes \bigotimes_{m\in G}|g\rangle_m \tag{5.51}$$

for some normalization constants $\mathcal{N}_k$ and $\mathcal{N}'_k$. $I$ denotes the set of atom pairs in state $|i\rangle$ and $G$ denotes the set of molecules in state $|g\rangle$. The sum runs over all possible choices of sets $I$ and $G$ such that $|G| = k$, $|I| = N - k$, and $I \cap G = \emptyset$. This can be easily confirmed by checking $\left|\psi^{(0)}\right\rangle = \bigotimes_n |i\rangle_n$ and $\hat{L}^{\kappa}_{\text{eff}}\left|\psi^{(k)}\right\rangle \propto \left|\psi^{(k+1)}\right\rangle$. In these states we get to leading order in $1/(N_g\bar{C})$:

$$\zeta_\kappa \approx \frac{2}{\tau}\frac{N_i}{(N_g+1)\bar{C}} \tag{5.52}$$

$$\zeta_\alpha \approx \frac{2f_\alpha}{\tau}\frac{N_i}{(N_g+1)^2\bar{C}^2}\,. \tag{5.53}$$

This also justifies in hindsight to look at the cavity dominated limit, as cavity decay dominates for $N_g\bar{C} \gg f_\alpha$. From these we get the equations of motion:

$$\dot{N}_i \approx -\frac{2}{\tau}\frac{N_i}{(N_g+1)\bar{C}} \tag{5.54}$$

$$\dot{N}_g \approx \frac{2}{\tau}\frac{N_i}{(N_g+1)\bar{C}} \tag{5.55}$$

$$\dot{N}_x \approx \frac{2f_x}{\tau}\frac{N_i}{(N_g+1)^2\bar{C}^2} \tag{5.56}$$

These equations are equivalent to Eqs. (5.6) and (5.7) and the rate equations $\dot{N}_{i,g,x}$ in the main paper for no disorder with the replacement $C \to \bar{C}$. This motivates the choice:

$$C_{\text{eff}} = \frac{\sum_n C_n}{N'} \tag{5.57}$$

where the sum over molecules with $C_n > C_{\text{thr}}$ and $N'$ is the number of these molecules.

Fig. 5.4(b) and (c) show a comparison of the effective model and a full simulation for 10 molecules and different disorder strengths. We find a good correspondence.

## 5.K. Finite Temperature Effects

Our scheme is intended to work in the ultracold regime, where temperatures $T$ are smaller than the inter-band lattice energy gap $h\nu_{\text{vib}}$ and the effects of finite $T$ are negligible. For typical lattice depths, this entails temperatures of several hundreds of nK (see below), which is achievable in many experiments. We note that it is commonly achieved to prepare a Mott insulator state in the lowest lattice band [52, 53]. However,

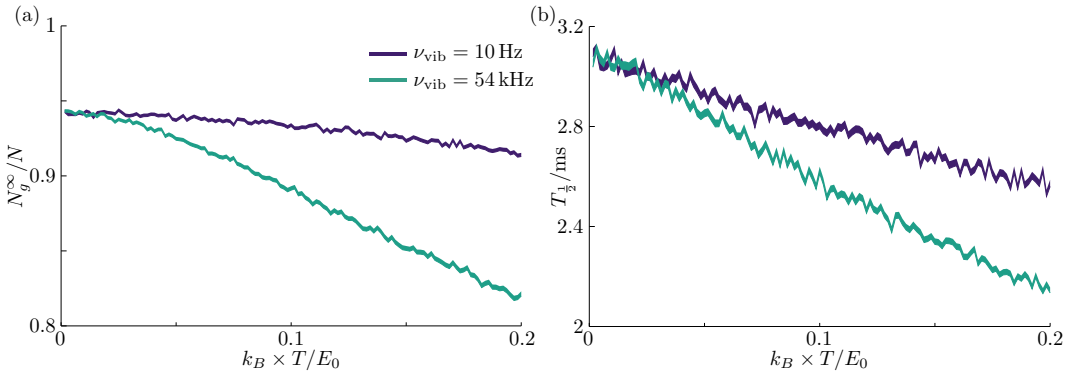


Figure 5.5. – Temperature dependence of (a) the final molecular fraction and (b) the transfer half time. We simulate $N = 6$ molecules, that oscillate classically at frequency $\nu_{\mathrm{vib}}$, for a peak cavity coupling constant $g_0/2\pi = 10\,\mathrm{MHz}$, with thermal energy up to 20 % of the lattice depth. The linewidth corresponds to the statistical error due to the trajectories and the choice of $z_{0,i}$ and $\phi_{0,i}$ (one standard deviation). The violet and green line correspond to $T_{\frac{1}{2}}\nu_{\mathrm{vib}} < 1$ and $T_{\frac{1}{2}}\nu_{\mathrm{vib}} > 1$, respectively.

the precise distribution of molecules in the lattice will depend on the chosen preparation and loading scheme. In the following we assume that molecules in any doubly occupied site are rapidly lost via three-body recombination or light-induced collisions in the early stages of our scheme. This leaves a lattice with at most one Feshbach molecule per site. In the following, we estimate the efficiency of our scheme when population of higher bands cannot be neglected, i.e., for $k_B T \gtrsim h\nu_{\mathrm{vib}}$ with $k_B$ the Boltzmann constant.

Due to the unfavorable scaling of the size of the density matrix with increasing $N$ and band number, a computation of the quantum many-body dynamics becomes impractical for just a few particles. We thus estimate the efficiency of the scheme in a classical approximation for the on-site motion of the molecules. This corresponds to treating the molecules in coherent states, which, compared to typical experimental scenarios, largely overestimates the number of molecules in higher bands. We distinguish two regimes depending on how fast the population transfer $T_{\frac{1}{2}}$ occurs compared to $1/\nu_{\mathrm{vib}}$, i.e. the characteristic oscillation time of a particle at the bottom of a lattice well. We find that if $T_{\frac{1}{2}}\nu_{\mathrm{vib}} < 1$, the system is well modelled by adding static disorder to the cavity coupling constant (due to positional disorder inside the lattice). In this case, we find that the efficiency of the scheme is only slightly decreased from the zero-temperature case [see Fig. 5.5, upper violet curves]. If instead $T_{\frac{1}{2}}\nu_{\mathrm{vib}} \gtrsim 1$, as for the parameters in the paper, the decrease in efficiency is larger. However, we estimate that reasonably good transfer rates are still possible, as discussed below [see also Fig. 5.5, lower green curves]. We note that the decrease in efficiency is always accompanied by a speed-up in the transfer dynamics. Finally, if the thermal energy is on the order of the lattice depth $E_0$, molecules are lost from the trap, leading to a steep decrease in transfer efficiency. In the following

we provide more details on our calculations.

The lattice band spacing can be calculated from the potential and its harmonic approximation:

$$V(\vec{x}) = E_0 \sin^2\left(\frac{2\pi x}{\lambda_{\text{latt}}}\right) + E_0 \sin^2\left[\frac{2\pi(\cos\theta z + \sin\theta y)}{\lambda_{\text{latt}}}\right] + E_0 \sin^2\left[\frac{2\pi(\cos\theta z - \sin\theta y)}{\lambda_{\text{latt}}}\right] \tag{5.58}$$

$$\approx \frac{4\pi^2 E_0}{\lambda_{\text{latt}}^2}\left[x^2 + \left(2\sin^2\theta\right)y^2 + \left(2\cos^2\theta\right)z^2\right] \tag{5.59}$$

with the parameters of the main text $\lambda_{\text{latt}} = 1064.5\,\text{nm}$, $\theta = 57°$, and $E_0 = 48E_R = k_B \times 1.8\,\mu\text{K}$ for the recoil energy $E_R = (2\pi\hbar/\lambda_{\text{latt}})^2/(2m_{\text{RbCs}})$. We will restrict this analysis to motion along the $z$-direction, as here the variation of the cavity coupling constant with motion is largest and consider the one dimensional potential $V(z) = V(x = y = 0, z)$. The oscillation frequency in the $z$-direction is given by $\nu_{\text{vib}} = (2\cos\theta/\lambda_{\text{latt}})\sqrt{E_0/m_{\text{RbCs}}} = 54\,\text{kHz}$. We model the thermal motion by

$$z_i(t) = z_{0,i}\cos(2\pi\nu_{\text{vib}}t + \phi_{0,i})\,, \tag{5.60}$$

with Boltzmann distributed amplitudes $z_{0,i}$ chosen according to $p(z_{0,i}) = \exp[-V(z_{0,i})/(k_BT)]/Z$ with the partition function $Z = \int \mathrm{d}z \exp[-V(z)/(k_BT)]$, and a random initial phase $\phi_{0,i} \in (0, 2\pi]$. This thermal motion leads to a time dependent cavity coupling constant for each molecule $g_i(z_i) = g_0\cos[2\pi z_i/\lambda_{eg}]$, which is incorporated in the simulation. We choose $g_0/2\pi = 10\,\text{MHz}$ to get $T_{\frac{1}{2}} \simeq 3\,\text{ms}$ in order to approximate the transfer half time $T_{\frac{1}{2}}$ computed in the main text for RbCs. This allows us to provide results for characteristic transfer half times $T_{\frac{1}{2}}\nu_{\text{vib}} \gtrsim 1$, similar to the large-$N$ case of the main text, however for the case of just a few particles. The results are presented in Fig. 5.5, which shows a moderate decrease of both transfer efficiency and transfer time. Since the key parameter is here the quantity $T_{\frac{1}{2}}\nu_{\text{vib}}$, we expect that similar results should hold also for larger $N$.

All temperature induced frequency shifts can be ignored, as both shifts of thermally excited states compared to the ground state $\Delta_\nu \sim k_BT/h$ as well as Doppler broadening $\sigma_D = \sqrt{k_BT/(m_{\text{RbCs}}\lambda^2)} \sim$ kHz are on the order of kHz, much smaller than the natural linewidth $\Gamma$ or cavity linewidth $\kappa$, which are on the order of MHz or GHz, respectively.

# Bibliography


[1] D. Wellnitz, S. Schütz, S. Whitlock, J. Schachenmayer, and G. Pupillo, "Collective Dissipative Molecule Formation in a Cavity," *Phys. Rev. Lett.*, p. 6, 2020.

[2] J. Doyle, B. Friedrich, R. V. Krems, and F. Masnou-Seeuws, "Editorial: Quo vadis, cold molecules?," *Eur. Phys. J. D*, vol. 31, pp. 149–164, Nov. 2004.

[3] L. D. Carr, D. DeMille, R. V. Krems, and J. Ye, "Cold and ultracold molecules: Science, technology and applications," *New J. Phys.*, vol. 11, p. 055049, May 2009.

[4] G. Quéméner and P. S. Julienne, "Ultracold Molecules under Control!," *Chem. Rev.*, vol. 112, pp. 4949–5011, Sept. 2012.

[5] S. A. Moses, J. P. Covey, M. T. Miecnikowski, D. S. Jin, and J. Ye, "New frontiers for quantum gases of polar molecules," *Nature Phys*, vol. 13, pp. 13–20, Jan. 2017.

[6] J. L. Bohn, A. M. Rey, and J. Ye, "Cold molecules: Progress in quantum engineering of chemistry and quantum matter," *Science*, vol. 357, pp. 1002–1010, Sept. 2017.

[7] J. G. Danzl, M. J. Mark, E. Haller, M. Gustavsson, R. Hart, J. Aldegunde, J. M. Hutson, and H.-C. Nägerl, "An ultracold high-density sample of rovibronic ground-state molecules in an optical lattice," *Nat. Phys.*, vol. 6, pp. 265–270, Apr. 2010.

[8] T. Takekoshi, L. Reichsöllner, A. Schindewolf, J. M. Hutson, C. R. Le Sueur, O. Dulieu, F. Ferlaino, R. Grimm, and H.-C. Nägerl, "Ultracold Dense Samples of Dipolar RbCs Molecules in the Rovibrational and Hyperfine Ground State," *Phys. Rev. Lett.*, vol. 113, p. 205301, Nov. 2014.

[9] F. Lang, K. Winkler, C. Strauss, R. Grimm, and J. H. Denschlag, "Ultracold Triplet Molecules in the Rovibrational Ground State," *Phys. Rev. Lett.*, vol. 101, p. 133005, Sept. 2008.

[10] S. A. Moses, J. P. Covey, M. T. Miecnikowski, B. Yan, B. Gadway, J. Ye, and D. S. Jin, "Creation of a low-entropy quantum gas of polar molecules in an optical lattice," *Science*, vol. 350, pp. 659–662, Nov. 2015.

[11] L. D. Marco, G. Valtolina, K. Matsuda, W. G. Tobias, J. P. Covey, and J. Ye, "A degenerate Fermi gas of polar molecules," *Science*, vol. 363, pp. 853–856, Feb. 2019.

[12] K. M. Jones, E. Tiesinga, P. D. Lett, and P. S. Julienne, "Ultracold photoassociation spectroscopy: Long-range molecules and atomic scattering," *Rev. Mod. Phys.*, vol. 78, pp. 483–535, May 2006.

[13] J. Deiglmayr, A. Grochola, M. Repp, K. Mörtlbauer, C. Glück, J. Lange, O. Dulieu, R. Wester, and M. Weidemüller, "Formation of Ultracold Polar Molecules in the Rovibrational Ground State," *Phys. Rev. Lett.*, vol. 101, p. 133004, Sept. 2008.

[14] M. A. Bellos, D. Rahmlow, R. Carollo, J. Banerjee, O. Dulieu, A. Gerdes, E. E. Eyler, P. L. Gould, and W. C. Stwalley, "Formation of ultracold Rb2 molecules in the v′′ = 0 level of the a3Σ+u state via blue-detuned photoassociation to the 13Πg state," *Phys. Chem. Chem. Phys.*, vol. 13, no. 42, p. 18880, 2011.

[15] P. Zabawa, A. Wakim, M. Haruza, and N. P. Bigelow, "Formation of ultracold $x\,^1\Sigma^+(v'' = 0)$ NaCs molecules via coupled photoassociation channels," *Phys. Rev. A*, vol. 84, p. 061401, Dec. 2011.

[16] J. Ulmanis, J. Deiglmayr, M. Repp, R. Wester, and M. Weidemüller, "Ultracold Molecules Formed by Photoassociation: Heteronuclear Dimers, Inelastic Collisions, and Interactions with Ultrashort Laser Pulses," *Chem. Rev.*, vol. 112, pp. 4890–4927, Sept. 2012.

[17] C. D. Bruzewicz, M. Gustavsson, T. Shimasaki, and D. DeMille, "Continuous formation of vibronic ground state RbCs molecules via photoassociation," *New J. Phys.*, vol. 16, p. 023018, Feb. 2014.

[18] J. M. Sage, S. Sainis, T. Bergeman, and D. DeMille, "Optical Production of Ultracold Polar Molecules," *Phys. Rev. Lett.*, vol. 94, p. 203001, May 2005.

[19] M. Viteau, A. Chotia, M. Allegrini, N. Bouloufa, O. Dulieu, D. Comparat, and P. Pillet, "Optical Pumping and Vibrational Cooling of Molecules," *Science*, vol. 321, pp. 232–234, July 2008.

[20] H. F. Passagem, R. Colín-Rodríguez, J. Tallant, P. C. Ventura da Silva, N. Bouloufa-Maafa, O. Dulieu, and L. G. Marcassa, "Continuous loading of ultracold ground-state $^{85}rb_2$ molecules in a dipole trap using a single light beam," *Phys. Rev. Lett.*, vol. 122, p. 123401, Mar. 2019.

[21] T. Kampschulte and J. Hecker Denschlag, "Cavity-controlled formation of ultracold molecules," *New J. Phys.*, vol. 20, p. 123015, Dec. 2018.

[22] J. Pérez-Ríos, M. E. Kim, and C.-L. Hung, "Ultracold molecule assembly with photonic crystals," *New J. Phys.*, vol. 19, p. 123035, Dec. 2017.

[23] N. V. Vitanov, A. A. Rangelov, B. W. Shore, and K. Bergmann, "Stimulated Raman adiabatic passage in physics, chemistry and beyond," *Rev. Mod. Phys.*, vol. 89, p. 015006, Mar. 2017.

[24] F. Reiter and A. S. Sørensen, "Effective operator formalism for open quantum systems," *Phys. Rev. A*, vol. 85, p. 032111, Mar. 2012.

[25] Y. Zhang, Y.-X. Zhang, and K. Mølmer, "Monte-Carlo Simulations of Superradiant Lasing," *New J. Phys.*, vol. 20, p. 112001, Nov. 2018.

[26] A. J. Daley, "Quantum trajectories and open many-body quantum systems," *Adv. Phys.*, vol. 63, pp. 77–149, Mar. 2014.

[27] M. Debatin, T. Takekoshi, R. Rameshan, L. Reichsöllner, F. Ferlaino, R. Grimm, R. Vexiau, N. Bouloufa, O. Dulieu, and H.-C. Nägerl, "Molecular spectroscopy for ground-state transfer of ultracold RbCs molecules," *Phys. Chem. Chem. Phys.*, vol. 13, no. 42, p. 18926, 2011.

[28] C. W. Gardiner and P. Zoller, *The Quantum World of Ultracold Atoms and Light Book Ii: The Physics of Quantum Optical Devices*, vol. 4. World Scientific Publishing Company, 2015.

[29] N. Shammah, N. Lambert, F. Nori, and S. De Liberato, "Superradiance with local phase-breaking effects," *Phys. Rev. A*, vol. 96, p. 023863, Aug. 2017.

[30] M. Gegg, A. Carmele, A. Knorr, and M. Richter, "Superradiant to subradiant phase transition in the open system Dicke model: Dark state cascades," *New J. Phys.*, vol. 20, p. 013006, Jan. 2018.

[31] S. Ospelkaus, K.-K. Ni, G. Quéméner, B. Neyenhuis, D. Wang, M. H. G. de Miranda, J. L. Bohn, J. Ye, and D. S. Jin, "Controlling the Hyperfine State of Rovibronic Ground-State Polar Molecules," *Phys. Rev. Lett.*, vol. 104, p. 030402, Jan. 2010.

[32] J. A. Hutchison, T. Schwartz, C. Genet, E. Devaux, and T. W. Ebbesen, "Modifying Chemical Landscapes by Coupling to Vacuum Fields," *Angew. Chem. Int. Ed.*, vol. 51, pp. 1592–1596, Feb. 2012.

[33] A. Thomas, L. Lethuillier-Karl, K. Nagarajan, R. M. A. Vergauwe, J. George, T. Chervy, A. Shalabney, E. Devaux, C. Genet, J. Moran, and T. W. Ebbesen, "Tilting a ground-state reactivity landscape by vibrational strong coupling," *Science*, vol. 363, pp. 615–619, Feb. 2019.

[34] F. Herrera and J. Owrutsky, "Molecular polaritons for controlling chemistry with quantum optics," *J. Chem. Phys.*, vol. 152, p. 100902, Mar. 2020.

[35] P. Törmä and W. L. Barnes, "Strong coupling between surface plasmon polaritons and emitters: A review," *Rep. Prog. Phys.*, vol. 78, p. 013901, Dec. 2014.

[36] T. W. Ebbesen, "Hybrid Light–Matter States in a Molecular and Material Science Perspective," *Acc. Chem. Res.*, vol. 49, pp. 2403–2412, Nov. 2016.

[37] A. Mandal, T. D. Krauss, and P. Huo, "Polariton-Mediated Electron Transfer via Cavity Quantum Electrodynamics," *J. Phys. Chem. B*, vol. 124, pp. 6321–6340, July 2020.

[38] D. Wellnitz, G. Pupillo, and J. Schachenmayer, "A quantum optics approach to photoinduced electron transfer in cavities," *J. Chem. Phys.*, vol. 154, p. 054104, Feb. 2021.

[39] A. Niezgoda, J. Chwedeńczuk, T. Wasak, and F. Piazza, "Cooperatively enhanced precision of hybrid light-matter sensors," *Phys. Rev. A*, vol. 104, p. 023315, Aug. 2021.

[40] D. Barberena, R. J. Lewis-Swan, J. K. Thompson, and A. M. Rey, "Driven-dissipative quantum dynamics in ultra-long-lived dipoles in an optical cavity," *Phys. Rev. A*, vol. 99, p. 053411, May 2019.

[41] J. A. Muniz, D. Barberena, R. J. Lewis-Swan, D. J. Young, J. R. K. Cline, A. M. Rey, and J. K. Thompson, "Exploring dynamical phase transitions with cold atoms in an optical cavity," *Nature*, vol. 580, pp. 602–607, Apr. 2020.

[42] P. Rabl, D. DeMille, J. M. Doyle, M. D. Lukin, R. J. Schoelkopf, and P. Zoller, "Hybrid Quantum Processors: Molecular Ensembles as Quantum Memory for Solid State Circuits," *Phys. Rev. Lett.*, vol. 97, p. 033003, July 2006.

[43] A. Imamoglu, D. D. Awschalom, G. Burkard, D. P. DiVincenzo, D. Loss, M. Sherwin, and A. Small, "Quantum Information Processing Using Quantum Dot Spins and Cavity QED," *Phys. Rev. Lett.*, vol. 83, pp. 4204–4207, Nov. 1999.

[44] J. Majer, J. M. Chow, J. M. Gambetta, J. Koch, B. R. Johnson, J. A. Schreier, L. Frunzio, D. I. Schuster, A. A. Houck, A. Wallraff, A. Blais, M. H. Devoret, S. M. Girvin, and R. J. Schoelkopf, "Coupling superconducting qubits via a cavity bus," *Nature*, vol. 449, pp. 443–447, Sept. 2007.

[45] R. Sawant, O. Dulieu, and S. A. Rangwala, "Detection of ultracold molecules using an optical cavity," *Phys. Rev. A*, vol. 97, p. 063405, June 2018.

[46] M. Zhu, Y.-C. Wei, and C.-L. Hung, "Resonator-assisted single-molecule quantum state detection," *Phys. Rev. A*, vol. 102, p. 023716, Aug. 2020.

[47] B. A. Chase and J. M. Geremia, "Collective processes of an ensemble of spin-12 particles," *Phys. Rev. A*, vol. 78, p. 052101, Nov. 2008.

[48] M. Bolaños and P. Barberis-Blostein, "Algebraic solution of the Lindblad equation for a collection of multilevel systems coupled to independent environments," *J. Phys. Math. Theor.*, vol. 48, p. 445301, Nov. 2015.

[49] S. Hartmann, "Generalized Dicke states," *Quantum Info. Comput.*, vol. 16, pp. 1333–1348, Nov. 2016.

[50] M. Gegg and M. Richter, "Efficient and exact numerical approach for many multilevel systems in open system CQED," *New J. Phys.*, vol. 18, p. 043037, Apr. 2016.

[51] N. Shammah, S. Ahmed, N. Lambert, S. De Liberato, and F. Nori, "Open quantum systems with local and collective incoherent processes: Efficient numerical simulations using permutational invariance," *Phys. Rev. A*, vol. 98, p. 063815, Dec. 2018.

[52] T. Rom, T. Best, O. Mandel, A. Widera, M. Greiner, T. W. Hänsch, and I. Bloch, "State Selective Production of Molecules in Optical Lattices," *Phys. Rev. Lett.*, vol. 93, Aug. 2004.

[53] J. P. Covey, S. A. Moses, J. Ye, and D. S. Jin, "Controlling a Quantum Gas of Polar Molecules in an Optical Lattice," in *Cold Chemistry*, pp. 537–578, Royal Society of Chemistry, Dec. 2017.

# Part III.

# Polaritonic Chemistry

# 6. Publication: A Quantum Optics Approach to Photo-Induced Electron Transfer Reactions in a Cavity

The following chapter is a reprint of a work investigating cavity-modified photo-induced electron transfer reactions, which was published in *J. Chem. Phys.* **154** 054104 (2021) [1]. In this work, we have studied a simple model for these reactions for the case of many donor-acceptor pairs that are collectively coupled to a lossy photon mode of a cavity. We have described both coherent and dissipative collective effects resulting from this coupling within the framework of a quantum optics Lindblad master equation. We have adiabatically eliminated the excited donor and acceptor states and the cavity mode to compute an effective rate equation, for which we have derived an analytic expression. This rate equation depends non-trivially on the time-varying number of pairs in the initial ground state. We have found that under proper resonance conditions, and in the presence of an incoherent drive, reaction rates can be enhanced by the cavity. This enhancement persists, and can even be largest, in the weak light-matter coupling regime. We also discuss how this cavity effect is relevant for realistic experiments. This study was one of the first detailed studies of dissipation for polaritonic chemistry especially with respect to collective, dissipative effects.

This chapter is organized as follows: In Section 6.1, we introduce the general physics and motivate the study. In Section 6.2, we discuss our model in detail. Section 6.3 contains a thorough discussion of the adiabatic elimination procedure, whose result is presented and scrutinized in Section 6.4. Section 6.5 concludes this chapter.

## 6.1. Introduction

Collectively coupling a large number of molecules to a cavity mode can lead to a significant modification of chemical reaction rates [2, 3]. This has been demonstrated in a series of recent breakthrough experiments where vibrational [4–8] or electronic [9–11] transitions have been strongly coupled to cavity modes or other confined electromagnetic fields. Theoretically understanding such collective cavity-modified chemistry is a major challenge due to the difficulty of modeling the dynamics of large ensembles of molecules with many internal (i.e., electronic, vibrational, etc.) and motional degrees of freedom together with those of the electromagnetic field. Cavity-induced effects in polaritonic

chemistry have often been described within a coherent Hamiltonian framework [12–18], however incoherent dissipation from molecular radiative and non-radiative transitions, different molecular environments, cavity losses, etc., can play an important role in the dynamics [19–26]. In particular, cavity losses represent an ultrafast (fs timescale) decay mechanism unique to polaritonic chemistry [27]. The interplay between coherent Hamiltonian dynamics and these dissipation channels adds an additional layer of complexity for theory.

In order to understand basic mechanisms underlying cavity-modified chemistry, it can be thus instructive to analyze simplified models of few-level systems, which can be efficiently described by standard quantum optics tools [19, 20, 28–30]. For example, in many situations where a large dissipation is present one can use an adiabatic elimination procedure [31, 32], a theoretical tool that can make it possible to significantly reduce the complexity of the problem by finding analytical solutions to the molecular dynamics of just a few key degrees of freedom [33]. Using these techniques for the case of ground-state atoms cooled to submillikelvin temperatures [34, 35], we have recently shown that collective dissipative effects can compete with, and even dominate over, coherent Hamiltonian dynamics for molecular formation in a cavity in realistic experiments with up to $10^5$ molecules – a dissipative form of polaritonic chemistry [33]. It is an interesting question to explore to what extent these dissipative mechanisms and theoretical techniques can be used to investigate reactions in more ordinary situations in chemistry.

Here, we study the Lindblad master equation dynamics that describes a photoinduced electron transfer reaction of many donor-acceptor pairs homogeneously coupled to a cavity. We simplify each pair to a 4-level system, an approximation which neglects internal and external motional degrees of freedom [36]. In our model an electron donor is excited by an incoherent external field, leaving a single electron loosely bound. This electron is then coherently transferred to an acceptor, which finally relaxes incoherently into a final state. We introduce and explain the concept of the adiabatic elimination procedure as a tool to analyze dissipative polariton chemistry, and clarify under which conditions it may be used. In order to obtain an analytical result for the modification of the transfer rate from the donor to the acceptor, we adiabatically eliminate the cavity mode and the excited donor/acceptor states. We show that for our specific problem this leads to a purely dissipative, and essentially classical, effective master equation without any coherent contribution, that is, with effective Hamiltonian

$$\hat{H}_{\text{eff}} = 0\,. \tag{6.1}$$

The master equation can be numerically simulated for a very large number of donor-acceptor pairs, and makes it possible to derive an analytical expression for the instantaneous transfer rate, given in Eq. (6.22). The coherent (quantum) dynamics of the excited states is implicitly included in this transfer rate, capturing the effects of virtually excited polaritons (in the strong coupling regime), superradiant states (in the weak coupling regime), and dark states, all within a single formula. We analyze the validity of the analytical formula and discuss the conditions under which it can describe observations in realistic experimental setups.

We find that electron transfer occurs via two distinct types of channels: One type comprises $N$ transfer channels that are activated by spontaneous absorption of an incoherent photon by an individual donor-acceptor pair. For large $N$, these transfer channels use mostly "dark states" that are decoupled from the cavity, and they are therefore essentially independent of the cavity coupling strength $g$. The other transfer channel is activated by absorption of an incoherent photon into the cavity. Here, the electron transfer occurs via the collective, cavity coupled states, in particular super-radiant or polaritonic states, which we call "bright states". This channel is added by the cavity and has a strong dependence on $g$. The transfer efficiency is maximal for an intermediate cavity coupling that can be in the weak or strong coupling regime, depending on the model parameters. We find that the transfer rate scales non-trivially with increasing number of donor-acceptor pairs and that for realistic situations the cavity transfer channel can dominate and enhance the transfer rate.

Those results are in line with recent theoretical studies for small system sizes [19–26] that have highlighted the role of dissipation, and possibilities for optimal coupling strengths close to the weak coupling regime. In contrast to previous works, here we confirm such observations in toy-models for macroscopic molecule numbers. Further, recent research has highlighted that collective effects lead to a modified reaction dynamics that differs from a simple increase of the Rabi splitting with $N$, in a coherent Hamiltonian framework without dissipation [37–39]. Here we derive a non-linear rate equation for a purely dissipative regime, and find that instantaneous transfer rates are non-trivial due to a combination of transfer through dark and polaritonics states, which depends on the instantaneous number of coupled pairs, $N(t)$. We note that while in our work the role of dark and bright states depends directly on the relative rates at which they are externally excited, the natural mixing of dark and bright states due to disorder and vibrational couplings has been also investigate in several recent works [17, 40–44].

The remainder of the paper is organized as follows: We start by introducing our simplified electron transfer model in Sec. 6.2. There, we explain how to describe both coherent and dissipative processes within the master equation approach in Sec. 6.2, and discuss the relevance of this model to realistic experiments in Sec. 6.2. We then present the adiabatic elimination procedure in detail in Sec. 6.3. In Sec. 6.4 we discuss the effective master equation: In Sec. 6.4 we provide an analytical expression for the electron transfer rate and clarify the contributions of the different transfer channels; in Sec. 6.4 we demonstrate the validity of our rate equation and analyze the resulting dynamics; and in Sec. 6.4 we evaluate the parameter dependencies of the transfer rate, and estimate when the cavity can increase it. We provide a conclusion and an outlook in Sec. 6.5.

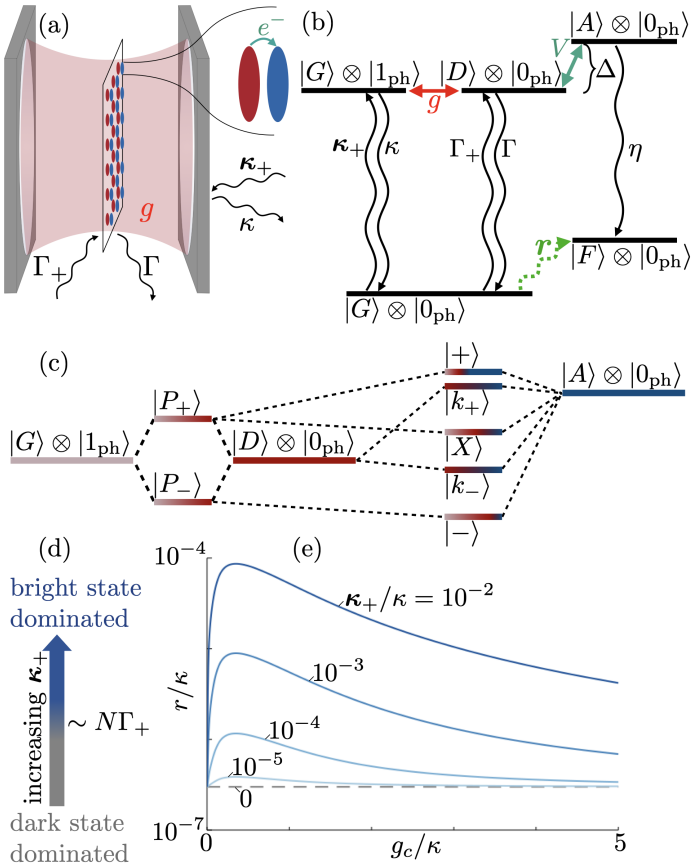


Figure 6.1. – (a) Schematic model. $N$ donor (red) - acceptor (blue) pairs are homogeneously coupled to a cavity with coupling constant $g$. Each pair and the cavity are incoherently pumped at rate $\Gamma_+$ and $\kappa_+$, and decay at rate $\Gamma$ and $\kappa$, respectively. (b) Level scheme of a single molecule coupled to the cavity: Each pair is described as a 4-level system with a ground state $|G\rangle$, excited donor ($|D\rangle$) and acceptor state ($|A\rangle$), and a final state $|F\rangle$, corresponding to the reaction product. The zero and one photon-number states of the cavity are denoted as $|0_{\rm ph}\rangle$ and $|1_{\rm ph}\rangle$, respectively. The cavity coherently couples the states $|G\rangle \otimes |1_{\rm ph}\rangle$ and $|D\rangle \otimes |0_{\rm ph}\rangle$ with strength $g$, while coherent coupling between $|D\rangle \otimes |0_{\rm ph}\rangle$ and $|A\rangle \otimes |0_{\rm ph}\rangle$ with strength $V$ and detuning $\Delta$ induces the electron transfer. After the adiabatic elimination, all coherent and dissipative dynamics can be captured by an effective transfer rate $r$ of population from $|G\rangle$ to $|F\rangle$ (green dotted arrow). (c) Schematic level-diagram for eigenstates of Hamiltonian Eq. (6.2) (not to scale). (d) For increasing $\kappa_+$, the dynamics transitions from being dominated by dark states to being dominated by bright states above $\kappa_+ \gtrsim N\Gamma_+$. (e) Transfer rate $r$ from Eq. (6.22) on a logarithmic scale as a function of the collective cavity coupling $g_c = \sqrt{N}g$ for various cavity pumping rates $0 \leq \kappa_+ \leq 10^{-2}\kappa$ with $N = 10^4$, $\Gamma = 3 \times 10^{-7}\kappa$, $\Gamma_+ = 10^{-4}\Gamma$, $\Delta = 0.2\kappa$, $V = 0.1\kappa$, and $\eta = 10^{-2}\kappa$.

# 6.2. Model

## Quantum optics master equation approach

We consider a model of $N$ donor-acceptor pairs homogeneously coupled to a single-mode cavity as schematically depicted in Fig. 6.1(a). Each donor-acceptor pair is described by a 4-level system with a ground state $|G\rangle$, an excited donor state $|D\rangle$, an excited acceptor state $|A\rangle$, and a final state $|F\rangle$; the cavity is described by a photon mode with annihilation operator $\hat{a}$. We are interested in the transfer dynamics from $|G\rangle$ to $|F\rangle$. The cavity is resonantly coupled to the $|G\rangle \leftrightarrow |D\rangle$ transition with single molecule coupling strength $g$. We further include the following dissipative processes: incoherent cavity pumping at rate $\kappa_+$, leading to the creation of a cavity photon, cavity decay at rate $\kappa$, leading to loss of photons from the cavity, pumping of the individual pairs from their ground state $|G\rangle$ to donor state $|D\rangle$ at rate $\Gamma_+$, the inverse decay process $\Gamma$, and an artificially introduced non-radiative relaxation from the acceptor state $|A\rangle$ to the final state $|F\rangle$ at rate $\eta$. The corresponding level scheme including the cavity states $|0_{\mathrm{ph}}\rangle$ and $|1_{\mathrm{ph}}\rangle$ with zero and one photon, respectively, is shown in Fig 6.1(b).

We set $\hbar = 1$ and work in a rotating frame[1] where we include the bare excited state energies derived from the operator $\hat{N}_e\omega_{DG} + \hat{N}_F\omega_{FG} = \hat{N}_e(E_D - E_G) + \hat{N}_F(E_F - E_G)$ in the definition of the states. Here, the operator $\hat{N}_e = \hat{N}_D + \hat{N}_A + \hat{a}^\dagger\hat{a}$ gives the excitation number, with the population number operators $\hat{N}_\psi = \sum_n |\psi\rangle\langle\psi|_n$, $\psi \in \{G, D, A, F\}$, and the subscript $n$ labeling the $n$th pair. We also make the rotating wave approximation, and neglect all counter-rotating terms, which is valid for $g_c \equiv \sqrt{N}g \ll \omega_{DG}$ [36]. Under these considerations, all coherent dynamics is described by the Hamiltonian

$$\begin{aligned}\hat{H} =& \Delta\hat{N}_A + \sum_{n=1}^{N} V(|D\rangle\langle A|_n + |A\rangle\langle D|_n) \\ &+ \sum_{n=1}^{N} g\big(|D\rangle\langle G|_n\,\hat{a} + |G\rangle\langle D|_n\,\hat{a}^\dagger\big)\,. \end{aligned} \tag{6.2}$$

The first line on the right hand side of Eq. (6.2) describes the contributions due to the energy difference $\Delta = E_A - E_D$ between the states $|A\rangle$ and $|D\rangle$, and the coherent coupling of the two states with strength $V$ associated with the tunneling of an electron from the donor to the acceptor. The second line describes Tavis-Cummings like coupling between the transition $|G\rangle \leftrightarrow |D\rangle$ and the cavity with strength $g$, in particular the absorption of a cavity photon by a pair in state $|G\rangle$, bringing it to the excited donor state $|D\rangle$, and the inverse process. This Hamiltonian part gives rise to two upper and lower polariton states $|P_\pm\rangle$ at energies $\pm g_c$. This term induces an indirect symmetric coupling between the pairs via the cavity, leading to collective effects.

1. Precisely, the rotating frame transformation is achieved by applying the unitary operator $\hat{U} = \exp\left[\mathrm{i}\omega_{DG}t\hat{N}_e\right]$, where the Hamiltonian and the states transform according to $\hat{H}' = \hat{U}\hat{H}\hat{U}^\dagger + \mathrm{i}(\partial_t\hat{U})\hat{U}^\dagger$ and $|\psi'\rangle = \hat{U}|\psi\rangle$, respectively.

The Hamiltonian in Eq. (6.2) commutes with $\hat{N}_e$ and thus cannot change the number of excitations. In the following we discuss the eigenstates of $\hat{H}$ in the single excitation limit $\langle \hat{N}_e \rangle \leq 1$ [see Fig. 6.1(c) for a level-diagram sketch]. Ignoring $|F\rangle$ for the moment, the total ground state $|G_c\rangle$ of the system ($\langle \hat{N}_e \rangle = 0$) is the state with all individual pairs in state $|G\rangle$, and no cavity photons. In the first excited manifold ($\langle \hat{N}_e \rangle = 1$), we find $2N-2$ dark states, labelled as $|k_\pm\rangle$, with zero photon weight and uncoupled from the cavity, as ensured by the condition $\left(\sum_n |G\rangle \langle D|_n\right) |k_\pm\rangle = \hat{a}\,|k_\pm\rangle = 0$. The coherent coupling between the states $|D\rangle$ and $|A\rangle$ induces a separation of the dark states into two sets of $N-1$ energetically degenerate states at energies $\Delta/2 \pm \sqrt{\Delta^2/4 + V^2}$. The label $k \neq 0$ indicates their $N-1$ "quasi-momenta" defined by a discrete Fourier transform, which means that there is a phase $\exp(-2\pi \mathrm{i} kn/N)$ for the $n$th pair in an excited state (see Appendix 6.A for their precise definition). The three remaining eigenstates of Eq. (6.2) are those states that couple to light. These states are labeled $|+\rangle$, $|-\rangle$, and $|X\rangle$, they are superpositions of $|P_\pm\rangle$ and $\sum_n |A\rangle_n / \sqrt{N}$, where $|A\rangle_n \equiv (|A\rangle \langle G|_n)\,|G_c\rangle$ labels the state with pair $n$ in state $|A\rangle$, and can be obtained by diagonalizing the remaining $3 \times 3$ block matrix in the Hamiltonian. Concerning the donor-acceptor pairs in state $|F\rangle$, we note that those pairs do not add any coherent contribution in the Hamiltonian Eq. (6.2). We can thus ignore them and construct the eigenstates as given above for a reduced number of pairs (see Appendix 6.A). Note that in our model we neglect disorder or vibrational couplings which would lead to a mixing of polariton states $|\pm, X\rangle$ with dark states $|k_\pm\rangle$ and give rise to effective coherent mixing and decay processes between those states [17, 40–44].

In order to model both coherent and dissipative dynamics, we use a Lindblad master equation [45]

$$\partial_t \hat{\rho} = -\mathrm{i}\left[\hat{H}, \hat{\rho}\right] + \sum_k \mathcal{D}\left[\hat{L}_k\right]\hat{\rho}\,, \tag{6.3}$$

with the dissipator $\mathcal{D}[\hat{L}]\hat{\rho} \equiv -\hat{L}^\dagger \hat{L}\hat{\rho} - \hat{\rho}\hat{L}^\dagger \hat{L} + 2\hat{L}\hat{\rho}\hat{L}^\dagger$, see below. The density matrix $\hat{\rho}$ is a hermitian matrix capturing all state populations on the diagonal and coherences between states on the off-diagonal. The sum runs over all decay channels, describing the dissipative processes characterized by Lindblad operators $\hat{L}_k$, induced by the exchange of energy between the system and a much larger "bath". Equation (6.3) is a valid description if the bath that the energy is transferred to is "Markovian" — that is, it thermalizes at a timescale much faster than the timescale associated with any coherent coupling back to the system. This is typically true for the background electromagnetic field in our setup. The incoherent decay processes considered here are described by

$2 + 3N$ Lindblad operators

$$\hat{L}_{\kappa_+} = \sqrt{\frac{\kappa_+}{2}}\hat{a}^\dagger \,, \tag{6.4}$$

$$\hat{L}_{\kappa} = \sqrt{\frac{\kappa}{2}}\hat{a} \,, \tag{6.5}$$

$$\hat{L}^{(n)}_{\Gamma_+} = \sqrt{\frac{\Gamma_+}{2}}\,|D\rangle\,\langle G|_n \ , \tag{6.6}$$

$$\hat{L}^{(n)}_{\Gamma} = \sqrt{\frac{\Gamma}{2}}\,|G\rangle\,\langle D|_n \ , \tag{6.7}$$

$$\hat{L}^{(n)}_{\eta} = \sqrt{\frac{\eta}{2}}\,|F\rangle\,\langle A|_n \ , \tag{6.8}$$

describing cavity pumping, cavity decay, pumping of individual pairs, decay of individual pairs back to the state $G$, and relaxation of pairs from $|A\rangle$ to $|F\rangle$, respectively.

In a system with dissipation, the spectrum is not characterized by the real eigenenergies of the Hamiltonian Eq. (6.2), but it is useful to characterize it by the complex eigenvalues of the non-hermitian Hamiltonian

$$\hat{H}_{\mathrm{NH}} = \hat{H} - \mathrm{i}\sum_k \hat{L}_k^\dagger \hat{L}_k \,, \tag{6.9}$$

which partly governs the density matrix evolution, as is seen by rewriting Eq. (6.3) as

$$\partial_t \hat{\rho} = -\mathrm{i}\left(\hat{H}_{\mathrm{NH}}\hat{\rho} - \hat{\rho}\hat{H}_{\mathrm{NH}}^\dagger\right) + 2\sum_k \hat{L}_k\hat{\rho}\hat{L}_k^\dagger. \tag{6.10}$$

The real parts of the eigenvalues of $\hat{H}_{\mathrm{NH}}$ correspond to the eigenenergies of the different states in the absence of dissipation, whereas the imaginary parts of the eigenvalues determine the width of the spectral peaks, corresponding to the rate at which one eigenstate decays into other eigenstates. For small dissipation, the eigenstates of the non-hermitian Hamiltonian are close to the eigenstates of Eq. (6.2). In contrast, for large dissipation, when the width of the peaks becomes comparable to their separation, different spectral peaks can merge. This happens e.g. at the transition from strong to weak coupling for increasing $\kappa$, when the difference between the eigenenergies of the two polaritons $|+\rangle$ and $|-\rangle$ vanishes, and instead two states with different decay rates, one more photon-like and one more exciton like, are the proper eigenstates of $\hat{H}_{\mathrm{NH}}$. Working with the full master equations and the non-hermitian Hamiltonian allows us to treat both weak and strong coupling in the same formalism.

## Discussion of possible model implementations

We choose our simple toy model in order to study fundamental collective quantum effects by using well established quantum optics tools, such as the adiabatic elimination

presented in Sec. 6.3. Here, we discuss in which limits this simple model can be a realistic model for experiments. In particular, we argue that the main effect observed in this manuscript, i.e. the cavity-enhanced transfer rates in the presence of dissipation, should also be observable in realistic setups.

The Hamiltonian Eq. (6.2) has been proposed by Mandal *et al.* [36] for an electron transfer setup with a single donor coupled to a cavity. There, it has been proposed that nanocrystal donors and organic molecular acceptors (e.g. CdS and anthraquinone [46]) could be a specific system to observe cavity modified electron transfer. In this case we identify the following states: $|G\rangle$ is the total ground state of the system before electron transfer, $|D\rangle$ corresponds to a state with an excited electron-hole pair in the nanocrystal. $|A\rangle$ corresponds to the state with an electron in the lowest unoccupied molecular orbital of the organic molecule and a hole remaining on the semiconductor. We consider the state $|A\rangle$ to have the same nuclear positions as the state $|D\rangle$, and is thus vibrationally excited. The additional state $|F\rangle$ corresponds to the vibrational ground state of the charged organic molecule.

Our setup is a generalization of the setup of Mandal *et al.* to many donor-acceptor pairs, but neglecting internal motion. Instead of a single pair [36], we consider $N = 10^4$ pairs, homogeneously coupled to the cavity field, e.g. by being placed in the central plane of a single-mode 210 nm Fabry-Perot cavity [see Fig. 6.1(a)]. For such a scenario, precise values of the parameters depend on the specific choices of the type and the size of the donor nanocrystal and the type of the organic molecule acceptor. Typical orders of magnitude are [36, 46, 47]: $g_c = 0.2\,\mathrm{eV}$, $\kappa = 1\,\mathrm{eV}$, $\Gamma = 3 \times 10^{-7}\,\mathrm{eV}$, $\Delta = 0.2\,\mathrm{eV}$, $V = 0.1\,\mathrm{eV}$, and $\omega_{DG} = 3\,\mathrm{eV}$. Note that here we consider the (untypical) case of a strong coherent donor-acceptor coupling strength $V$ outside the regime of validity of Marcus theory $V \ll k_B T$ [36]. For the internal relaxation in the acceptor, which we artificially summarize in the decay rate $\eta$, we choose a value of $10^{-2}\,\mathrm{eV}$. We choose it not too large to avoid blocking population transfer into the state $|A\rangle$ by the continuous Zeno effect [48], and not too small such that population can decay into $|F\rangle$. Note that the precise choice of $\eta$ does not influence our conclusions on the scaling behavior of transfer rates discussed below. Note further that here we focus on unidirectional electron transfer from donor to acceptor and thus ignore electron transfer back to the donor after the molecule has relaxed into the final state $|F\rangle$ [46]. We also ignore the dynamics of the hole in the semiconductor, which can be important in real experiments [46], and any temperature induced effects, as the thermal energy at room temperature $k_B T \approx 25\,\mathrm{meV}$ is much smaller than any energy scale associated with the Hamiltonian in Eq. (6.2). In the following, we discuss possible implementations of the incoherent photon pumping, and the role of motional degrees of freedom.

### Incoherent pumping

We assume that the experiment takes place in an external, incoherent electromagnetic field, which pumps photons into the system. Such an external field could be e.g. created by a lamp or sunlight, as long as there is sufficient emission around 3 eV. The light can be either absorbed by the cavity or by the donor-acceptor pairs, which is described

by Lindblad operators $\hat{L}_{\kappa_+}$ and $\hat{L}^{(n)}_{\Gamma_+}$, respectively. The geometry of the cavity and the incoming light can be used to control the relative magnitude of the two terms: If all incoming light is aimed at the cavity mirrors, only $\hat{L}_{\kappa_+}$ is non-zero, whereas if the light enters perpendicular to the cavity axis, $\hat{L}_{\kappa_+}$ will vanish and the $\hat{L}^{(n)}_{\Gamma_+}$ will be non-zero. In order to compare both processes, in the following we first keep $\Gamma_+ = 10^{-4}\Gamma$ constant and vary $\kappa_+$ [see Fig. 6.1(e) and 6.3], and later analyze the role of the individual processes (Figs. 6.4 and 6.5).

Note that for transitions with an excitation energy $\sim 3\,\mathrm{eV}$ as considered here, thermal excitations are negligible because the Boltzmann factor completely vanishes at room temperature $T$, $\exp[-\omega_{DG}/(k_B T)] \sim 10^{-61}$ ($k_B$ is the Boltzmann constant). For experiments that use transitions in the infrared spectrum, or work at higher temperatures, thermal photon populations might also be an incoherent photon source.

### External motion

For nanocrystal donors, we can consider stationary donor-acceptor pairs in the center of the cavity. However, one may argue that our results may also hold for some more general setups with external motion, such as liquid solutions. One can argue for this since the distances over which the pairs are moving on relevant time-scales are irrelevant, even in a gas phase at room temperature (see argument below). In experiments, collisions with solvent molecules might further suppress these already negligible effects. However, in many experiments solvents play a crucial role in the reaction by drastically modifying the local potential energy landscape. This could e.g. lead to energetic disorder and a mixing of bright and dark states, which for simplicity we do not consider here.

At room temperature, in a gas phase, donor-acceptor pairs move at velocities $v \sim \sqrt{k_B T/m} \lesssim 160\,\mathrm{m\,s^{-1}}$, where $m \gtrsim 100\,\mathrm{u}$ is the mass of a donor-acceptor pair, and $T \approx 300\,\mathrm{K}$ is the temperature. The bright state lifetime is $\sim 1/\kappa \approx 0.66\,\mathrm{fs}$, the dark state lifetime is $\sim 1/\eta \approx 66\,\mathrm{fs}$, during which each pair moves by $\sim v/\kappa \approx 0.1\,\mathrm{pm}$, or $v/\eta \approx 10\,\mathrm{pm}$, respectively. This is negligible compared to the wavelength of the cavity mode $\lambda \sim 210\,\mathrm{nm}$, so that entanglement between motion and electronic degrees of freedom should be suppressed over relevant timescales. Thermal motion also leads to a negligible Doppler broadening of $\sqrt{k_B T/(mc^2)}\omega_{DG} \approx 1.6\,\mu\mathrm{eV}$.

### Internal motion

By internal motion, we mean the relative motion of the nuclei in the donor and the acceptor, i.e. vibrations, which generally couple to the electronic degrees of freedom. Depending on the type of donors and acceptors, this coupling can be large and lead to important effects such as vibrational decoupling [12, 49], conical intersections [15, 17], or even entanglement between vibrations and electronic degrees of freedom [50]. In nanocrystals, however, this coupling is typically small [36]. Therefore, for such systems it can be realistic to neglect it. For the organic molecule acceptors we include the effects of internal motion in the effective rate $\eta$. This then allows for a disentangled

description, where both internal and external motional degrees of freedom separate from the electronic dynamics. In the following, we will only focus on the electronic dynamics.

## 6.3. Adiabatic Elimination

Numerically simulating the full master equation Eq. (6.3) becomes impossible for just a few donor-acceptor pairs $N \gtrsim 10$ even for our simplified model, as the number of elements in the density matrix scales as $4^{2N}$. We thus proceed by introducing an adiabatic elimination procedure which allows us to significantly reduce this complexity. Adiabatic elimination is a standard technique in quantum optics [31, 32, 51, 52] that can be used if the system can be split into fast and slow evolving subspaces. In this case, the fast subspace is typically close to its equilibrium state. Adiabatic elimination then allows us to eliminate the fast degrees of freedom by approximating them with their equilibrium value, and derive an effective master equation for the slow degrees of freedom only, significantly reducing the complexity of the problem. Here, we choose the photons and the excited states $|D\rangle$ or $|A\rangle$ as fast degrees of freedom and the states $|G\rangle$ and $|F\rangle$ as slow ones, such that the effective master equation following adiabatic elimination describes direct population transfer from $|G\rangle$ to $|F\rangle$ [see Fig 6.1(b)]. In our case the elimination condition is fulfilled when the excited states decay much faster than they are pumped, and thus $\langle \hat{N}_e \rangle \ll 1$.

Adiabatic elimination can be formalized by defining projection operators, $\hat{P} = \bigotimes_n (|G\rangle\langle G|_n + |F\rangle\langle F|_n)$ and $\hat{Q} = \hat{I} - \hat{P}$, into the slow and fast manifold, respectively, where $\bigotimes_n$ denotes a tensor product over all pairs. The goal is to derive an effective equation of motion for $\hat{P}\hat{\rho}\hat{P}$ under the condition $\langle \hat{N}_e \rangle \ll 1$. In order to simplify notation, we define superoperators, which are linear operators acting on operators, i.e. they can be expressed as matrices acting on operators written as vectors. The relevant projection superoperators are $\mathcal{P}$ and $\mathcal{Q} = \mathcal{I} - \mathcal{P}$, where $\mathcal{I}$ is the superoperator identity. They are defined by $\mathcal{P}\hat{\rho} = \hat{P}\hat{\rho}\hat{P}$, and $\mathcal{Q}\hat{\rho} = \hat{P}\hat{\rho}\hat{Q} + \hat{Q}\hat{\rho}\hat{P} + \hat{Q}\hat{\rho}\hat{Q}$, respectively. We further define the evolution superoperator $\mathcal{L} = -\mathrm{i}[\hat{H}, \cdot] + \sum_k \mathcal{D}[\hat{L}_k]$, such that the master equation Eq. (6.3) can be written as $\partial_t \hat{\rho} = \mathcal{L}\hat{\rho}$. Superoperators can be written as a tensor product of two operators: one acting from the right as a transpose, and one acting from the left that is: $\mathcal{O}\vec{\rho} = (\hat{O}_1 \otimes \hat{O}_2)\vec{\rho} \equiv \hat{O}_2\hat{\rho}\hat{O}_1^T$. In general, a superoperator is the sum of multiple such terms. For example, we can write $\mathcal{P} = \hat{P} \otimes \hat{P}$, $\mathcal{Q} = \hat{P} \otimes \hat{Q} + \hat{Q} \otimes \hat{P} + \hat{Q} \otimes \hat{Q}$ and

$$\mathcal{L} = -\mathrm{i}\hat{I} \otimes \hat{H}_{\mathrm{NH}} + \mathrm{i}\hat{H}_{\mathrm{NH}}^* \otimes \hat{I} + 2\sum_k \hat{L}_k^* \otimes \hat{L}_k \,, \tag{6.11}$$

where $\hat{O}^* \equiv (\hat{O}^\dagger)^T$ denotes the element-wise complex conjugate of an operator $\hat{O}$.

As shown by Finkelstein-Shapiro *et al.* [31], with these definitions we can write the effective master equation as

$$\partial_t(\mathcal{P}\hat{\rho}) = \mathcal{L}_{\mathrm{eff}}(\mathcal{P}\hat{\rho}) \tag{6.12}$$

$$\mathcal{L}_{\mathrm{eff}} = \mathcal{P}\mathcal{L}\mathcal{P} - \mathcal{P}\mathcal{L}\mathcal{Q}(\mathcal{Q}\mathcal{L}\mathcal{Q})^{-1}\mathcal{Q}\mathcal{L}\mathcal{P} \,, \tag{6.13}$$

where the first term in $\mathcal{PLP}$ describes the direct evolution in the slow subspace (i.e. $|G\rangle$ and $|F\rangle$ in our case), the second term $\mathcal{PLQ}(\mathcal{QLQ})^{-1}\mathcal{QLP}$ describes an excitation into the excited subspace, some excited state evolution, followed by a decay back into the slow subspace. The formula Eq. (6.13) strongly resembles other forms of perturbation theory, and reduces to textbook second order perturbation theory in quantum mechanics [53], if all dissipative terms vanish. In this case $\mathcal{PLQ}$ and $\mathcal{QLP}$ reduce to the perturbation Hamiltonian, and $\mathcal{PLP} + \mathcal{QLQ}$ reduces to the bare Hamiltonian. In the remainder of this section, we evaluate $\mathcal{L}_{\text{eff}}$ by only considering a single excitation for the excited state propagator $(\mathcal{QLQ})^{-1}$. The solution is given below by Eqs. (6.14) and (6.21) and a formula for the instantaneous transfer rate can be cast into the simple analytical form of Eq. (6.22).

We first discuss the individual contributions to the dynamics governed by Eq. (6.13):
The term $\mathcal{PLP}$ describes the dynamics confined to the ground state manifold. In our model this is only loss of population into the excited state due to pumping of the cavity ($\kappa_+$) or via pumping of individual donors ($\Gamma_+$) by the external incoherent light source, leading to

$$\begin{aligned}\mathcal{PLP} = &-\hat{P}\otimes\hat{P}\left(\frac{\kappa_+}{2}+\frac{\Gamma_+}{2}\hat{N}_G\right)\\ &-\left(\frac{\kappa_+}{2}+\frac{\Gamma_+}{2}\hat{N}_G\right)\hat{P}\otimes\hat{P}.\end{aligned} \tag{6.14}$$

The term $\mathcal{QLP}$ describes the population transfer from the ground state to the excited state manifold, due to the pumping terms above:

$$\mathcal{QLP} = \kappa_+\left(\hat{a}^\dagger\right)^*\otimes\hat{a}^\dagger + \Gamma_+\sum_n\left(|D\rangle\langle G|_n\right)^*\otimes|D\rangle\langle G|_n\,. \tag{6.15}$$

The term $\mathcal{PLQ}$ describes decay from the excited state into the ground state, either due to photon loss from the cavity ($\kappa$), due to spontaneous emission from the molecules back into the ground state ($\Gamma$), or due to relaxation of the acceptor state ($\eta$):

$$\begin{aligned}\mathcal{PLQ} = &\kappa\hat{a}^*\otimes\hat{a} + \Gamma\sum_n\left(|G\rangle\langle D|_n\right)^*\otimes|G\rangle\langle D|_n\\ &+\eta\sum_n\left(|F\rangle\langle A|_n\right)^*\otimes|F\rangle\langle A|_n\,.\end{aligned} \tag{6.16}$$

The term $\mathcal{QLQ}$ describes the excited state evolution. This includes coherent transfer between donor state $|D\rangle$ and acceptor state $|A\rangle$, the coherent energy exchange between donor state $|D\rangle$ and cavity, as well as population loss due to emission:

$$\begin{aligned}\mathcal{QLQ} = &-\mathrm{i}\hat{I}\otimes\hat{Q}\hat{H}_{\text{NH}}\hat{Q} + \mathrm{i}\hat{Q}\hat{H}^*_{\text{NH}}\hat{Q}\otimes\hat{I}\\ &-\mathrm{i}\hat{Q}\otimes\hat{P}\hat{H}_{\text{NH}}\hat{P} + \mathrm{i}\hat{P}\hat{H}^*_{\text{NH}}\hat{P}\otimes\hat{Q}\,,\end{aligned} \tag{6.17}$$

with the projections of the non-hermitian Hamiltonian

$$\hat{P}\hat{H}_{\mathrm{NH}}\hat{P} = -\mathrm{i}\frac{\kappa_+}{2} - \mathrm{i}\frac{\Gamma_+}{2}\hat{N}_G, \tag{6.18}$$

$$\begin{aligned}\hat{Q}\hat{H}_{\mathrm{NH}}\hat{Q} = {} & g\sum_n \left(|D\rangle\langle G|_n\,\hat{a} + |G\rangle\langle D|_n\,\hat{a}^\dagger\right) \\ & + V\sum_n \left(|A\rangle\langle D|_n + |D\rangle\langle A|_n\right) \\ & + \left(\Delta - \mathrm{i}\frac{\eta}{2}\right)\hat{N}_A - \mathrm{i}\frac{\kappa}{2}\hat{a}^\dagger\hat{a} - \mathrm{i}\frac{\Gamma}{2}\hat{N}_D.\end{aligned} \tag{6.19}$$

Note that since we only consider a single excitation, there can be neither further pumping from the excited state, nor relaxation into the excited state.

We can now directly proceed to diagonalize $\mathcal{QLQ}$ using the eigenstates and complex eigenenergies of $\hat{H}_{\mathrm{NH}}$ discussed above and given in Appendix 6.A. We label the eigenstates $|\mathcal{N}_F, \psi\rangle$, where $\mathcal{N}_F = \{i_1, \ldots, i_{N-M}\}$ is the set of pairs in state $|F\rangle$, $|\mathcal{N}_F|$ and $M = N - |\mathcal{N}_F|$ are the numbers of pairs in and outside of state $|F\rangle$, respectively, and $\psi \in \{G_c, k_\pm, +, -, X\}$ is one of the eigenstates of $\hat{H}_{\mathrm{NH}}$ for given $\mathcal{N}_F$. The corresponding complex eigenenergies are denoted as $E_\psi^{(M)}$. We label the elements of the excited state propagator $(\mathcal{QLQ})^{-1}$ by $\mathcal{G}$, with elements

$$\begin{aligned}&\mathcal{G}(\mathcal{N}_F', \psi; \mathcal{N}_F, \phi) \\ \equiv&(\langle\mathcal{N}_F, \psi| \otimes \langle\mathcal{N}_F', \phi|)(\mathcal{QLQ})^{-1}(|\mathcal{N}_F, \psi\rangle \otimes |\mathcal{N}_F', \phi\rangle) \\ =&\left[\mathrm{i}\left(E_\psi^{(N-|\mathcal{N}_F|)}\right)^* - \mathrm{i}E_\phi^{(N-|\mathcal{N}_F'|)}\right]^{-1},\end{aligned} \tag{6.20}$$

Using the expressions $\mathcal{QLP}$ and $\mathcal{PLQ}$ in the diagonal basis of $\hat{H}_{\mathrm{NH}}$ given in Appendix 6.C, calculating $\mathcal{PLQ}(\mathcal{QLQ})^{-1}\mathcal{QLP}$ is straightforward. We find:

$$\begin{aligned}&\mathcal{PLQ}(\mathcal{QLQ})^{-1}\mathcal{QLP} = \\ &\sum_{\substack{\mathcal{N}_F, \mathcal{N}_F' \\ \psi, \phi \in \{k_\pm, \pm, X\}}} \Bigg\{ \left[\kappa_+\left(c_\psi^{\mathrm{ph}}\right)^* c_\phi^{\mathrm{ph}} + \Gamma_+ \sum_n \left(c_\psi^{D_n}\right)^* c_\phi^{D_n}\right] \mathcal{G}(\mathcal{N}_F, \psi; \mathcal{N}_F', \phi) \\ &\quad \times \left[\kappa\left(\bar{c}_\psi^{\mathrm{ph}}\right)^* \bar{c}_\phi^{\mathrm{ph}} + \Gamma \sum_{n'} \left(\bar{c}_\psi^{D_{n'}}\right)^* \bar{c}_\phi^{D_{n'}}\right] \\ &\quad \times |\mathcal{N}_F, G\rangle\langle\mathcal{N}_F, G| \otimes |\mathcal{N}_F', G\rangle\langle\mathcal{N}_F', G| \\ &+ \left[\kappa_+\left(c_\psi^{\mathrm{ph}}\right)^* c_\phi^{\mathrm{ph}} + \Gamma_+ \sum_n \left(c_\psi^{D_n}\right)^* c_\phi^{D_n}\right] \mathcal{G}(\mathcal{N}_F, \psi; \mathcal{N}_F', \phi) \left[\eta \sum_{n'} \left(\bar{c}_\psi^{A_{n'}}\right)^* \bar{c}_\phi^{A_{n'}}\right] \\ &\quad \times |\mathcal{N}_F \dot{\cup} \{n\}, G\rangle\langle\mathcal{N}_F, G| \otimes |\mathcal{N}_F' \dot{\cup} \{n\}, G\rangle\langle\mathcal{N}_F', G| \Bigg\},\end{aligned} \tag{6.21}$$

where $c_\phi^\psi$ and $\bar{c}_\phi^\psi$ are state overlaps defined in Appendix 6.B, and the state notation "$\mathcal{N}_F \dot{\cup} \{n\}$" indicates that an electron was transferred in pair $n$, bringing it from state $|G\rangle$ to state $|F\rangle$. The first two lines in the right hand side of Eq. (6.21) describe processes that do not contribute to population transfer: A photon is injected into the cavity ($\kappa_+$ terms) or a molecule is brought into the donor state ($\Gamma_+$ terms), and then after some coherent evolution the excitation is lost back into the initial state via cavity decay ($\kappa$ terms) or spontaneous emission ($\Gamma$ terms). The third and fourth line describe population transfer of a donor-acceptor pair from the ground state $|G\rangle$ to the final state $|F\rangle$: A pair is excited or a photon is absorbed by the cavity, the excitation is transferred to a pair in the acceptor state, and the excitation is lost via the $\hat{L}_\eta$ channel to reach the final state $|F\rangle$, as discussed in detail in Sec. 6.4. Note that no coherences between states with different $\mathcal{N}_F$ are generated by these terms. Thus there will be no coherences between $|G\rangle$ and $|F\rangle$ other than those already present in the initial state. For the default case where in the initial state $\mathcal{N}_F' = \mathcal{N}_F$, we use the short hand notation for the propagator $\mathcal{G}(M, \psi, \phi) = \mathcal{G}(\mathcal{N}_F, \psi; \mathcal{N}_F, \phi)$ with $M = N - |\mathcal{N}_F|$.

# 6.4. Results

## Rate equation

Our effective master equation Eq. (6.13) with the term of Eq. (6.21) describes purely dissipative population transfer from $|G\rangle$ to $|F\rangle$. Only the last two lines in Eq. (6.21) contribute. The transfer is characterized by the instantaneous transfer rate from states $|G\rangle$ to $|F\rangle$ [see Fig. 6.1(b)], that is, the situation where $M$ pairs are transiently in state $|G\rangle$,

$$r = \sum_{\phi,\psi} \left[ \kappa_+ \left( c_\psi^{\mathrm{ph}} \right)^* c_\phi^{\mathrm{ph}} + \Gamma_+ \sum_n \left( c_\psi^{D_n} \right)^* c_\phi^{D_n} \right] \times \mathcal{G}(M, \psi, \phi) \left[ \eta \sum_{n'} \left( \bar{c}_\psi^{A_{n'}} \right)^* \bar{c}_\phi^{A_{n'}} \right]. \tag{6.22}$$

This instantaneous transfer rate $r$, which can be computed efficiently for arbitrary system parameters, is the main result of our paper.

The rate $r$ in Eq. (6.22) is determined by a sum over contributions from the eigenstates of $\hat{H}_{\mathrm{NH}}$, $\psi, \phi \in \{k_\pm, \pm, X\}$. We identify two independent processes driving population transfer, given by the $\kappa_+$ and $\Gamma_+$ terms, respectively: i) Cavity photons that are incoherently excited at rate $\kappa_+$ are transformed into excitations of $|D\rangle$ and $|A\rangle$ via *collective* excitations $\{\pm, X\}$, which is reflected by the state overlaps of those eigenstates with the photon mode, $c_\psi^{\mathrm{ph}}$ (see Appendix 6.B for state overlap definitions). Note that the overlap with the (localized) dark states vanishes $c_{k_\pm}^{\mathrm{ph}} = 0$. The second line in Eq. (6.22) describes a transfer of the excitation to the final state $|F\rangle$ via the acceptor states $|A\rangle$, which is seen by the overlaps $\bar{c}_\psi^{A_n}$, and the decay rate $\eta$ for decaying into the final state $|F\rangle$;

ii) Alternatively, each molecule in state $|G\rangle$ can be *individually* excited into the donor states $|D\rangle$ at rate $\Gamma_+$, which overlaps with all states $\{k_\pm, \pm, X\}$ via $c_\psi^{D_n}$. With the same mechanism as in i) [second line in Eq. (6.22)] the excitation can then be transferred into the acceptor state $|A\rangle$, and finally to the state $|F\rangle$.

The "propagator" relevant to both processes, is [from Eq. (6.20)]:

$$\mathcal{G}(M,\psi,\phi) = \left[\mathrm{i}\left(E_\psi^{(M)}\right)^* - \mathrm{i}E_\phi^{(M)}\right]^{-1} \tag{6.23}$$

with $E_\psi^{(M)}$ the complex excited state eigenvalues. For $\psi = \phi$, $\mathcal{G}$ reduces to the inverse decay rate, i.e. the life-time, of the excited state $\psi$. Although all excited states decay fast compared to pumping rates, in the propagator $\mathcal{G}$ transfer via relatively long-lived states is preferred over transfer via states that decay quickly back into the state $|G\rangle$.

The relative importance of the two processes i) and ii) above depends directly on the relative magnitude of $\kappa_+$ and $\Gamma_+$ [see Fig. 6.1(d)], on the instantaneous ground state population $M$, and indirectly on the other system parameters via state overlaps $c_\phi^\psi$, and the propagator $\mathcal{G}$. Note that Eq. (6.22) is independent of the total number of pairs $N$, as pairs in the state $|F\rangle$ do not participate in any dynamics. Fig. 6.1(e) shows the dependence of the rate $r$ on the collective cavity coupling $g_c = g\sqrt{N}$ for different values of $\kappa_+$. For $\kappa_+ = 0$, only the $\Gamma_+$-channels contribute and the transfer rate is essentially independent of $g_c$. This indicates that the transfer occurs dominantly via dark states, which are unmodified by $g_c$. In contrast, if we increase $\kappa_+$, we find a strong dependence of $r$ on $g_c$. In both extreme cases $g_c = 0$ and $g_c \to \infty$, the $\kappa_+$-channels do not contribute, but the transfer rate $r$ has a maximum for a small $g_c$. The relative importance of the two channels and their dependence on different system parameters are discussed in detail in Subsection 6.4.

## Time evolution

From Eq. (6.22), we can numerically compute the $|G\rangle \to |F\rangle$ transfer time evolution. In particular, we are interested in the evolution of the populations $\langle \hat{N}_G \rangle$ and $\langle \hat{N}_F \rangle$ in states $|G\rangle$ and $|F\rangle$, respectively. With the rates from Eq. (6.22) we can do this easily for very large system sizes $N \sim 10^4$. To do so, we describe the density matrix as a statistical mixture of pure states, each of which can be stochastically evolved in time. Such a technique is well developed and known as quantum trajectories or quantum Monte-Carlo wavefunction method [54]. Here, such a quantum trajectory algorithm is trivially simplified by the fact that there is no coherence in the effective dynamics, i.e. $\hat{H}_{\text{eff}} = 0$ (see Appendix 6.D).

To check the validity of our adiabatic elimination, we initially compare our results to a numerical simulation of the full master equation (6.3) for a small system. For this simulation we also use a quantum trajectory approach [54]. In Fig. 6.2 we compare the results for $N = 8$. We find that for typical parameters, the elimination condition $\langle \hat{N}_e \rangle \ll 1$ is fulfilled and both descriptions match even for the largest considered cavity drive that we consider, $\kappa_+/\kappa = 10^{-2}$. Note that when varying $N$, to make small and

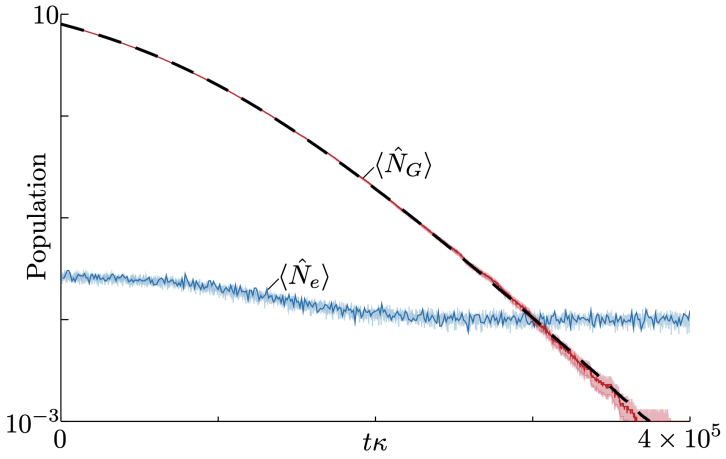


Figure 6.2. – Test of validity for a small system. Comparison of the time evolution (log-log scale) of state populations described by the full master equation (continuous lines, red and blue) with the ones obtained from the effective rate equation Eq. (6.22) (dashed black line) for $N = 8$. The upper red and dashed black lines show the ground state population $\langle \hat{N}_G \rangle$, the blue line the excited state population $\langle \hat{N}_e \rangle$ (which vanishes in the limit of validity of the effective equation). For the full simulations, the shaded area corresponds to two standard deviations of the mean calculated from $10^4$ quantum trajectories. Parameters for the simulations: $g_c = 0.2\kappa$, $\kappa_+ = 10^{-2}\kappa$, $\Gamma = 3 \times 10^{-7}\kappa$, $\Gamma_+ = \Gamma/6$, $\Delta = 0.2\kappa$, $V = 0.1\kappa$, and $\eta = 10^{-2}\kappa$.

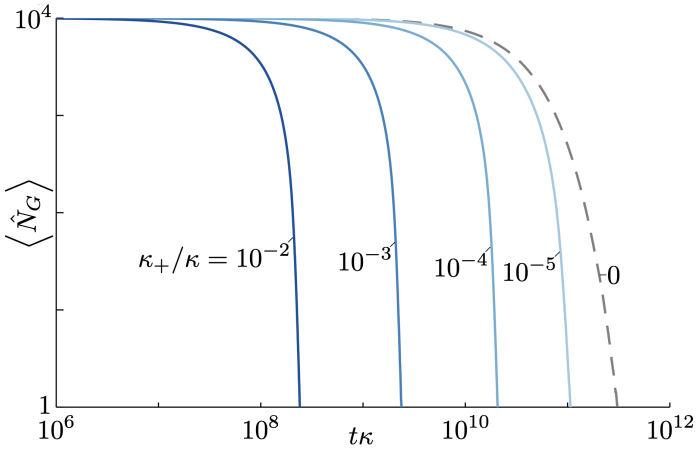


Figure 6.3. – Large system time evolution with initially $N = 10^4$ ground-state pairs. Shown is the evolution of $\langle \hat{N}_G \rangle$ for different cavity pumping rates $0 \leq \kappa_+ \leq 10^{-2}\kappa$ (log-log scale). We simulate Eq. (6.22) for with $g_c = 0.2\kappa$, $\Gamma = 3 \times 10^{-7}\kappa$, $\Gamma_+ = 10^{-4}\Gamma$, $\Delta = 0.2\kappa$, $V = 0.1\kappa$, and $\eta = 10^{-2}\kappa$.

large system sizes comparable we approximately match the collective cavity coupling $g_c = \sqrt{N}g$ and pumping rate $N\Gamma_+$ (instead of $g$ and $\Gamma_+$). In this way we achieve an equivalent mixing of photons and excited states and equivalent total incoherent transfer rates.

The algorithm to compute $\langle \hat{N}_G \rangle$ from Eq. (6.22) scales only linearly with the number of pairs, which allows us to consider $N = 10^4$ pairs in Fig. 6.3. In this figure we show the time evolution of the number of ground state donor-acceptor pairs for different values of $\kappa_+$. We observe that a weak cavity pump of only $\kappa_+/\kappa = 10^{-5}$ already leads to a significant acceleration of the ground-state depletion at times when only few ground-state pairs remain coupled to the cavity. While the initial dynamics is barely modified, we find that the long-time depletion becomes even super-exponential. For larger values of $\kappa_+/\kappa$, also the earlier dynamics speeds up. For example increasing $\kappa_+/\kappa$ from $10^{-3}$ to $10^{-2}$, the entire dynamics shifts by a factor of 10, indicating that the transfer is completely dominated by the cavity in this regime, as the transfer rate $r$ is proportional to the rate at which the cavity is pumped $\kappa_+$.

## Discussion of the rate equation

In this subsection, we analyze the dependence of the transfer rate $r$ given by Eq. (6.22) on the various model parameters, and identify for which parameters the presence of a cavity increases $r$. Fig. 6.4(a) to (c) are contour plots of the rate modification due to the cavity: $r_{\mathrm{cav}}/r_{\mathrm{bare}}$, where $r_{\mathrm{cav}}$ is given by setting $\Gamma_+ = 0$ in Eq. (6.22), and $r_{\mathrm{bare}}$ is given by setting $\kappa_+ = 0$ and $g = 0$ in Eq. (6.22), describing transfer via the cavity only and without the cavity, respectively. The white lines in Fig. 6.4 highlight parameter points where $r_{\mathrm{cav}} = r_{\mathrm{bare}}$, i.e. where both setups perform equally well. We set $\kappa_+/\kappa = \Gamma_+/\Gamma = 10^{-3}$ for both scenarios to compare situations with the same driving field: If interaction with the background photon field is the dominant loss and excitation mechanism, we have $\kappa_+/\kappa = \langle \hat{n}_{\mathrm{ph}} \rangle/(1 + \langle \hat{n}_{\mathrm{ph}} \rangle) = \Gamma_+/\Gamma$, for $\langle \hat{n}_{\mathrm{ph}} \rangle$ the average photon density in the background field. This can be shown by a standard derivation of the master equation [55]. Here we analyze the experimentally relevant limit (see Sec. 6.2), where $\kappa \gg \Gamma$, and thus $\kappa_+ \gg \Gamma_+$. Note that in an opposite limit, the bare transfer would dominate over the one via the cavity.

In all contour plots we can see that for vanishing cavity coupling $g_c = \sqrt{N}g \to 0$, the cavity transfer rate vanishes $r_{\mathrm{cav}} \to 0$. This happens because for $g_c = 0$, photons cannot be transformed into donor states $|D\rangle$, and thus cannot drive any population transfer. Similarly, for diverging coupling $g_c \to \infty$, $r_{\mathrm{cav}}$ also vanishes, because both upper and lower polariton states [i.e. eigenstates of the second line of Eq. (6.2), $|P_\pm\rangle$ in Fig. 6.1(c)] are far detuned from the state $|A\rangle$. This suppresses coherent population transfer from the polariton states to $|A\rangle$. Between both extreme cases, we find an optimal value of $g_c$, for which $r_{\mathrm{cav}}$ is maximal and the cavity enhances the transfer. Notably, for a large parameter regime, the optimal $g_c$ lies in the weak coupling regime $g_c \leq \kappa/4$, a regime where the polariton splitting is not observable [2].

2. $g_c \leq \kappa/4$ is the condition for having two eigenstates with different eigenenergies However, the

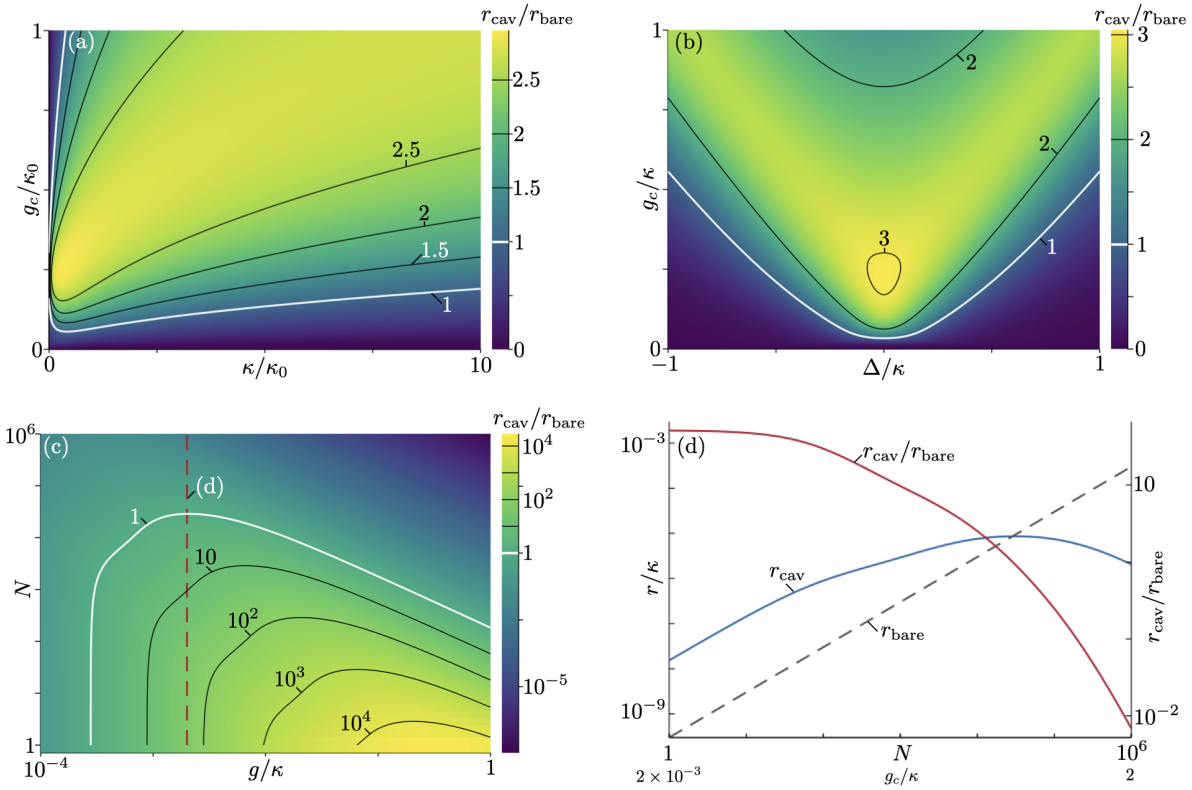


Figure 6.4. – Cavity modification of the transfer rate. (a, b, c) Contour plots of the transfer rate $r_{\mathrm{cav}}/r_{\mathrm{bare}}$. $r_{\mathrm{cav}}$ is given by setting $\kappa_+ = 10^{-3}\kappa$ and $\Gamma_+ = 0$ in Eq. (6.22); $r_{\mathrm{bare}}$ is given by setting $\kappa_+ = 0$, $\Gamma_+ = 10^{-3}\Gamma$ and $g = 0$ in Eq. (6.22) (see text). We define normalized units $\kappa_0$ (e.g. $\kappa_0 = 1\,\mathrm{eV}$) and set: $V = 0.1\kappa_0$, $\Gamma = 3 \times 10^{-7}\kappa_0$, and $\eta = 10^{-2}\kappa_0$. Black and white lines are contours of constant cavity enhancement as indicated in the colorbar, white lines correspond to $r_{\mathrm{cav}} = r_{\mathrm{bare}}$. (a) $r_{\mathrm{cav}}/r_{\mathrm{bare}}$ as a function of $g_c$ and $\kappa$ for $N = 10^4$ and $\Delta = 0.2\kappa_0$. (b) $r_{\mathrm{cav}}/r_{\mathrm{bare}}$ as a function of $g_c$ and $\Delta$ for $N = 10^4$ and $\kappa = \kappa_0$. (c) $r_{\mathrm{cav}}/r_{\mathrm{bare}}$ as a function of $N$ and $g$ for $\Delta = 0.2\kappa_0$ and $\kappa = \kappa_0$ (log-scale for all axes and colorbar). (d) $r_{\mathrm{cav}}$ (blue solid, left axis) and $r_{\mathrm{bare}}$ (grey dashed, left axis) and $r_{\mathrm{cav}}/r_{\mathrm{bare}}$ (red solid, right axis) as a function of $N$, corresponding to a cut (red dashed line) in (c) with $g = 2 \times 10^{-3}\kappa_0$. The horizontal axis shows $g_c = g\sqrt{N}$ as second scale (log-scale on all axes).

For which parameters weak or strong coupling is optimal is e.g. seen in Fig. 6.4(a), which shows $r_{\mathrm{cav}}/r_{\mathrm{bare}}$ as a function of $\kappa$ and $g_c$ in normalized units $\kappa_0$. In the limit of small $\kappa$, the enhancement is maximal for a collective coupling strength matching the energy difference between states $|A\rangle$ and $|D\rangle$, $g_c \sim \Delta = 0.2\kappa_0$. This can be understood from taking the limit $V \to 0$ in the Hamiltonian Eq. (6.2). Then, $|A\rangle$ is in resonance with an upper polariton state [$|P_+\rangle$ in Fig. 6.1(c)] of the Tavis-Cummings part [second line in Eq. (6.2)]. We thus find that in this strong coupling limit, the enhancement is efficiently mediated by a polaritonic state. In contrast, for larger values of $\kappa$, $r_{\mathrm{cav}}$ is maximal for a $g_c$ inside the weak coupling regime. There, although no polariton splitting is present, the mixing between cavity and donor state induced by the non-hermitian Hamiltonian (6.9) can still be important. Thus, there is an excited state with both cavity and $|A\rangle$ state contribution which can enable coherent transfer, although in many cases the cavity photon decays before this coherent transfer takes place. For a given $g_c$ there exists an optimal finite $\kappa > 0$. This optimal $\kappa$ is larger than zero, since in the limit $\kappa \to 0$ the cavity cannot be excited by the incoherent pump. In the limit $\kappa \to \infty$, the cavity photons are lost before they can be absorbed by a donor-acceptor pair. We find that lines of constant enhancement correspond to $g_c \propto \sqrt{\kappa}$, indicating that the proper figure of merit is the collective Purcell factor $g_c^2/\kappa$, which is not tied to weak or strong coupling.

Similar effects can be observed for variable energy difference between the states $|D\rangle$ and $|A\rangle$ in Fig. 6.4(b), which shows $r_{\mathrm{cav}}/r_{\mathrm{bare}}$ as a function of $\Delta$ and $g_c$. For large $\Delta$, the transfer efficiency is maximal for $g_c \approx |\Delta|$. We again attribute these points of efficient populations transfer to respective resonances with the upper and lower polariton states of the Tavis-Cummings part in the Hamiltonian. For larger $g_c \gg |\Delta|$, the large detuning leads to a large suppression of the transfer rate, as both polaritons are out of resonance. In contrast, for small values of $|\Delta|$, $r_{\mathrm{cav}}/r_{\mathrm{bare}}$ is maximal for a small $g_c$ close to the weak coupling regime. Note that we still find significant cavity enhancement inside this weak coupling regime.

In Fig. 6.4(c) we analyze $r_{\mathrm{cav}}/r_{\mathrm{bare}}$ as function of $g$ and $N$. Here, we find that increasing $N$ decreases the cavity enhancement factor $r_{\mathrm{cav}}/r_{\mathrm{bare}}$, although it increases the collective cavity coupling $g_c$. Fig. 6.4(d) is a cut through Fig. 6.4(c) for fixed $g$. For increasing $N$, initially the collective effects increase the cavity transfer rate $r_{\mathrm{cav}}$. However, this effect competes with an increase of $r_{\mathrm{bare}} \propto N$ due to the increasing number of transfer channels. For small $N$, the collective effects compensate for the increasing number of transfer channels, keeping $r_{\mathrm{cav}}/r_{\mathrm{bare}}$ approximately constant. This can also be seen as vertical sections of contours in Fig. 6.4(c) for small $g$. Further increasing $N$, the collective enhancement becomes weaker and $r_{\mathrm{cav}}/r_{\mathrm{bare}}$ decreases. For $g_c \gtrsim (\kappa, \Delta)$, $r_{\mathrm{cav}}$ decreases for increasing $N$ due to a too large polariton splitting. Note that here $N$ is the number of pairs in state $|G\rangle$, such that even if initially the enhancement is only weak, at later times a larger enhancement can be observed [see also Fig. 6.3].

In the analysis of Fig. 6.4 we found that the main features of the cavity modification

difference can be only spectrally resolved at a larger $g_c$. Note also that we neglected other dissipation $\Gamma, \eta \ll \kappa$, in this approximate condition.

of initial transfer rates can be understood in terms of resonance conditions of collective bright states, which is included in the state overlaps [compare Fig. 6.1(c)]. It is important to point out that in general the dynamics can also involve dark states, populated through individual pumping. Therefore, lastly we also analyze the instantaneous rates with both cavity ($\kappa_+ > 0$) and individual pair ($\Gamma_+ > 0$) pumping. To distinguish a scaling in the number of pairs $N$ from simple polaritonic resonance conditions, we now compare rates as function of the collective cavity coupling, $g_c = g\sqrt{N}$ and $N$ in Fig. 6.5. In general, we now find that, depending on $g_c$, for large enough $N$, the overall instantaneous transfer rate $r_{\mathrm{tot}}$ exhibits a dependence on $N$ [Fig. 6.5(a)]. This can be explained by a dominance of dark state transfer for large $N$ [as sketched in Fig. 6.1(d)]. This is exemplified in Fig. 6.5(b), where we compare the contributions to $r_{\mathrm{tot}} = r_{\mathrm{cav}} + r_{\mathrm{ind}}$, which besides the cavity rate $r_{\mathrm{cav}}$ now also contains the bare individual pumping part $r_{\mathrm{ind}}$. We define the latter by setting $\kappa_+ = 0$ in Eq. (6.22), which is different from $r_{\mathrm{bare}}$ which is defined outside the cavity by setting $g = \kappa_+ = 0$. Note that in accordance with the discussion above, $r_{\mathrm{cav}}$ does not depend on $N$ for constant $g_c$, whereas $r_{\mathrm{ind}}$ grows with increasing $N$. We find that for large enough $N$, $r_{\mathrm{tot}}$ is dominated by $r_{\mathrm{ind}}$. Furtheremore, for large $N$, the cavity influence on the individual pumping vanishes and $r_{\mathrm{ind}} \approx r_{\mathrm{bare}}$. This can be understood from the fact that the states excited by $\Gamma_+$ have vanishing polariton contribution [$c^{D_n}_{\pm,X} \to 0$ as $N \to \infty$ in Eq. (6.22)], and in our model the dark states $|k_\pm\rangle$ decouple from the cavity. Note that in the regime of small $N$, where individual pumping excites a significant fraction of bright states, we find $r_{\mathrm{ind}} < r_{\mathrm{bare}}$.

It is worth to re-emphasize that the dynamics is governed by a non-linear rate equation, which implies that the instantaneous rate from Eq. (6.22) also depends on time. Then, the time dependence of resonance conditions, together with the dependence on rates on $N$ due to bright and dark state contributions from Fig. 6.5, give rise to non-trivial decay dynamics, as the super-exponential behavior observed in Fig. 6.3.

Finally, we want to emphasize that we conclude from Fig. 6.4, that for the numbers relevant for nanocrystal setups as described in Sec. 6.2, the initial transfer rate can be enhanced by a factor $r_{\mathrm{cav}}/r_{\mathrm{bare}} \sim 2.5$ in the cavity-coupled scenario.

## 6.5. Conclusion & Outlook

We have presented a Lindblad master equation approach to analyze electron transfer in donor-acceptor pairs coupled to a cavity, in a model where we treat each pair as a 4-level system. Despite neglecting essential mechanisms such as external and internal motional degrees of freedom, such a toy model can help us to discover fundamental mechanics in polaritonic chemistry, using standard tools from quantum optics. By using an adiabatic elimination procedure, we could simplify the problem by eliminating the excited donor and acceptor states, and the cavity, to derive an effective, classical, rate equation for the population transfer between donor and acceptor. This allowed us to gain analytical insight and to perform numerical simulations for very large system sizes. We verified the validity of this approach by benchmarking it for small systems.

We have found that transfer occurs via two types of channels: One channel is driven

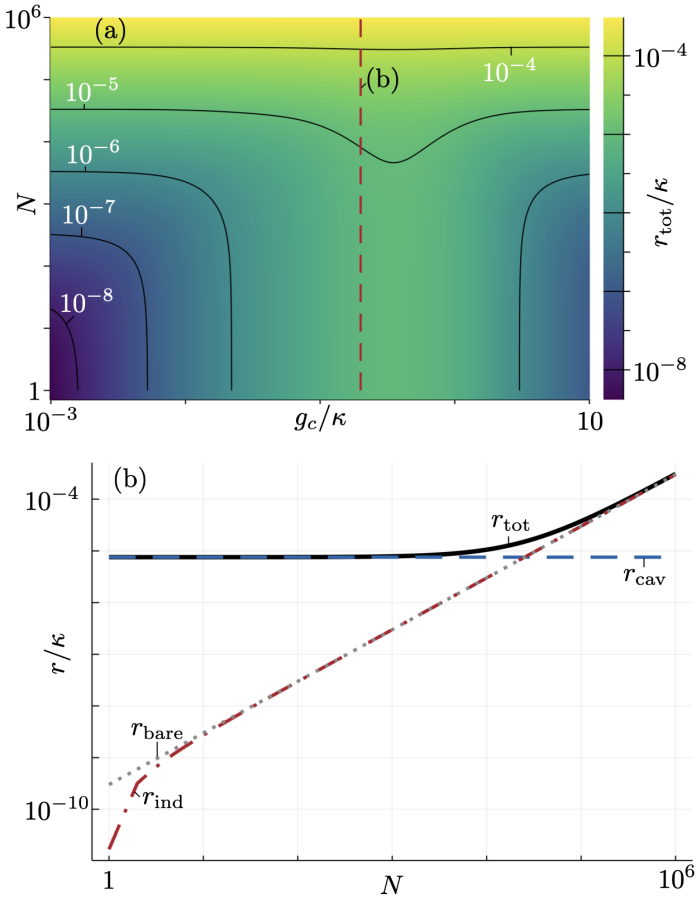


Figure 6.5. – Cavity modification of instantaneous transfer rates including individual pumping [parameters as in Fig. 6.4(c/d), $\Gamma_+ = 10^{-3}\Gamma$]. The total rate $r_{\rm tot}$ is the sum of the individual pumping $r_{\rm ind}$ [obtained by setting $\kappa_+ = 0$ in Eq. (6.22)] and $r_{\rm cav}$. (a) $r_{\rm tot}$, as a function of $g_c$ and $N$ (both axes and color bar are on a log scale). (b) Cut through (a) at the red dashed line $g_c = 0.2\kappa$, and comparison with $r_{\rm ind}$ (red dash-dotted) and $r_{\rm ind}$ (blue dashed, log scale axes). $g_c$ is held constant by choosing $g = g_c/\sqrt{N}$.

by pumping incoherent photons into the cavity and strongly depends on the cavity parameters; the other $N$ channels are driven by individual excitation processes and are essentially unchanged with respect to the no-cavity scenario. Whereas the first channel uses only the three bright states modified by the cavity, the other $N$ channels transfer population via all excited states, and are dominated by the dark states. As the population transfer is purely dissipative and does not require long-lived coherences between different pairs, we expect it to be robust with respect to perturbations such as dephasing, weak static disorder, and weak coupling to external and internal motion. We have simulated the transfer process for large systems and found that the cavity can enhance reaction rates for realistic magnitudes of parameters. This effect is largest for a finite coupling strength between molecules and cavity that falls into the weak coupling regime for strong dissipation. We have analyzed the relevance of the toy-model approximation with regard to recent experimental setups.

It will be interesting to apply the full adiabatic elimination procedure also in the presence of internal and external motional degrees of freedom, and for thermally activated electron transfer. While our effective master equation is purely dissipative and does not build up any coherence, it will be also interesting to investigate the role of entanglement between electronic and motional degrees of freedom, when including the latter. Even without entanglement, it will be interesting to analyze the role of vibrational decoupling on the final transfer rate [12, 49].

The effects observed here are similar to those used to enhance electron transfer or electron-hole generation by plasmonic nano-particles [56–58]. It is an interesting prospect to investigate how the theory developed here may be helpful to understand those types of systems.

As the model presented here uses generic states, our theory can be directly generalized to other types of photo-activated reactions, such as photoisomerization [9], long-range energy transfer [59–61] or singlet triplet transitions [62–66].

## Acknowledgements

We are grateful to Stefan Schütz, Cyriaque Genet, and Thomas Ebbesen for stimulating discussions. This work is supported by ANR 5 “ERA-NET QuantERA” - Projet “RouTe” (ANR-18-QUAN-0005-01), LabEx NIE (“Nanostructures in Interaction with their Environment”) under contract ANR-11-LABX-0058 NIE within the Investissement d’Avenir program ANR-10-IDEX-0002-02. D. W. acknowledges financial support from Agence Nationale de la Recherche (Grant ANR-17-EURE-0024 EUR QMat). G. P. acknowledges support from the Institut Universitaire de France (IUF) and the University of Strasbourg Institute of Advanced Studies (USIAS). Research was carried out using computational resources of the Centre de calcul de l’Université de Strasbourg.

# Appendix

## 6.A. Eigenstates and eigenenergies of $\hat{H}_{\mathrm{NH}}$

As discussed in the main text, pairs in state $|F\rangle$ do not participate in the dynamics and can be largely ignored. We label the set of pairs in state $|F\rangle$ by $\mathcal{N}_F$. The remaining pairs are labeled $1, \ldots, M$.

For a given $\mathcal{N}_F$, we construct the $2M-2$ dark states of the cavity $|k_\pm\rangle$ with general form

$$|k_\pm\rangle = \sum_{n=1}^{M} \frac{\exp(-2\pi \mathrm{i} k n/M)}{\sqrt{M}} \left(\alpha_{k_\pm} |D\rangle_n + \beta_{k_\pm} |A\rangle_n\right), \tag{6.24}$$

where $k \in \{1, \ldots, M-1\}$ is the quasi-momentum, and $\alpha_{k_\pm}$ and $\beta_{k_\pm}$ are the amplitudes of $|D\rangle$ and $|A\rangle$, respectively. Due to destructive interference of the different phases of pairs in state $|D\rangle$, the overall coupling to the cavity vanishes: $\left(\sum_n |G\rangle \langle D|_n\right) |k_\pm\rangle = 0$. The amplitudes $\alpha_{k_\pm}$ and $\beta_{k_\pm}$, as well as the corresponding eigenenergies $E_{k_\pm}^{(M)}$, are given by the components of the normalized eigenvectors and the eigenvalues of the matrix

$$\begin{pmatrix} -\mathrm{i}\frac{\Gamma}{2} & V \\ V & \Delta - \mathrm{i}\frac{\eta}{2} \end{pmatrix}, \tag{6.25}$$

respectively, and are independent of $k$. Note that these eigenstates are in general not orthogonal, i. e. $\langle k_+ | k_- \rangle \neq 0$, because the matrix Eq. (6.25) is not hermitian.

The three remaining eigenstates have the form

$$|\pm/X\rangle = \left(\alpha_{\pm/X} |G_c\rangle \otimes |1_{\mathrm{ph}}\rangle + \beta_{\pm/X} \sum_{n=1}^{M} \frac{|D\rangle_n}{\sqrt{M}} + \gamma_{\pm/X} \sum_{n=1}^{M} \frac{|A\rangle_n}{\sqrt{M}}\right). \tag{6.26}$$

The prefactors $\alpha_{\pm/X}, \beta_{\pm/X}, \gamma_{\pm/X}$, and the eigenenergies are given by the components of the eigenvectors and the eigenvalues of the non-hermitian Hamiltonian in the basis $|G_c\rangle \otimes |1_{\mathrm{ph}}\rangle$, $|D\rangle_n$, and $|A\rangle_n$

$$\begin{pmatrix} -\mathrm{i}\frac{\kappa}{2} & \sqrt{M}g & 0 \\ \sqrt{M}g & -\mathrm{i}\frac{\Gamma}{2} & V \\ 0 & V & \Delta - \mathrm{i}\frac{\eta}{2} \end{pmatrix}, \tag{6.27}$$

respectively. The eigenvalue with the largest, intermediate, and smallest real part and the respective eigenvectors are assigned to $|+\rangle$, $|X\rangle$, and $|-\rangle$, respectively. The full solution can be easily computed numerically or analytically, but it is rather long and uninsightful, so it is not given here.[3] Note that also these states are not necessarily orthogonal. A complete set of eigenstates of the first excited manifold ($\langle \hat{N}_e \rangle = 1$) is given by $|\mathcal{N}_F, \psi\rangle$ with $\psi \in \{k_+, k_-, +, -, X : k \in \{1, \ldots, M-1\}\}$.

3. see https://www.wolframalpha.com/input/?i=%7B%7Bd0%2C+sqrt%7BM%7D*g%2C+0%7D%2C+%7Bsqrt%7BM%7D*g%2C+d1%2C+V%7D%2C+%7B0%2C+V%2C+d2%7D%7D for the full expression

## 6.B. State overlaps

We define the inverse bras by $\langle\overline{k_\pm}|$ etc., such that $\langle\overline{k_\pm}|k'_\pm\rangle = \delta_{kk'}$ and $\langle\overline{k_\pm}|k'_\mp\rangle = 0$. With these definitions, we can rewrite the non-hermitian Hamiltonian as

$$\hat{Q}\hat{H}_{\mathrm{NH}}\hat{Q} = \sum_{\mathcal{N}_F,\phi\in\{k_\pm,\pm,X\}} E_\phi^{(M)} \left|\mathcal{N}_F,\phi\right\rangle \left\langle\overline{\mathcal{N}_F,\phi}\right| . \tag{6.28}$$

For a fixed $\mathcal{N}_F$, we define the state overlaps with the notation $|1_{\mathrm{ph}}\rangle \equiv |G_c\rangle \otimes |1_{\mathrm{ph}}\rangle$:

$$c_\phi^{\mathrm{ph}} = \langle\overline{\phi}|1_{\mathrm{ph}}\rangle , \tag{6.29}$$
$$c_\phi^{\mathrm{D_n}} = \langle\overline{\phi}|D\rangle_n , \tag{6.30}$$
$$c_\phi^{\mathrm{A_n}} = \langle\overline{\phi}|A\rangle_n , \tag{6.31}$$
$$\overline{c}_\phi^{\mathrm{ph}} = \langle 1_{\mathrm{ph}}|\phi\rangle , \tag{6.32}$$
$$\overline{c}_\phi^{\mathrm{D_n}} = \langle D|_n |\phi\rangle , \tag{6.33}$$
$$\overline{c}_\phi^{\mathrm{A_n}} = \langle A|_n |\phi\rangle , \tag{6.34}$$

Using that the identity can be written as $\hat{I} = \sum_\phi |\phi\rangle\langle\overline{\phi}|$, we can use the $c_\phi^\psi$ to expand the states $|1_{\mathrm{ph}}\rangle$, $|D\rangle_n$, and $|A\rangle_n$ in the eigenbasis of $\hat{H}_{\mathrm{NH}}$

$$|1_{\mathrm{ph}}\rangle = \sum_\phi c_\phi^{\mathrm{ph}} |\phi\rangle , \tag{6.35}$$
$$|D\rangle_n = \sum_\phi c_\phi^{D_n} |\phi\rangle , \tag{6.36}$$
$$|A\rangle_n = \sum_\phi c_\phi^{A_n} |\phi\rangle , \tag{6.37}$$
$$\langle 1_{\mathrm{ph}}| = \sum_\phi \overline{c}_\phi^{\mathrm{ph}} \langle\overline{\phi}| , \tag{6.38}$$
$$\langle D|_n = \sum_\phi \overline{c}_\phi^{D_n} \langle\overline{\phi}| , \tag{6.39}$$
$$\langle A|_n = \sum_\phi \overline{c}_\phi^{A_n} \langle\overline{\phi}| . \tag{6.40}$$

The sums run over all eigenstates of the first excited manifold of $\hat{H}_{\mathrm{NH}}$. These identities are useful when computing $\mathcal{PLQ}$ and $\mathcal{QLP}$.

The indices $c_{+/X/-}^{\mathrm{ph}}$ can be computed as the top row of

$$\begin{pmatrix} \alpha_+ & \beta_+ & \gamma_+ \\ \alpha_X & \beta_X & \gamma_X \\ \alpha_- & \beta_- & \gamma_- \end{pmatrix}^{-1} . \tag{6.41}$$

In order to calculate the $c_\psi^{D_n,A_n}$ terms, we first calculate its Fourier transform $\tilde{c}_\psi^{D_k,A_k} = \sum_n \exp(-2\pi \mathrm{i} kn/M) c_\psi^{D_n,A_n}/M$, where $\psi \in \{k_+, k_-, +, -, X\}$. The terms $\tilde{c}_+^{D_0,A_0}$, $\tilde{c}_X^{D_0,A_0}$, and $\tilde{c}_-^{D_0,A_0}$ are obtained by dividing the second, third row of the result of Eq. (6.41) by $\sqrt{M}$. The $k \neq 0$ indices can be computed as

$$\begin{pmatrix} \tilde{c}_{k_+}^{D_k} & \tilde{c}_{k_-}^{D_k} \\ \tilde{c}_{k_+}^{A_k} & \tilde{c}_{k_-}^{A_k} \end{pmatrix} = \begin{pmatrix} \frac{\alpha_{k_+}}{\sqrt{M}} & \frac{\beta_{k_+}}{\sqrt{M}} \\ \frac{\alpha_{k_-}}{\sqrt{M}} & \frac{\beta_{k_-}}{\sqrt{M}} \end{pmatrix}^{-1} . \tag{6.42}$$

Note that due to quasi-momentum conservation, all cross-terms $\tilde{c}_{k'_-}^{D_k,A_k}$ with $k \neq k'$ vanish. Finally, we can compute $c_\psi^{D/A_n}$ by Fourier transforming

$$c_\psi^{D_n,A_n} = \sum_{k=0}^{M} \exp(2\pi \mathrm{i} kn/M) \tilde{c}_\psi^{D_k,A_k} \tag{6.43}$$

The $\bar{c}_{+,-,X}^{\mathrm{ph}}$ indices are directly given by the coefficients $\alpha_{+,-,X}$. To compute $\bar{c}_\psi^{D_n,A_n}$, we again define its Fourier transform $\tilde{\bar{c}}^{D_k,A_k}$, which is given by $\beta_\psi/\sqrt{M}$ and $\gamma_\psi/\sqrt{M}$ for $\psi \in \{+, X, -\}$, or $\alpha_\psi/\sqrt{M}$ and $\beta_\psi/\sqrt{M}$ for $\psi \in \{k_+, k_-\}$.

The computation of the transfer rate Eq. (6.22) is simplified by the straightforward to proof identities

$$\begin{aligned} &\sum_{\substack{\psi\in\{+,-,X\} \\ \phi\in\{k_+,k_-:k\in\{1,\dots,M-1\}\}}} \left[\kappa_+ \left(c_\psi^{\mathrm{ph}}\right)^* c_\phi^{\mathrm{ph}} + \Gamma_+ \sum_n \left(c_\psi^{D_n}\right)^* c_\phi^{D_n}\right] \mathcal{G}(M,\psi,\phi) \left[\eta \sum_{n'} \left(\bar{c}_\psi^{A_{n'}}\right)^* \bar{c}_\phi^{A_{n'}}\right] \\ + &\sum_{\substack{\psi\in\{k_+,k_-:k\in\{1,\dots,M-1\}\} \\ \phi\in\{+,-,X\}}} \left[\kappa_+ \left(c_\psi^{\mathrm{ph}}\right)^* c_\phi^{\mathrm{ph}} + \Gamma_+ \sum_n \left(c_\psi^{D_n}\right)^* c_\phi^{D_n}\right] \mathcal{G}(M,\psi,\phi) \left[\eta \sum_{n'} \left(\bar{c}_\psi^{A_{n'}}\right)^* \bar{c}_\phi^{A_{n'}}\right] \\ &\qquad = 0 , \end{aligned} \tag{6.44}$$

$$\begin{aligned} &\sum_{\substack{\psi\in\{k_+,k_-:k\in\{1,\dots,M-1\}\} \\ \phi\in\{k_+,k_-:k\in\{1,\dots,M-1\}\}}} \left[\kappa_+ \left(c_\psi^{\mathrm{ph}}\right)^* c_\phi^{\mathrm{ph}} + \Gamma_+ \sum_n \left(c_\psi^{D_n}\right)^* c_\phi^{D_n}\right] \mathcal{G}(M,\psi,\phi) \left[\eta \sum_{n'} \left(\bar{c}_\psi^{A_{n'}}\right)^* \bar{c}_\phi^{A_{n'}}\right] \\ = &\sum_{i,j\in\{+,-\}} M^2(M-1)\Gamma_+ \left(\tilde{c}_{k_i}^{D_k}\right)^* \tilde{c}_{k_j}^{D_k} \mathcal{G}(M,k_i,k_j) \eta \left(\tilde{\bar{c}}_{k_i}^{A_k}\right)^* \tilde{\bar{c}}_{k_j}^{A_k} . \end{aligned} \tag{6.45}$$

## 6.C. $\mathcal{PLQ}$ and $\mathcal{QLP}$ in the eigenbasis of $\hat{H}_{\mathrm{NH}}$

In order to rewrite $\mathcal{QLP}$ and $\mathcal{PLQ}$ in the eigenbasis of $\hat{H}_{\mathrm{NH}}$, we use definitions Eqs. (6.36) to (6.40). Dropping the index $\mathcal{N}_F$ for convenience, we find

$$\begin{aligned}\mathcal{QLP} = \kappa_+ \Big\{ &\Big[ \left(c_+^{\mathrm{ph}}\right)^* |+\rangle + \left(c_-^{\mathrm{ph}}\right)^* |-\rangle + \left(c_X^{\mathrm{ph}}\right)^* |X\rangle \Big] \langle G_c| \\ &\otimes \Big[ c_+^{\mathrm{ph}} |+\rangle + c_-^{\mathrm{ph}} |-\rangle + c_X^{\mathrm{ph}} |X\rangle \Big] \langle G_c| \Big\} \\ &+ \Gamma_+ \sum_n \left[ \sum_{\psi\in\{k_\pm,+,-,X\}} \left(c_\psi^{D_n}\right)^* |\psi\rangle \langle G_c| \otimes \sum_{\phi\in\{k_\pm,+,-,X\}} c_\phi^{D_n} |\phi\rangle \langle G_c| \right] , \end{aligned} \tag{6.46}$$

$$\begin{aligned}\mathcal{PLQ} = \kappa \Big\{ &|G_c\rangle \Big[ \left(\bar{c}_+^{\mathrm{ph}}\right)^* \langle +| + \left(\bar{c}_-^{\mathrm{ph}}\right)^* \langle -| + \left(\bar{c}_X^{\mathrm{ph}}\right)^* \langle X| \Big] \\ &\otimes |G_c\rangle \left( \bar{c}_+^{\mathrm{ph}} \langle +| + \bar{c}_-^{\mathrm{ph}} \langle -| + \bar{c}_X^{\mathrm{ph}} \langle X| \right) \Big\} \\ &+ \Gamma \sum_n \left[ \sum_{\psi\in\{k_\pm,+,-,X\}} \left(\bar{c}_\psi^{D_n}\right)^* |G_c\rangle \langle \psi| \otimes \sum_{\phi\in\{k_\pm,+,-,X\}} \bar{c}_\phi^{D_n} |G_c\rangle \langle \phi| \right] \\ &+ \eta \sum_n \left[ \sum_{\psi\in\{k_\pm,+,-,X\}} \left(\bar{c}_\psi^{A_n}\right)^* |F_n\rangle \langle \psi| \otimes \sum_{\phi\in\{k_\pm,+,-,X\}} \bar{c}_\phi^{A_n} |F_n\rangle \langle \phi| \right] , \end{aligned} \tag{6.47}$$

where we used the notation $|F_n\rangle \equiv |\mathcal{N}_F \dot{\cup} \{n\}, G_c\rangle$.

## 6.D. Quantum trajectories for full dynamics

Quantum trajectories offer an efficient way to simulate quantum open system dynamics [54], by reducing the complexity of simulating the time evolution of the full density matrix to simulating the time evolution of an ensemble of states, and reconstructing the density matrix from this ensemble. In the quantum trajectories algorithm, each state is evolved by the non-hermitian Hamiltonian $\hat{H}_{\mathrm{NH}} = \hat{H} - \mathrm{i} \sum_k \hat{L}_k^\dagger \hat{L}_k$, according the the modified Schrödinger equation

$$\partial_t |\psi\rangle = -\mathrm{i} \hat{H}_{\mathrm{NH}} |\psi\rangle \ . \tag{6.48}$$

The state $|\psi\rangle$ looses norm in this evolution, and when its norm $\langle\psi|\psi\rangle$ drops below $p$, a uniformly distributed random variable between 0 and 1, a quantum jump occurs. A random Lindblad operator $\hat{L}$ is chosen for the jump, where each Lindblad operator $\hat{L}_i$ has probability

$$p_i = \frac{\langle\psi| \hat{L}_i^\dagger \hat{L}_i |\psi\rangle}{\sum_k \langle\psi| \hat{L}_k^\dagger \hat{L}_k |\psi\rangle} \, . \tag{6.49}$$

The jump is then executed by computing

$$|\psi'\rangle = \frac{\hat{L}_i |\psi\rangle}{\sqrt{\langle\psi| \hat{L}_i^\dagger \hat{L}_i |\psi\rangle}}. \tag{6.50}$$

Identifying this with the master equation dynamics in Eq. (6.10), Eq. (6.48) corresponds to the first part, and the jumps correspond to the second part.

As the state $|F\rangle$ does not take part in any dynamics, we describe each pair as a 3-level system with levels $|G\rangle$, $|D\rangle$, and $|A\rangle$. We treat emission to state $|F\rangle$ as effective pair loss, and compute a new Hamiltonian and Lindblad operators each time a pair is "lost". We consider a maximum of 1 cavity photon, which we find to be sufficient. If the system is in its ground state $|G_c\rangle$, there is no coherent evolution $\hat{H}|G_c\rangle = 0$, and we can compute the decay rate $l = \langle G_c| \sum_k \hat{L}_k^\dagger \hat{L}_k |G_c\rangle$, and calculate the time until the next jump analytically $T = -\ln(p)/l$. To compute the excited state evolution, we compute

$$|\psi(t+dt)\rangle = \exp\Big(-\mathrm{i}\hat{H}_{\mathrm{NH}} dt\Big) |\psi(t)\rangle \tag{6.51}$$

for a small timestep $dt = 0.01/\kappa$, and calculate the norm of $\langle\psi|\psi\rangle$ after every timestep.

## 6.E. Quantum trajectories for effective dynamics

In order to simulate a trajectory defined by the instantaneous decay rate $r(M)$, which depends only on the number of pairs in state $|G\rangle$, we can use the method described above for evolution out of the ground state. For a random number $p$, we can compute the time until the first jump as $t_1 = -\ln(p)/r(N)$. For each jump exactly one pair is transferred from state $|G\rangle$ into state $|F\rangle$. A full trajectory can thus be calculated from a set of random numbers $p_1, \ldots, p_N$ according to $t_i = t_{i-1} - \ln(p_i)/r(N-i+1)$. Between timestep $t_i$ and $t_{i+1}$, exactly $i$ pairs are in state $|F\rangle$, and $N-i$ pairs are in state $|G\rangle$. The state is efficiently stored as the number $M$ of ground state pairs. The average and standard deviation are computed by sampling over many trajectories.

# Bibliography


[1] D. Wellnitz, G. Pupillo, and J. Schachenmayer, "A quantum optics approach to photoinduced electron transfer in cavities," *J. Chem. Phys.*, vol. 154, p. 054104, Feb. 2021.

[2] T. W. Ebbesen, "Hybrid Light–Matter States in a Molecular and Material Science Perspective," *Acc. Chem. Res.*, vol. 49, pp. 2403–2412, Nov. 2016.

[3] F. Herrera and J. Owrutsky, "Molecular polaritons for controlling chemistry with quantum optics," *J. Chem. Phys.*, vol. 152, p. 100902, Mar. 2020.

[4] A. Thomas, J. George, A. Shalabney, M. Dryzhakov, S. J. Varma, J. Moran, T. Chervy, X. Zhong, E. Devaux, C. Genet, J. A. Hutchison, and T. W. Ebbesen, "Ground-State Chemical Reactivity under Vibrational Coupling to the Vacuum Electromagnetic Field," *Angew. Chem. Int. Ed.*, vol. 55, no. 38, pp. 11462–11466, 2016.

[5] A. D. Dunkelberger, B. T. Spann, K. P. Fears, B. S. Simpkins, and J. C. Owrutsky, "Modified relaxation dynamics and coherent energy exchange in coupled vibration-cavity polaritons," *Nat Commun*, vol. 7, p. 13504, Nov. 2016.

[6] A. Thomas, L. Lethuillier-Karl, K. Nagarajan, R. M. A. Vergauwe, J. George, T. Chervy, A. Shalabney, E. Devaux, C. Genet, J. Moran, and T. W. Ebbesen, "Tilting a ground-state reactivity landscape by vibrational strong coupling," *Science*, vol. 363, pp. 615–619, Feb. 2019.

[7] J. Lather, P. Bhatt, A. Thomas, T. W. Ebbesen, and J. George, "Cavity Catalysis by Cooperative Vibrational Strong Coupling of Reactant and Solvent Molecules," *Angew. Chem. Int. Ed.*, vol. 58, no. 31, pp. 10635–10638, 2019.

[8] H. Hiura, A. Shalabney, and J. George, "Vacuum-Field Catalysis: Accelerated Reactions by Vibrational Ultra Strong Coupling," May 2021.

[9] J. A. Hutchison, T. Schwartz, C. Genet, E. Devaux, and T. W. Ebbesen, "Modifying Chemical Landscapes by Coupling to Vacuum Fields," *Angew. Chem. Int. Ed.*, vol. 51, pp. 1592–1596, Feb. 2012.

[10] B. Munkhbat, M. Wersäll, D. G. Baranov, T. J. Antosiewicz, and T. Shegai, "Suppression of photo-oxidation of organic chromophores by strong coupling to plasmonic nanoantennas," *Sci. Adv.*, vol. 4, p. eaas9552, July 2018.

[11] V. N. Peters, M. O. Faruk, J. Asane, R. Alexander, D. A. Peters, S. Prayakarao, S. Rout, and M. A. Noginov, "Effect of strong coupling on photodegradation of the semiconducting polymer P3HT," *Optica, OPTICA*, vol. 6, pp. 318–325, Mar. 2019.

[12] F. Herrera and F. C. Spano, "Cavity-Controlled Chemistry in Molecular Ensembles," *Phys. Rev. Lett.*, vol. 116, p. 238301, June 2016.

[13] M. Kowalewski, K. Bennett, and S. Mukamel, "Cavity Femtochemistry: Manipulating Nonadiabatic Dynamics at Avoided Crossings," *J. Phys. Chem. Lett.*, vol. 7, pp. 2050–2054, June 2016.

[14] J. Flick, M. Ruggenthaler, H. Appel, and A. Rubio, "Atoms and molecules in cavities, from weak to strong coupling in quantum-electrodynamics (QED) chemistry," *PNAS*, vol. 114, pp. 3026–3034, Mar. 2017.

[15] J. Feist, J. Galego, and F. J. Garcia-Vidal, "Polaritonic Chemistry with Organic Molecules," *ACS Photonics*, vol. 5, pp. 205–216, Jan. 2018.

[16] J. Flick and P. Narang, "Cavity-Correlated Electron-Nuclear Dynamics from First Principles," *Phys. Rev. Lett.*, vol. 121, p. 113002, Sept. 2018.

[17] O. Vendrell, "Collective Jahn-Teller Interactions through Light-Matter Coupling in a Cavity," *Phys. Rev. Lett.*, vol. 121, p. 253001, Dec. 2018.

[18] J. A. Campos-Gonzalez-Angulo, R. F. Ribeiro, and J. Yuen-Zhou, "Resonant catalysis of thermally activated chemical reactions with vibrational polaritons," *Nat Commun*, vol. 10, p. 4685, Oct. 2019.

[19] J. Fregoni, G. Granucci, M. Persico, and S. Corni, "Strong Coupling with Light Enhances the Photoisomerization Quantum Yield of Azobenzene," *Chem*, vol. 6, pp. 250–265, Jan. 2020.

[20] F. Herrera, "Photochemistry with Quantum Optics from a Non-Adiabatic Quantum Trajectory Perspective," *Chem*, vol. 6, pp. 7–9, Jan. 2020.

[21] I. S. Ulusoy and O. Vendrell, "Dynamics and spectroscopy of molecular ensembles in a lossy microcavity," *J. Chem. Phys.*, vol. 153, p. 044108, July 2020.

[22] S. Felicetti, J. Fregoni, T. Schnappinger, S. Reiter, R. de Vivie-Riedle, and J. Feist, "Photoprotecting Uracil by Coupling with Lossy Nanocavities," *J. Phys. Chem. Lett.*, Sept. 2020.

[23] D. S. Wang, T. Neuman, J. Flick, and P. Narang, "Light–matter interaction of a molecule in a dissipative cavity from first principles," *J. Chem. Phys.*, vol. 154, p. 104109, Mar. 2021.

[24] P. Antoniou, F. Suchanek, J. F. Varner, and J. J. Foley, "Role of Cavity Losses on Nonadiabatic Couplings and Dynamics in Polaritonic Chemistry," *J. Phys. Chem. Lett.*, vol. 11, pp. 9063–9069, Nov. 2020.

[25] E. Davidsson and M. Kowalewski, "Simulating photodissociation reactions in bad cavities with the Lindblad equation," *J. Chem. Phys.*, vol. 153, p. 234304, Dec. 2020.

[26] J. Torres-Sánchez and J. Feist, "Molecular photodissociation enabled by ultrafast plasmon decay," *J. Chem. Phys.*, vol. 154, p. 014303, Jan. 2021.

[27] F. Herrera and F. C. Spano, "Theory of Nanoscale Organic Cavities: The Essential Role of Vibration-Photon Dressed States," *ACS Photonics*, vol. 5, pp. 65–79, Jan. 2018.

[28] J. del Pino, J. Feist, and F. J. Garcia-Vidal, "Quantum theory of collective strong coupling of molecular vibrations with a microcavity mode," *New J. Phys.*, vol. 17, p. 053040, May 2015.

[29] L. A. Martínez-Martínez, M. Du, R. F. Ribeiro, S. Kéna-Cohen, and J. Yuen-Zhou, "Polariton-Assisted Singlet Fission in Acene Aggregates," *J. Phys. Chem. Lett.*, vol. 9, pp. 1951–1957, Apr. 2018.

[30] M. Reitz, C. Sommer, and C. Genes, "Langevin Approach to Quantum Optics with Molecules," *Phys. Rev. Lett.*, vol. 122, p. 203602, May 2019.

[31] D. Finkelstein-Shapiro, D. Viennot, I. Saideh, T. Hansen, T. Pullerits, and A. Keller, "Adiabatic elimination and subspace evolution of open quantum systems," *Phys. Rev. A*, vol. 101, Apr. 2020.

[32] F. Reiter and A. S. Sørensen, "Effective operator formalism for open quantum systems," *Phys. Rev. A*, vol. 85, p. 032111, Mar. 2012.

[33] D. Wellnitz, S. Schütz, S. Whitlock, J. Schachenmayer, and G. Pupillo, "Collective Dissipative Molecule Formation in a Cavity," *Phys. Rev. Lett.*, p. 6, 2020.

[34] D. S. Jin and J. Ye, "Introduction to Ultracold Molecules: New Frontiers in Quantum and Chemical Physics," *Chem. Rev.*, vol. 112, pp. 4801–4802, Sept. 2012.

[35] O. Dulieu and A. Osterwalder, *Cold Chemistry*. The Royal Society of Chemistry, 2017.

[36] A. Mandal, T. D. Krauss, and P. Huo, "Polariton-Mediated Electron Transfer via Cavity Quantum Electrodynamics," *J. Phys. Chem. B*, vol. 124, pp. 6321–6340, July 2020.

[37] I. S. Ulusoy, J. A. Gomez, and O. Vendrell, "Modifying the Nonradiative Decay Dynamics through Conical Intersections via Collective Coupling to a Cavity Mode," *J. Phys. Chem. A*, vol. 123, pp. 8832–8844, Oct. 2019.

[38] T. Szidarovszky, G. J. Halász, and Á. Vibók, "Three-player polaritons: Nonadiabatic fingerprints in an entangled atom–molecule–photon system," *New J. Phys.*, vol. 22, p. 053001, May 2020.

[39] E. Davidsson and M. Kowalewski, "Atom Assisted Photochemistry in Optical Cavities," *J. Phys. Chem. A*, vol. 124, pp. 4672–4677, June 2020.

[40] C. Gonzalez-Ballestero, J. Feist, E. Gonzalo Badía, E. Moreno, and F. J. Garcia-Vidal, "Uncoupled Dark States Can Inherit Polaritonic Properties," *Phys. Rev. Lett.*, vol. 117, p. 156402, Oct. 2016.

[41] G. Groenhof, C. Climent, J. Feist, D. Morozov, and J. J. Toppari, "Tracking Polariton Relaxation with Multiscale Molecular Dynamics Simulations," *J. Phys. Chem. Lett.*, vol. 10, pp. 5476–5483, Sept. 2019.

[42] C. Sommer, M. Reitz, F. Mineo, and C. Genes, "Molecular polaritonics in dense mesoscopic disordered ensembles," *Phys. Rev. Research*, vol. 3, p. 033141, Aug. 2021.

[43] T. Botzung, D. Hagenmüller, S. Schütz, J. Dubail, G. Pupillo, and J. Schachenmayer, "Dark state semilocalization of quantum emitters in a cavity," *Phys. Rev. B*, vol. 102, p. 144202, Oct. 2020.

[44] N. C. Chávez, F. Mattiotti, J. A. Méndez-Bermúdez, F. Borgonovi, and G. L. Celardo, "Disorder-Enhanced and Disorder-Independent Transport with Long-Range Hopping: Application to Molecular Chains in Optical Cavities," *Phys. Rev. Lett.*, vol. 126, p. 153201, Apr. 2021.

[45] C. W. Gardiner, "Quantum noise and quantum Langevin equations," *IBM J. Res. Dev.*, vol. 32, pp. 127–136, Jan. 1988.

[46] H. Zhu, Y. Yang, K. Hyeon-Deuk, M. Califano, N. Song, Y. Wang, W. Zhang, O. V. Prezhdo, and T. Lian, "Auger-Assisted Electron Transfer from Photoexcited Semiconductor Quantum Dots," *Nano Lett.*, vol. 14, pp. 1263–1269, Mar. 2014.

[47] S. Gupta and E. Waks, "Spontaneous emission enhancement and saturable absorption of colloidal quantum dots coupled to photonic crystal cavity," *Opt. Express, OE*, vol. 21, pp. 29612–29619, Dec. 2013.

[48] B. Misra and E. C. G. Sudarshan, "The Zeno's paradox in quantum theory," *J. Math. Phys.*, vol. 18, pp. 756–763, Apr. 1977.

[49] M. A. Zeb, P. G. Kirton, and J. Keeling, "Exact States and Spectra of Vibrationally Dressed Polaritons," *ACS Photonics*, vol. 5, pp. 249–257, Jan. 2018.

[50] J. del Pino, F. A. Y. N. Schröder, A. W. Chin, J. Feist, and F. J. Garcia-Vidal, "Tensor Network Simulation of Non-Markovian Dynamics in Organic Polaritons," *Phys. Rev. Lett.*, vol. 121, Nov. 2018.

[51] C. W. Gardiner and P. Zoller, *Quantum Noise*. Springer Series in Synergetics, Springer Berlin Heidelberg, 3rd ed., 2004.

[52] C. W. Gardiner, *Stochastic Methods*. Springer Series in Synergetics, Springer Berlin Heidelberg, 2009.

[53] J. J. Sakurai and J. Napolitano, *Modern Quantum Mechanics*. Cambridge University Press, third ed., 2021.

[54] A. J. Daley, "Quantum trajectories and open many-body quantum systems," *Adv. Phys.*, vol. 63, pp. 77–149, Mar. 2014.

[55] C. Cohen-Tannoudji, J. Dupont-Roc, and G. Grynberg, *Atom-Photon Interactions: Basic Processes and Applications*. New York: Wiley, 1992.

[56] H. A. Atwater and A. Polman, "Plasmonics for improved photovoltaic devices," *Nature Mater*, vol. 9, pp. 205–213, Mar. 2010.

[57] K. Ikeda, K. Takahashi, T. Masuda, and K. Uosaki, "Plasmonic Enhancement of Photoinduced Uphill Electron Transfer in a Molecular Monolayer System," *Angew. Chem. Int. Ed.*, vol. 50, no. 6, pp. 1280–1284, 2011.

[58] X. Zhang, Y. L. Chen, R.-S. Liu, and D. P. Tsai, "Plasmonic photocatalysis," *Rep. Prog. Phys.*, vol. 76, p. 046401, Mar. 2013.

[59] D. M. Coles, N. Somaschi, P. Michetti, C. Clark, P. G. Lagoudakis, P. G. Savvidis, and D. G. Lidzey, "Polariton-mediated energy transfer between organic dyes in a strongly coupled optical microcavity," *Nature Mater*, vol. 13, pp. 712–719, July 2014.

[60] X. Zhong, T. Chervy, S. Wang, J. George, A. Thomas, J. A. Hutchison, E. Devaux, C. Genet, and T. W. Ebbesen, "Non-Radiative Energy Transfer Mediated by Hybrid Light-Matter States," *Angew. Chem. Int. Ed.*, vol. 55, no. 21, pp. 6202–6206, 2016.

[61] X. Zhong, T. Chervy, L. Zhang, A. Thomas, J. George, C. Genet, J. A. Hutchison, and T. W. Ebbesen, "Energy Transfer between Spatially Separated Entangled Molecules," *Angew. Chem. Int. Ed.*, vol. 56, no. 31, pp. 9034–9038, 2017.

[62] K. Stranius, M. Hertzog, and K. Börjesson, "Selective manipulation of electronically excited states through strong light–matter interactions," *Nat. Commun.*, vol. 9, p. 2273, June 2018.

[63] S. Takahashi, K. Watanabe, and Y. Matsumoto, "Singlet fission of amorphous rubrene modulated by polariton formation," *J. Chem. Phys.*, vol. 151, p. 074703, Aug. 2019.

[64] E. Eizner, L. A. Martínez-Martínez, J. Yuen-Zhou, and S. Kéna-Cohen, "Inverting singlet and triplet excited states using strong light-matter coupling," *Sci. Adv.*, vol. 5, p. eaax4482, Dec. 2019.

[65] Y. Yu, S. Mallick, M. Wang, and K. Börjesson, "Barrier-free reverse-intersystem crossing in organic molecules by strong light-matter coupling," *Nat Commun*, vol. 12, p. 3255, May 2021.

[66] D. Polak, R. Jayaprakash, T. P. Lyons, L. Á. Martínez-Martínez, A. Leventis, K. J. Fallon, H. Coulthard, D. G. Bossanyi, K. Georgiou, I. I. Anthony J. Petty, J. Anthony, H. Bronstein, J. Yuen-Zhou, A. I. Tartakovskii, J. Clark, and A. J. Musser, "Manipulating molecules with strong coupling: Harvesting triplet excitons in organic exciton microcavities," *Chem. Sci.*, vol. 11, pp. 343–354, Jan. 2020.

# 7. The Holstein Tavis Cummings Model

At room temperature, molecular dynamics is often not restricted to just a few states per molecule. Instead, generally multiple vibrational and rotational degrees of freedom are relevant, in addition to the electronic energy levels. The vibrational and electronic degrees of freedom are usually also coupled to each other, and both may play an important role in chemical reactions [1, 2].

The purpose of this chapter is to introduce the basic physics of the Holstein-Tavis-Cummings (HTC) model, which is analyzed in detail in Chapters 9 and 10. The HTC model is a toy model for cavity-coupled molecules includes coupled electronic, photonic, and vibrational degrees of freedom on a minimalist level. This chapter is organized as follows: In Section 7.1, the HTC model is introduced. Then, in Section 7.2, polaron decoupling phenomenon is discussed as the main result of previous theoretical work on this model.

## 7.1. The Model

The Holstein Tavis Cummings (HTC) model was introduced by Cwik *et al.* to study organic polariton condensates [3], and subsequently used in polaritonic chemistry to study fundamental phenomena in cavity-coupled molecules [4–7]. This model describes molecules by a single harmonic vibrational coordinate which is coupled to two electronic levels. The electronic transitions are in turn coupled to a single mode cavity. These toy model molecules are schematically illustrated in Figure 7.1(a), together with the different degrees of freedom and their coupling in Figure 7.1(b).

This toy model is used to qualitatively understand coupled vibrational-electro-photonic dynamics in a bottom up approach. To some extend, it may also be directly relevant for diatomic molecules, which only have a single vibrational coordinate, or even more complex molecules if the nuclear dynamics is dominated by a single vibrational mode. However, even in those scenarios, the vibration may generally be an-harmonic, especially far from the minima during a chemical reaction [see Figure 7.1(a)].

The HTC Hamiltonian is a sum of the Tavis-Cummings Hamiltonian introduced in Chapter 3, independent harmonic vibrations of the different molecules, and a Holstein-type coupling between vibrations and electronic coordinates of each molecule

$$\hat{H}_{\mathrm{HTC}} = \hat{H}_{\mathrm{TC}} + \hat{H}_{\mathrm{vib}} + \hat{H}_{\mathrm{H}} \tag{7.1}$$

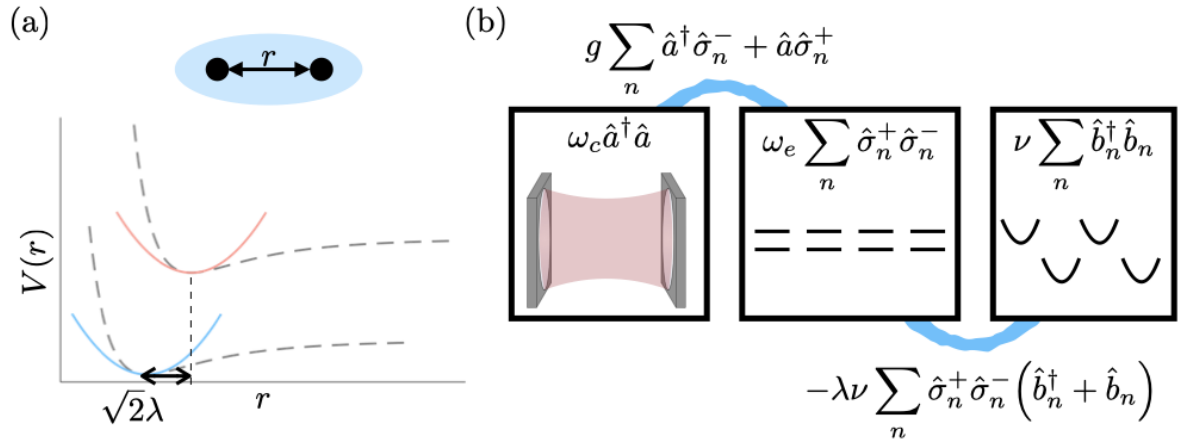


Figure 7.1. – (a) Schematic picture of the approximation to a molecule and the parameters. (b) Degrees of freedom and how they are coupled by the different terms in the Hamiltonian.

with

$$\hat{H}_{\mathrm{TC}} = \omega_e \sum_{n=1}^{N} \hat{\sigma}_n^+\hat{\sigma}_n^- + \omega_c\hat{a}^\dagger\hat{a} + g\sum_{n=1}^{N} \hat{\sigma}_n^+\hat{a} + \hat{\sigma}_n^-\hat{a}^\dagger\,, \tag{7.2}$$

$$\hat{H}_{\mathrm{vib}} = \nu \sum_{n=1}^{N} \hat{b}_n^\dagger\hat{b}_n\,, \tag{7.3}$$

$$\hat{H}_{\mathrm{H}} = -\lambda\nu \sum_{n=1}^{N} \hat{\sigma}_n^+\hat{\sigma}_n^-\left(\hat{b}_n + \hat{b}_n^\dagger\right). \tag{7.4}$$

Here, $\omega_e$ and $\omega_c$ are the frequency of the electronic transition and the cavity, respectively, while $g$ denotes the single molecule coupling strength to the cavity. Both the vibrational frequency $\nu$ and the vibronic coupling $\lambda\nu$ are typically much smaller than the electronic transition energy $\nu, \lambda\nu \ll \omega_e$. The distance between the two potential minima is $\sqrt{2}\lambda$ (in units of the zero point motion of the vibration). The Huang-Rhys factor $\lambda^2$ quantifies the shift of the electronic energy level spacings, i.e. the energy difference between the vibrational ground state of the two electronic energy levels is $\omega_e - \lambda^2\nu$.

## 7.2. Polaron Decoupling

This simple model has been studied to gain insight into the underlying mechanisms of cavity-modified chemistry. In particular, it has been noted that the displacement of the excited polariton state is collectively reduced compared to the bare value $\sqrt{2}\lambda$ in the regime $g_c \gg \lambda^2\nu$ [4, 7]. This is rooted in the fact that the polariton is a symmetric superposition with the excitation distributed amongst all $N$ molecules. Consequently, each

individual molecule is only excited with a probability $1/(2N)$, so that the displacement of the minimum of each individual oscillator is reduced by a factor $1/(2N)$. Finally, when considering the symmetrical displacement coordinate of all oscillators $(\sum_n \hat{b}_n + \hat{b}_n^\dagger)/\sqrt{2N}$, this corresponds to a collective reduction of the displacement by a factor $1/(2\sqrt{N})$.

Analytically, the lower polariton can be approximately written down as [4]

$$|LP\rangle = |-\rangle \otimes \hat{D}_{\tilde{0}}^\dagger \left[\lambda/\left(2\sqrt{N}\right)\right] |0_{\text{vib}}\rangle \tag{7.5}$$

with the vibrational vacuum state $|0_{\text{vib}}\rangle$. Here,

$$\hat{D}_{\tilde{0}}(x) = \exp\left[x \sum_n \left(\hat{b}_n^\dagger - \hat{b}_n\right)/\sqrt{N}\right] \tag{7.6}$$

is the displacement operator acting on the symmetric vibrational mode. As a result, the coupling of the vibration to the polariton state is suppressed by a factor $1/(2\sqrt{N})$, an effect termed polaron decoupling. Equivalently, this reduced displacement corresponds to a reduced coupling between between electronic and vibrational degrees of freedom, which leads to suppressed reaction rates in a simple model [4].

Notably, the lower polariton state $|LP\rangle$ given above has no entanglement between photo-electronic and vibrational degrees of freedom. Instead, it is a direct product state between these two degrees of freedom. This is because in the regime $g_c \gg \lambda^2\nu$, the delocalization of the excitation is much faster than the reorganization of the nuclei to adjust to the electronic excitation. This is different for a symmetric superposition of polaron-like excitations of individual molecules, which would be the correct eigenstate for perturbative cavity coupling [7]. Here, the vibrational state of each molecule is entangled with its electronic state.

In Chapters 9 and 10, the dynamics of the HTC model is analyzed numerically in detail. A particular focus is put on the entanglement dynamics, which may be viewed as a quantifier for the simulation complexity. In Chapter 9, we study the effects of disorder on the vibrational and entanglement dynamics in detail, and show that disorder can also lead to entanglement even for small $\lambda$. In Chapter 10, we study the case of large excitation numbers, and show that entanglement is enhanced for intermediate excitation fractions. Furthermore, we develop an efficient product state approximation that is valid for small entanglement.

# Bibliography


[1] A. Nitzan, *Chemical Dynamics in Condensed Phases: Relaxation, Transfer and Reactions in Condensed Molecular Systems*. Oxford Graduate Texts, Oxford ; New York: Oxford University Press, 2006.

[2] F. Herrera and F. C. Spano, "Theory of Nanoscale Organic Cavities: The Essential Role of Vibration-Photon Dressed States," *ACS Photonics*, vol. 5, pp. 65–79, Jan. 2018.

[3] J. A. Ćwik, S. Reja, P. B. Littlewood, and J. Keeling, "Polariton condensation with saturable molecules dressed by vibrational modes," *EPL Europhys. Lett.*, vol. 105, p. 47009, Feb. 2014.

[4] F. Herrera and F. C. Spano, "Cavity-Controlled Chemistry in Molecular Ensembles," *Phys. Rev. Lett.*, vol. 116, p. 238301, June 2016.

[5] F. Herrera and J. Owrutsky, "Molecular polaritons for controlling chemistry with quantum optics," *J. Chem. Phys.*, vol. 152, p. 100902, Mar. 2020.

[6] M. Reitz, C. Sommer, and C. Genes, "Langevin Approach to Quantum Optics with Molecules," *Phys. Rev. Lett.*, vol. 122, p. 203602, May 2019.

[7] M. A. Zeb, P. G. Kirton, and J. Keeling, "Exact States and Spectra of Vibrationally Dressed Polaritons," *ACS Photonics*, vol. 5, pp. 249–257, Jan. 2018.

# 8. Numerical Studies of Polaritonic Chemistry

The field of polaritonic chemistry analyzes the modification of chemical reactions under strong coupling to a cavity [1, 2]. In Chapter 7, the Holstein-Tavis-Cummings model was introduced as a toy model to qualitatively investigate cavity-induced modifications. The present chapter gives an overview over the more common approach to analyze realistic molecular models numerically. In this case, in order to analyze large molecular ensembles, the dynamics is often approximated using different techniques. In Section 8.1, the Born-Oppenheimer approximation is introduced as a strong approximation, together with two extensions. In Section 8.2, numerically exact methods are discussed. Matrix Product States, which have been used to analyze the short-time dynamics in heuristic models, are the topic of Section 8.3. Section 8.4 gives a short overview over some other methods used. Finally, the simulation of dissipation is considered in Section 8.5. Finally, Section 8.6 concludes by discussing how our work in the following two chapters relates to this literature.

## 8.1. Born-Oppenheimer based methods

The Born-Oppenheimer approximation is a drastic approximation based on a separation of time scales between the nuclear and electronic dynamics in a molecule, which makes it possible to efficiently simulate large molecular ensembles. This separation of time scales is seen from the typically much larger separation of electronic energy levels compared to vibrational energy levels. The Born-Oppenheimer approximation then consists of assuming that the electronic eigenstates adiabatically adjust to any changes in the nuclear coordinates. As a result, potential energy surface can be computed for adiabatically connected electronic states on which the nuclear dynamics takes place. In the presence of a cavity which is strongly coupled to an electronic transition, the electronic and photonic degrees of freedom hybridize to form new polaritonic eigenstates. In this case, the Born-Oppenheimer approximation can be generalized by computing polaritonic potential energy surfaces [3], assuming that the combined electro-photonic dynamics is much faster than the nuclear dynamics.

If different potential energy surfaces approach each other in avoided crossings or intersect in conical intersections, the non-adiabatic coupling between the potential energy surfaces can become important, and the Born-Oppenheimer approximation breaks down. Cavities have been shown to induce such conical intersections especially between dark states in the collective regime [4–6]. This can be understood as a consequence of the

degeneracy of the dark states for two level systems. In this case, the dynamics cannot be restricted to a single potential energy surface and non-adiabatic couplings need to be considered. Below, two extensions of the Born-Oppenheimer approximation are introduced to account for non-adiabatic couplings.

## Mean-field Ehrenfest

One possible extension of the Born-Oppenheimer approximation to include non-adiabatic couplings is to allow the electronic state to be in superpositions of different potential energy surfaces, and then calculate the "mean-field" nuclear dynamics for this superposition. Alternatively, this approximation can be seen as assuming a product state between nuclear degrees of freedom on the one, and electronic and photonic degrees of freedom on the other hand. If, in addition, the nuclear dynamics is also treated classically, this approximation is known as the mean-field Ehrenfest method [7].

Due to the strength of its assumption, this method can be used to simulate large ensembles of molecules. It has been applied to simulate the excited state dynamics of large ensembles of dye molecules coupled to a cavity including their environment [8, 9]. However, this mean-field dynamics completely neglects any entanglement between vibrational and electro-photonic degrees of freedom. This assumption is investigated in detail in Chapters 9 and 10.

## Fewest Switches Surface Hopping

Another extension of the Born-Oppenheimer approximation to include non-adiabatic couplings are Fewest Switches Surface Hopping methods [7, 10]. Here, instead of considering states with superpositions of electronic states, the dynamics remains restricted to just one potential energy surface at all times. The non-adiabatic couplings are then implemented as stochastic jumps between different potential energy surfaces. In particular, jump probabilities are computed from the non-adiabatic couplings and then stochastically jumps are implemented conceptionally reminiscent of a quantum trajectories simulation as described in Chapter 2 Section 2.2. At each jump, energy conservation is enforced by transforming potential energy into kinetic energy and vice versa. By averaging over multiple trajectories with different jumps, the quantum dynamics is then approximated. As a result, this method can reproduce correlations between electronic and nuclear degrees of freedom, in contrast to multi-trajectory Ehrenfest methods.

This method was used to simulate the excited state dynamics of ensembles of organic molecules coupled to a cavity [11, 12]. However, as the number of potential energy surfaces that are close to each other increases, the number of jumps between them increases as well. Thus, the number of trajectories needed for the simulation can become very large. This is especially important in the dark state manifold, where there are typically many potential energy surfaces in close energetic proximity, rendering large scale simulations intractable [8].

## 8.2. Quasi-exact Numerical Methods

Small systems can be directly investigated using numerically exact methods for propagating quantum states. Such methods choose a basis for the Hilbert space and then compute the time evolution according to the Schrödinger equation. This can be further generalized to propagate with the non-hermitian Hamiltonian to treat open systems, as discussed below.

One efficient choice of basis is physically motivated by the Born-Oppenheimer potential energy surfaces. In particular, a combined electro-nuclear basis is given by expanding the nuclear coordinates in real space, and at each real space coordinate choose the electronic basis according to the potential energy surfaces. The kinetic energy term then contains non-adiabatic coupling terms between the potential energy surfaces, as the electronic basis changes in space [4]. This basis has been used to investigate collective effects in the photo-dissociation of $MgH^+$ coupled to a cavity together with several atoms [13].

Alternatively, the multi configurational time dependent Hatree Fock method (MCTDH) expands the wave function into more abstract, adaptive orbitals, to increase the efficiency. This method has been used to investigate the photo-dissociation dynamics of up to 6 NaI molecules collectively coupled to a cavity [5, 14, 15]. However, even with such advanced methods, problems involving more than just a few small molecules become intractable.

## 8.3. Tensor Network Methods

Moving away from ab initio methods, tensor networks have been used in order to simulate the excited state dynamics. For these methods, heuristic molecular models have been build from vibronic spectra by extracting vibrational frequencies and Huang-Rhys factors. The resulting model contains harmonic vibrational degrees of freedom coupled to the electronic levels analogous to the HTC model introduced in Chapter 7, however with many vibrations.

Del Pino *et al.* investigated the full vibrational-electro-photonic quantum dynamics of multiple organic dye molecules coupled to a common cavity mode [16, 17]. The tensor networks were build with chain mapping for the vibrations of the individual molecules. For dye molecules that have been used in strong coupling experiments with $J$-aggregates, they showed that the dynamics is not adequately described by treating the vibrations in a Markovian approximation. However, due to the computation of many vibrations for each molecule, this method becomes intractable for large molecule numbers, and only small systems have been analyzed.

## 8.4. Other Methods

Also other methods have been used to simulate molecular dynamics in cavities. For example, Density Functional Theory (DFT) is an ab initio framework to describe quantum mechanics in terms of equations of motion for the density functionals of electrons, nuclei.

This method has been extended to include photons in a framework labeled QEDFT [18], and has been used to simulate small molecular ensembles [18, 19].

Coupled cluster theory provides an alternative heuristic ansatz do describe molecular ground state wave functions and dynamics. However, so far, it has only been applied to strong coupling with single molecules single molecules [20, 21].

## 8.5. Dissipation

Many of the above methods have been recently extended to also account for dissipation of the cavity mode. This dissipation occurs often at similar time scale as the system dynamics, and may thus greatly influence the dynamics [22]. For single molecules, the dynamics when coupling to a lossy cavity has been analyzed using exact non-Hermitian Hamiltonian and master equation formalisms [23–25], and QEDFT methods [26]. Using MCTDH with a non-Hermitian Hamiltonian, up to 5 NaI molecules were analyzed. In order to analyze larger ensembles, the Fewest Switches Surface Hopping Method has been used [27, 28].

## 8.6. Conclusion

In conclusion, various methods have been developed for simulating polaritonic chemistry problems, which can be categorized into two classes. For small systems, highly accurate methods such as wave-function propagation, tensor networks, or QEDFT are available. However, the restriction to just a few molecules hinders a systematic analysis of collective effects. In order to simulate larger systems, one must instead rely on extensions of the Born-Oppenheimer approximation, which make strong assumptions. Here, collective effects can be systematically studied, but the quantum nature of the problem is partially neglected.

As a result, the importance of quantum effects in large molecular ensembles has not yet been analyzed. Understanding these effects is not only fundamentally interesting, but also relevant for estimating the regime of validity of the different approximation methods. The Chapters 9 and 10 present a detailed study of quantum effects for large molecular ensembles, and their relevance for the vibrational dynamics.

# Bibliography


[1] F. Herrera and J. Owrutsky, "Molecular polaritons for controlling chemistry with quantum optics," *J. Chem. Phys.*, vol. 152, p. 100902, Mar. 2020.

[2] F. J. Garcia-Vidal, C. Ciuti, and T. W. Ebbesen, "Manipulating matter by strong coupling to vacuum fields," *Science*, vol. 373, p. eabd0336, July 2021.

[3] J. Galego, F. J. Garcia-Vidal, and J. Feist, "Cavity-Induced Modifications of Molecular Structure in the Strong-Coupling Regime," *Phys. Rev. X*, vol. 5, p. 041022, Nov. 2015.

[4] M. Kowalewski, K. Bennett, and S. Mukamel, "Non-adiabatic dynamics of molecules in optical cavities," *J. Chem. Phys.*, vol. 144, p. 054309, Feb. 2016.

[5] O. Vendrell, "Collective Jahn-Teller Interactions through Light-Matter Coupling in a Cavity," *Phys. Rev. Lett.*, vol. 121, p. 253001, Dec. 2018.

[6] C. Fábri, G. J. Halász, L. S. Cederbaum, and Á. Vibók, "Born–Oppenheimer approximation in optical cavities: From success to breakdown," *Chem. Sci.*, vol. 12, pp. 1251–1258, Feb. 2021.

[7] R. Crespo-Otero and M. Barbatti, "Recent Advances and Perspectives on Nonadiabatic Mixed Quantum–Classical Dynamics," *Chem. Rev.*, vol. 118, pp. 7026–7068, Aug. 2018.

[8] G. Groenhof, C. Climent, J. Feist, D. Morozov, and J. J. Toppari, "Tracking Polariton Relaxation with Multiscale Molecular Dynamics Simulations," *J. Phys. Chem. Lett.*, vol. 10, pp. 5476–5483, Sept. 2019.

[9] Y. Zhang, T. Nelson, and S. Tretiak, "Non-adiabatic molecular dynamics of molecules in the presence of strong light-matter interactions," *J. Chem. Phys.*, vol. 151, p. 154109, Oct. 2019.

[10] J. C. Tully, "Molecular dynamics with electronic transitions," *The Journal of Chemical Physics*, vol. 93, pp. 1061–1071, July 1990.

[11] J. Fregoni, G. Granucci, E. Coccia, M. Persico, and S. Corni, "Manipulating azobenzene photoisomerization through strong light–molecule coupling," *Nat. Commun.*, vol. 9, Dec. 2018.

[12] H. L. Luk, J. Feist, J. J. Toppari, and G. Groenhof, "Multiscale Molecular Dynamics Simulations of Polaritonic Chemistry," *J. Chem. Theory Comput.*, vol. 13, pp. 4324–4335, Sept. 2017.

[13] E. Davidsson and M. Kowalewski, "Atom Assisted Photochemistry in Optical Cavities," *J. Phys. Chem. A*, vol. 124, pp. 4672–4677, June 2020.

[14] O. Vendrell, "Coherent dynamics in cavity femtochemistry: Application of the multi-configuration time-dependent Hartree method," *Chemical Physics*, vol. 509, pp. 55–65, June 2018.

[15] I. S. Ulusoy, J. A. Gomez, and O. Vendrell, "Modifying the Nonradiative Decay Dynamics through Conical Intersections via Collective Coupling to a Cavity Mode," *J. Phys. Chem. A*, vol. 123, pp. 8832–8844, Oct. 2019.

[16] J. del Pino, F. A. Y. N. Schröder, A. W. Chin, J. Feist, and F. J. Garcia-Vidal, "Tensor network simulation of polaron-polaritons in organic microcavities," *Phys. Rev. B*, vol. 98, p. 165416, Oct. 2018.

[17] J. del Pino, F. A. Y. N. Schröder, A. W. Chin, J. Feist, and F. J. Garcia-Vidal, "Tensor Network Simulation of Non-Markovian Dynamics in Organic Polaritons," *Phys. Rev. Lett.*, vol. 121, Nov. 2018.

[18] R. Jestädt, M. Ruggenthaler, M. J. T. Oliveira, A. Rubio, and H. Appel, "Light-matter interactions within the Ehrenfest–Maxwell–Pauli–Kohn–Sham framework: Fundamentals, implementation, and nano-optical applications," *Advances in Physics*, vol. 68, pp. 225–333, Oct. 2019.

[19] D. Sidler, C. Schäfer, M. Ruggenthaler, and A. Rubio, "Polaritonic Chemistry: Collective Strong Coupling Implies Strong Local Modification of Chemical Properties," *J. Phys. Chem. Lett.*, vol. 12, pp. 508–516, Jan. 2021.

[20] U. Mordovina, C. Bungey, H. Appel, P. J. Knowles, A. Rubio, and F. R. Manby, "Polaritonic coupled-cluster theory," *Phys. Rev. Research*, vol. 2, p. 023262, June 2020.

[21] T. S. Haugland, E. Ronca, E. F. Kjønstad, A. Rubio, and H. Koch, "Coupled Cluster Theory for Molecular Polaritons: Changing Ground and Excited States," *Phys. Rev. X*, vol. 10, p. 041043, Dec. 2020.

[22] F. Herrera and F. C. Spano, "Theory of Nanoscale Organic Cavities: The Essential Role of Vibration-Photon Dressed States," *ACS Photonics*, vol. 5, pp. 65–79, Jan. 2018.

[23] E. Davidsson and M. Kowalewski, "Simulating photodissociation reactions in bad cavities with the Lindblad equation," *J. Chem. Phys.*, vol. 153, p. 234304, Dec. 2020.

[24] S. Felicetti, J. Fregoni, T. Schnappinger, S. Reiter, R. de Vivie-Riedle, and J. Feist, "Photoprotecting Uracil by Coupling with Lossy Nanocavities," *J. Phys. Chem. Lett.*, Sept. 2020.

[25] J. Torres-Sánchez and J. Feist, "Molecular photodissociation enabled by ultrafast plasmon decay," *J. Chem. Phys.*, vol. 154, p. 014303, Jan. 2021.

[26] D. S. Wang, T. Neuman, J. Flick, and P. Narang, "Light–matter interaction of a molecule in a dissipative cavity from first principles," *J. Chem. Phys.*, vol. 154, p. 104109, Mar. 2021.

[27] P. Antoniou, F. Suchanek, J. F. Varner, and J. J. Foley, "Role of Cavity Losses on Nonadiabatic Couplings and Dynamics in Polaritonic Chemistry," *J. Phys. Chem. Lett.*, vol. 11, pp. 9063–9069, Nov. 2020.

[28] J. Fregoni, G. Granucci, M. Persico, and S. Corni, "Strong Coupling with Light Enhances the Photoisomerization Quantum Yield of Azobenzene," *Chem*, vol. 6, pp. 250–265, Jan. 2020.

# 9. Publication: Disorder Enhanced Vibrational Entanglement and Dynamics in Polaritonic Chemistry

The following chapter is a reprint of the preprint arXiv:2107.06053 (2021) [1], which discusses the effect of disorder on entanglement in polaritonic chemistry. The aim of this chapter is to study quantum entanglement between vibrational and electro-photonic degrees of freedom as a proxy to understand the role of quantum effects in polaritonic chemistry setups. Such entanglement is often neglected in semi-classical theoretical descriptions, e.g. by computing the Ehrenfest dynamics (see Chapter 8). In this work, we have shown that disorder can strongly enhance the build-up of vibrational entanglement on short timescales after incoherent photo-excitation of either the cavity or a single molecule. We have found that this can have direct consequences for reaction coordinate dynamics, whose probability distribution is modified by the entanglement. In particular, we have analyzed this phenomenon in a disordered Holstein-Tavis-Cummings model (see Chapter 7). Using a numerical technique based on matrix product states, we have simulated the exact quantum dynamics of more than 100 molecules.

This chapter is organized as follows: Section 9.1 introduces the main physics. Then, the disordered Holstein-Tavis-Cummings model is quickly re-introduced in Section 9.2, and realistic parameters are discussed in Section 9.3. In Section 9.4, we summarize the main results of this chapter, which we subsequently discuss in more detail. In Section 9.5, we scrutinize how disorder modifies excitation transfer and as a result also the mean vibrational dynamics. In Section 9.6, we then analyze the influence of entanglement on the nuclear distribution along the reaction coordinates. The scaling of the entanglement and modifications to the distribution with the different system parameters is presented in Section 9.7. Finally, Section 9.8 concludes this chapter.

## 9.1. Introduction

Polaritonic chemistry, or the modification of chemical reactivity using effects of cavity quantum electrodynamics (cavity-QED), is an emerging field of research at the interface of quantum chemistry and physics [2–8]. Experiments have demonstrated that a collective coupling of electronic [9–17] or vibrational [18–22] transitions of large ensembles of molecules to confined non-local electromagnetic fields can provide means to control chemical reactivity. Many experiments have achieved a collective strong coupling regime, where the cavity and the molecules can coherently exchange energy at a rate faster than

their decay processes. In such scenarios, the cavity-molecule system has to be considered as one entity with new "polaritonic" eigenstates, which are collective superpositions of photonic and molecular degrees of freedom. Identifying the underlying mechanisms of collective cavity-modified chemistry remains to be a major challenge. A theoretical understanding of the problem requires to solve complex quantum many-body dynamics in large systems with coupled electronic, photonic, and vibrational degrees of freedom.

Numerically computing the collective time evolution of all degrees of freedom in polaritonic chemistry is an important — yet extremely challenging — task for understanding chemical reaction dynamics, which has been attempted at different levels of approximations. For small systems, the Schrödinger equation can be solved directly [23] or using quantum chemistry tools such as multi-configurational time-dependent Hartree-Fock methods [24]. Density functional theory can be used for ab initio simulations of few realistic molecules [25]. For larger systems, stronger approximations are needed. Standard approaches are based on the Born-Oppenheimer approximation. In the Born-Oppenheimer approximation, electro-photonic dynamics are treated as instantaneous compared to nuclear dynamics so that polaritonic (and dark) potential energy surfaces can be computed [26]. On these adiabatic potential energy surfaces, nuclear dynamics can then be computed. However, this method neglects non-adiabatic couplings between potential energy surfaces and thus fails if the separation between potential energy surfaces becomes small, as it is often the case in polaritonic chemistry [6, 27, 28]. In order to include the non-adiabatic couplings, two common methods are fewest switches surface hopping [29–31] or mean-field Ehrenfest dynamics [32, 33]. Ehrenfest dynamics assumes a product state between nuclear and electro-photonic degrees of freedom, completely neglecting any entanglement between them. As a consequence, such entanglement can serve as a measure for the validity of approximations relying on the separability of nuclear and electro-photonic degrees of freedom, and more generally the complexity of the dynamics.

The role of "quantum effects" in molecular dynamics is also a fundamentally interesting research question [34–37]. Entanglement is often used to determine the importance of quantum effects by quantifying quantum correlations without classical equivalent [38–40]. In this context, the entanglement between electronic and nuclear degrees of freedom of molecules has been previously studied for single molecules [41, 42]. For cavity-coupled molecules, it is known that a collective cavity-coupling can strongly suppress this entanglement by reducing vibronic couplings, an effect termed "polaron decoupling" [43, 44]. However this effect neglects local disorder in the electronic level spacings of individual molecules. In this paper, we will show that the combined effect of local disorder and a cavity coupling can lead to a *strong enhancement* of electro-vibrational entanglement build-up on a typical timescale for coherent molecular dynamics (femtoseconds) after an incoherent photo-excitation.

To analyze this entanglement build-up we make use of a matrix product state (MPS) approach. Recently, MPSs (more broadly: tensor networks) have been suggested to numerically tackle dynamics in polaritonic chemistry [45] also for larger system sizes. An MPS can be thought of as a generalization of a product state, which by definition does

not include any entanglement, into a larger space with small but finite entanglement. The entanglement of an MPS is limited by a so called "bond dimension", which can be systematically increased until convergence is reached [46]. Since excessively large entanglement rarely plays an important role in physical dynamics, MPS simulations often become numerically exact. By construction, MPS concepts provide a direct access for studying the entanglement dynamics of a system, and they have been used in that context extensively, e.g. for spin-chain or Hubbard-type models in many-body physics [39, 40].

Here, using this numerical approach we study the femtosecond-scale dynamics of more than 100 molecules with electronic transitions collectively strongly coupled to a cavity mode (electronic strong coupling) after an incoherent photo-excitation (see Fig. 9.1 for a sketch). We analyze a minimal disordered version of the Holstein-Tavis-Cummings (HTC) model [43, 47, 48], which despite its simplicity includes the main ingredients for microscopically understanding physical mechanisms in polaritonic chemistry. We find that disorder enhances excitation transfer from the initially excited state to a number of molecules selected by a resonance condition [see Fig. 9.1(b/c)] [49–51]. This leads to coherent out-of-phase oscillations of the vibrational modes of these molecules. As a consequence, disorder enhances entanglement between vibrations and electronic degrees of freedom several-fold [see sketch in Fig. 9.1(d)]. This effect is largest in a regime where disorder is energetically comparable to collective cavity-couplings. Importantly, we find that the disorder-induced focused excitation transfer to a few molecules leads to an enhanced cavity-modified vibrational dynamics on the single molecule level, compared to a disorder-less scenario where the excitation is diluted among all coupled molecules equally. This effect crucially depends on whether the initial incoherent excitation is absorbed by a single molecule or the cavity, and we analyze both scenarios [see Fig. 9.1(b)]. We further relate large entanglement to modifications of the shape of the nuclear wave packets, which become broadened and non-Gaussian. In this respect, the vibrational entanglement may have direct consequences for chemical processes.

## 9.2. Theoretical Model

We consider a system of $N$ toy model molecules coupled to a single mode optical cavity, i.e. a disordered version of the Holstein-Tavis-Cummings (HTC) model [43, 47, 48]. Here, each molecule has two electronic energy levels. Different nuclear equilibrium configurations in the ground and excited state result in two displaced harmonic one dimensional potential energy "surfaces" as shown in Fig. 9.1a. We further include an inhomogeneous broadening, i.e. disorder of the electronic energy stemming from random energy spacings of the electronic levels [52], typically induced by the environment in experiments. The disordered HTC Hamiltonian reads [43]

$$\hat{H} = \hat{H}_{\mathrm{TC}} + \hat{H}_{\mathrm{vib}} + \hat{H}_{\mathrm{H}} + \hat{H}_{\mathrm{dis}}\,. \tag{9.1}$$

The coupling of the cavity is described by the Tavis-Cummings (TC) Hamiltonian, which, in a frame rotating at the cavity frequency $\omega_{\mathrm{C}}$, reads ($\hbar = 1$ throughout this paper)

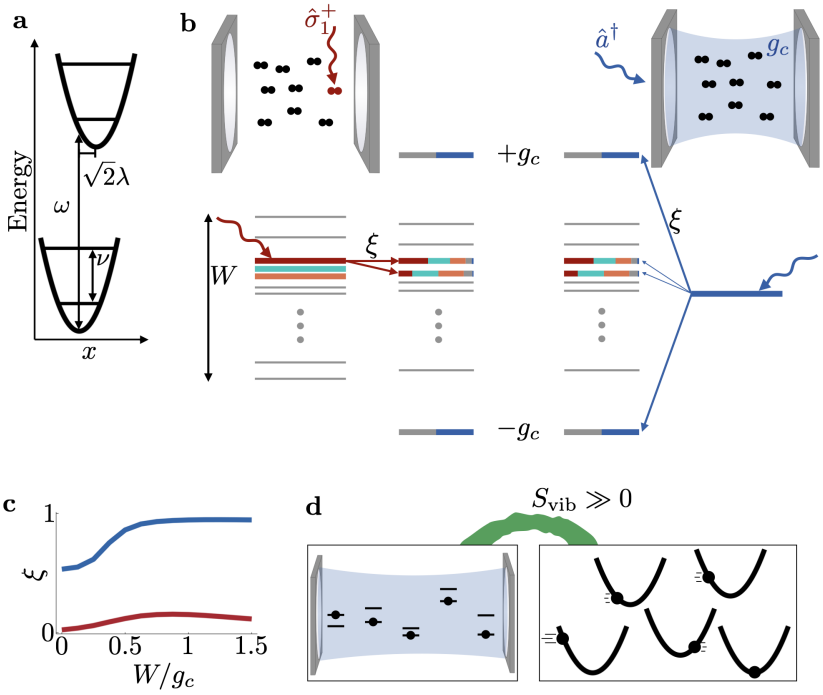


Figure 9.1. – **Setup and main physics**. **a** We consider toy-model molecules with two harmonic potential energy surfaces (vibrational level spacing $\nu$). Both surfaces are energetically separated by the electronic level spacing $\omega$ and displaced by $\sqrt{2}\lambda$ along the reaction coordinate $x$. **b** An ensemble of molecules is coupled to a cavity with collective strength $g_c$. We analyze dynamics after incoherent photo-excitation of either an individual molecule (red, left) or the cavity (blue, right). An energy level scheme for electro-photonic excitations is sketched. Disorder leads to inhomogeneous broadening by $W$ (left). The coupling of $N$ electronic excitation states (left; gray, red, cyan, orange lines) and a single cavity excitation (right; blue line) lead to new eigenstates (center) that are superpositions with contributions indicated by the different colors. For $g_c \gg W$, two polariton states at energies $\pm g_c$ are formed (half grey, half blue), as well as $N-1$ dark states (other lines). Due to disorder, the dark states are superpositions of a few energetically resonant electronic excitations. All dark states also acquire a small photon weight (very small blue contribution). After incoherent excitation, energy is transferred through the coupled eigenstates as indicated by straight arrows (transfer probability $\xi$). For a molecule excitation, energy is predominantly transferred through dark states, for a cavity excitation through polariton states (arrow thickness). **c** Disorder enhances the transfer away from the initially excited state after molecular (red) or cavity (blue) excitation. The plot shows a time averaged transfer probability $\xi = \nu/(2\pi)\int_0^{2\pi/\nu} dt\,[1-\langle\hat{O}^\dagger\hat{O}\rangle(t)]$ where $\hat{O} = \hat{\sigma}_1^-, \hat{a}$ in a system with 100 molecules. **d** Excitation transfer leads to a coherent out-of-phase oscillation of different molecules and thus large entanglement entropy, $S_{\mathrm{vib}}$, between electro-photonic (left) and vibrational (right) degrees of freedom.

$$\hat{H}_{\mathrm{TC}} = \sum_{n=1}^{N} \Delta \hat{\sigma}_n^+ \hat{\sigma}_n^- + g \sum_{n=1}^{N} \left( \hat{a} \hat{\sigma}_n^+ + \hat{a}^\dagger \hat{\sigma}_n^- \right), \tag{9.2}$$

where $\hat{a}$ is the destruction operator for a cavity photon, $\hat{\sigma}_n^\pm$ are the raising/lowering operators for the electronic level of the $n$-th molecule. $\Delta = \omega - \omega_{\mathrm{C}}$ is the detuning between the electronic transition frequency at the Condon point $\omega$ and $\omega_{\mathrm{C}}$, chosen to be $\Delta = 0$ in the remainder of this paper. The coupling strength of a single molecule to the cavity is given by $g \equiv g_c/\sqrt{N}$. In the single-excitation Hilbert space considered here, the TC Hamiltonian has two polariton eigenstates $|\pm\rangle = \hat{a}^\dagger/\sqrt{2} \pm \sum_n \hat{\sigma}_n^+/\sqrt{2N}\,|0\rangle_{\mathrm{exc+ph}}$ for the ground state $|0\rangle_{\mathrm{exc+ph}}$ without any excitations, split by the Rabi splitting of $2g_c$. The other $N-1$ eigenstates are degenerate dark states with zero energy.

The nuclear coordinates are described by harmonic potentials

$$\hat{H}_{\mathrm{vib}} = \nu \sum_{n=1}^{N} \hat{b}_n^\dagger \hat{b}_n \,, \tag{9.3}$$

where $\hat{b}_n$ is the lowering operator of the $n$-th molecule and $\nu$ the molecular oscillation frequency. The eigenstates of $\hat{H}_{\mathrm{vib}}$ are Fock states $\prod_n (\hat{b}_n^\dagger)^{a_n} |0_{\mathrm{vib}}\rangle$ with $a_n$ vibrational quanta on the $n$-th molecule and the total (undisplaced) vibrational ground state $|0_{\mathrm{vib}}\rangle$. We define dimensionless oscillator position and momentum variables as $\hat{x}_n = (\hat{b}_n + \hat{b}_n^\dagger)/\sqrt{2}$ and $\hat{p}_n = -\mathrm{i}(\hat{b}_n - \hat{b}_n^\dagger)/\sqrt{2}$, respectively.

The nuclear coordinate of each molecule is coupled to its electronic state by a Holstein coupling

$$\hat{H}_{\mathrm{H}} = -\lambda\nu \sum_{n=1}^{N} \left( \hat{b}_n + \hat{b}_n^\dagger \right) \hat{\sigma}_n^+ \hat{\sigma}_n^- \,. \tag{9.4}$$

This corresponds to a shift of the excited state potential energy surface. The dimensionless Huang-Rhys factor $\lambda^2$ quantifies the minimum of the excited state harmonic potential at position $\sqrt{2}\lambda$ with energy $\omega - \lambda^2\nu$.

Finally, we include disorder by

$$\hat{H}_{\mathrm{dis}} = \sum_n \epsilon_n \hat{\sigma}_n^+ \hat{\sigma}_n^- \,, \tag{9.5}$$

where $\epsilon_n = \omega_n - \omega$ is the deviation of the electronic transition energy of the $n$-th molecule from the mean. We take the $\epsilon_n$ as independent, normally distributed random variables with mean 0 and variance $W^2$.

**Dynamics & Entanglement** – In the following, we analyze the short-time Hamiltonian dynamics on the scale of a single nuclear vibration period, $0 \leq t \leq 2\pi/\nu$ for two

different initial states. In one case, a single molecule ($n = 1$) is excited by the incoherent absorption of a photon, i.e. we consider the initial state $|\psi_0^m\rangle = \hat{\sigma}_1^+ |0\rangle_{\text{ph}} |0\rangle_{\text{exc}} |0\rangle_{\text{vib}}$ [Fig. 9.1(b), left]. In the other case the photon is incoherently absorbed by the cavity, $|\psi_0^c\rangle = \hat{a}^\dagger |0\rangle_{\text{ph}} |0\rangle_{\text{exc}} |0\rangle_{\text{vib}}$ [Fig. 9.1(b), right]. Here, $|0\rangle_{\text{exc,vib,ph}}$ denote the respective ground states of the bare electronic, vibrational and photonic Hamiltonian.

In order to analyze entanglement between electro-photonic and nuclear degrees of freedom, we separate the full Hilbert space as $\mathcal{H} = \mathcal{H}_{\text{ph}} \otimes \mathcal{H}_{\text{exc}} \otimes \mathcal{H}_{\text{vib}}$ into three sub-Hilbert spaces for the cavity photon, electronic excitations, and vibrations, respectively. For a pure state $|\psi\rangle$, the entanglement between the two subsystems $\mathcal{H}_{\text{ph}} \otimes \mathcal{H}_{\text{exc}}$ and $\mathcal{H}_{\text{vib}}$ can be quantified by the von Neumann entropy of either subsystem [39, 40], e.g.

$$S_{\text{vib}} = -\operatorname{Tr}\left[\hat{\rho}_{\text{vib}} \log_2(\hat{\rho}_{\text{vib}})\right], \tag{9.6}$$

where $\hat{\rho}_{\text{vib}}$ is the reduced density matrix which can be obtained from the state $|\psi\rangle$ by tracing over $\mathcal{H}_{\text{ph}} \otimes \mathcal{H}_{\text{exc}}$: $\hat{\rho}_{\text{vib}} = \operatorname{Tr}_{\text{ph+exc}}(|\psi\rangle\langle\psi|)$. In the case of a product state (or "mean-field") assumption, the state of the system would be assumed to factorize throughout the evolution of the system

$$|\psi(t)\rangle = |\phi_{\text{ph+exc}}(t)\rangle \otimes |\phi_{\text{vib}}(t)\rangle . \tag{9.7}$$

In this scenario, $\hat{\rho}_{\text{vib}}(t) = |\phi_{\text{vib}}(t)\rangle\langle\phi_{\text{vib}}(t)|$ and $S_{\text{vib}}(t) = 0$ at all times. An entangled state $|\psi\rangle$ is a linear superposition of many such terms, resulting in $S_{\text{vib}} > 0$. The von Neumann entropy $S_{\text{vib}}$ can be readily computed in the MPS framework (see Appendix). It is noteworthy that this product state assumption is equivalent to the one made in mean-field Ehrenfest dynamics, where in addition the nuclear motion is treated classically. Since in our case the nuclear wavefunction always stays coherent and thus follows classical equations of motion, our product state results are equivalent to mean-field Ehrenfest results.

## 9.3. Parameter Regimes

We choose parameter values that are motivated by a setup with Rhodamine 800, for which strong coupling has been demonstrated [53], and which has been previously considered in tensor network studies of strong coupling experiments [45]. In particular, we set $0.1 \leq \lambda \leq 0.5$ and $\nu = 0.3 g_c$. For an experimentally demonstrated vacuum Rabi splitting of $2g_c = 700\text{meV}$ [9], this corresponds to $\nu = 105\text{meV}$ and reorganization energies $1\text{meV} \lesssim \lambda^2\nu \lesssim 26\text{meV}$, similar to measured values [54]. Thermal excitation fractions $\sim \exp(-\nu/k_BT)$ are negligible at room temperature ($k_BT \approx 26\text{meV}$). Although the Rabi splitting of 700meV falls into the ultra-strong coupling regime for the relevant electronic transition of Rhodamine 800 at $\sim 2\text{eV}$ [53], we do not include counter-rotating terms here in order to derive general results which are relevant for strong coupling experiments.

For our case of $\lambda\nu \ll \nu \ll g_c$, the Hamiltonian Eq. (9.1) can be categorized into strong ($W \gg g_c$) and weak ($W \ll g_c$) coupling regimes depending on the relative magnitude of $\hat{H}_{\mathrm{TC}}$ and $\hat{H}_{\mathrm{dis}}$. The strong coupling regime features polaritonic and dark eigenstates of $\hat{H}_{\mathrm{TC}}$ which are mixed perturbatively (Fig. 9.1a). In perturbation theory we find that "gray" states $|d\rangle$ acquire photo-contributions of $\sum_d |\langle d|1_{\mathrm{ph}}\rangle|^2 \sim \lambda^2\nu^2/(2g_c^2)$ and $\sum_d |\langle d|1_{\mathrm{ph}}\rangle|^2 \approx W^2/g_c^2$ due to small vibronic coupling and disorder, respectively (see Appendix and [51, 52, 55, 56] for details). In the weak coupling regime, polariton states cease to exist and all eigenstates are structurally similar to the "gray" states in Fig. 9.1a. We vary $0 \leq W \leq 1.5g_c$ analyzing both weak and strong coupling scenarios. The timescale of vibrational evolution $t \sim 2\pi/\nu$ corresponds to tens of femtoseconds, and can be faster than dissipative mechanisms which we do not include explicitly. For quality factors $Q \gtrsim 1000$ which have e.g. been achieved for distributed Bragg reflectors, cavity decay is negligible on these timescales [57]. Similarly, relaxation of molecular excitation into vibrational or electromagnetic reservoirs typically occurs on even slower timescales of picoseconds or nanoseconds, respectively [48]. In fact, on a microscopic level the coherent dynamics due to disorder and vibronic coupling terms $\hat{H}_{\mathrm{dis}}$ and $\hat{H}_{\mathrm{H}}$ that we simulate here can be considered as one of the mechanisms responsible for electronic dephasing.

## 9.4. Main Results

Fig. 9.2 visualizes the main feature of the entanglement and vibrational dynamics after initial molecular ($|\psi_0^m\rangle$, panels a,c,e), and cavity ($|\psi_0^c\rangle$, panels b,d,f) excitation. Strikingly, in both scenarios we find that increasing the disorder in the range $0 \leq W \leq g_c$ leads to a drastically enhanced entanglement entropy build-up, seen in the evolution of the disorder averaged entropy $\overline{S_{\mathrm{vib}}}$ in Fig. 9.2a,b. For $W = 0$, the entanglement entropy remains below values of one, and, in the cavity excitation case only, exhibits oscillatory features which we can attribute to collective Rabi oscillation due to a predominant excitation transfer to the polariton states. For $W > g_c/2$ those features disappear and we observe a strong increase to a maximum value at $t \sim 2\pi/\nu$ and $t \sim \pi/\nu$ in Fig. 9.2a and b, respectively. This entanglement build-up is matched by modifications of the phase space dynamics (Fig. 9.2c,d) and the shape of the probability distribution $P_i(x_i, t)$ (Fig. 9.2e,f) of the reaction coordinate. Below, we will relate all three effects to disorder enhanced excitation transfer. We will see that neither the entanglement build-up nor the distribution shape changes can be captured by a product state assumption Eq. (9.7), i.e. they go beyond the mean-field Ehrenfest dynamics.

Fig. 9.2c,d shows the phase space dynamics of the disorder averaged expectation values $\overline{x_i}$ and $\overline{p_i}$ of the reaction coordinate position and momentum operators $\hat{x}_i$ and $\hat{p}_i$ on molecule $i$, respectively. In the molecular excitation case in Fig. 9.2c, we observe phase space circles for the initially excited molecule ($i = 1$). In the disorder-less case $W = 0$, we find an oscillation around the displaced equilibrium position of the excited state oscillator, $\sqrt{2}\lambda \approx 0.57$. In this case the evolution is very close to the no-cavity scenario

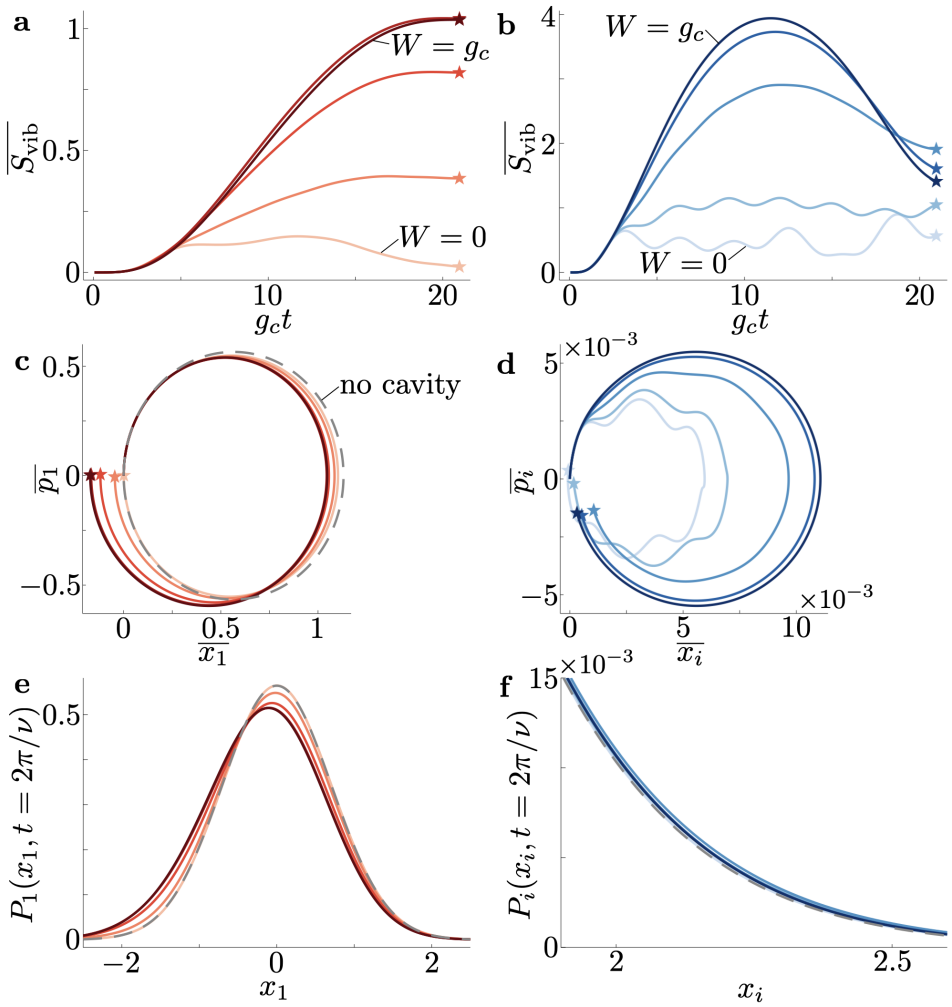


Figure 9.2. – **Main results**. **a**,**b** Time evolution of the disorder averaged entanglement entropy $\overline{S_{\mathrm{vib}}}$ in the time-range $0 \leq t \leq 2\pi/\nu$ for disorder strengths $0 \leq W \leq g_c$ (from light to dark $W = 0$, $g_c/4$, $g_c/2$, $3g_c/4$, $g_c$). Stars indicate the final time $t = 2\pi/\nu$. The left panels (red lines) correspond to the initial molecule excitation state $|\psi_0^m\rangle$, the right panels (blue lines) to the initial cavity excitation $|\psi_0^c\rangle$. **c**,**d** Vibrational phase space evolution. Shown are the disorder averaged expectation values $\overline{x_i}$ and $\overline{p_i}$ of the oscillator position and momentum operators, $\hat{x}_i$ and $\hat{p}_i$, for values of $W$ correpsonding to **a**. The gray dashed-line shows the no-cavity case. In **c** the dynamics of the initially excited molecule is shown, in **d** an additional average over all molecules is taken. **e**,**f** Averaged probability distributions of the reaction coordinate $x$ at time $t = 2\pi/\nu$ (stars in other panels, gray dashed line: no-cavity case). In all panels, we average over 64 disorder realizations, $N = 100$, $\nu = 0.3g_c$, $\lambda = 0.4$.

(gray dashed line), for which we obtain a perfect circle around $\sqrt{2}\lambda$ corresponding to the usual coherent harmonic oscillator evolution.

However, the situation changes drastically for $W > 0$. Now, the centers of the phase space circles dynamically shift to smaller values of $\overline{x_1}$. We note that this behavior can be rationalized without requiring the large entanglement build-up seen in Fig. 9.2a. Assuming the product state ansatz from Eq. (9.7), one would expect that the Holstein term $\hat{H}_{\mathrm{H}}$ [Eq. (9.4)] leads to an effective excited state oscillator equilibrium position of $\sqrt{2}\lambda\langle\hat{\sigma}_1^+\hat{\sigma}_1^-\rangle$ and thus effectively to a time-dependent shift of the minimum depending on $\langle\sigma_1^+\hat{\sigma}_1^-\rangle(t)$. For $W = 0$ the initial state $|\psi_0^m\rangle$ is almost a dark eigenstate of $\hat{H}_{\mathrm{TC}}$, such that cavity induced excitation transfer is strongly suppressed and the excitation remains on the molecule, $\langle\hat{\sigma}_1^+\hat{\sigma}_1^-\rangle(t) \sim 1$ (see Appendix). In contrast, for finite disorder $W > 0$, the excitation transfer is significantly enhanced and we perturbatively derive $1-\langle\hat{\sigma}_1^+\hat{\sigma}_1^-\rangle(t) \sim Wt/N$ for $g \ll W \ll g_c$ (see Appendix). This is in qualitative agreement with recent results predicting that disorder can enhance excitation transfer in models without vibrations [49–51].

For an initial cavity excitation $|\psi_0^c\rangle$, the phase space evolution traces much smaller circles. As expected, for $W = 0$ the phase space evolution is approximately centered at $\overline{x_i} \sim \sqrt{2}\lambda/(2N)$, and exhibits oscillations at polariton Rabi frequencies. For increasing disorder $W \to g_c$, the center of the circle now shifts in the opposite direction compared to Fig. 9.2c, to roughly twice the value $\overline{x_i} \to \sqrt{2}\lambda/N$. This can again be rationalized by looking at the evolution of the expected local molecule excitations $\langle\hat{\sigma}_i^+\hat{\sigma}_i^-\rangle(t)$. For $W = \lambda\nu = 0$, the hybrid nature of the polariton states induces Rabi oscillations between the initial cavity photon state and a collective excitation of all molecules, such that for each molecule the excitation fraction oscillates according to $\langle\hat{\sigma}_i^+\hat{\sigma}_i^-\rangle(t) = \cos^2(g_c t)/N$, leading to the observed phase space evolution for $W = 0$. Finite disorder, however, leads to a photo-contribution of all dark states (perturbatively $\sim W^2/g_c^2$). Therefore, excitations are now transferred quickly (timescale $1/g_c$) from the cavity to individual molecules, and one thus expects a disorder averaged excitation population on each molecule $\overline{\langle\hat{\sigma}_i^+\hat{\sigma}_i^-\rangle} \to 1/N$ for sufficiently large $W$. This explains the observed shift.

Fig. 9.2e,f shows the probability distribution $P_i(x_i, t)$ of the reaction coordinate at time $t = 2\pi/\nu$. Without cavity, at this time the distribution is a Gaussian centered at $x_1 = 0$ with variance $1/2$, corresponding to a coherent state (grey dashed line). We find that in a cavity and for $W = 0$, the distribution is extremely close to the no-cavity scenario. For increasing $W$, however, for the molecular excitation $|\psi_0^m\rangle$, the distribution of the reaction coordinate of the initially excited molecule $P_1(x_1, t = 2\pi/\nu)$ clearly shifts to smaller values of $x_1$. In addition, the distribution broadens and acquires an asymmetric shape in Fig. 9.2e. For an initial cavity excitation $|\psi_0^c\rangle$, we observe that finite $W$ leads to modifications in the tails of the distribution only, i.e. for large values of $x_i$ (Fig. 9.2f). Note that the tail modifications in Fig. 9.2f seem very small, since a single molecule only receives a $\sim 1/N$ contribution of the excitation energy (here, $N = 100$). However, below we see that the cumulative effect on the wave function shape can still have important consequences for many molecules.

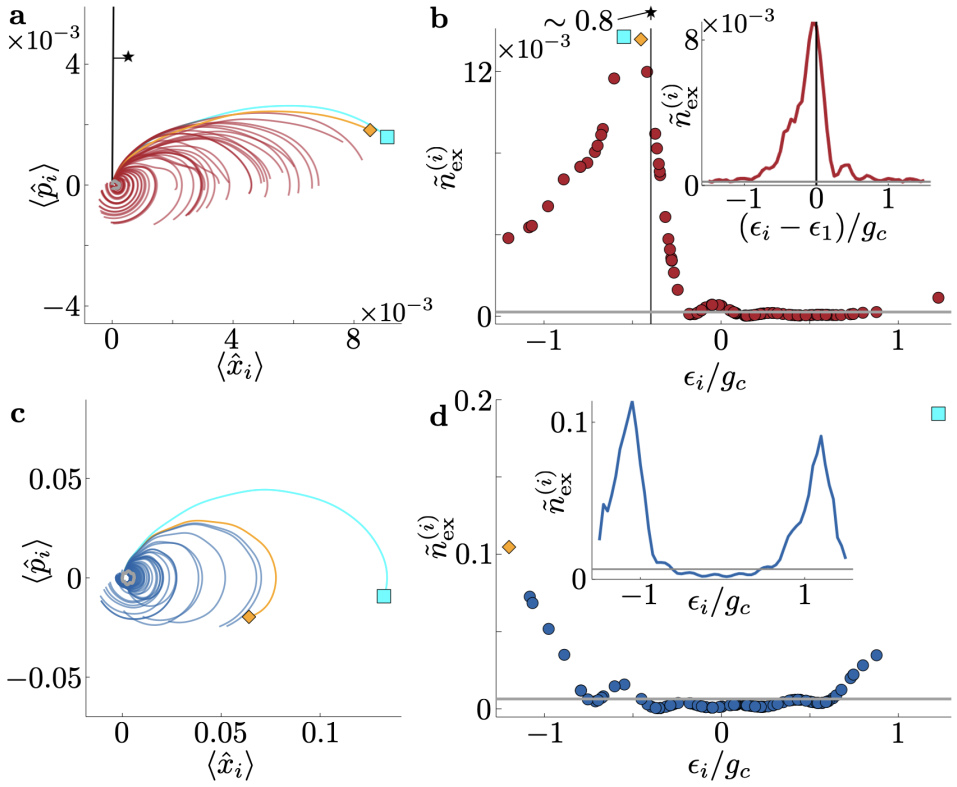


Figure 9.3. – **Excitation transfer dynamics. a** Microscopic phase space evolution of 100 molecular oscillators for a single disorder realization with $W = g_c/2$. The black star and line correspond to the initially excited molecule, the other lines to the 99 initially un-excited ones. The gray line (barely visible around the origin) represents the $W = 0$ reference. The cyan square and orange diamond are two example molecules with most strongly modified vibrational dynamics, also identified in **b**. **b** Excitation probability $\tilde{n}_{\mathrm{ex}}^{(i)} = \langle \hat{\sigma}_i^+ \hat{\sigma}_i^- \rangle (t = 2\pi/\nu)$ as a function of the energy off-set $\epsilon_i$ of the respective molecule. The inset shows the disorder-averaged excitation probability as a function of the energy difference to the initially excited state. The gray horizontal lines are the $W = 0$ reference. **c**,**d** identical plots for a cavity excitation. Parameters: $N = 100$, $\nu = 0.3 g_c$, $\lambda = 0.4$, disorder drawn from a normal distribution with width $W$, 256 disorder realizations.

## 9.5. Excitation Transfer Dynamics

In Fig. 9.3, we now exemplify the connection between the time-dependent local molecular excitation and the phase space evolution for an intermediate disorder strength $W = g_c/2$ microscopically. Fig. 9.3a shows the vibrational evolution of each of the 100 molecules for a single disorder realization, after exciting one molecule initially (line with star: excited molecule, other red/cyan/yellow lines: 99 initially unexcited molecules). Strikingly, we observe that the molecules whose dynamics is modified most strongly correspond to the ones with a random energy very close to the initially excited one. The reason for this is seen in comparison with Fig. 9.3b where we plot the excitation numbers of the molecules at $t = 2\pi/\nu$ as function of their random energy offset $\epsilon_i$. There we identify the molecules with the strongest phase space modification (cyan square and orange diamond), and the initially excited one (blue star and vertical line). Crucially, the excitation fraction of these molecules, and thus their phase space dynamics, is much larger than for the homogeneous disorder-less case with $W = 0$ (gray lines in Fig. 9.3a,b, barely visible in a). The same behavior is generally seen also after disorder-averaging (see inset). We attribute a visible asymmetry towards smaller energies in Fig. 9.3b to additional resonances with states of higher vibrational energies. It is also interesting to point out that in contrast to the initially excited molecule, the phase space variables of the other molecules generally do not complete one revolution until $t = 2\pi/\nu$ (Fig. 9.3a), and all molecular oscillators evolve out-of-phase.

A similar picture presents itself when initially exciting the cavity-mode (Fig. 9.3c,d). The excitation is again primarily transferred from the cavity to several molecules, but now with energies $\epsilon_i \sim \pm g_c$ close to resonance with the bare polaritons in the strong coupling regime. These molecules acquire much larger excitation fractions than the no disorder reference (gray line in Fig. 9.3d). As a result, molecular oscillations of molecules with an energy offset $\epsilon_n \sim \pm g_c$ are most strongly modified, as confirmed in Fig. 9.3c.

We can deduce the following microscopic picture from our analysis in Fig. 9.3: While in the $W = 0$ case the initial excitation is generally diluted throughout the system, disorder $W > 0$ leads to a strongly enhanced excitation transfer to a few molecules in the energetic vicinity of either the initially excited molecule or the polariton states, depending on the scenario (as sketched in Fig. 9.1b). In a product state picture, this then modifies the vibrational dynamics of those molecules depending on the amount of local excitation, $\langle \hat{\sigma}_i^+ \hat{\sigma}_i^- \rangle$. However, the product state assumption contradicts the build-up of large vibrational entanglement seen in Fig. 9.2a/b. Rather, the out-of-phase oscillator dynamics should be considered quantum-mechanically coherent, leading to the large entanglement entropies. In the following we will study the direct implications of this entanglement.

## 9.6. Reaction Coordinate Distribution Shapes

We are now interested in the time evolution of the full reaction coordinate distribution $P_n(x_n, t)$ of molecule $n$ and in particular, we will analyze the evolution of its tails in Fig. 9.4. In a product state ansatz [Eq. (9.7)], the instantaneous nuclear potential corresponds to a shifted harmonic oscillator. Then, nuclear wave packets of the individual molecules would always stay in a Gaussian shape. Crucially, this is not the case if we allow for finite entanglement. Then, in general, the Holstein coupling $\propto \hat{x}_n \hat{\sigma}_n^+ \hat{\sigma}_n^-$ does not factorize and thus modifies the wave packet shape over time (see e.g. Fig. 9.2e). To exemplify this, consider a single molecule $n$ with a constant excitation fraction $\beta$ (without cavity coupling). The time evolution under the Holstein Hamiltonian [Eq. (9.4)] leads to the following state at time $t$: $|\phi_\beta(t)\rangle = \sqrt{1-\beta}\,|0\rangle_{\text{exc}}\,|0\rangle_{\text{vib}} + \sqrt{\beta}\exp[i\phi(t)]\,|1\rangle_{\text{exc}}\,|x(t)+\mathrm{i}p(t)\rangle_{\text{vib}}$ with the coherent state $|\alpha\rangle_{\text{vib}} = \exp(\alpha\hat{b}_n^\dagger - \alpha^*\hat{b}_n)\,|0\rangle_{\text{vib}}$ and the phase $\phi(t)$ due to the energy difference between states $|0\rangle_{\text{exc}}$ and $|1\rangle_{\text{exc}}$. For $\beta \neq 0, 1$, this is generally an entangled state, and the shape of the nuclear wave packet (after tracing out the spin degree of freedom) is modified from the Gaussian shape, dependent on $\beta$.

In order to numerically study the shape of $P_n(x_n, t)$ with our exact MPS method, we define its tails by $x_n < x_{\text{thr}}^l$ and $x_n > x_{\text{thr}}^r$, respectively. Here we choose a threshold value such that the tails of a ground state molecule include one percent of the weight $\eta_0 = \{1 \pm \text{erf}[x_{\text{thr}}^{l/r}]\}/2 = 10^{-2}$, which corresponds to $x_{\text{thr}}^{l/r} \approx \mp 1.6$. We have confirmed that the underlying physics is generally independent of the specific choice of $\eta_0$ for $0.1 > \eta_0 > 10^{-4}$, however the relative magnitude of the changes generally increases for decreasing $\eta_0$. We define the time-dependent tail weights:

$$\eta^{l/r}(t) = \mp \sum_n \int_{x_{\text{thr}}^{l/r}}^{\mp\infty} dx_n\, P_n(x_n, t)\,. \tag{9.8}$$

In a simplified reaction picture, $\eta^{l/r}(t)$ may be related to a reaction probability, e.g. for dissociation, if the coordinate $x$ corresponds to the stretching of a critical bond in the system [24].

Without cavity, we can analytically solve the dynamics of the tail weights. For an initial single molecular excitation, the $(N-1)$ ground state molecules exhibit no dynamics, and the excited molecule oscillates between $x_1 = 0$ and $x_1 = 2\sqrt{2}\lambda$ according to $x_1(t) = \sqrt{2}\lambda[1 - \cos(\nu t)]$. The tails are then given by $\eta^{l/r}(t) = (N-1) \times \eta_0 + \{1 \pm \text{erf}[x_{\text{thr}}^{l/r} - x_1(t)]\}/2$, with $\text{erf}(x) = 2\int_0^x dz \exp(-z^2)/\sqrt{\pi}$ the error function. This is shown as gray dashed lines in Fig. 9.4.

The influence of cavity and disorder on the evolution of $\eta^{l/r}(t)$ is shown in Fig. 9.4 for both an initial molecule excitation (Fig. 9.4a,b) and the cavity excitation scenario (Fig. 9.4c,d). We first discuss the disorder-less case $W = 0$. For the molecule excitation (light dash-dotted lines in Fig. 9.4a/b), we observe only a minimal modification from the no-cavity case (gray dashed line). In contrast, for an initial cavity excitation (Fig. 9.4c/d,

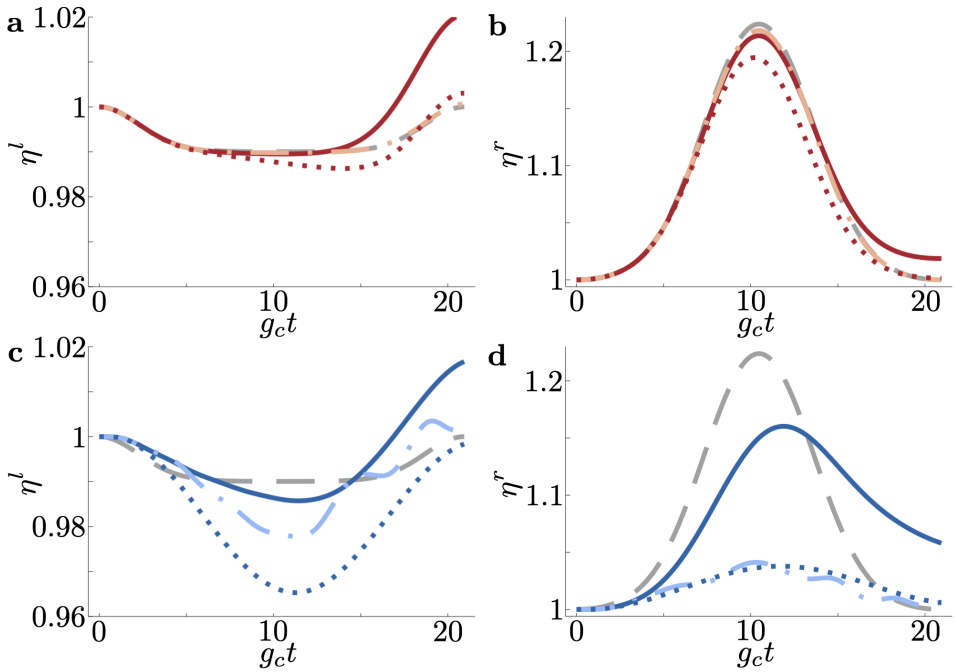


Figure 9.4. – **Tail weight dynamics.** **a**,**b** Time evolution of the cumulative left tail weight $\eta^l$ (**a**) and the right tail weight $\eta^r$ (**b**) as defined in Eq. (9.8) for an initial molecule excitation. The dark red solid line is the disorder-averaged exact time evolution for $W = g_c/2$, whereas the red dotted line shows equivalent results computed with a product state approximation [Eq. (9.7)]. The light red dash-dotted line displays the results for $W = 0$. The grey dashed line is the no-cavity reference. **c**,**d** Results for an initial cavity excitation with analogous line styles. The parameters are $N = 100$, $\lambda = 0.4$, and $\nu = 0.3 g_c$. Averaged over 256 disorder realizations.

we find a strong suppression, in particular of the right tail weights due to the cavity. This is a manifestation of the polaron decoupling [43].

For $W = g_c/2$, in contrast, we find a distinctively different behavior. Focusing first on the right tail, we observe that disorder on average leads to a reduction of the tail at $t \sim \pi/\nu$ compared to the no-cavity scenario, followed by an increase at later times, seen in Figs. 9.4b,d. This effect is significantly more pronounced for an initial cavity excitation (Fig. 9.4d) than for a molecule excitation (Fig. 9.4b). We attribute the dynamics observed in Fig. 9.4b/d to the out-of-phase oscillation of the different molecular vibrations (cf. Fig. 9.3). It implies that reaction coordinates reach large values of $x_n$ at different times and thus reduce the maximum weight of $\eta^r$ at $t \sim \pi/\nu$, but lead to a larger tail weight on average at later times. Importantly, we point again out that this out-of-phase oscillation should be considered as a quantum coherent process, i.e. the time-dependent state is a large superposition where the vibrational degrees of freedom enter as linear superposition, as for the single molecule state $|\phi_\beta\rangle$, but with molecule and time-dependent excitation fractions. The importance of vibrational entanglement for modeling the exact dynamics of the nuclear distribution is strikingly illustrated by the fact that product state simulations in Fig. 9.4 (dotted lines) fail to describe the correct dynamics.

We note that when we consider a time integration of the right tail-weights, $\eta^r_{\text{avg}} = \int_0^{2\pi/\nu} dt\, \eta^r(t)$, i.e. the surface under the curves in Fig. 9.4b/d, we find that for large $W$, the exact $\eta^r_{\text{avg}}$ approximately agrees with the no-cavity scenario. This phenomenon can be rationalized by the fact that, although the excitation is time-dependently distributed over many molecules, in total there still only approximately remains one molecular excitation driving vibrational dynamics. Interestingly, this is not the case when time integrating the left tail weight, $\eta^l_{\text{avg}}$. In fact, this integrated weight increases significantly compared to the no-cavity case, which highlights the importance of the broadening and the non-Gaussian shapes of the nuclear distributions.

## 9.7. Parameter Scaling

Lastly we want to systematically investigate the importance of the effects introduced in this paper as function of disorder strength $W$, vibronic coupling strength $\propto \lambda$, and molecule number $N$. In Fig. 9.5 we focus on the entanglement entropies and the right tail weights at time $t = 2\pi/\nu$ (red: initial molecule excitation, blue: initial cavity excitation). We find that the entanglement entropy $S_{\text{vib}}$ and the right tail weight $\eta^r$ scale extremely similarly with all parameters (comparing left a,c,e and right b,d,f panels in Fig. 9.5, respectively). This confirms the close relation between both quantities. Furthermore, we find that for sufficiently large $\lambda$ and $W$, the product state approximation (dotted lines in Fig. 9.5) breaks down completely and predicts only negligible modifications compared to the exact MPS simulations. This coincides with large values of $S_{\text{vib}}$, and thus underlines the essential role of entanglement between electro-photonic and vibrational degrees of freedom in the dynamics.

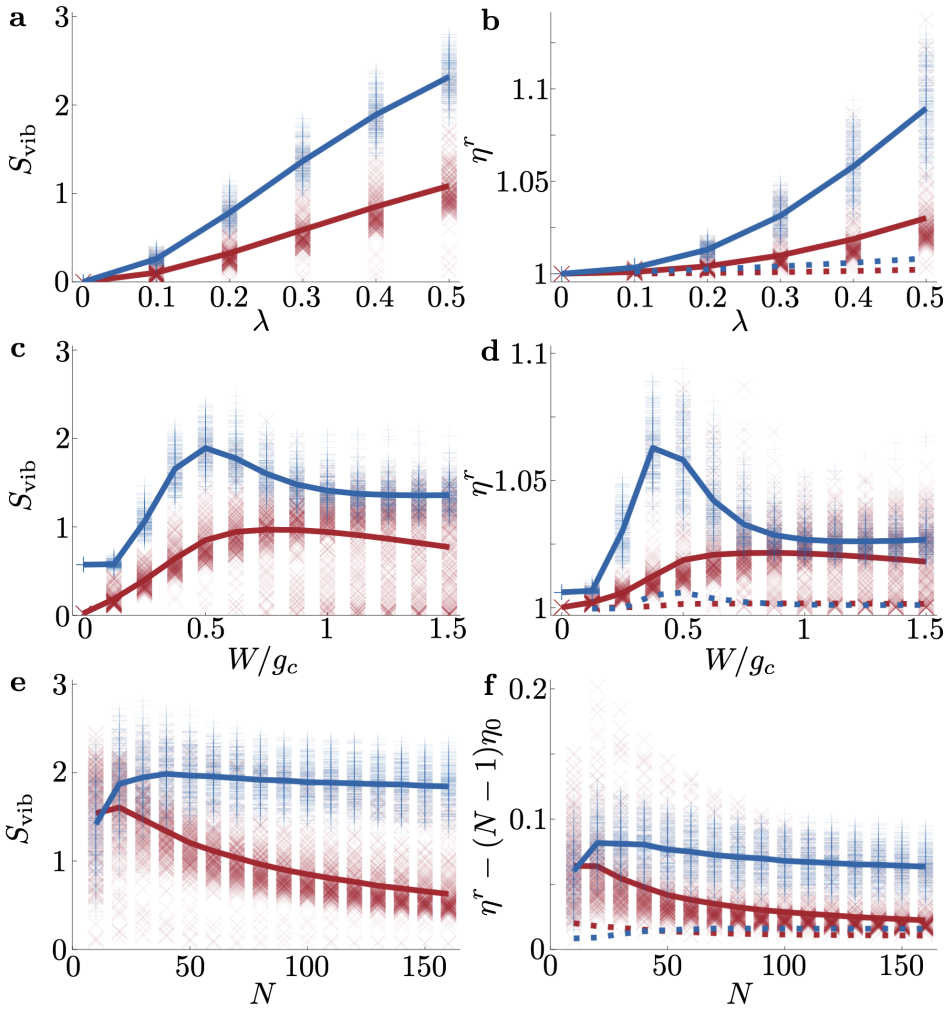


Figure 9.5. – **Parameter scaling.** The left panels (**a**, **c**, **e**) show the entanglement entropy $S_{\mathrm{vib}}$, while the right panels (**b**, **d**, **f**) show the right tail weight $\eta^r$ [defined in Eq. (9.8)] as a function of vibronic coupling strength $\lambda$ (**a**, **b**), disorder width $W$ (**c**, **d**), and molecule number $N$ (**e**, **f**), evaluated at time $t = 2\pi/\nu$. Red "×" symbols correspond to a molecular excitation, blue "+" symbols correspond to a cavity excitation. The symbols represent individual disorder realizations. The continuous line is a guide to the eye through averages of all 256 disorder realizations. The dotted lines in panels b, d, and f represent the disorder averaged product state results for reference. $\eta_0 = 10^{-2}$ is the tail weight in the ground state. Parameters are $N = 100$, $\nu = 0.3g_c$, $\lambda = 0.4$, and $W = g_c/2$ unless specified.

We observe that both $S_{\text{vib}}$ and $\eta^r$ grow with $\lambda$ (see Fig. 9.5a,b. As discussed above, both entanglement and modifications to the right tail can be directly attributed to $\hat{H}_H$, which scales with $\lambda$ [Eq. (9.4)]. For small disorder $W < g_c/2$, i.e. in the strong coupling regime, we find that increasing disorder results in an increase of entanglement entropies and right tail weights (Fig. 9.5c,d), consistent with disorder enhanced excitation transfer. Interestingly, $S_{\text{vib}}$ and $\eta^r$ exhibit a peak between the weak and strong coupling limits. It becomes only weakly dependent on $W$ in the weak coupling regime, i.e. for $W > g_c$. This behavior and the clear difference between excitation scenarios exemplifies the rich physics in the intermediate coupling regime.

Strikingly, we also observe different scaling behaviors with the molecule number $N$ between both initial states (Fig. 9.5e,f). For an individually excited molecule, the entanglement and the right tail weight decrease for large $N$ [we subtract the ground state contribution $(N-1)\eta_0$ from the tail weight], in line with the analytical estimate for the scaling of excitation transfer between molecules $\sim Wt/N$ in the strong coupling regime. In contrast, for an initial cavity-excitation, the entanglement and tail weight remain approximately constant for large $N$. Here, the excitation transfer from cavity to molecules occurs on the same timescale as Rabi oscillations, and the total amount of excitation transferred is perturbatively given by $W^2/g_c^2$ in the strong coupling regime, and thus to first order independent of $N$. This further highlights the important distinction between the two initial states, especially for large molecule numbers.

## 9.8. Conclusion and Outlook

In summary, we have analyzed the coherent femtosecond dynamics in a disordered Holstein-Tavis-Cummings model after incoherent photo-excitation. This minimal model features necessary ingredients for analyzing key quantum processes in polaritonic chemistry, including dynamics of electronic, vibrational, and photonic degrees of freedom [43]. Using a matrix product state approach we have simulated the exact quantum many-body dynamics for realistic parameter regimes for mesoscopic system sizes. We have shown that disorder-enhanced excitation transfer [49–51], both between the molecules and from the cavity to molecules, leads to coherent out-of-phase oscillations of the individual vibrational modes. Disorder thus strongly enhances the build-up of vibrational entanglement and modifications of the time-dependent nuclear probability distributions, which are not captured in a product state (mean-field Ehrenfest) picture where electronic and nuclear degrees of freedom are treated as separable. We have highlighted that for large molecule numbers, an initial excitation in the cavity leads to much larger modifications than an initial molecular excitation. In general, disorder-enhanced entanglement is a remarkable effect, since typically disorder is known to lead to a suppression of entanglement in various quantum many-body models [58].

Our results have direct implications for understanding the role of collective and quantum-mechanical effects in cavity modified chemistry. While approximations based on wave-functions which are separable between the electronic and the vibrational Hilbert space can provide useful insight in disorder-free systems, our work implies that the pres-

ence of disorder leads to a breakdown of such approaches. Our work emphasizes that for cavity-modified photo-chemistry with incoherent excitations, it is crucial to distinguish scenarios where the cavity or individual molecules are activated by the photon. The observation of large-scale entanglement entropy build-up on very short femtosecond timescales suggests that quantum effects can play an important role in polaritonic chemistry experiments on timescales faster then the cavity-decay, and thus for experimentally feasible cavities with quality factors of $Q \gtrsim 1000$. Our work highlights the general importance of disorder for understanding polaritonic chemistry [59–61].

In the future it will be interesting to consider more realistic molecular models, including beyond-harmonic potential energy landscapes with more than one reaction coordinate, and featuring chemical reactions e.g. via electron transfer between multiple electronic levels, or conical intersections of energy surfaces. It will be interesting to extend our analysis to much longer times, when disorder enhanced transfer becomes even more relevant [62]. Our numerical approach further allows to also access regimes with multiple excitations, which will be an interesting regime to explore. Furthermore our method can also easily include dissipative mechanisms, e.g. using a quantum trajectory approach [63], which has been proposed to lead to further modifications of the involved chemistry [31, 64–67], an interesting prospect for future research.

## Acknowledgements

We are grateful to Felipe Herrera, Claudiu Genes, David Hagenmüller, Jerôme Dubail and Guido Masella for stimulating discussions. This work was supported by LabEx NIE ("Nanostructures in Interaction with their Environment") under contract ANR-11-LABX0058 NIE and "ERA-NET QuantERA" - Projet "RouTe" (ANR-18-QUAN-0005-01). This work of the Interdisciplinary Thematic Institute QMat, as part of the ITI 2021 2028 program of the University of Strasbourg, CNRS and Inserm, was supported by IdEx Unistra (ANR 10 IDEX 0002), SFRI STRAT'US project (ANR 20 SFRI 0012), and EUR QMAT ANR-17-EURE-0024 under the framework of the French Investments for the Future Program. G. P. acknowledges support from the Institut Universitaire de France (IUF) and the University of Strasbourg Institute of Advanced Studies (USIAS). Our MPS codes make use of the intelligent tensor library (ITensor) [68]. Computations were carried out using resources of the High Performance Computing Center of the University of Strasbourg, funded by Equip@Meso (as part of the Investments for the Future Program) and CPER Alsacalcul/Big Data.

# Appendix

## 9.A. Matrix product state method

We write the time-dependent quantum state on the full electro-photonic-vibrational Hilbert space in the form

$$|\psi(t)\rangle = \sum_{\{i_n=0,1\}} \sum_{\{b_n=0\}}^{n^v_{\max}} \sum_{a=0}^{n^p_{\max}} c_{i_1,i_2,\ldots,i_N;b_1,b_2,\ldots,b_N;a} \; |i_1, i_2, \ldots, i_N\rangle_{\text{exc}} \otimes |b_1, b_2, \ldots, b_N\rangle_{\text{vib}} \otimes |a\rangle_{\text{ph}} \tag{9.9}$$

Here, the different indices denote electronic excitation numbers for molecule $n$, $i_n = 0, 1$, the vibrational excitation number on molecule $n$, $b_n = 0, \ldots, n^v_{\max}$ and the cavity mode occupation number, $a = 0, \ldots, n^p_{\max}$. While in principle $n^{v/p}_{\max} \to \infty$, in practice the vibrational Hilbert space can be truncated at some reasonable occupation number. For this work we found that to capture all relevant physics of the tails of the nuclear coordinate distributions, $n^v_{\max} = 10$ is sufficient (see below). Due to our choice of initial state and the conservation of $\sum_n \hat{\sigma}^+_n \hat{\sigma}^-_n + \hat{a}^\dagger \hat{a}$, furthermore we can set a photon cutoff at $n^v_{\max} = 1$ without any approximation. For $N = 100$ molecules, this implies a full Hilbert space size of $11^N 2^{N+1} \gtrsim 10^{134}$, clearly out of reach for any classical computer memory. In order to still make the high-dimensional complex state tensor $c$ amenable for storage in computer memory, we utilize a decomposition into products of smaller tensors, a matrix product state (MPS) [46]. In particular we utilize an MPS with $2N + 1$ tensors:

$$c_{i_1,i_2,\ldots,i_N;b_1,b_2,\ldots,b_N;a} = \sum_{\alpha_1,\ldots,\alpha_{2N}=1}^{\chi} \Gamma^{[p];\alpha_0,\alpha_1}_{a} \prod_{n=1}^{N} \left( \Gamma^{[n];\alpha_{2n-1}\alpha_{2n}}_{i_n} \Gamma^{[v];\alpha_{2n}\alpha_{2n+1}}_{b_n} \right). \tag{9.10}$$

Here we introduced 3-dimensional tensors for the photonic, electronic and vibrational degrees of freedom, $\Gamma^{[p];\alpha_0\alpha_1}_{a}$, $\Gamma^{[n];\alpha_m\alpha_{m+1}}_{i_n}$, and $\Gamma^{[v];\alpha_m\alpha_{m+1}}_{b_n}$, respectively. The tensors are connected by the virtual indices $\alpha_m$ with $m = 0, \ldots, 2N + 1$ and bond dimension $\chi$ (except for the edge indices, which are trivially $\alpha_0 = \alpha_{2N+1} = 1$). The MPS can be brought, and updated, in a canonical form. Then, the virtual indices $\alpha_m$ correspond to an orthonormal basis, which is the eigenbasis of the reduced density matrix of the two blocks that the index connects [46]. This effectively limits the entanglement entropy between the two blocks to $< \log_2(\chi)$. For the MPS decomposition to become exact, one would need to choose very large values for $\chi \sim \exp(N)$. However, limiting $\chi$ to computationally treatable magnitudes allows to effectively simulate dynamics on a truncated Hilbert space with restricted entanglement. In our simulations, we verified that all results converge with increasing $\chi$, and therefore that our simulations capture all necessary entanglement and are quasi-exact. In practice, we use $\chi = 128$ for all

plots (see below for convergence plots). In our MPS form, tensors can be updated using the time-evolving Block decimation (TEBD) algorithm [69]. Then, HTC coupling terms can be incorporated with "nearest-neighbor" gate updates, while cavity-couplings can be incorporated using index-swap gates between the tensors and nearest-neighbor gates. In practice, we choose a second order TEBD decomposition of the Hamiltonian with a time step of $g_c/100$, which we have verified to be sufficiently small for errors due to a finite time step to be negligible (see Appendix). In case of spin-boson dynamics, TEBD in combination with swap gates have been previously shown to exhibit very well behaved convergence, which are preferable compared to updates that use variational concepts [63]. Similarly, in order to compute $S_{\mathrm{vib}}$ we re-organize all vibrational degrees of freedom into a single block (using swap gates) and compute the entropy over the virtual index into that block. The excitation number conservation can be exploited to enhance the efficiency of tensor contractions and decompositions.

## 9.B. Dark state contribution to $|\psi_0^m\rangle$ without disorder

The eigenstates of $\hat{H}_{\mathrm{TC}}$ are given by two polaritons $|\pm\rangle = \hat{a}^\dagger/\sqrt{2} \pm \sum_n \hat{\sigma}_n^+/\sqrt{2N}\,|0\rangle_{\mathrm{exc+ph}}$, and $N-1$ degenerate dark states, for which any orthonormal basis of $\mathcal{H}_{\mathrm{ph}} \otimes \mathcal{H}_{\mathrm{exc}}$ that does not contain the polaritons may be chosen. The most straightforward way to compute the dark state contribution of a state $|\psi\rangle$ is thus $\sum_d |\langle d|\psi\rangle|^2 = 1 - |\langle +|\psi\rangle|^2 - |\langle -|\psi\rangle|^2$. We find $\sum_d |\langle d|\psi_0^m\rangle|^2 = 1 - 1/N$.

## 9.C. Perturbative photo-contribution to the dark states

In this section, we compute the photo-contribution to the dark states perturbatively in the regime $g_c \gg W, \nu, \lambda\nu$. Starting from the analytically solvable Hamiltonian $\hat{H}_0 = \hat{H}_{\mathrm{TC}} + \hat{H}_{\mathrm{vib}}$ given by Eqs. (9.2) and (9.3) of the main text, we compute the perturbative corrections to the photo-contribution of the polaritons. The perturbative photo-contribution to the dark states can then be computed as $\sum_d |\langle d|1\rangle_{\mathrm{ph}}|^2 = 1 - |\langle +|1\rangle_{\mathrm{ph}}|^2 - |\langle -|1\rangle_{\mathrm{ph}}|^2$, analogous to the previous section.

The eigenstates of $\hat{H}_0$ are product states of the eigenstates of $\hat{H}_{\mathrm{TC}}$ and the eigenstates of $\hat{H}_{\mathrm{vib}}$, because the two sub-spaces remain uncoupled. The eigenstates of $\hat{H}_{\mathrm{TC}}$ are the two polaritons $|\pm\rangle$ and the $N-1$ degenerate dark states, for which we choose a momentum basis $|k\rangle = \left[\sum_{n=1}^N \exp(-2\pi \mathrm{i} k n/N)\hat{\sigma}_n^+/\sqrt{N}\right]|0\rangle_{\mathrm{exc+ph}}$. The eigenstates of $\hat{H}_{\mathrm{vib}}$ are Fock states $(\prod_n \hat{(b_n^\dagger)}^{i_n}/\sqrt{i_n!})\,|0\rangle_{\mathrm{vib}}$ with $i_n$ vibrational excitations on the $n$-th molecule.

### Disorder

We first compute the perturbative corrections due to disorder $\hat{H}_{\mathrm{dis}}$, only. In this case, the vibrations are not entangled with the photo-electronic degrees of freedom, and we

can restrict the perturbative analysis to the photo-electronic degrees of freedom, only. The second order corrections to the states $|\pm\rangle$ are given by [70]

$$|\pm\rangle = \left|\pm^{(0)}\right\rangle + \left|\pm^{(1)}\right\rangle + \left|\pm^{(2)}\right\rangle + \mathcal{O}(W^3/g_c^3) \tag{9.11}$$

$$\left\langle\psi^{(0)}\middle|\phi^{(1)}\right\rangle = \begin{cases} 0 & \text{for } \psi = \phi \\ \frac{\langle\psi^{(0)}|\hat{H}_{\text{dis}}|\phi^{(0)}\rangle}{E_\phi^{(0)} - E_\psi^{(0)}} & \text{else} \end{cases} \tag{9.12}$$

$$\left\langle\psi^{(0)}\middle|\phi^{(2)}\right\rangle = \begin{cases} -\frac{1}{2}\sum_{\eta\neq\phi} \frac{\langle\psi^{(0)}|\hat{H}_{\text{dis}}|\eta^{(0)}\rangle\langle\eta^{(0)}|\hat{H}_{\text{dis}}|\phi^{(0)}\rangle}{\left(E_\phi^{(0)} - E_\eta^{(0)}\right)^2} & \text{for } \psi = \phi \\ \sum_{\eta\neq\phi} \frac{\langle\psi^{(0)}|\hat{H}_{\text{dis}}|\eta^{(0)}\rangle\langle\eta^{(0)}|\hat{H}_{\text{dis}}|\phi^{(0)}\rangle}{\left(E_\phi^{(0)} - E_\eta^{(0)}\right)\left(E_\phi^{(0)} - E_\psi^{(0)}\right)} - \frac{\langle\psi^{(0)}|\hat{H}_{\text{dis}}|\phi^{(0)}\rangle\langle\phi^{(0)}|\hat{H}_{\text{dis}}|\phi^{(0)}\rangle}{\left(E_\phi^{(0)} - E_\psi^{(0)}\right)^2} & \text{else} \end{cases} \tag{9.13}$$

with $\left|\psi^{(0)}\right\rangle$ and $E_\psi^{(0)}$ the eigenstates and eigenenergies for $W = 0$, and $\left|\psi^{(n)}\right\rangle$ the corrections to the eigenstates at order $(W/g_c)^n$. We find

$$\left\langle\mp^{(0)}\middle|\pm^{(1)}\right\rangle = \mp\frac{\tilde{\epsilon}_0}{4g_c}\,, \tag{9.14}$$

$$\left\langle k^{(0)}\middle|\pm^{(1)}\right\rangle = \pm\frac{\tilde{\epsilon}_k}{\sqrt{2}g_c}\,, \tag{9.15}$$

$$\left\langle\pm^{(0)}\middle|\pm^{(2)}\right\rangle = -\frac{|\tilde{\epsilon}_0|^2}{32g_c^2} - \sum_{k=1}^{N-1}\frac{|\tilde{\epsilon}_k|^2}{4g_c^2}\,, \tag{9.16}$$

$$\left\langle\mp^{(0)}\middle|\pm^{(2)}\right\rangle = -\sum_{k=1}^{N-1}\frac{|\tilde{\epsilon}_k|^2}{4g_c^2}\,, \tag{9.17}$$

with $\tilde{\epsilon}_k = [\sum_{n=1}^{N}\exp(2\pi i k n/N)\epsilon_n]/N$ the Fourier transform of the random energies. Using $|1_{\text{ph}}\rangle = (\left|+^{(0)}\right\rangle + \left|-^{(0)}\right\rangle)/\sqrt{2}$, we find further

$$|\langle 1_{\text{ph}}|\pm\rangle|^2 = \frac{1}{2} \mp \frac{\tilde{\epsilon}_0}{4g_c} - \frac{1}{2}\sum_{k=1}^{N-1}\frac{|\tilde{\epsilon}_k|^2}{g_c^2} + \mathcal{O}\left[(\tilde{\epsilon}/g_c)^3\right]. \tag{9.18}$$

and finally for the photon weight of the dark states

$$\sum_d |\langle 1_{\text{ph}}|d\rangle|^2 = \sum_{k=1}^{N-1}\frac{|\tilde{\epsilon}_k|^2}{g_c^2}\,. \tag{9.19}$$

Until here, the results are independent of the specific disorder model. We now assume that the energies $\epsilon_i$ are distributed according to a Gaussian with mean zero and standard deviation $W$. Then, we can further use that the discrete Fourier transform of a set of $N$ Gaussian random variables is a set of $N$ complex Gaussian random variables with real and imaginary part mean zero and standard deviation $W/\sqrt{2N}$, as can be straightforwardly shown by Fourier transforming the definition of $P(\tilde{\epsilon}_k)$. Taking the disorder average leaves us with

$$\overline{\sum_d |\langle 1_{\text{ph}}|d\rangle|^2} = \frac{(N-1)W^2}{Ng_c^2} + \mathcal{O}(W^3/g_c^3) \xrightarrow{N\to\infty} \frac{W^2}{g_c^2}\,. \tag{9.20}$$

## Vibronic coupling

We now proceed to compute the corrections due to vibronic coupling $\hat{H}_{\mathrm{H}}$ for $W = 0$. $\hat{H}_{\mathrm{H}}$ couples states with different numbers of vibrations, so that we need to take the vibrations into account explicitly. We write the states as $|\psi\rangle = |\psi_{\mathrm{exc+ph}}, n_{\mathrm{vib}}, v_1, \ldots, v_{n_{\mathrm{vib}}}\rangle \equiv \mathcal{N} |\psi_{\mathrm{exc+ph}}\rangle \prod_{i=1}^{n_{\mathrm{vib}}} \sum_n \exp(2\pi \mathrm{i} v_i n/N) \hat{b}_n^\dagger |0\rangle_{\mathrm{vib}}$, where $\psi_{\mathrm{exc+ph}} = \pm, k$ is the state in the electro-photonic sub-space, $n_{\mathrm{vib}}$ is the number of vibrations, and $v_i$ is the Fourier mode of the vibration and $\mathcal{N}$ is a normalization factor. We are specifically interested in the contribution of the initial state $|\psi_0^c\rangle = |1_{\mathrm{ph}}, 0\rangle$ to the dark states. Plugging $\hat{H}_{\mathrm{H}}$ instead of $\hat{H}_{\mathrm{dis}}$ into Eqs. (9.11) to (9.13), we find

$$\left\langle \pm^{(0)}, 1, 0 \middle| \pm^{(1)}, 0 \right\rangle = \frac{\lambda}{2\sqrt{N}}\,, \tag{9.21}$$

$$\left\langle \mp^{(0)}, 1, 0 \middle| \pm^{(1)}, 0 \right\rangle = \frac{\pm\lambda\nu}{2\sqrt{N}(2g_c \mp \nu)}\,, \tag{9.22}$$

$$\left\langle k^{(0)}, 1, -k \middle| \pm^{(1)}, 0 \right\rangle = \frac{-\lambda\nu}{\sqrt{2N}(g_c \mp \nu)}\,, \tag{9.23}$$

$$\left\langle \pm^{(0)}, 0 \middle| \pm^{(2)}, 0 \right\rangle = -\frac{\lambda^2}{8N} - \frac{\lambda^2\nu^2}{8N(2g_c \mp \nu)^2} - \frac{(N-1)\lambda^2\nu^2}{4N(g_c \mp \nu)^2}\,, \tag{9.24}$$

$$\left\langle \mp^{(0)}, 0 \middle| \pm^{(2)}, 0 \right\rangle = \pm\frac{\lambda^2\nu}{8Ng_c} - \frac{\lambda^2\nu^2}{8Ng_c(2g_c \mp \nu)} - \frac{(N-1)\lambda^2\nu^2}{4N(g_c \mp \nu)g_c}\,, \tag{9.25}$$

$$\left\langle \pm^{(0)}, 0 \middle| \pm^{(2)}, 2, 0, 0 \right\rangle = \frac{\sqrt{2}\lambda^2}{8N} \pm \frac{\sqrt{2}\lambda^2\nu}{8N(2g_c \pm \nu)}\,, \tag{9.26}$$

$$\left\langle \pm^{(0)}, 0 \middle| \pm^{(2)}, 2, k, -k \right\rangle = \pm\frac{\lambda^2\nu}{4N(g_c \pm \nu)}\,, \tag{9.27}$$

$$\left\langle \mp^{(0)}, 0 \middle| \pm^{(2)}, 2, 0, 0 \right\rangle = \mp\frac{\sqrt{2}\lambda^2\nu}{8N(g_c \pm \nu)} - \frac{\sqrt{2}\lambda^2\nu^2}{8N(2g_c \pm \nu)(g_c \pm \nu)}\,, \tag{9.28}$$

$$\left\langle \mp^{(0)}, 0 \middle| \pm^{(2)}, 2, k, -k \right\rangle = -\frac{\lambda^2\nu^2}{4N(g_c \pm \nu)^2}\,, \tag{9.29}$$

$$\left\langle \pm^{(0)}, 0 \middle| \pm^{(1)}, 1, 0 \right\rangle = -\frac{\lambda}{2\sqrt{N}}\,, \tag{9.30}$$

$$\left\langle \mp^{(0)}, 0 \middle| \pm^{(1)}, 1, 0 \right\rangle = \pm\frac{\lambda\nu}{2\sqrt{N}(2g_c \pm \nu)}\,. \tag{9.31}$$

Analogous to above, we can compute the dark state amplitude of the state $|1_{\mathrm{ph}},0\rangle$ including an arbitrary number of vibrations as

$$\begin{aligned}\sum_d |\langle 1_{\mathrm{ph}},0|d\rangle|^2 = 1 &- |\langle 1_{\mathrm{ph}},0|+,0\rangle|^2 - |\langle 1_{\mathrm{ph}},0|+,1,0\rangle|^2 - |\langle 1_{\mathrm{ph}},0|+,2,0,0\rangle|^2 \\ &- \sum_k |\langle 1_{\mathrm{ph}},0|+,2,k,-k\rangle|^2 \\ &- |\langle 1_{\mathrm{ph}},0|-,0\rangle|^2 - |\langle 1_{\mathrm{ph}},0|-,1,0\rangle|^2 - |\langle 1_{\mathrm{ph}},0|-,2,0,0\rangle|^2 \\ &- \sum_k |\langle 1_{\mathrm{ph}},0|-,2,k,-k\rangle|^2 . \end{aligned} \tag{9.32}$$

Using $|1_{\mathrm{ph}},0\rangle = (\big|+^{(0)},0\big\rangle + \big|-^{(0)},0\big\rangle)/\sqrt{2}$, the only non-vanishing term for large $N$ reads

$$|\langle 1_{\mathrm{ph}},0|\pm,0\rangle|^2 = \frac{1}{2} - \frac{\lambda^2\nu^2}{4(g_c \mp \nu)^2} - \frac{\lambda^2\nu^2}{4(g_c\mp\nu)g_c} + \mathcal{O}\big[(\lambda\nu/g_c)^3\big] . \tag{9.33}$$

As a result, the photo-contribution to the dark states is approximately

$$\sum_d |\langle 1_{\mathrm{ph}}|d\rangle|^2 \approx \frac{\lambda^2\nu^2}{4(g_c\mp\nu)^2} + \frac{\lambda^2\nu^2}{4(g_c\mp\nu)g_c} \approx \frac{\lambda^2\nu^2}{2g_c^2} , \tag{9.34}$$

where we used $\nu \ll g_c$ in the last step.

## 9.D. Excitation Transfer Estimates

In the following, we derive analytical estimates for excitation transfer away from the initially excited molecule for the initial state $|\psi_0^m\rangle = \hat{\sigma}_1^+ |0\rangle$ (see main text). We consider disorder induced transfer only, i.e. we set $\lambda = 0$. We further restrict the analysis to the perturbative case by assuming $W \ll g_c$.

### $W = 0$

We start by analyzing the disorder-free scenario. For $W = \lambda = 0$, the electro-photonic state evolves with the Tavis-Cummings Hamiltonian $\hat{H}_{\mathrm{TC}}$, only. By diagonalizing $\hat{H}_{\mathrm{TC}} = (g_c |+\rangle\langle+| - g_c |-\rangle\langle-|)$, we compute the time-dependent excitation probability of the initially excited molecule

$$\begin{aligned}\langle\hat{\sigma}_1^+\hat{\sigma}_1^-\rangle(t) &= \langle 0|\,\hat{\sigma}_1^- \exp\Big(\mathrm{i}\hat{H}_{\mathrm{TC}}t\Big)\hat{\sigma}_1^+\hat{\sigma}_1^- \exp\Big(-\mathrm{i}\hat{H}_{\mathrm{TC}}t\Big)\hat{\sigma}_1^+ |0\rangle \\ &= \frac{(N-1)^2}{N^2} + \frac{2(N-1)}{N^2}\cos(g_c t) + \frac{1}{2N^2} + \frac{1}{2N^2}\cos(2g_c t) \qquad (9.35) \\ &= 1 + \frac{2}{N}[\cos(g_c t) - 1] + \mathcal{O}\left(\frac{1}{N^2}\right) . \qquad (9.36)\end{aligned}$$

### 9.D.1. $W > 0$

In the following we compute the excitation probability of the initially excited molecule for finite disorder. Here, we choose a box disorder model, because the finite probability for a single molecule to have extreme energies (i.e. $\epsilon_i > +g_c$ or $\epsilon_i < -g_c$) adds significant complexity to the analytical treatment. In particular, we assume a uniform probability $P(\epsilon_i) = 1/(2W)$ for $-W < \epsilon_i < W$, and $P(\epsilon_i) = 0$ otherwise. We do not expect this choice for $P(\epsilon_i)$ to modify the overall scaling of our results with respect to the Gaussian choice in the rest of the paper.

In order to compute the time-dependent excitation probability of the first molecule, we treat the cavity coupling of the first molecule $g(\hat{\sigma}_1^+\hat{a} + \hat{\sigma}_1^-\hat{a}^\dagger)$ as a perturbation. The unperturbed Hamiltonian is given by $\hat{H}_0 = \hat{H}_{\mathrm{TC}} + \hat{H}_{\mathrm{dis}} - g(\hat{\sigma}_1^+\hat{a} + \hat{\sigma}_1^-\hat{a}^\dagger)$. In this case, the perturbation condition becomes that the single molecule coupling $g$ is smaller than the energy differences between different states, which is on the order of $\sim W$ for most pairs of states. As $g = g_c/\sqrt{N}$ becomes very small for large $N$, this condition is fulfilled for most energy levels. However, a few resonant energy levels do typically not fulfill this condition, with implications discussed below.

One eigenstate of $\hat{H}_0$ is the initial state $\left|1^{(0)}\right\rangle \equiv |\psi_0^m\rangle$. For $W < g_c$, the other eigenstates can be classified as polaritons and dark states. Although we cannot compute these states exactly, we can make sufficient statements about their statistics [49, 51, 62] to compute the time evolution of $\langle\hat{\sigma}_1^+\hat{\sigma}_1^-\rangle$. In particular, we can perturbatively compute their average photo contribution for $W < g_c$ and large $N$ as in the previous section. We find $|\langle 1_{\mathrm{ph}}|+\rangle| \approx 1/2 - W^2/(24g_c^2)$ and $|\langle 1_{\mathrm{ph}}|d_i\rangle|^2 \sim W^2/(12Ng_c^2)$, where the additional factor of 12 comes in due to the different disorder model. The eigenstates of $\hat{H}_0$ are thus

$$\left|1^{(0)}\right\rangle = \hat{\sigma}_1^+ |0\rangle \,, \tag{9.37}$$

$$\left|\pm^{(0)}\right\rangle = \left[\sqrt{\frac{1 - W^2/(12g_c^2)}{2}}\hat{a}^\dagger \pm \sum_{n=2}^{N} b_n^\pm \hat{\sigma}_n^+\right]|0\rangle \,, \tag{9.38}$$

$$\left|d_i^{(0)}\right\rangle = \left[\frac{W}{\sqrt{12}Ng}\hat{a}^\dagger + \sum_{n=2}^{N} c_n^{(i)}\hat{\sigma}_n^+\right]|0\rangle \,, \tag{9.39}$$

where we took the disorder-average of the photon-contribution on the state level. This approximation may be valid due to self-averaging for sufficiently large $N$, and it is validated by the agreement of the final results with the numerical simulations. The $b_n^\pm$ and $c_n^{(i)}$ are constants that determine the excitation probability of the specific molecules and are not needed in the following. The corresponding eigenenergies are

$$E_1^{(0)} = \epsilon_1 \,, \tag{9.40}$$

$$E_\pm^{(0)} = \pm g_c \,, \tag{9.41}$$

$$E_{d,i}^{(0)} \equiv E_i \,, \tag{9.42}$$

where the dark state energies $E_i$ follow the same distribution as the random molecular excitation energies [51].

Importantly, all states $\left|\pm^{(0)}\right\rangle$ and $\left|d_i^{(0)}\right\rangle$ have no excitation probability for the first molecule. As a result, there are no corrections to the eigenenergies at first order. The perturbative corrections to the states are

$$\begin{aligned}\left|1^{(1)}\right\rangle &= \frac{\sqrt{1-W^2/(12g_c^2)}g}{\sqrt{2}(\epsilon_1-g_c)}\left|+^{(0)}\right\rangle + \frac{\sqrt{1-W^2/(12g_c^2)}g}{\sqrt{2}(\epsilon_1+g_c)}\left|-^{(0)}\right\rangle \\ &\quad + \sum_i \frac{W}{\sqrt{12}N(\epsilon_1-E_i)}\left|d_i^{(0)}\right\rangle , \qquad (9.43)\\ \left|d_i^{(1)}\right\rangle &= \frac{W}{\sqrt{12}N(E_i-\epsilon_1)}\left|1^{(0)}\right\rangle , \qquad (9.44)\\ \left|\pm^{(1)}\right\rangle &= \frac{\sqrt{1-W^2/(12g_c^2)}g}{\sqrt{2}(\pm g_c-\epsilon_1)}\left|1^{(0)}\right\rangle , \qquad (9.45)\\ \left\langle 1^{(0)}\middle|1^{(2)}\right\rangle &= -\frac{1}{2}\left\langle 1^{(1)}\middle|1^{(1)}\right\rangle . \qquad (9.46)\end{aligned}$$

Here, unphysical divergences appear for the resonance condition $\epsilon_1 \to E_i$. These are related to the perturbation assumption $g \ll |\epsilon_1 - E_i|$. We will deal with these divergences below.

The time evolution is computed as

$$\begin{aligned}\langle\hat{\sigma}_1^+\hat{\sigma}_1^-\rangle(t) &= \langle\psi_0^m|\exp\left(\mathrm{i}\hat{H}t\right)\hat{\sigma}_1^+\hat{\sigma}_1^-\exp\left(-\mathrm{i}\hat{H}t\right)|\psi_0^m\rangle \\ &= \left\langle 1^{(0)}\middle|\exp\left(\mathrm{i}\hat{H}t\right)\middle|1^{(0)}\right\rangle\left\langle 1^{(0)}\middle|\exp\left(-\mathrm{i}\hat{H}t\right)\middle|1^{(0)}\right\rangle . \qquad (9.47)\end{aligned}$$

We expand $\exp(\mathrm{i}\hat{H}t) = \sum_\psi |\psi\rangle\langle\psi|\exp(\mathrm{i}E_\psi t)$ and keep terms only up to second order in $W$. We furthermore ignore second order corrections to the energies, which would lead to higher order corrections of the final result. We find

$$\begin{aligned}&\left\langle 1^{(0)}\middle|1\right\rangle\exp(\mathrm{i}\epsilon_1 t)\left\langle 1\middle|1^{(0)}\right\rangle = \\ &\left[1-\frac{g_c^2-W^2/12}{2N(\epsilon_1-g_c)^2}-\frac{g_c^2-W^2/12}{2N(\epsilon_1+g_c)^2}-\sum_i\frac{W^2}{12N^2(\epsilon_1-E_i)^2}\right]\exp(\mathrm{i}\epsilon_1 t)\,, \qquad (9.48)\\ &\left\langle 1^{(0)}\middle|\pm\right\rangle\exp(\pm\mathrm{i}g_c t)\left\langle\pm\middle|1^{(0)}\right\rangle = \frac{g_c^2-W^2/12}{2N(\pm g_c-\epsilon_1)^2}\exp(\pm\mathrm{i}g_c t)\,, \qquad (9.49)\\ &\left\langle 1^{(0)}\middle|d_i\right\rangle\exp(\mathrm{i}E_i t)\left\langle d_i\middle|1^{(0)}\right\rangle = \frac{W^2}{12N^2(\epsilon_1-E_i)^2}\exp(\mathrm{i}E_i t)\,. \qquad (9.50)\end{aligned}$$

These terms lead to oscillations of the energy between the initially excited molecule and the other states at frequencies $g_c \pm \epsilon_1$ for the polaritons, and $E_i - \epsilon_1$ for the dark states, respectively. The combined effect of the slightly out-of-phase oscillations of the large number of dark states leads to an effective dephasing and a resulting unidirectional transfer of energy away from the initially excited molecule on timescales analyzed in the

paper. This behavior can be computed as

$$\sum_i \left\langle 1^{(0)}\middle|1\right\rangle \exp(\mathrm{i}\epsilon_1 t)\left\langle 1\middle|1^{(0)}\right\rangle \left\langle 1^{(0)}\middle|d_i\right\rangle \exp(\mathrm{i}E_i t)\left\langle d_i\middle|1^{(0)}\right\rangle + \text{h.c.}$$
$$= \sum_i \frac{W^2}{6N^2(E_i-\epsilon_1)^2}\cos[(E_i-\epsilon_1)t]\,. \tag{9.51}$$

We finally take the disorder average $E_i \to \int dE/W$ to find:

$$N \times \frac{W}{6N^2}\int_{-W/2}^{W/2} dE \frac{\cos[(E-\epsilon_1)t]}{(E-\epsilon_1)^2} \quad = \quad \frac{Wt}{6N}\int_{(-W/2-\epsilon_1)t}^{(W/2-\epsilon_1)t} d\Delta \frac{\cos(\Delta)}{\Delta^2}\,, \tag{9.52}$$

where we substituted $(E-\epsilon_1)t \to \Delta$. Note that again an unphysical divergence arises due to the perturbation assumption $g^2 \ll (E_i-\epsilon_1)^2$, which we ignore here as we are only interested in the overall scaling behavior. As the integrand scales like $1/\Delta^2$, the integral becomes time independent for diverging boundaries, i.e. sufficiently large $t$. In this case, the population of the first state evolves like $1-\langle\hat{\sigma}_1^+\hat{\sigma}_1^-\rangle \sim Wt/N$ in addition to Rabi-oscillations. By straightforwardly evaluating all other terms we find that this term is indeed the largest contribution to the energy transfer. Botzung *et al.* [49] derived similar results in the long time limit for $N \to \infty$.

## 9.E. Convergence of MPS simulations

Fig. 9.6 shows the time evolution of $S_{\text{vib}}$, the phase space evolution, and $\eta^r$ computed with increasing bond dimension $\chi$ for a single disorder realization. We find that the vibrational entanglement $S_{\text{vib}}$ generally reaches larger values for larger $\chi < 128$, and for $\chi = 128, 256, 512$ the data points overlap perfectly. This indicates convergence for $\chi = 128$. For both the phase space evolution and the right tail the trajectories overlap for $\chi > 16$ ($\chi > 8$ for a molecular excitation), indicating much faster convergence for these observables. We attribute the slow convergence of $S_{\text{vib}}$ with $\chi$ to the large number of swap operations $\sim N^2$ and the unfavorable MPS structure when computing $S_{\text{vib}}$.

Fig. 9.7 shows the time evolution of the same observables computed using different time steps $dt$ used in the second order sweep. All lines overlap, indicating that convergence is already reached for $dt = 0.2$. The small differences in the final data points are rounding errors $\sim dt$ for the choice of final time.

Fig. 9.8 shows the time evolution of the same observables computed with different cutoffs for the number of vibrational excitations per molecule $n^v_{\text{max}}$. We find again that all lines overlap, indicating convergence for $n^v_{\text{max}} > 6$.

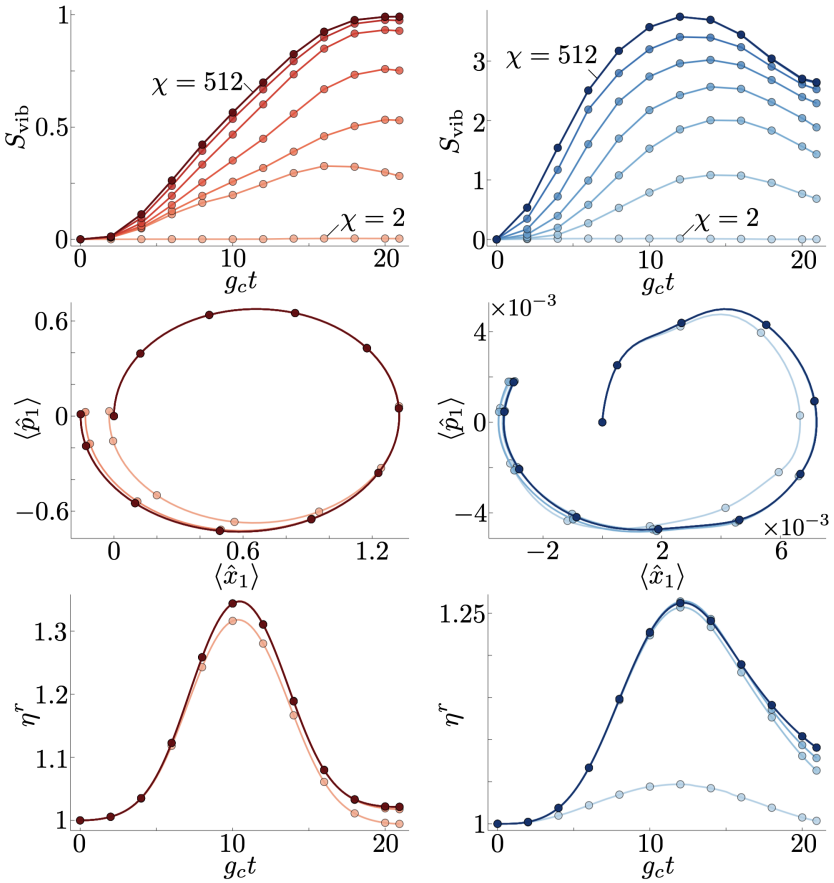


Figure 9.6. – **Convergence with the bond dimension $\chi$.** **a**,**b** Time evolution of the vibrational entropy $S_{\mathrm{vib}}$ for an initial molecular (left, red) or cavity (right, blue) excitation. Darkness indicates $\chi$ on a log-scale ($\chi \in \{2, 4, 8, 16, 32, 64, 128, 256, 512\}$). Trajectories already fully overlap for for $\chi \geq 128$ indicating convergence. In **a**,**b**, the lines are a guide to the eye, whereas in **c**-**f** the lines represent additional data points. **c**,**d** Phase-space evolution of a single molecule. Same color-code as in **a**,**b**. **e**,**f** Time evolution of the right tail weight $\eta^r$ (see paper for definition). Same color-code as in **a**,**b**. Parameters for all plots: $N = 100$, $\lambda = 0.5$, $\nu = 0.3 g_c$, $W = g_c/2$, $dt = 0.01$, $n^v_{\mathrm{max}} = 10$. Results for a single disorder realization.

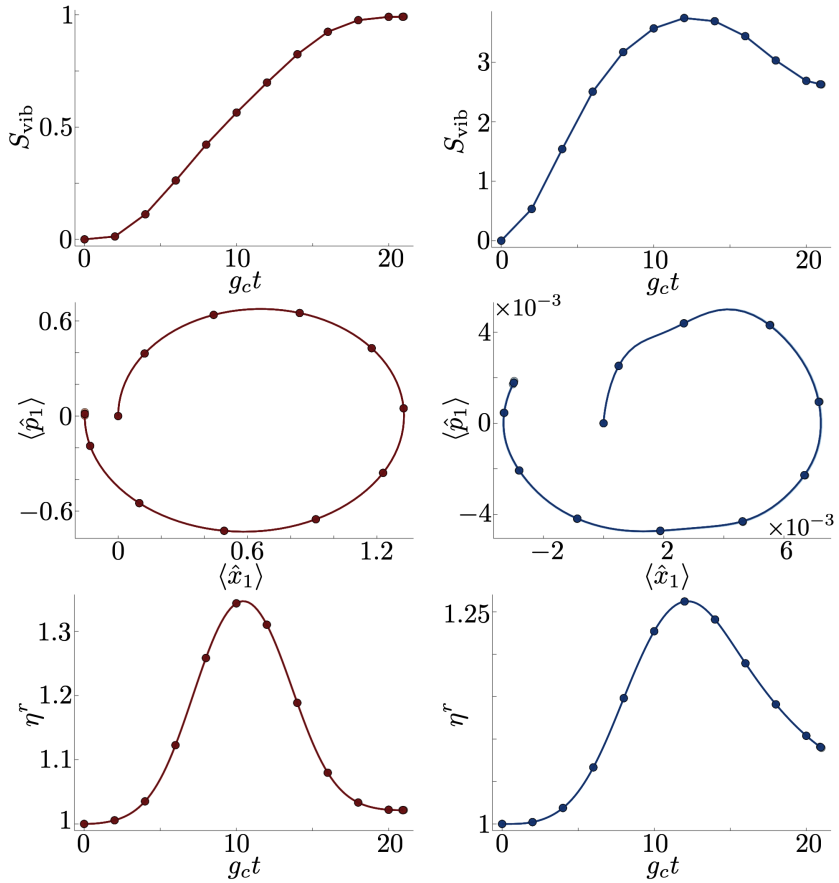


Figure 9.7. – **Convergence with the time step $dt$ of the simulation.** **a**,**b** Time evolution of the vibrational entropy $S_{\mathrm{vib}}$ for an initial molecular (left, red) or cavity (right, blue) excitation. Darkness indicates $dt$ on a log-scale ($dt \times g_c \in \{0.2, 0.1, 0.04, 0.02, 0.01, 0.005, 0.0025\}$). Fully overlapping trajectories indicate convergence for $dt < 0.2$. In **a**,**b**, the lines are a guide to the eye, whereas in **c**-**f** the lines represent additional data points. **c**,**d** Phase-space evolution of a single molecule. Same color-code as in **a**,**b**. **e**,**f** Time evolution of the right tail weight $\eta^r$ (see paper for definition). Same color-code as in **a**,**b**. Parameters for all plots: $N = 100$, $\lambda = 0.5$, $\nu = 0.3 g_c$, $W = g_c/2$, $\chi = 128$, $n^v_{\mathrm{max}} = 10$. Results for a single disorder realization.

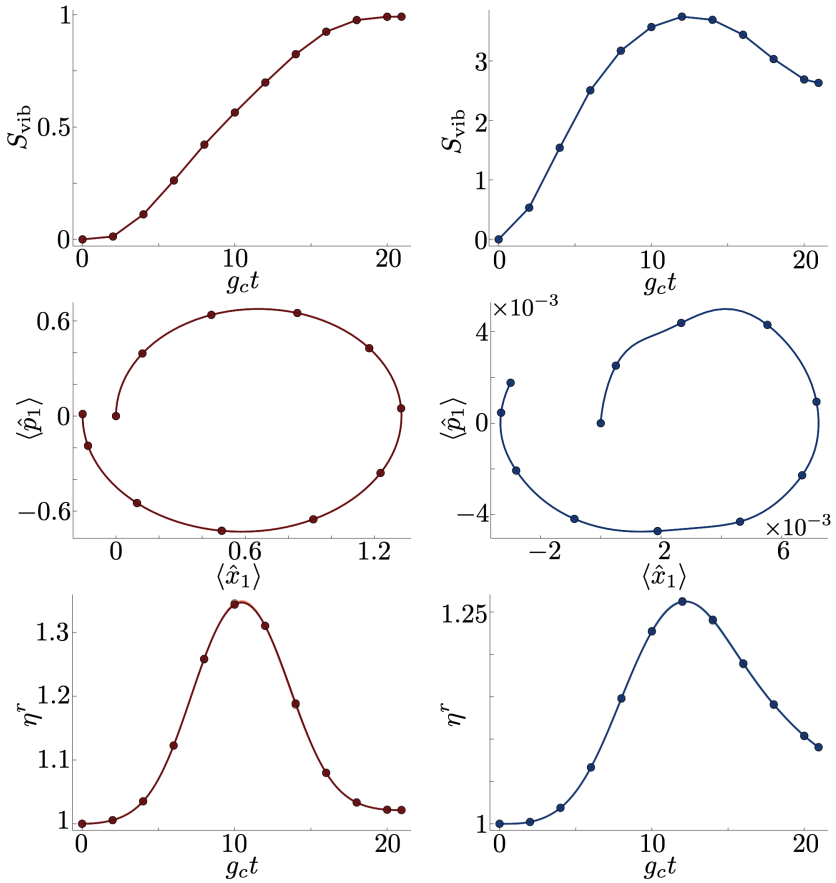


Figure 9.8. – **Convergence with the maximum number of vibrations $n^v_{\mathrm{max}}$. a,b** Time evolution of the vibrational entropy $S_{\mathrm{vib}}$ for an initial molecular (left, red) or cavity (right, blue) excitation. Darkness indicates $n^v_{\mathrm{max}}$. ($n^v_{\mathrm{max}} \in \{6, 8, 10, 12\}$). Overlapping of the trajectories indicates convergence for $n^v_{\mathrm{max}} > 6$. In **a**,**b**, the lines are a guide to the eye, whereas in **c**-**f** the lines represent additional data points. **c**,**d** Phase-space evolution of a single molecule. Same color-code as in **a**,**b**. **e**,**f** Time evolution of the right tail weight $\eta_r$ (see paper for definition). Same color-code as in **a**,**b**. Parameters for all plots: $N = 100$, $\lambda = 0.5$, $\nu = 0.3 g_c$, $W = g_c/2$, $\chi = 128$, $dt = 0.01$. Results for a single disorder realization.

# Bibliography


[1] D. Wellnitz, G. Pupillo, and J. Schachenmayer, "Disorder enhanced vibrational entanglement and dynamics in polaritonic chemistry," *ArXiv210706053 Phys. Physicsquant-Ph*, Nov. 2021.

[2] P. Törmä and W. L. Barnes, "Strong coupling between surface plasmon polaritons and emitters: A review," *Rep. Prog. Phys.*, vol. 78, p. 013901, Dec. 2014.

[3] T. W. Ebbesen, "Hybrid Light–Matter States in a Molecular and Material Science Perspective," *Acc. Chem. Res.*, vol. 49, pp. 2403–2412, Nov. 2016.

[4] R. F. Ribeiro, L. A. Martínez-Martínez, M. Du, J. Campos-Gonzalez-Angulo, and J. Yuen-Zhou, "Polariton chemistry: Controlling molecular dynamics with optical cavities," *Chem. Sci.*, vol. 9, pp. 6325–6339, Aug. 2018.

[5] J. Flick, N. Rivera, and P. Narang, "Strong light-matter coupling in quantum chemistry and quantum photonics," *Nanophotonics*, vol. 7, pp. 1479–1501, Sept. 2018.

[6] J. Feist, J. Galego, and F. J. Garcia-Vidal, "Polaritonic Chemistry with Organic Molecules," *ACS Photonics*, vol. 5, pp. 205–216, Jan. 2018.

[7] M. Hertzog, M. Wang, J. Mony, and K. Börjesson, "Strong light–matter interactions: A new direction within chemistry," *Chem. Soc. Rev.*, vol. 48, pp. 937–961, Feb. 2019.

[8] F. Herrera and J. Owrutsky, "Molecular polaritons for controlling chemistry with quantum optics," *J. Chem. Phys.*, vol. 152, p. 100902, Mar. 2020.

[9] J. A. Hutchison, T. Schwartz, C. Genet, E. Devaux, and T. W. Ebbesen, "Modifying Chemical Landscapes by Coupling to Vacuum Fields," *Angew. Chem. Int. Ed.*, vol. 51, pp. 1592–1596, Feb. 2012.

[10] D. M. Coles, N. Somaschi, P. Michetti, C. Clark, P. G. Lagoudakis, P. G. Savvidis, and D. G. Lidzey, "Polariton-mediated energy transfer between organic dyes in a strongly coupled optical microcavity," *Nature Mater*, vol. 13, pp. 712–719, July 2014.

[11] X. Zhong, T. Chervy, S. Wang, J. George, A. Thomas, J. A. Hutchison, E. Devaux, C. Genet, and T. W. Ebbesen, "Non-Radiative Energy Transfer Mediated by Hybrid Light-Matter States," *Angew. Chem. Int. Ed.*, vol. 55, no. 21, pp. 6202–6206, 2016.

[12] X. Zhong, T. Chervy, L. Zhang, A. Thomas, J. George, C. Genet, J. A. Hutchison, and T. W. Ebbesen, "Energy Transfer between Spatially Separated Entangled Molecules," *Angew. Chem. Int. Ed.*, vol. 56, no. 31, pp. 9034–9038, 2017.

[13] B. Munkhbat, M. Wersäll, D. G. Baranov, T. J. Antosiewicz, and T. Shegai, "Suppression of photo-oxidation of organic chromophores by strong coupling to plasmonic nanoantennas," *Sci. Adv.*, vol. 4, p. eaas9552, July 2018.

[14] V. N. Peters, M. O. Faruk, J. Asane, R. Alexander, D. A. Peters, S. Prayakarao, S. Rout, and M. A. Noginov, "Effect of strong coupling on photodegradation of the semiconducting polymer P3HT," *Optica, OPTICA*, vol. 6, pp. 318–325, Mar. 2019.

[15] D. Polak, R. Jayaprakash, T. P. Lyons, L. Á. Martínez-Martínez, A. Leventis, K. J. Fallon, H. Coulthard, D. G. Bossanyi, K. Georgiou, I. I. Anthony J. Petty, J. Anthony, H. Bronstein, J. Yuen-Zhou, A. I. Tartakovskii, J. Clark, and A. J. Musser, "Manipulating molecules with strong coupling: Harvesting triplet excitons in organic exciton microcavities," *Chem. Sci.*, vol. 11, pp. 343–354, Jan. 2020.

[16] Y. Yu, S. Mallick, M. Wang, and K. Börjesson, "Barrier-free reverse-intersystem crossing in organic molecules by strong light-matter coupling," *Nat Commun*, vol. 12, p. 3255, May 2021.

[17] J. Mony, C. Climent, A. U. Petersen, K. Moth-Poulsen, J. Feist, and K. Börjesson, "Photoisomerization Efficiency of a Solar Thermal Fuel in the Strong Coupling Regime," *Adv. Funct. Mater.*, vol. 31, p. 2010737, Mar. 2021.

[18] A. Thomas, J. George, A. Shalabney, M. Dryzhakov, S. J. Varma, J. Moran, T. Chervy, X. Zhong, E. Devaux, C. Genet, J. A. Hutchison, and T. W. Ebbesen, "Ground-State Chemical Reactivity under Vibrational Coupling to the Vacuum Electromagnetic Field," *Angew. Chem. Int. Ed.*, vol. 55, no. 38, pp. 11462–11466, 2016.

[19] A. Thomas, L. Lethuillier-Karl, K. Nagarajan, R. M. A. Vergauwe, J. George, T. Chervy, A. Shalabney, E. Devaux, C. Genet, J. Moran, and T. W. Ebbesen, "Tilting a ground-state reactivity landscape by vibrational strong coupling," *Science*, vol. 363, pp. 615–619, Feb. 2019.

[20] R. M. A. Vergauwe, A. Thomas, K. Nagarajan, A. Shalabney, J. George, T. Chervy, M. Seidel, E. Devaux, V. Torbeev, and T. W. Ebbesen, "Modification of Enzyme Activity by Vibrational Strong Coupling of Water," *Angew. Chem. Int. Ed.*, vol. 58, no. 43, pp. 15324–15328, 2019.

[21] J. Lather, P. Bhatt, A. Thomas, T. W. Ebbesen, and J. George, "Cavity Catalysis by Cooperative Vibrational Strong Coupling of Reactant and Solvent Molecules," *Angew. Chem. Int. Ed.*, vol. 58, no. 31, pp. 10635–10638, 2019.

[22] K. Hirai, R. Takeda, J. A. Hutchison, and H. Uji-i, "Modulation of Prins Cyclization by Vibrational Strong Coupling," *Angew. Chem. Int. Ed.*, vol. 59, no. 13, pp. 5332–5335, 2020.

[23] E. Davidsson and M. Kowalewski, "Atom Assisted Photochemistry in Optical Cavities," *J. Phys. Chem. A*, vol. 124, pp. 4672–4677, June 2020.

[24] O. Vendrell, "Coherent dynamics in cavity femtochemistry: Application of the multi-configuration time-dependent Hartree method," *Chemical Physics*, vol. 509, pp. 55–65, June 2018.

[25] C. Schäfer, M. Ruggenthaler, H. Appel, and A. Rubio, "Modification of excitation and charge transfer in cavity quantum-electrodynamical chemistry," *PNAS*, vol. 116, pp. 4883–4892, Mar. 2019.

[26] J. Galego, F. J. Garcia-Vidal, and J. Feist, "Cavity-Induced Modifications of Molecular Structure in the Strong-Coupling Regime," *Phys. Rev. X*, vol. 5, p. 041022, Nov. 2015.

[27] O. Vendrell, "Collective Jahn-Teller Interactions through Light-Matter Coupling in a Cavity," *Phys. Rev. Lett.*, vol. 121, p. 253001, Dec. 2018.

[28] C. Fábri, G. J. Halász, L. S. Cederbaum, and Á. Vibók, "Born–Oppenheimer approximation in optical cavities: From success to breakdown," *Chem. Sci.*, vol. 12, pp. 1251–1258, Feb. 2021.

[29] J. Fregoni, G. Granucci, E. Coccia, M. Persico, and S. Corni, "Manipulating azobenzene photoisomerization through strong light–molecule coupling," *Nat. Commun.*, vol. 9, Dec. 2018.

[30] H. L. Luk, J. Feist, J. J. Toppari, and G. Groenhof, "Multiscale Molecular Dynamics Simulations of Polaritonic Chemistry," *J. Chem. Theory Comput.*, vol. 13, pp. 4324–4335, Sept. 2017.

[31] P. Antoniou, F. Suchanek, J. F. Varner, and J. J. Foley, "Role of Cavity Losses on Nonadiabatic Couplings and Dynamics in Polaritonic Chemistry," *J. Phys. Chem. Lett.*, vol. 11, pp. 9063–9069, Nov. 2020.

[32] G. Groenhof, C. Climent, J. Feist, D. Morozov, and J. J. Toppari, "Tracking Polariton Relaxation with Multiscale Molecular Dynamics Simulations," *J. Phys. Chem. Lett.*, vol. 10, pp. 5476–5483, Sept. 2019.

[33] Y. Zhang, T. Nelson, and S. Tretiak, "Non-adiabatic molecular dynamics of molecules in the presence of strong light-matter interactions," *J. Chem. Phys.*, vol. 151, p. 154109, Oct. 2019.

[34] G. S. Engel, T. R. Calhoun, E. L. Read, T.-K. Ahn, T. Mančal, Y.-C. Cheng, R. E. Blankenship, and G. R. Fleming, "Evidence for wavelike energy transfer through quantum coherence in photosynthetic systems," *Nature*, vol. 446, pp. 782–786, Apr. 2007.

[35] M. Mohseni, P. Rebentrost, S. Lloyd, and A. Aspuru-Guzik, "Environment-assisted quantum walks in photosynthetic energy transfer," *J. Chem. Phys.*, vol. 129, p. 174106, Nov. 2008.

[36] F. Caruso, A. W. Chin, A. Datta, S. F. Huelga, and M. B. Plenio, "Highly efficient energy excitation transfer in light-harvesting complexes: The fundamental role of noise-assisted transport," *J. Chem. Phys.*, vol. 131, p. 105106, Sept. 2009.

[37] E. Collini, C. Y. Wong, K. E. Wilk, P. M. G. Curmi, P. Brumer, and G. D. Scholes, "Coherently wired light-harvesting in photosynthetic marine algae at ambient temperature," *Nature*, vol. 463, pp. 644–647, Feb. 2010.

[38] R. Horodecki, P. Horodecki, M. Horodecki, and K. Horodecki, "Quantum entanglement," *Rev. Mod. Phys.*, vol. 81, pp. 865–942, June 2009.

[39] L. Amico, R. Fazio, A. Osterloh, and V. Vedral, "Entanglement in many-body systems," *Rev. Mod. Phys.*, vol. 80, pp. 517–576, May 2008.

[40] J. Eisert, M. Cramer, and M. B. Plenio, "Colloquium: Area laws for the entanglement entropy," *Rev. Mod. Phys.*, vol. 82, pp. 277–306, Feb. 2010.

[41] L. K. McKemmish, R. H. McKenzie, N. S. Hush, and J. R. Reimers, "Quantum entanglement between electronic and vibrational degrees of freedom in molecules," *J. Chem. Phys.*, vol. 135, p. 244110, Dec. 2011.

[42] M. Vatasescu, "Measures of electronic-vibrational entanglement and quantum coherence in a molecular system," *Phys. Rev. A*, vol. 92, p. 042323, Oct. 2015.

[43] F. Herrera and F. C. Spano, "Cavity-Controlled Chemistry in Molecular Ensembles," *Phys. Rev. Lett.*, vol. 116, p. 238301, June 2016.

[44] M. A. Zeb, P. G. Kirton, and J. Keeling, "Exact States and Spectra of Vibrationally Dressed Polaritons," *ACS Photonics*, vol. 5, pp. 249–257, Jan. 2018.

[45] J. del Pino, F. A. Y. N. Schröder, A. W. Chin, J. Feist, and F. J. Garcia-Vidal, "Tensor network simulation of polaron-polaritons in organic microcavities," *Phys. Rev. B*, vol. 98, p. 165416, Oct. 2018.

[46] U. Schollwöck, "The density-matrix renormalization group in the age of matrix product states," *Annals of Physics*, vol. 326, pp. 96–192, Jan. 2011.

[47] J. A. Ćwik, S. Reja, P. B. Littlewood, and J. Keeling, "Polariton condensation with saturable molecules dressed by vibrational modes," *EPL Europhys. Lett.*, vol. 105, p. 47009, Feb. 2014.

[48] F. Herrera and F. C. Spano, "Theory of Nanoscale Organic Cavities: The Essential Role of Vibration-Photon Dressed States," *ACS Photonics*, vol. 5, pp. 65–79, Jan. 2018.

[49] T. Botzung, D. Hagenmüller, S. Schütz, J. Dubail, G. Pupillo, and J. Schachenmayer, "Dark state semilocalization of quantum emitters in a cavity," *Phys. Rev. B*, vol. 102, p. 144202, Oct. 2020.

[50] N. C. Chávez, F. Mattiotti, J. A. Méndez-Bermúdez, F. Borgonovi, and G. L. Celardo, "Disorder-Enhanced and Disorder-Independent Transport with Long-Range Hopping: Application to Molecular Chains in Optical Cavities," *Phys. Rev. Lett.*, vol. 126, p. 153201, Apr. 2021.

[51] J. Dubail, T. Botzung, J. Schachenmayer, G. Pupillo, and D. Hagenmüller, "Large Random Arrowhead Matrices: Multifractality, Semi-Localization, and Protected Transport in Disordered Quantum Spins Coupled to a Cavity," *ArXiv210508444 Quant-Ph*, May 2021.

[52] R. Houdré, R. P. Stanley, and M. Ilegems, "Vacuum-field Rabi splitting in the presence of inhomogeneous broadening: Resolution of a homogeneous linewidth in an inhomogeneously broadened system," *Phys. Rev. A*, vol. 53, pp. 2711–2715, Apr. 1996.

[53] F. Valmorra, M. Bröll, S. Schwaiger, N. Welzel, D. Heitmann, and S. Mendach, "Strong coupling between surface plasmon polariton and laser dye rhodamine 800," *Appl. Phys. Lett.*, vol. 99, p. 051110, Aug. 2011.

[54] N. Christensson, B. Dietzek, A. Yartsev, and T. Pullerits, "Electronic photon echo spectroscopy and vibrations," *Vibrational Spectroscopy*, vol. 53, pp. 2–5, May 2010.

[55] V. M. Agranovich, M. Litinskaia, and D. G. Lidzey, "Cavity polaritons in microcavities containing disordered organic semiconductors," *Phys. Rev. B*, vol. 67, Feb. 2003.

[56] P. Michetti and G. C. La Rocca, "Exciton-phonon scattering and photoexcitation dynamics in $j$-aggregate microcavities," *Phys. Rev. B*, vol. 79, p. 035325, Jan. 2009.

[57] S. Hou, M. Khatoniar, K. Ding, Y. Qu, A. Napolov, V. M. Menon, and S. R. Forrest, "Ultralong-Range Energy Transport in a Disordered Organic Semiconductor at Room Temperature Via Coherent Exciton-Polariton Propagation," *Adv. Mater.*, vol. 32, no. 28, p. 2002127, 2020.

[58] D. A. Abanin, E. Altman, I. Bloch, and M. Serbyn, "Colloquium: Many-body localization, thermalization, and entanglement," *Rev. Mod. Phys.*, vol. 91, p. 021001, May 2019.

[59] G. D. Scholes, "Polaritons and excitons: Hamiltonian design for enhanced coherence," *Proc. R. Soc. Math. Phys. Eng. Sci.*, vol. 476, p. 20200278, Oct. 2020.

[60] C. Sommer, M. Reitz, F. Mineo, and C. Genes, "Molecular polaritonics in dense mesoscopic disordered ensembles," *Phys. Rev. Research*, vol. 3, p. 033141, Aug. 2021.

[61] M. Du and J. Yuen-Zhou, "Can Dark States Explain Vibropolaritonic Chemistry?," *ArXiv210407214 Quant-Ph*, Apr. 2021.

[62] T. Botzung, *Study of Strongly Correlated One-Dimensional Systems with Long-Range Interactions*. PhD thesis, University of Strasbourg, Strasbourg, 2019.

[63] M. L. Wall, A. Safavi-Naini, and A. M. Rey, "Simulating generic spin-boson models with matrix product states," *Phys. Rev. A*, vol. 94, p. 053637, Nov. 2016.

[64] S. Felicetti, J. Fregoni, T. Schnappinger, S. Reiter, R. de Vivie-Riedle, and J. Feist, "Photoprotecting Uracil by Coupling with Lossy Nanocavities," *J. Phys. Chem. Lett.*, Sept. 2020.

[65] D. Wellnitz, G. Pupillo, and J. Schachenmayer, "A quantum optics approach to photoinduced electron transfer in cavities," *J. Chem. Phys.*, vol. 154, p. 054104, Feb. 2021.

[66] J. Torres-Sánchez and J. Feist, "Molecular photodissociation enabled by ultrafast plasmon decay," *J. Chem. Phys.*, vol. 154, p. 014303, Jan. 2021.

[67] E. Davidsson and M. Kowalewski, "Simulating photodissociation reactions in bad cavities with the Lindblad equation," *J. Chem. Phys.*, vol. 153, p. 234304, Dec. 2020.

[68] M. Fishman, S. R. White, and E. M. Stoudenmire, "The ITensor Software Library for Tensor Network Calculations," *ArXiv200714822 Cond-Mat Physicsphysics*, July 2020.

[69] G. Vidal, "Efficient Simulation of One-Dimensional Quantum Many-Body Systems," *Phys. Rev. Lett.*, vol. 93, p. 040502, July 2004.

[70] J. J. Sakurai and J. Napolitano, *Modern Quantum Mechanics*. Cambridge University Press, third ed., 2021.

# 10. Multi-Excitation Holstein Tavis Cummings Model

In this chapter, the Holstein-Tavis-Cummings model is analyzed for multiple excitations. This chapter is very similar to the previous one, however without any disorder. Section 10.1 provides a short introduction of the system that is analyzed and gives an overview over the main results. In Section 10.2, the different methods used to approximate the dynamics are introduced. Then, the exact and approximate dynamics of the vibrations, excitations, and entanglement are discussed in Section 10.3. The regimes of validity of these methods are determined in Section 10.4. Large system sizes are then analyzed using the approximations in Section 10.5. Finally, Section 10.6 concludes this chapter.

## 10.1. Introduction

A series of breakthrough experiments in the group of Thomas Ebbesen in Strasbourg have demonstrated that chemical reactions can be modified by coupling electronic [1] or vibrational [2, 3] molecular transitions to a cavity mode. Understanding this effect has been a longstanding theoretical challenge, which is complicated by the large number of photonic, electronic, and vibrational degrees of freedom.

In the previous chapters, I have introduced the Holstein-Tavis-Cummings model as a toy mode for describing electronic strong coupling experiments, and I have summarized previous numerical studies. So far, most research in polaritonic chemistry (experimental, numerical, and analytical) is focused on the low excitation regime. In this regime, polaritons are well described as bosonic quasi-particles. This can be seen e.g. from the commutator $[\hat{p}_\pm, \hat{p}_\pm^\dagger] = 1/2 - \hat{S}^z/N$ with $\hat{p}_\pm = \hat{a}/\sqrt{2} \pm \hat{S}^-/\sqrt{2N}$ the polariton annihilation operators, which is approximately 1 for small excitation fractions. $\hat{S}^{\pm,z} = \sum \hat{\sigma}^{\pm,z}$ are the collective spin operators for single spin raising, lowering, and $z$ operators $\hat{\sigma}^{\pm,z}$. Then, if the excitations do not interact, as is typically the case for organic materials, neither do the polaritons [4]. Physically speaking, exciting the symmetric mode multiple times is possible without corrections for large ensembles of molecules, since each molecule individually has a low excitation probability.

However, if the excitation probability becomes large, saturation effects become relevant, in other words, the polaritons effectively interact [4–7]. This type of saturation effects has been argued to be a source of the blue shift in organic polariton condensates [4, 8], where excitation fractions up to 6% have been reported [8]. At the same time, vibrational strong coupling experiments have reached excitation fractions of up to

40% [9, 10].

I analyze the multi-excitation dynamics in the Holstein-Tavis-Cummings model, which was introduced in detail in Chapter 7. The Hamiltonian is given by [11, 12] ($\hbar = 1$)

$$\hat{H}_{\mathrm{HTC}} = \Delta \hat{a}^\dagger \hat{a} + g \sum_{n=1}^{N} \left( \hat{\sigma}_n^+ \hat{a} + \hat{\sigma}_n^- \hat{a}^\dagger \right) + \nu \sum_{n=1}^{N} \hat{b}_n^\dagger \hat{b}_n - \lambda\nu \sum_{n=1}^{N} \hat{\sigma}_n^+ \hat{\sigma}_n^- \left( \hat{b}_n + \hat{b}_n^\dagger \right). \tag{10.1}$$

Here, $\Delta$ is the detuning between cavity and electronic transition, $g$ is the single molecule cavity coupling strength, $\nu$ is the vibrational frequency, and $\lambda$ is the square root of the Huang-Rhys factor. We further label $\hat{H}_{\mathrm{TC}} = \Delta \hat{a}^\dagger \hat{a} + g \sum_{n=1}^{N} (\hat{\sigma}_n^+ \hat{a} + \hat{\sigma}_n^- \hat{a}^\dagger)$, $\hat{H}_{\mathrm{vib}} = \nu \sum_{n=1}^{N} \hat{b}_n^\dagger \hat{b}_n$, and $\hat{H}_{\mathrm{H}} = -\lambda\nu \sum_{n=1}^{N} \hat{\sigma}_n^+ \hat{\sigma}_n^- (\hat{b}_n + \hat{b}_n^\dagger)$. We also define the dimensionless vibrational position and momentum operators $\hat{x}_n = (\hat{b}_n + \hat{b}_n^\dagger)/\sqrt{2}$ and $\hat{p}_n = -\mathrm{i}(\hat{b}_n - \hat{b}_n^\dagger)/\sqrt{2}$, respectively.

The short-time dynamics is analyzed after an initial excitation of $N_{\mathrm{exc}}$ molecules, with $N - N_{\mathrm{exc}}$ molecules remaining in the ground state

$$|\psi(t=0)\rangle = \left( \prod_{i=1}^{N_{\mathrm{exc}}} \hat{\sigma}_i^+ \right) |0\rangle_{\mathrm{ph}} \otimes |0\rangle_{\mathrm{exc}} \otimes |0\rangle_{\mathrm{vib}} \,. \tag{10.2}$$

Here, $|0\rangle_{\mathrm{ph}}$ is the vacuum state of the cavity, the state $|0\rangle_{\mathrm{exc}}$ indicates that all electrons are in the ground state, and $|0\rangle_{\mathrm{vib}}$ is the non-displaced vibrational ground state. This initial state is illustrated in Figure 10.1(a). Such states could be experimentally prepared by starting from a ground state ensemble, and then instantaneously pumping $N_{\mathrm{exc}}$ molecules in the excited state, e.g. by a $\pi/2$ laser pulse or by an incoherent light pulse much shorter than any time scale of the system. If the laser pulse overlaps with the all molecules, then $N_{\mathrm{exc}} = N$, whereas if it only overlaps with a part of the molecules, $N_{\mathrm{exc}} < N$. An incoherent light pulse will not create a state with well-defined $N_{\mathrm{exc}}$, but rather an incoherent mixture with different $N_{\mathrm{exc}}$, which evolve independently.

In the analysis, I focus on the vibrational dynamics, which is chemically relevant, and on the entanglement between the different subsystems, which is important for numerical simulations (see Chapter 4). This is illustrated in Figure 10.1(b), where the system is split into photonic, electronic, and vibrational degrees of freedom, which can be entangled with each other. The entanglement of a bipartition into subsystems $X$ and $\bar{X}$ for a pure state $|\psi\rangle$ can be quantified by the von Neumann entropy of either subsystem [13, 14]

$$S_X = -\operatorname{Tr}[\hat{\rho}_X \log_2(\hat{\rho}_X)] \,, \tag{10.3}$$

$$\hat{\rho}_X = \operatorname{Tr}_{\bar{X}} |\psi\rangle \bar{\psi} \,. \tag{10.4}$$

Here, $\operatorname{Tr}_{\bar{X}}$ indicates the partial trace over the degrees of freedom of that subsystem.

I find that the vibrational dynamics is reduced compared to the no-cavity scenario [see Figure 10.1(c)]. I relate this to a reduced excitation fraction, as shown in Figure 10.1(d).

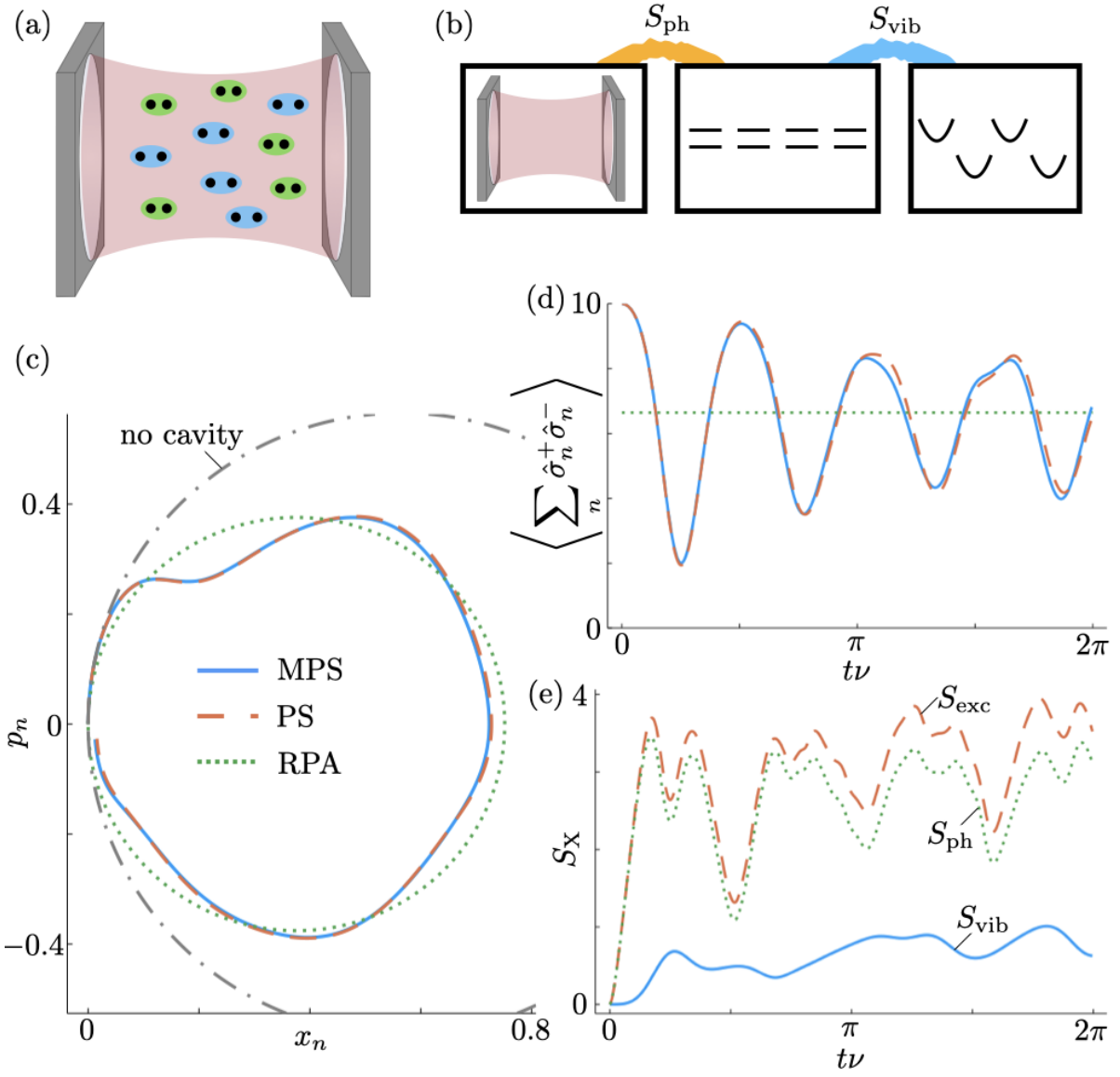


Figure 10.1. – Overview of the setup. (a) Schematic setup and initial state. (b) Illustration of the degrees of freedom and the entanglement entropies $S_{\mathrm{ph}}$ and $S_{\mathrm{vib}}$. (c) Phase space evolution in the different models, in units of the zero-point motion. For comparison, also the no cavity line is shown (grey dash-dotted) (d) Excitation number in the different models. The Rotating Polariton Approximation treats the excitation as constant. (e) Evolution of the entanglement entropy of different partitions of the system.

Finally, I show that in a large parameter regime, the entanglement between vibrational and electro-photonic degrees of freedom remains small [Figure 10.1(e)]. Based on this observation, a product state between vibrational and photonic degrees of freedom can be assumed, and I show that this assumption reproduces the excited state and vibrational dynamics well, as can be seen in Figures 10.1(c/d). In addition, by averaging out the fast excited state oscillations, I implement the rotating polariton approximation (RPA), which correctly predicts the reduction of the vibrational dynamics, but cannot reproduce its details.

The small vibrational entanglement is related to the permutations symmetry of different molecules, which keeps the Hilbert space small. This symmetry is also used for efficient simulations. Partially breaking this permutation symmetry due to excitation of only a subset of molecules then significantly enhances the entanglement. Ultimately, these results together with works on disorder enhanced transport in cavities [15, 16] motivated us to investigate energetic disorder as a means of breaking permutation symmetry. This is the topic of the next chapter.

This is a toy model, which does not capture all relevant effects. In particular, any dissipation or dephasing is neglected. This is realistic for cavities with a sufficiently large quality factor, such as distributed Bragg reflectors [17, 18]. I also neglect any symmetry breaking effects between the molecules caused by molecular orientations, interactions, and spatial distribution, such as local cavity coupling constants or inhomogeneous broadening [15, 16, 19–21], the latter of which is analyzed in Chapter 9.

## 10.2. Methods

### Matrix Product States

In order to simulate the dynamics exactly, I use a simulation based on matrix product state (MPS), which were introduced in Chapter 4. In particular, the system is mapped to a chain with the cavity on the first site on the left, followed by the electronic and vibrational degrees of freedom of each molecule directly next to each other shown in Figure 10.2. In this layout, the vibronic coupling $\hat{H}_{\mathrm{H}}$ can be implemented directly, and the cavity coupling $\hat{H}_{\mathrm{TC}}$ can be included by swapping the cavity through the system as indicated in Figure 10.2(b).

This simulation was implemented by Dr. Johannes Schachenmayer analogous to simulations of vibrations in ion-arrays [22]. For each molecule $n$, first the gate corresponding to the photo-electronic interaction is applied, and then the gate corresponding to the vibronic interaction. Subsequently, the cavity is swapped with both sites corresponding to the $n$th molecule, and the procedure is repeated with the $(n+1)$th molecule. Upon reaching the $N$th molecule, the process is reversed, swapping the cavity back and applying first vibronic and then photo-electronic gates. This is a second order algorithm in the time step.

In order to compute the entanglement entropies of a sub-system, the respective subsystem is swapped to one end of the chain. The entanglement entropy of the respective

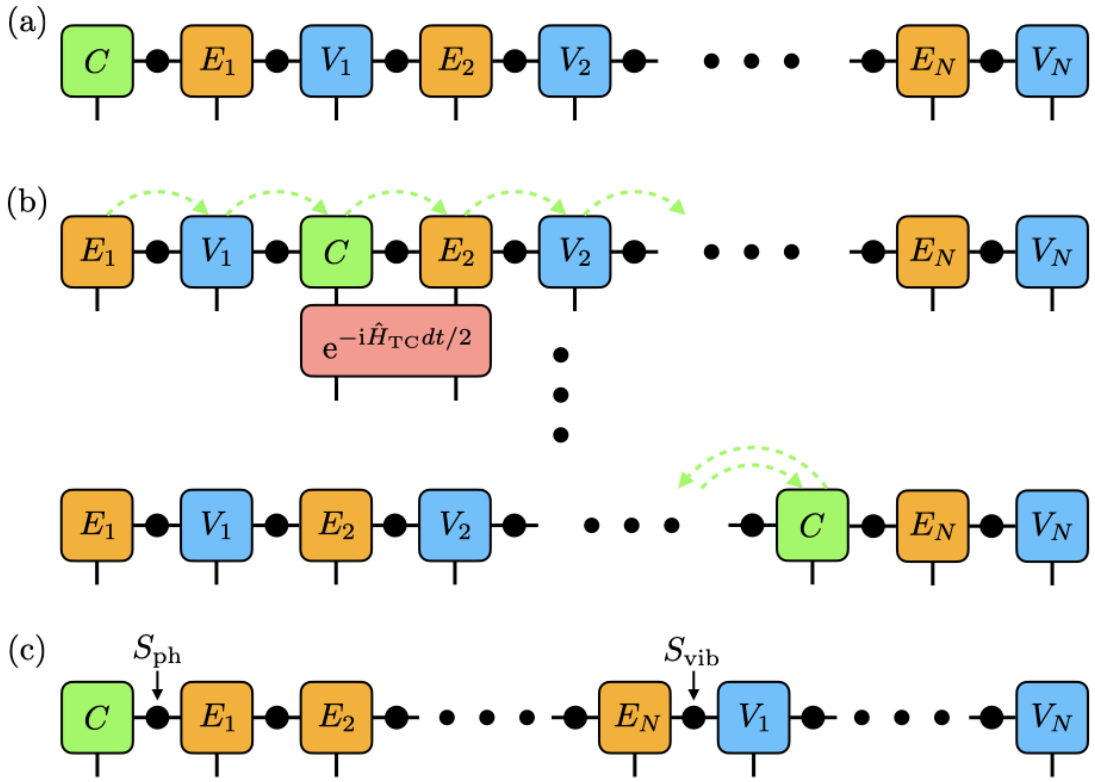


Figure 10.2. – Schematic illustration of the MPS algorithm. (a) Default layout of the MPS. The cavity site is labeled by $C$ and drawn in green, the site corresponding to the electronic degree of freedom of the $n$th molecule is labeled by $E_n$ and drawn in orange, and the corresponding $n$th vibrational degree of freedom is blue labeled by $V_n$. (b) The cavity gates are implemented by swapping the cavity to the corresponding excitation (indicated by the green arrows) and then applying the corresponding gate for half a timestep (red). After reaching the last site, the cavity is swapped back and the other half of the timestep is applied (not shown). (c) MPS layout used to compute the entanglement entropy $S_{vib}$.

subsystem is then the bipartite entropy at the respective cut of the chain. This is schematically illustrated in Figure 10.2(c) for the vibrational and photonic entanglement. The electronic entanglement is computed by swapping the cavity to the center of the chain in this configuration. As a side-note: In order to reach the configuration shown in Figure 10.2(c), $\mathcal{O}(N^2)$ swaps are necessary, making the entropy calculation the bottleneck of the simulation for large $N$.

## Product State Approximation

Alternatively, any type of entanglement between the vibrational Hilbert space $\mathcal{H}_{\text{vib}}$ and the rest of the system can be directly neglected by making the product state ansatz $|\psi\rangle = |\psi\rangle_{\text{ph+exc}} |\psi\rangle_{\text{vib}}$. Beyond the numerical observation of low vibrational entanglement, this is motivated by previous results predicting that the coupling between spins and vibrations is reduced to $\sim \lambda\nu/(2\sqrt{N})$ in the collective strong coupling regime for perturbative $\lambda\nu$ in the single excitation limit [12]. Assuming these results are also valid in the multi-excitation regime, for not too large $\lambda\nu$ [23], the entanglement between vibrational and electro-photonic degrees of freedom should remain small. The equations of motion then become:

$$\partial_t |\psi\rangle_{\text{ph+exc}} = -\mathrm{i} \left\langle \hat{H} \right\rangle_{\text{vib}} |\psi\rangle_{\text{ph+exc}} \tag{10.5}$$

$$= -\mathrm{i} \left( \hat{H}_{\text{TC}} - \sqrt{2}\lambda\nu \sum_n \langle \hat{x}_n \rangle \, \hat{\sigma}_n^+ \hat{\sigma}_n^- \right) |\psi\rangle_{\text{ph+exc}} \tag{10.6}$$

$$\partial_t |\psi\rangle_{\text{vib}} = \left\langle \hat{H} \right\rangle_{\text{ph+exc}} |\psi\rangle_{\text{vib}} \tag{10.7}$$

$$= -\mathrm{i} \left( \hat{H}_{\text{vib}} - \sqrt{2}\lambda\nu \sum_n \left\langle \hat{\sigma}_n^+ \hat{\sigma}_n^- \right\rangle \hat{x}_n \right) |\psi\rangle_{\text{vib}} \tag{10.8}$$

With the partial or "mean-field" expectation values $\langle \hat{O} \rangle_{\text{X}} \equiv \langle \psi |_{\text{X}} \hat{O} \, |\psi\rangle_{\text{X}}$.

In principal, the dimensions of both $|\psi\rangle_{\text{ph+exc}}$ and $|\psi\rangle_{\text{vib}}$ still scale exponentially with the system size, which would make a direct simulation of Equation (10.6) and (10.8) intractable for large $N$. However, this complexity is significantly reduced by the permutation symmetry of the Hamiltonian Equation (10.1) and the partial permutation symmetry of the initial state in Equation (10.2) with respect to the initially excited and ground state molecules.

First, consider a fully excited initial state $N_{\text{exc}} = N$. In this case, both the Hamiltonian and the initial state are symmetric with respect to the exchange of any two molecules $n$ and $n'$. As a consequence, the states $|\psi\rangle_{\text{exc}}$ and $|\psi\rangle_{\text{vib}}$ remain permutation symmetric at all times. For the electronic subspace, these states were introduced as Dicke states in Chapter 3, which are uniquely defined by the spin-$z$-component of the collective spin $M$ (with $J = N/2$). As the number of electro-photonic excitations is conserved, this excitation number immediately defines the photon number $N/2 - M$, and thus the state $|\psi\rangle_{\text{ph+exc}}$. In the vibrational state $|\psi\rangle_{\text{vib}}$, only the symmetric vibrational mode

$(\sum_n \hat{b}_n)/\sqrt{N}$ is populated. This can be directly seen from Equation (10.8), since $\langle \hat{\sigma}_n^+ \hat{\sigma}_n^- \rangle$ is independent of $n$. Furthermore, Equation (10.8) simply describes a displaced harmonic oscillator potential. Since the initial state is a coherent state (in particular, the undisplaced vibrational vacuum state), the vibrational state always remains coherent and is well described by just two real numbers, its position and momentum. The resulting state $|\psi\rangle_{\text{ph+exc}} \otimes |\psi\rangle_{\text{vib}}$ is thus described by just $N+2$ complex numbers.

For $N_{\text{exc}} < N$, the initial state is only symmetric with respect to a permutation of molecules $n$ and $n'$ if either both $n, n' \leq N_{\text{exc}}$ or both $n, n' > N_{\text{exc}}$. Due to this permutation symmetry, two Dicke states and two coherent states (one for each the initially excited and initial ground state manifold) are needed to fully describe the states $|\psi\rangle_{\text{ph+exc}}$ and $|\psi\rangle_{\text{vib}}$, respectively. The details of how to write the states and operators in this basis are given in Appendix 10.B.

This method is equivalent to the mean-field Ehrenfest method, which has been previously used to simulate molecular dynamics in the strong coupling regime in the low excitation limit [24, 25]. There, in addition to the product state assumption, the nuclear dynamics is treated classically, which however does not modify the result for a coherent state in a harmonic oscillator, as analyzed here.

## Rotating Polariton Approximation

If the states $|\psi\rangle_{\text{ph+exc}}$ oscillate at a much higher frequency than the vibrations $|\psi\rangle_{\text{vib}}$ — this corresponds to the limit $\sqrt{N}g \gg \nu, \lambda\nu$ — one can additionally assume that the vibrational dynamics depends only on the time averaged exciton number. In particular, the term $\langle \hat{\sigma}_n^+ \hat{\sigma}_n^- \rangle$ in Equation (10.8) can be replaced by its time average $\overline{\langle \hat{\sigma}_n^+ \hat{\sigma}_n^- \rangle}$. Formally, this approximation can be derived analogous to the rotating wave approximation in quantum optics. Here we closely follow the derivation given in Reference [26].

Starting from the full Hamiltonian in Eq. (10.1), we transform into the interaction picture with respect to $\hat{H}_{\text{TC}}$ by applying the unitary transform $\mathcal{U} = \exp\left(-\mathrm{i}\hat{H}_{\text{TC}}t\right)$ so that

$$|\psi_{\text{int}}\rangle = \mathcal{U}^{-1} |\psi\rangle \,, \tag{10.9}$$

$$\hat{H}_{\text{int}} = \mathcal{U}^{-1}\hat{H}\mathcal{U} + \mathrm{i}\frac{\mathrm{d}\mathcal{U}^{-1}}{\mathrm{d}t}\mathcal{U} \,, \tag{10.10}$$

$$\hat{O}_{\text{int}} = \mathcal{U}^{-1}\hat{O}\mathcal{U} \,. \tag{10.11}$$

Note that the unitary transform acts only on $\mathcal{H}_{\text{ph}} \otimes \mathcal{H}_{\text{exc}}$, such that any operators measuring the vibrational dynamics remain unchanged.

The Hamiltonian $\hat{H}_{\text{int}}$ reads

$$\begin{aligned}\hat{H}_{\text{int}} = \nu \sum_{n=1}^{N} \hat{b}_n^\dagger \hat{b}_n - \lambda\nu \sum_{n,\phi,\psi} \left(\hat{b}_n^\dagger + \hat{b}_n\right) \\ \times \langle\phi| \hat{\sigma}_n^+ \sigma_n^- |\psi\rangle |\phi\rangle \langle\psi| \, \mathrm{e}^{-\mathrm{i}(E_\psi - E_\phi)t}\end{aligned} \tag{10.12}$$

where the sum over $\phi$ and $\psi$ runs over all pairs of eigenstates of $\hat{H}_{\mathrm{TC}}$, and $E_\psi$ is the eigenenergy corresponding to state $|\psi\rangle$: $\hat{H}_{\mathrm{TC}} |\psi\rangle = E_\psi |\psi\rangle$. If now the energy differences $E_\psi - E_\phi$ lead to oscillations much faster than the time scale of the system dynamics, the cross terms $|\psi\rangle \neq |\phi\rangle$ oscillate quickly and can be neglected (see Appendix 10.A for details).

Neglecting the cross terms $\hat{H}_{\mathrm{int}}$ reads

$$\hat{H}_{\mathrm{int}}^{(0)} = \nu \sum_{n=1}^{N} \hat{b}_n^\dagger \hat{b}_n - \lambda\nu \sum_{n,\psi} \left( \hat{b}_n^\dagger + \hat{b}_n \right) \langle\psi| \hat{\sigma}_n^+ \sigma_n^- |\psi\rangle |\psi\rangle \langle\psi| \ . \tag{10.13}$$

This Hamiltonian does not couple different electro-photonic states. As a consequence, the resulting dynamics is a purely vibrational dynamics. Furthermore, the vibrational dynamics of all $N$ molecules is just that of independent harmonic oscillators that are displaced by the time averaged excitation number. In principal, this approximation can be made for both full excitation and partial excitation scenarios. However, in this chapter it is only applied to the full exitation case.

Conceptionally, this approximation is close to the Born-Oppenheimer (BO) approximation. However, in contrast to the RPA, in the BO approximation the photo-electronic subspace is diagonalized at each value of the vibrational coordinate including the vibronic shift, leading to eigenstates $|\psi\rangle$ and eigenenergies $E_\psi$ which depend on the vibrational coordinate. Therefore, the BO approximation should be slightly more accurate than the RPA. However, this comes at the added computational cost of needing to diagonalize at every point in space. Since this correction is small for $|E_\psi - E_\phi| \gg \nu$, and both approximations are only valid if this condition is fulfilled, the errors of the RPA and the BO approximation should generally be similar. Hence, the additional cost is not justified for us. In particular, mean-field Ehrenfest dynamics is generally seen as more accurate than BO dynamics much in the same way that the product states are a better description than the RPA. As a result, the hierarchy considered here is sufficient to analyze the dynamics.

## 10.3. Exact Results

### Full Excitation

First, consider a scenario in which all molecules are initially excited. Figure 10.3 shows the dynamics over one vibrational oscillation period starting in the state $|\psi(t=0)\rangle$ as defined in Equation (10.2). Panels (a) to (c) show the entanglement entropies for different bipartitions of the system for increasing vibronic coupling $\lambda\nu$. In all cases, both the cavity entropy and the electronic entropy quickly rise to a value $S_{\mathrm{ph/exc}} \sim 3$ and then oscillate synchronously, indicating that the cavity and the electronic degrees of freedom quickly build up entanglement between each other. The apparent change in oscillation frequency between the panels is actually a change in time-scale, which is given in units of the inverse vibrational frequency.

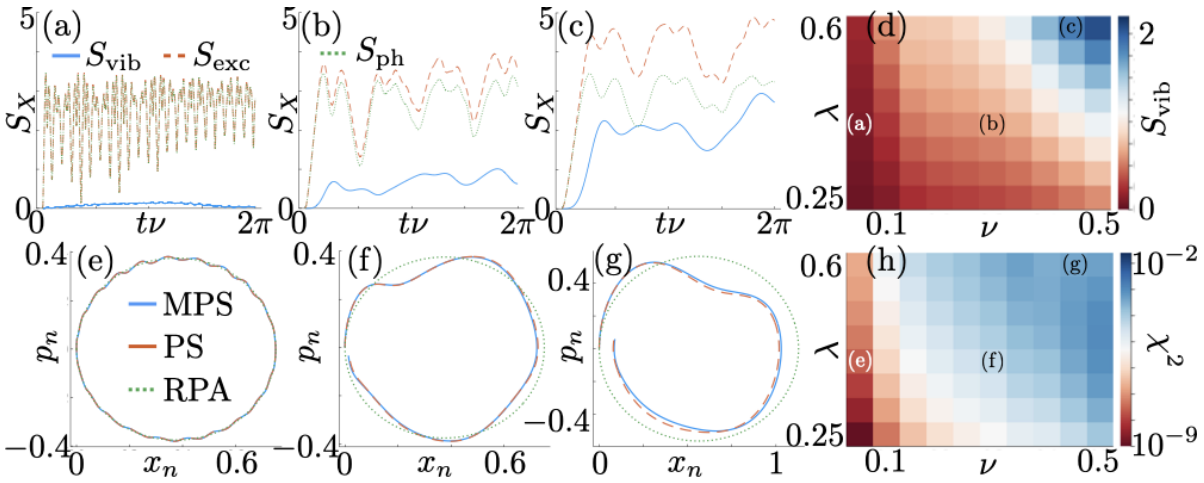


Figure 10.3. – Entanglement and vibrational dynamics in the HTC model. We consider 10 molecules with $N_{\text{exc}} = N$, and set $g_c = 1$. (a) to (c) show the time evolution of the von Neumann entropies $S_{\text{vib}}$ (blue, continuous), $S_{\text{exc}}$ (orange, dashed), and $S_{\text{ph}}$ (green, dotted) for different values of $\lambda$ and $\nu$ indicated in (d). (d) shows the dependence of the time averaged vibrational entropy $\overline{S_{\text{vib}}}$ on $\lambda$ and $\nu$ . (e) to (g) show the phase space trajectories of the vibration of a single molecule computed with MPS (continuous, blue), PS (dashed, orange), and RPA (dotted, green), for different values of $\lambda$ and $\nu$. Figure (h) gives the $\chi^2$ value between the trajectories corresponding to MPS and PS on a logarithmic scale, according to Equation (10.14).

For small $\lambda\nu$, the vibrational entropy remains very small at all times $S_{\text{vib}} \sim 0$, indicating that the system is well-described by a product state [panel (a)]. For increasing $\lambda\nu$, the vibrational entropy increases, and even becomes comparable to the cavity entanglement in the extreme case. In this case, the electronic entropy also increases to $S_{\text{exc}} \sim 4$, indicating that the vibrations are entangled with the electronic, but not directly with the photonic degrees of freedom, as indicated in Figure 10.1(b).

Panel (d) shows the time averaged value of $S_{\text{vib}}$ for various $\lambda$ and $\nu$. For small $\lambda$ and $\nu$, $S_{\text{vib}}$ vanishes. For increasing $\lambda$ and $\nu$, $S_{\text{vib}}$ can become large, and the entanglement entropy grows similarly with respect to changes of $\lambda$ and $\nu$.

These results are explained by the vibronic coupling $\hat{H}_{\text{H}} = -\lambda\nu \sum_n \hat{\sigma}_n^+ \hat{\sigma}_n^- (\hat{b}_n + \hat{b}_n^\dagger)$, which couples electronic and vibrational degrees of freedom. For small $\lambda\nu$, this coupling vanishes, and the dynamics becomes separable. However, for increasing $\lambda\nu$, the vibronic coupling becomes important and leads to entanglement between vibrational and electronic degrees of freedom.

Panels (e) to (g) show the phase space dynamics of the (quantum mechanical) mean position and momentum of the vibration simulated with the different methods introduced in Section 10.2, which is identical for all molecules. For small $\lambda$ and $\nu$, the phase space dynamics is essentially circular for all methods. In addition, small oscillations around this circular dynamics can be seen for PS and MPS simulation. For increasing $\nu$, the number of these additional oscillations decreases and the deviation from the RPA increases [Figure 10.3(f/g)]. Finally, for very large $\lambda\nu$, the oscillation does not return to 0, as expected for a time dependent displacement.

The circular dynamics corresponds to a displaced harmonic oscillator, and the oscillations stem from Rabi oscillations between the cavity and the electronic excitation, which are averaged out in the RPA. As these oscillations occur on a timescale $\sim g_c$ independently of $\nu$, for increasing vibrational oscillation frequency fewer Rabi oscillations fit into a single vibrational period. The increase in $\nu$ also means the separation of timescales is less accurate, leading to stronger deviations between the RPA and exact dynamics.

Intriguingly, in all cases, the PS and MPS simulations match well. Panel (h) is a parameter scan over the summed up error of the product state approximation, defined as the time averaged deviation in phase space coordinates

$$\chi^2 = \nu/(2\pi) \times \int \mathrm{d}t[(x_{\text{PS}} - x_{\text{MPS}})^2 + (p_{\text{PS}} - p_{\text{MPS}})^2] \,. \tag{10.14}$$

Here, $x_{\text{(M)PS}}$ and $p_{\text{(M)PS}}$ are the expectation values of the position and momentum of a single molecule according to (M)PS simulation, respectively. This error is smallest for small $\lambda\nu$, but it remains small for all values of $\lambda$ and $\nu$ considered (note the logarithmic color scale).

This can be explained by the entanglement modifying the probability distribution along the vibrational coordinate, but not the mean. This assumption is analyzed in detail in Chapter 9 in the presence of disorder.

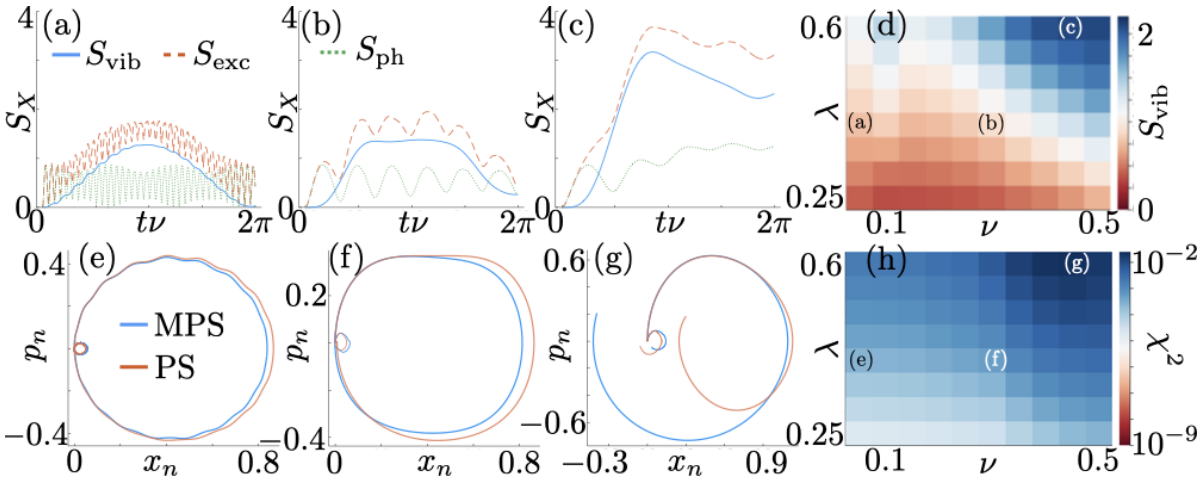


Figure 10.4. – Same as Figure 10.3, but for $N_{\mathrm{exc}} = 2$. In (e) to (g) the inner trajectory is for a molecule initially in the ground state, whereas the outer trajectory describes a molecule that is initially in the excited state. The $\chi^2$ integral in (h) is readjusted to average initial excited and ground state molecules according to Equation (10.15).

## Partial Excitation

In this section, I discuss an initial excitation of $N_{\mathrm{exc}} < N$ molecules at the example $N = 10$ and $N_{\mathrm{exc}} = 2$ in Figure 10.4. In panels (a) to (c) the entanglement entropies are shown. $S_{\mathrm{ph}}$ reaches vales $S_{\mathrm{ph}} \sim 1$, much smaller than in the full excitation scenario, and oscillates quickly. The vibrational entanglement is significantly enhanced compared to the full excitation scenario, and is largest for large $\lambda\nu$. $S_{\mathrm{exc}}$ is larger than both $S_{\mathrm{vib}}$ and $S_{\mathrm{ph}}$ and shows features of both.

The oscillations of $S_{\mathrm{ph/exc}}$ and the scaling with $\lambda\nu$ is analogous to the full excitation scenario. However, the much smaller photonic Hilbert space $\dim(\mathcal{H}_{\mathrm{ph}}) = N_{\mathrm{exc}}+1$ leads to an overall reduction in entanglement entropy, which is limited by $S_{\mathrm{ph}} \leq \log_2[\dim(\mathcal{H}_{\mathrm{ph}})]$. Analogously, the increase of $S_{\mathrm{vib}}$ is attributed to the breaking of permutation symmetry, which results in a larger part of the vibrational Hilbert space being accessible.

Figure 10.4(d) gives a parameter scan of the time averaged $S_{\mathrm{vib}}$. As in the fully excited case, the entanglement is small for a small interaction $\lambda\nu$, but increases with the interaction strength. Interestingly, there is an additional peak at $\nu = g_c/10$, for which the entanglement is comparatively large. This peak may be due to a resonance between electronic and vibrational transitions (e.g. between electronic states from a different $J$ manifold), and will be interesting to investigate in more detail.

Panels (e) to (g) show the mean phase space dynamics for the excited and ground state molecules with product state and MPS simulation. Due to permutation symmetry among excited and ground state molecules, only one representative is shown in either case. For all parameters, the phase space dynamics is predominantly located on the initially excited molecules. However, with increasing $\lambda\nu$, the relative dynamics of the

initial ground state molecules increases slightly.

The asymmetry between the vibrational dynamics of initially excited and ground state molecules is due to negligible excitation transfer from initially excited to initial ground state molecules discussed in more detail below. Large vibrational coupling reduces this trapping, leading to a larger relative oscillation (see also Chapter 9).

Importantly, with increasing $\lambda\nu$, also the product state approximation becomes less accurate. While for small and intermediate coupling [panels (e) and (f)] the product states only slightly overestimate the dynamics of the initially excited and slightly underestimate the dynamics of the initial ground states, for large $\lambda\nu$ [panel (g)], the product state significantly deviates from the exact results. This effect is systematically analyzed in panel (h).

In order to include both initially excited and ground state, $\chi^2$ is re-defined as the average of the $\chi^2$ for the initially excited and ground states

$$\begin{aligned}\chi^2 = \nu/(2\pi) \times \int dt (N_{\mathrm{exc}}/N)[(x_{\mathrm{PS}}^{\mathrm{exc}} - x_{\mathrm{MPS}}^{\mathrm{exc}})^2 + (p_{\mathrm{PS}}^{\mathrm{exc}} - p_{\mathrm{MPS}}^{\mathrm{exc}})^2] \\ + (N_{\mathrm{gs}}/N)[(x_{\mathrm{PS}}^{\mathrm{gs}} - x_{\mathrm{MPS}}^{\mathrm{gs}})^2 + (p_{\mathrm{PS}}^{\mathrm{gs}} - p_{\mathrm{MPS}}^{\mathrm{gs}})^2]\,, \end{aligned} \tag{10.15}$$

where $x_{\mathrm{(M)PS}}^{\mathrm{exc/gs}}$ is the expectation value of the position of an initially excited/ground state molecule according to (M)PS simulation, respectively, and $p_{\mathrm{(M)PS}}^{\mathrm{exc/gs}}$ is the corresponding momentum. For all parameters, the matching is drastically worse than in the fully excited state, and especially for large $\lambda\nu$ the two curves are expected to differ significantly.

We attribute this discrepancy to the large vibrational entropy for large $\lambda\nu$. Furthermore, the excitation transfer between initially excited and ground states may be mediated by the vibrations especially for large $\lambda\nu$, an effect discussed in more detail in the next chapter. This contribution to the excitation transfer is completely neglected in the product state picture, leading to large errors for large $\lambda\nu$.

## 10.4. Validity of Product States

In this section, I discuss and compare different methods to quantify the errors made by the product state approximation. As discussed in the previous section, the error of the product state assumption is directly given by the entanglement between the vibrational and electro-photonic degrees of freedom, which can be quantified by $S_{\mathrm{vib}}$. Furthermore $\chi^2$ was introduced as the error of the mean dynamics.

Another method is based on the fact that in the product state approximation, only the symmetric vibrational modes are populated. As a consequence, the population of the anti-symmetric modes can be seen as a measure of the deviations of the vibrational state from a product state. More fundamentally, it can be shown that the dominant deviations from the product state equations are due to scattering into these modes, making them a good witness of general deviations from the product state approximation. The anti-

symmetric vibrational modes are computed as

$$\sum_{k=1}^{N_{\mathrm{exc}}-1} \hat{\tilde{b}}_k^{(e)\dagger} \hat{\tilde{b}}_k^{(e)} + \sum_{k=1}^{N-N_{\mathrm{exc}}-1} \hat{\tilde{b}}_k^{(g)\dagger} \hat{\tilde{b}}_k^{(g)} \,, \tag{10.16}$$

with

$$\hat{\tilde{b}}_k^{(e)} = \frac{1}{\sqrt{N_{\mathrm{exc}}}} \sum_{n=1}^{N_{\mathrm{exc}}} \exp(\mathrm{i}kn/N_{\mathrm{exc}}) \hat{b}_n \,, \tag{10.17}$$

$$\hat{\tilde{b}}_k^{(g)} = \frac{1}{\sqrt{N-N_{\mathrm{exc}}}} \sum_{n=N_{\mathrm{exc}}+1}^{N} \exp[\mathrm{i}kn/(N-N_{\mathrm{exc}})] \hat{b}_n \,. \tag{10.18}$$

The three quantities mentioned above ($\chi^2$, $S_{\mathrm{vib}}$, anti-symmetric vibrations) can only be computed if the exact results are known. In order to estimate the error of the product state approximation in regimes where exact simulations are not viable, we compute the relative magnitude of the deviation of the product state from the exact dynamics in Appendix 10.C. Importantly, quantity can be computed knowing the product state result, only. We find

$$\frac{\left\| [\partial_t |\psi\rangle]^{(\mathrm{ps})} - \partial_t |\psi\rangle \right\|^2}{\left\| [\partial_t |\psi\rangle]^{(\mathrm{ps})} \right\|^2} = \frac{\left\langle \Delta \hat{H}^2 \right\rangle}{\left\langle \hat{H}^2 \right\rangle} \,, \tag{10.19}$$

where $[\partial_t |\psi\rangle]^{(\mathrm{ps})}$ is the evolution described by the product state ansatz, $\Delta \hat{H} = \hat{H} - \hat{H}^{(\mathrm{ps})}$, and $\hat{H}^{(\mathrm{ps})}$ is the Hamiltonian describing the product state evolution. This formula is evaluated according to Equations (10.41) and (10.42) in Appendix 10.C.

Figure 10.5(a) and (b) compare the different error measures for varying $N$ for $N_{\mathrm{exc}} = N/2$ (a) and $N_{\mathrm{exc}} = 2$ (b). Since the displayed quantities are fundamentally different quantities, only the scaling with $N$ can be meaningfully compared, but not the absolute values. For constant excitation fraction, all four measures rise strongly for small $N$ and then flatten (on a log-scale) for $N \gtrsim 10$. In particular $\chi^2$ and $\langle \Delta \hat{H}^2 \rangle / \langle \hat{H}^2 \rangle$ become approximately constant, whereas $S_{\mathrm{vib}}$ the asymmetric vibrational population rise more slowly. This can be understood since the entropy and the number of vibrational quanta are measures for the total error, whereas the relative deviation and the averaged error of the means measure the error on a the individual molecule level.

This relative scaling changes drastically if $N_{\mathrm{exc}}$ is kept constant [panel (b)]. In this case, $S_{\mathrm{vib}}$, the asymmetric mode population, and $\chi^2$ decrease with increasing $N$, with $\chi^2$ decreasing the fastest of the three quantities. Interestingly, in contrast to the other measures, $\langle \Delta \hat{H}^2 \rangle / \langle \hat{H}^2 \rangle$ remains constant.

Figure 10.5(c) now extrapolates the error estimate $\langle \Delta \hat{H}^2 \rangle / \langle \hat{H}^2 \rangle$ to large system sizes. For these sizes, direct comparison to exact simulations is not possible since only product state results are available. In contrast to the results for small systems, For large systems the error estimate decreases also for this measure, with the largest errors for intermediate size systems at intermediate excitation fractions. As a result, the product state simulations can be expected to be reliable for large systems.

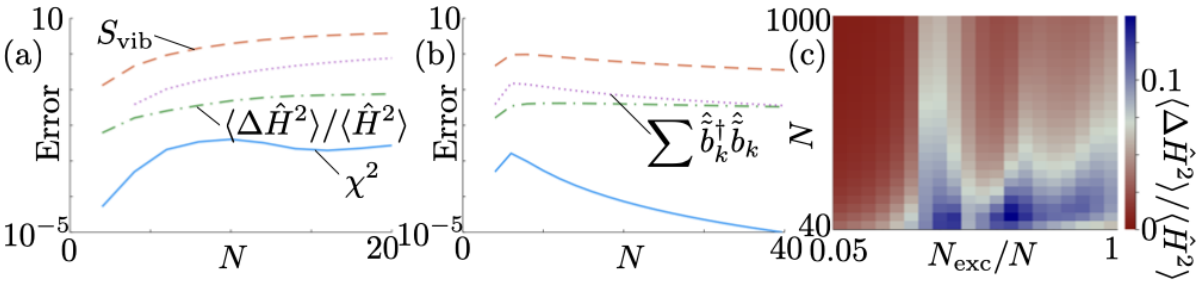


Figure 10.5. – Dependence of errors on the system size. (a/b) Errors of the product state simulation time-averaged over one oscillation period quantified by per molecule deviation $\chi^2$ (blue solid), vibrational entanglement entropy $S_{\mathrm{vib}}$ (orange dashed), the population of the asymmetric vibrational modes (purple dotted), and the relative error of each time step (green dash-dotted). Panel (a) shows the results for $N_{\mathrm{exc}} = N/2$, panel (b) shows the results for $N_{\mathrm{exc}} = 2$. The $y$-axis is logarithmic. (c) Averaged relative error of each time step over one oscillation period computed for different molecule numbers $N$ and excitation fractions $N_{\mathrm{exc}}/N$. We choose parameters $\lambda = 0.4$, $\nu = 0.3 g_c$.

## 10.5. Large Systems and Size Scaling

Figure 10.6 shows the scaling of the time-averaged mean excitation number and displacement of the initially excited and ground state molecules as a function of $N$ and $N_{\mathrm{exc}}/N$. In general, the displacement is found to be almost exactly proportional to the excitation fraction, as expected from the Holstein coupling $\sim \hat{\sigma}_n^+ \hat{\sigma}_n^- \hat{x}_n$, considering e.g. a mean-field picture. For small excitation fractions $N_{\mathrm{exc}}/N \lesssim 0.3$, the excitation remains well localized on the initially excited molecules, and only the initially excited molecules oscillate significantly. For $N_{\mathrm{exc}}/N \sim 1/2$, around half the excitation is transferred to the initial ground state molecules, and both have a similar displacement. Increasing $N_{\mathrm{exc}}$ further, a larger fraction of excitations remains on the initially excited molecules, leading to a smaller fraction on the initial ground state molecules.

For small $N_{\mathrm{exc}}$, a large fraction of the excitation is trapped in dark states $|d\rangle$. These are states in the bottom of the Dicke ladder that cannot interact with the cavity, i.e. $|d\rangle \sim |J, M = -J\rangle$ and $\hat{S}^- |d\rangle = 0$ (see Chapter 3 for details). These states do not undergo any dynamics, and, as a consequence, the excitation remains trapped in the initially excited states. For $N_{\mathrm{exc}}/N = 1/2$, in contrast, only a small fraction of the excited state population is in such a state. Instead, the symmetry between initially excited and ground states leads to a fast exchange of excitation with no preference for either site, and thus an approximately equal distribution of excitation. Increasing $N_{\mathrm{exc}}$ beyond that breaks the symmetry between initially excited and ground states, and thus restores preference for the excitation to remain where they were initially. However, the excitation is not trapped, but instead partially transferred to the initially ground state molecules.

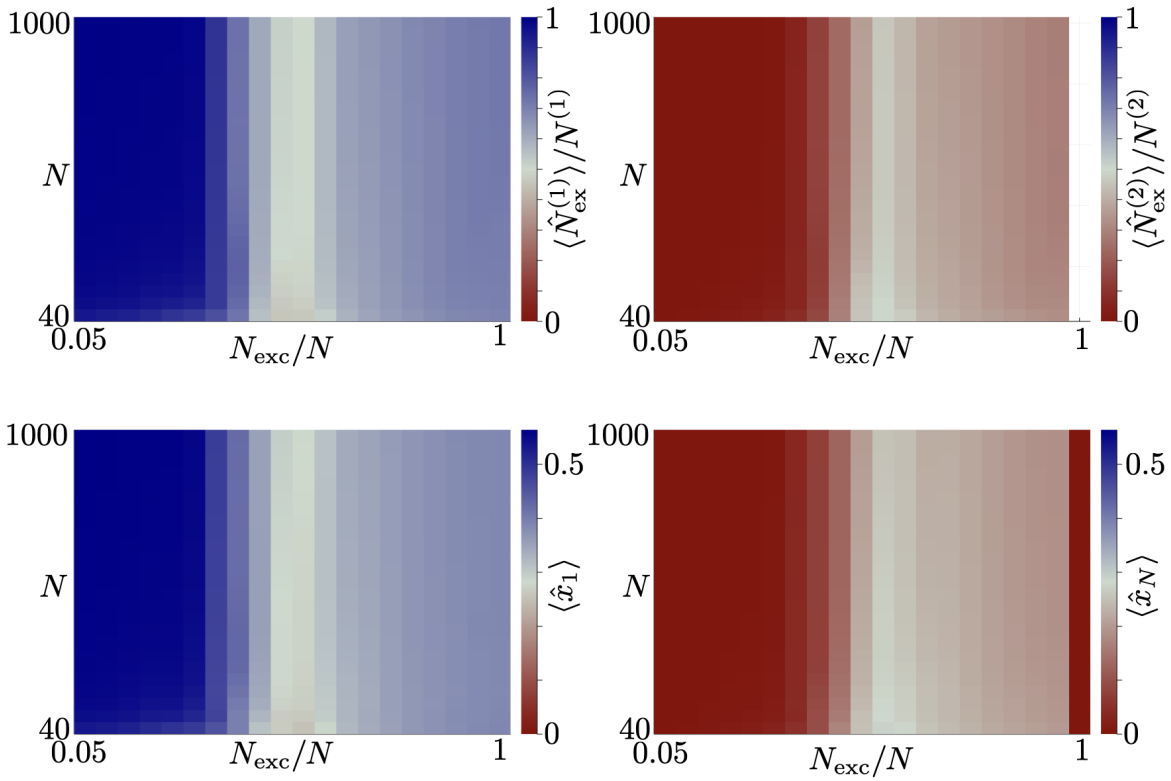


Figure 10.6. – Scaling of the displacement and excitation fractions with molecule number and initial excitation fraction. $g_c = 1$, $\lambda = 0.4$, $\nu = 0.3$. $\hat{N}_{\mathrm{exc}}^{(1)} = \sum_{n=1}^{N_{\mathrm{exc}}} \hat{\sigma}_n^+ \hat{\sigma}_n^-$. $N^{(1)} = N_{\mathrm{exc}}$, $N^{(2)} = N - N_{\mathrm{exc}}$ Product state simulations.

## 10.6. Conclusion

In this chapter, the short-time dynamics in the Holstein-Tavis-Cummings model was analyzed beyond the single excitation limit. For small vibronic coupling $\lambda\nu$, the entanglement between vibrational and electro-photonic degrees of freedom remains small, and the states can be well approximated by product states. If all molecules are initially excited, even for larger $\lambda\nu$ product states are sufficient to approximate the dynamics of simple expectation values. For $N_{\text{exc}}/N < 1$, the vibrational entanglement is significantly enhanced, and the accuracy of the product state approximation decreases. This has been attributed to a breaking of permutation symmetry. Within the product state approximation and for large molecule numbers, vibrational dynamics is most efficiently transferred from the initially excited to ground state molecules for $N_{\text{exc}}/N \sim 1/2$. This effect is linked to the excitation transfer, which is largest in this regime For smaller excitation fractions, the transfer is almost negligible, while for larger $N_{\text{exc}}$ it remains significant but still supressed.

On the computational level, I have developed a method to simulate large numbers of molecules within the product state approximation based on permutation symmetry. I have furthermore shown that in the extreme regime $g_c \gg \nu, \lambda\nu$, the dynamics can be approximated by averaging the quick oscillations in a rotating polariton approximation.

More generally, I have shown that the permutation symmetry plays a crucial role in the dynamics. Breaking the permutation symmetry, e.g. by introducing an asymmetry between initially excited and ground states, can significantly enhance excitation transfer between molecules and vibrational entanglement. Similar results for excitation transfer in the presence of energetically disordered spins coupled to a cavity motivated us to look at the Holstein-Tavis-Cummings model with disorder, which is the topic of the previous Chapter 9.

For the future it will be interesting to investigate in which experimental setups such an excitation dependent transfer of vibrational dynamics and vibrational entanglement may be observed. In vibrational strong coupling setups large excitation fractions have been experimentally observed [9], however, these setups are not generally described by the HTC model, which would need to be adapted. Alternatively, organic molecules electronically coupled to cavities may offer a more natural platform [4]. As a third option, cold and ultracold molecules offer a toolbox with good experimental control and much more precise measurements [27–31].

## 10.A. Cross Terms in the Rotating Polariton Approximation

In order to formally derive the approximation, we write down the von Neumann equation in the interaction picture

$$\partial_t \hat{\rho}_{\text{int}} = -\mathrm{i}\left[\hat{H}_{\text{int}}, \hat{\rho}_{\text{int}}\right] \tag{10.20}$$

with $\hat{\rho}_{\text{int}} = |\psi_{\text{int}}\rangle\langle\psi_{\text{int}}|$. We define an intermediate time scale $1/(E_\psi - E_\phi) \ll \Delta t \ll 1/\nu$, on which we resolve the system dynamics. The integrated equation then reads

$$\frac{\hat{\rho}_{\text{int}}(t+\Delta t) - \hat{\rho}_{\text{int}}(t)}{\Delta t} = \frac{-\mathrm{i}}{\Delta t}\int_t^{t+\Delta t} \mathrm{d}t' \Big[\hat{H}_{\text{int}}(t'), \hat{\rho}_{\text{int}}(t')\Big] \tag{10.21}$$

$$= \frac{-\mathrm{i}}{\Delta t}\int_t^{t+\Delta t} \mathrm{d}t' [\hat{H}_{\text{int}}(t'), \hat{\rho}_{\text{int}}(t) + \mathcal{O}(\nu\Delta t)] \tag{10.22}$$

$$\begin{aligned} &= \frac{-\mathrm{i}}{\Delta t}\int_t^{t+\Delta t} \mathrm{d}t' [\hat{H}_{\text{int},0}, \hat{\rho}_{\text{int}}(t)] \\ &\quad + \frac{\mathrm{i}\lambda\nu}{\Delta t}\sum_{n,\phi\neq\psi}\int_t^{t+\Delta t} \mathrm{d}t' e^{-\mathrm{i}(E_\psi - E_\phi)t'} \\ &\quad\quad \times \Big[\Big(\hat{b}_n^\dagger + \hat{b}_n\Big)\langle\phi|\,\hat{\sigma}_n^+\sigma_n^-\,|\psi\rangle\,|\phi\rangle\langle\psi|\,, \hat{\rho}_{\text{int}}(t)\Big] \\ &\quad + \mathcal{O}(\nu^2\Delta t) \end{aligned} \tag{10.23}$$

$$= -\mathrm{i}\Big[\hat{H}_{\text{int}}^{(0)}, \hat{\rho}_{\text{int}}(t)\Big] + \mathcal{O}\left(\frac{\nu}{(E_\psi - E_\psi)\Delta t}\right) + \mathcal{O}(\nu^2\Delta t) \tag{10.24}$$

with

$$\hat{H}_{\text{int}}^{(0)} = \nu\sum_{n=1}^{N}\hat{b}_n^\dagger\hat{b}_n - \lambda\nu\sum_{n,\psi}\Big(\hat{b}_n^\dagger + \hat{b}_n\Big)\langle\psi|\,\hat{\sigma}_n^+\sigma_n^-\,|\psi\rangle\,|\psi\rangle\langle\psi| \tag{10.25}$$

This is Eq. (10.13) of the main text. Because the dynamics introduced by the Hamiltonaian Eq. (10.25) is on the order of $\nu$ (as long as $\lambda \lesssim 1$), the oscillating terms in Eq. (10.12) can be neglected if a time scale $\Delta t$ can be defined such that $\nu\Delta t \ll 1$ and $(E_\psi - E_\phi)\Delta t \gg 1$. Importantly, this condition is not fulfilled in general, however, in the other cases the overlap $\langle\phi|\,\hat{\sigma}_n^+\sigma_n^-\,|\psi\rangle$ is small so that also these terms contribute negligibly.

## 10.B. Double Dicke States

We start by constructing a basis for the electro-photonic states that accounts for the permutation symmetry within the subsets $\{1,\ldots,N_{\text{exc}}\}$ and $\{N_{\text{exc}}+1,\ldots,N\}$ that accounts for the permutation symmetry based on separate Dicke states in each subspace (Chapter 3). First, note that a product of two Dicke states $|I_{\text{exc}}\rangle$ and $|I_{\text{gs}}\rangle$ with $|I_{\text{ex}}\rangle = |J = N_{\text{exc}}/2, M = -N_{\text{exc}}/2 + I_{\text{exc}}\rangle$ a Dicke state for molecules 1,...,$N_{\text{exc}}$ and $|I_{\text{gs}}\rangle$ analogously a Dicke state for molecules $N_{\text{exc}}+1$,...,$N$ fulfills the required permutation symmetry. Furthermore, the set of all product states $|I_{\text{ex}}\rangle\,|I_{\text{gs}}\rangle$ with $0 \leq I_{\text{ex}} \leq N_{\text{exc}}$ and $0 \leq I_{\text{gs}} \leq N - N_{\text{exc}}$ is a complete basis of all electronic states with the required permutation symmetry. The states are given by

$$\begin{aligned} |I_{\text{ex}}, I_{\text{gs}}\rangle = &|J = N_{\text{exc}}/2, M = -N_{\text{exc}}/2 + I_{\text{ex}}\rangle \\ &\otimes |J = (N - N_{\text{exc}})/2, M = -(N - N_{\text{exc}})/2 + I_{\text{gs}}\rangle\ , \end{aligned} \tag{10.26}$$

which are product states between the initially excited and ground states.

As the excitation number $\hat{a}^\dagger\hat{a} + \sum_n \hat{\sigma}_n^+\hat{\sigma}_n^-$ is a conserved quantity, we have the additional condition $I_{\text{ex}}+I_{\text{gs}} \leq N_{\text{exc}}$, and we can infer the photon number $\langle I_{\text{ex}}, I_{\text{gs}}| \hat{a}^\dagger\hat{a} |I_{\text{ex}}, I_{\text{gs}}\rangle = N_{\text{exc}} - (I_{\text{ex}} + I_{\text{gs}})$. Thus, a basis of the electro-photonic states is given by $\{|I_{\text{ex}}, I_{\text{gs}}\rangle : (I_{\text{ex}} + I_{\text{gs}} \leq N_{\text{exc}}) \wedge (0 \leq I_{\text{gs}} \leq N - N_{\text{exc}})\}$. The corresponding Hilbert space has dimension $(N_{\text{exc}} + 1)(N_{\text{exc}} + 2)/2$ for $N_{\text{exc}} \leq N/2$ and $(N - N_{\text{exc}} + 1)(3N_{\text{exc}} - N + 2)/2$ for $N_{\text{exc}} \geq N/2$. For numerical efficiency, we cast each state into a single vector of the Hilbert space dimension.

Next, we compute the action of the relevant operators on $|I_{\text{ex}}, I_{\text{gs}}\rangle$. We already saw

$$\hat{a}^\dagger\hat{a} \,|I_{\text{ex}}, I_{\text{gs}}\rangle = (N_{\text{exc}} - I_{\text{ex}} - I_{\text{gs}}) \,|I_{\text{ex}}, I_{\text{gs}}\rangle \ . \tag{10.27}$$

Analogously, we find

$$\sum_n \hat{\sigma}_n^+\hat{\sigma}_n^- \,|I_{\text{ex}}, I_{\text{gs}}\rangle = (I_{\text{ex}} + I_{\text{gs}}) \,|I_{\text{ex}}, I_{\text{gs}}\rangle \ . \tag{10.28}$$

In order to compute the action of $\hat{S}^-\hat{a}^\dagger$ and $\hat{S}^+\hat{a}$, we note $\hat{S}^- = \sum_{n=1}^{N} \hat{\sigma}_n^- = \sum_{n=1}^{N_{\text{exc}}} \hat{\sigma}_n^- + \sum_{n=N_{\text{exc}}+1}^{N} \hat{\sigma}_n^- \equiv \hat{S}_{\text{ex}}^- + \hat{S}_{\text{gs}}^-$. This makes it easy to see that

$$\begin{aligned}
\hat{a}^\dagger\hat{S}^- \,|I_{\text{ex}}, I_{\text{gs}}\rangle &= \sqrt{(N_{\text{exc}} - I_{\text{ex}} + 1)I_{\text{ex}}(N_{\text{exc}} - I_{\text{ex}} - I_{\text{gs}} + 1)} \,|I_{\text{ex}} - 1, I_{\text{gs}}\rangle \\
&\quad + \sqrt{(N - N_{\text{exc}} - I_{\text{gs}} + 1)I_{\text{gs}}(N_{\text{exc}} - I_{\text{ex}} - I_{\text{gs}} + 1)} \,|I_{\text{ex}}, I_{\text{gs}} - 1\rangle \qquad (10.29) \\
\hat{a}\hat{S}^+ \,|I_{\text{ex}}, I_{\text{gs}}\rangle &= \sqrt{(N_{\text{exc}} - I_{\text{ex}})(I_{\text{ex}} + 1)(N_{\text{exc}} - I_{\text{ex}} - I_{\text{gs}})} \,|I_{\text{ex}} + 1, I_{\text{gs}}\rangle \\
&\quad + \sqrt{(N - N_{\text{exc}} - I_{\text{gs}})(I_{\text{gs}} + 1)(N_{\text{exc}} - I_{\text{ex}} - I_{\text{gs}})} \,|I_{\text{ex}}, I_{\text{gs}} + 1\rangle \qquad (10.30)
\end{aligned}$$

Note that with these results recover the correct formulas for $N_{\text{exc}} = N$.

Considering the vibrational states, the two symmetric vibrational modes, defined separately for molecules 1,...,$N_{\text{exc}}$ and $N_{\text{exc}} + 1, \ldots, N$, give all symmetric states. As in the fully excited case, the initial state of both vibrational modes is a coherent state (the vacuum state), and the Hamiltonian is a displaced harmonic oscillator. Thus, all states during the evolution are coherent states, and we can describe the vibrations by two complex numbers (two positions and momenta). Eq. (10.8) is then separately valid for the initially excited and the initial ground state molecules.

## 10.C. Error of the Product State Approximation

In this section, we derive an estimate for the error made with the product state ansatz. In particular, we compute

$$\frac{\left\| [\partial_t |\psi\rangle]^{(\text{ps})} - \partial_t |\psi\rangle \right\|^2}{\left\| [\partial_t |\psi\rangle]^{(\text{ps})} \right\|^2} = \frac{\left\langle \Delta\hat{H}^2 \right\rangle}{\left\langle \hat{H}^2 \right\rangle}, \tag{10.31}$$

where $[\partial_t |\psi\rangle]^{(\mathrm{ps})}$ is the evolution described by the product state ansatz, $\Delta\hat{H} = \hat{H} - \hat{H}^{(\mathrm{ps})}$, and $\hat{H}^{(\mathrm{ps})}$ is the Hamiltonian describing the product state evolution. Note that $\Delta\hat{H}$ is time dependent. Note also that this is only the instantaneous error. I particular, in order to compute the error of the wavefunction at time $t$, also correlations $\left\langle \Delta\hat{H}(t)\Delta\hat{H}(t') \right\rangle$ will be important. We choose the offset of $\hat{H}^{(\mathrm{ps})}$ such that $\langle \Delta\hat{H} \rangle = 0$, in particular

$$\begin{aligned}
\hat{H}^{(\mathrm{ps})} &= \hat{H}_{\mathrm{TC}} + \hat{H}_{\mathrm{vib}} - \lambda\nu \sum_n \left\langle \hat{b}_n^\dagger + \hat{b}_n \right\rangle \hat{\sigma}_n^+ \hat{\sigma}_n^- \\
&\quad - \lambda\nu \sum_n \left( \hat{b}_n^\dagger + \hat{b}_n \right) \langle \hat{\sigma}_n^+ \hat{\sigma}_n^- \rangle + \lambda\nu \sum_n \left\langle \hat{b}_n^\dagger + \hat{b}_n \right\rangle \langle \hat{\sigma}_n^+ \hat{\sigma}_n^- \rangle \ , \qquad (10.32) \\
\Delta\hat{H} &= -\lambda\nu \sum_n \Big[ \hat{\sigma}_n^+ \hat{\sigma}_n^- \left( \hat{b}_n^\dagger + \hat{b}_n \right) - \langle \hat{\sigma}_n^+ \hat{\sigma}_n^- \rangle \left( \hat{b}_n^\dagger + \hat{b}_n \right) \\
&\quad - \hat{\sigma}_n^+ \hat{\sigma}_n^- \left\langle \hat{b}_n^\dagger + \hat{b}_n \right\rangle + \langle \hat{\sigma}_n^+ \hat{\sigma}_n^- \rangle \left\langle \hat{b}_n^\dagger + \hat{b}_n \right\rangle \Big] \ . \qquad (10.33)
\end{aligned}$$

The square is then given by

$$\begin{aligned}
\Delta\hat{H}^2 = \lambda^2\nu^2 \sum_{n,n'} \Big[ & \hat{\sigma}_n^+ \hat{\sigma}_n^- \hat{\sigma}_{n'}^+ \hat{\sigma}_{n'}^- \left( \hat{b}_n^\dagger + \hat{b}_n \right) \left( \hat{b}_{n'}^\dagger + \hat{b}_{n'} \right) - \langle \hat{\sigma}_n^+ \hat{\sigma}_n^- \rangle \hat{\sigma}_{n'}^+ \hat{\sigma}_{n'}^- \left( \hat{b}_n^\dagger + \hat{b}_n \right) \left( \hat{b}_{n'}^\dagger + \hat{b}_{n'} \right) \\
& - \hat{\sigma}_n^+ \hat{\sigma}_n^- \langle \hat{\sigma}_{n'}^+ \hat{\sigma}_{n'}^- \rangle \left( \hat{b}_n^\dagger + \hat{b}_n \right) \left( \hat{b}_{n'}^\dagger + \hat{b}_{n'} \right) - \hat{\sigma}_n^+ \hat{\sigma}_n^- \hat{\sigma}_{n'}^+ \hat{\sigma}_{n'}^- \left\langle \hat{b}_n^\dagger + \hat{b}_n \right\rangle \left( \hat{b}_{n'}^\dagger + \hat{b}_{n'} \right) \\
& - \hat{\sigma}_n^+ \hat{\sigma}_n^- \hat{\sigma}_{n'}^+ \hat{\sigma}_{n'}^- \left( \hat{b}_n^\dagger + \hat{b}_n \right) \left\langle \hat{b}_{n'}^\dagger + \hat{b}_{n'} \right\rangle + \langle \hat{\sigma}_n^+ \hat{\sigma}_n^- \rangle \langle \hat{\sigma}_{n'}^+ \hat{\sigma}_{n'}^- \rangle \left( \hat{b}_n^\dagger + \hat{b}_n \right) \left( \hat{b}_{n'}^\dagger + \hat{b}_{n'} \right) \\
& + \langle \hat{\sigma}_n^+ \hat{\sigma}_n^- \rangle \hat{\sigma}_{n'}^+ \hat{\sigma}_{n'}^- \left\langle \hat{b}_n^\dagger + \hat{b}_n \right\rangle \left( \hat{b}_{n'}^\dagger + \hat{b}_{n'} \right) + \langle \hat{\sigma}_n^+ \hat{\sigma}_n^- \rangle \hat{\sigma}_{n'}^+ \hat{\sigma}_{n'}^- \left( \hat{b}_n^\dagger + \hat{b}_n \right) \left\langle \hat{b}_{n'}^\dagger + \hat{b}_{n'} \right\rangle \\
& + \hat{\sigma}_n^+ \hat{\sigma}_n^- \langle \hat{\sigma}_{n'}^+ \hat{\sigma}_{n'}^- \rangle \left\langle \hat{b}_n^\dagger + \hat{b}_n \right\rangle \left( \hat{b}_{n'}^\dagger + \hat{b}_{n'} \right) + \hat{\sigma}_n^+ \hat{\sigma}_n^- \langle \hat{\sigma}_{n'}^+ \hat{\sigma}_{n'}^- \rangle \left( \hat{b}_n^\dagger + \hat{b}_n \right) \left\langle \hat{b}_{n'}^\dagger + \hat{b}_{n'} \right\rangle \\
& + \hat{\sigma}_n^+ \hat{\sigma}_n^- \hat{\sigma}_{n'}^+ \hat{\sigma}_{n'}^- \left\langle \hat{b}_n^\dagger + \hat{b}_n \right\rangle \left\langle \hat{b}_{n'}^\dagger + \hat{b}_{n'} \right\rangle - \langle \hat{\sigma}_n^+ \hat{\sigma}_n^- \rangle \langle \hat{\sigma}_{n'}^+ \hat{\sigma}_{n'}^- \rangle \left\langle \hat{b}_n^\dagger + \hat{b}_n \right\rangle \left( \hat{b}_{n'}^\dagger + \hat{b}_{n'} \right) \\
& - \langle \hat{\sigma}_n^+ \hat{\sigma}_n^- \rangle \langle \hat{\sigma}_{n'}^+ \hat{\sigma}_{n'}^- \rangle \left( \hat{b}_n^\dagger + \hat{b}_n \right) \left\langle \hat{b}_{n'}^\dagger + \hat{b}_{n'} \right\rangle - \langle \hat{\sigma}_n^+ \hat{\sigma}_n^- \rangle \hat{\sigma}_{n'}^+ \hat{\sigma}_{n'}^- \left\langle \hat{b}_n^\dagger + \hat{b}_n \right\rangle \left\langle \hat{b}_{n'}^\dagger + \hat{b}_{n'} \right\rangle \\
& - \hat{\sigma}_n^+ \hat{\sigma}_n^- \langle \hat{\sigma}_{n'}^+ \hat{\sigma}_{n'}^- \rangle \left\langle \hat{b}_n^\dagger + \hat{b}_n \right\rangle \left\langle \hat{b}_{n'}^\dagger + \hat{b}_{n'} \right\rangle + \langle \hat{\sigma}_n^+ \hat{\sigma}_n^- \rangle \langle \hat{\sigma}_{n'}^+ \hat{\sigma}_{n'}^- \rangle \left\langle \hat{b}_n^\dagger + \hat{b}_n \right\rangle \left\langle \hat{b}_{n'}^\dagger + \hat{b}_{n'} \right\rangle \Big] \ . \qquad (10.34)
\end{aligned}$$

In the evolution described by the product state Hamiltonian $\hat{H}^{(\mathrm{ps})}$, we stay in a product state between spin-cavity and vibrations, and only two vibrational modes are in a non-vacuum state: the zero momentum vibrations for the initially excited and initial ground state molecules (see Appendix 10.B). These two modes are not entangled and each mode is in a coherent state. With this, it is straightforward to proof the following identities

for expectation values:

$$\left\langle \hat{X}^{(1)}\hat{X}^{(2)}\right\rangle = \left\langle \hat{X}^{(1)}\right\rangle \left\langle \hat{X}^{(2)}\right\rangle , \tag{10.35}$$

$$\left\langle \left[\hat{X}^{(i)}\right]^2\right\rangle = \left\langle \hat{X}^{(i)}\right\rangle^2 + \frac{N^{(i)}}{2} , \tag{10.36}$$

$$\sum_n \left\langle \left(\hat{b}_n^\dagger + \hat{b}_n\right)\hat{\sigma}_n^+\hat{\sigma}_n^-\right\rangle = \sum_n \sqrt{2}\left\langle \hat{x}_n\right\rangle \left\langle \hat{\sigma}_n^+\hat{\sigma}_n^-\right\rangle , \tag{10.37}$$

$$\begin{aligned}\sum_{n,n'} \left\langle \hat{\sigma}_n^+\hat{\sigma}_n^-\hat{\sigma}_{n'}^+\hat{\sigma}_{n'}^-\left(\hat{b}_n^\dagger + \hat{b}_n\right)\right\rangle \left\langle \hat{b}_{n'}^\dagger + \hat{b}_{n'}\right\rangle &= \sum_{n,n'} \left\langle \hat{\sigma}_n^+\hat{\sigma}_n^-\hat{\sigma}_{n'}^+\hat{\sigma}_{n'}^-\right\rangle \left\langle \hat{b}_n^\dagger + \hat{b}_n\right\rangle \left\langle \hat{b}_{n'}^\dagger + \hat{b}_{n'}\right\rangle \\ &= \frac{2\left\langle \hat{X}^{(1)}\right\rangle^2 \left\langle \left[\hat{N}_{\mathrm{exc}}^{(1)}\right]^2\right\rangle}{\left[N^{(1)}\right]^2} + \frac{2\left\langle \hat{X}^{(2)}\right\rangle^2 \left\langle \left[\hat{N}_{\mathrm{exc}}^{(2)}\right]^2\right\rangle}{\left[N^{(2)}\right]^2} \\ &\quad + \frac{4\left\langle \hat{X}^{(1)}\right\rangle \left\langle \hat{X}^{(2)}\right\rangle \left\langle \hat{N}_{\mathrm{exc}}^{(1)}\hat{N}_{\mathrm{exc}}^{(2)}\right\rangle}{N^{(1)}N^{(2)}} ,\end{aligned} \tag{10.38}$$

$$\begin{aligned}\sum_{n,n'} \left\langle \hat{\sigma}_{n'}^+\hat{\sigma}_{n'}^-\right\rangle \left\langle \hat{\sigma}_n^+\hat{\sigma}_n^-\left(\hat{b}_n^\dagger + \hat{b}_n\right)\left(\hat{b}_{n'}^\dagger + \hat{b}_{n'}\right)\right\rangle &= \sum_{n,n'} \left\langle \hat{\sigma}_{n'}^+\hat{\sigma}_{n'}^-\right\rangle \left\langle \hat{\sigma}_n^+\hat{\sigma}_n^-\right\rangle \left\langle \left(\hat{b}_n^\dagger + \hat{b}_n\right)\left(\hat{b}_{n'}^\dagger + \hat{b}_{n'}\right)\right\rangle \\ &= \frac{2\left\langle \hat{N}_{\mathrm{exc}}^{(1)}\right\rangle^2 \left\langle \hat{X}^{(1)}\right\rangle^2}{\left[N^{(1)}\right]^2} + \frac{\left\langle \hat{N}_{\mathrm{exc}}^{(1)}\right\rangle^2}{N^{(1)}} + \frac{2\left\langle \hat{N}_{\mathrm{exc}}^{(2)}\right\rangle^2 \left\langle \hat{X}^{(2)}\right\rangle^2}{\left[N^{(2)}\right]^2} + \frac{\left\langle \hat{N}_{\mathrm{exc}}^{(2)}\right\rangle^2}{N^{(2)}} \\ &\quad + \frac{4\left\langle \hat{N}_{\mathrm{exc}}^{(1)}\right\rangle \left\langle \hat{N}_{\mathrm{exc}}^{(2)}\right\rangle \left\langle \hat{X}^{(1)}\right\rangle \left\langle \hat{X}^{(2)}\right\rangle}{N^{(1)}N^{(2)}} ,\end{aligned} \tag{10.39}$$

$$\begin{aligned}\sum_{n,n'} \left\langle \left(\hat{b}_n^\dagger + \hat{b}_n\right)\left(\hat{b}_{n'}^\dagger + \hat{b}_{n'}\right)\hat{\sigma}_n^+\hat{\sigma}_n^-\hat{\sigma}_{n'}^+\hat{\sigma}_{n'}^-\right\rangle &= \left\langle \hat{N}_{\mathrm{exc}}^{(1)}\right\rangle + \frac{2\left\langle \left[\hat{N}_{\mathrm{exc}}^{(1)}\right]^2\right\rangle \left\langle \hat{X}^{(1)}\right\rangle^2}{\left[N^{(1)}\right]^2} \\ &\quad + \left\langle \hat{N}_{\mathrm{exc}}^{(2)}\right\rangle + \frac{2\left\langle \left[\hat{N}_{\mathrm{exc}}^{(2)}\right]^2\right\rangle \left\langle \hat{X}^{(2)}\right\rangle^2}{\left[N^{(2)}\right]^2} + \frac{4\left\langle \hat{N}_{\mathrm{exc}}^{(1)}\hat{N}_{\mathrm{exc}}^{(2)}\right\rangle \left\langle \hat{X}^{(1)}\right\rangle \left\langle \hat{X}^{(2)}\right\rangle}{N^{(1)}N^{(2)}} ,\end{aligned} \tag{10.40}$$

where all the sums run from 1 to $N$, and the superscripts (1) and (2) indicate the initially excited and ground state subspace, respectively, in particular $N^{(1)} = N_{\mathrm{exc}}$ and $N^{(2)} = N - N_{\mathrm{exc}}$. It is then straightforward to calculate

$$\left\langle \Delta\hat{H}^2\right\rangle = \lambda^2\nu^2\left[\left\langle \hat{N}_{\mathrm{exc}}^{(1)}\right\rangle + \left\langle \hat{N}_{\mathrm{exc}}^{(2)}\right\rangle - \frac{\left\langle \hat{N}_{\mathrm{exc}}^{(1)}\right\rangle^2}{N_{\mathrm{exc}}} - \frac{\left\langle \hat{N}_{\mathrm{exc}}^{(2)}\right\rangle^2}{N - N_{\mathrm{exc}}}\right] . \tag{10.41}$$

This shows that $\left\langle \Delta\hat{H}^2\right\rangle$ scales linear in $N$.

We further compute

$$\begin{aligned}\hat{H}^2 = \sum_{n,n'} & g^2\big(\hat{a}\hat{\sigma}_n^+ + \hat{a}^\dagger\hat{\sigma}_n^-\big)\big(\hat{a}\hat{\sigma}_{n'}^+ + \hat{a}^\dagger\hat{\sigma}_{n'}^-\big) + 2g\nu\big(\hat{a}\hat{\sigma}_n^+ + \hat{a}^\dagger\hat{\sigma}_n^-\big)\hat{b}_{n'}^\dagger\hat{b}_{n'} \\ & - 2g\lambda\nu\big(\hat{a}\hat{\sigma}_n^+ + \hat{a}^\dagger\hat{\sigma}_n^-\big)\Big(\hat{b}_{n'} + \hat{b}_{n'}^\dagger\Big)\hat{\sigma}_{n'}^+\hat{\sigma}_{n'}^- + \nu^2\hat{b}_n^\dagger\hat{b}_n\hat{b}_{n'}^\dagger\hat{b}_{n'} \\ & - 2\lambda\nu^2\hat{b}_n^\dagger\hat{b}_n\Big(\hat{b}_{n'} + \hat{b}_{n'}^\dagger\Big)\hat{\sigma}_{n'}^+\hat{\sigma}_{n'}^- + \lambda^2\nu^2\Big(\hat{b}_n + \hat{b}_n^\dagger\Big)\hat{\sigma}_n^+\hat{\sigma}_n^-\Big(\hat{b}_{n'} + \hat{b}_{n'}^\dagger\Big)\hat{\sigma}_{n'}^+\hat{\sigma}_{n'}^- .\end{aligned} \tag{10.42}$$

All terms can straightforwardly be brought into a form that can be evaluated directly from the product state wave function. In order to avoid bias through the arbitrary choice of energy offset, we choose the offset such that $\langle\hat{H}\rangle = 0$, i.e. we compute $\langle\hat{H}^2\rangle - \langle\hat{H}\rangle^2$

# Bibliography


[1] James A. Hutchison, Tal Schwartz, Cyriaque Genet, Eloïse Devaux, and Thomas W. Ebbesen. Modifying Chemical Landscapes by Coupling to Vacuum Fields. *Angew. Chem. Int. Ed.*, 51(7):1592–1596, February 2012.

[2] Anoop Thomas, Jino George, Atef Shalabney, Marian Dryzhakov, Sreejith J. Varma, Joseph Moran, Thibault Chervy, Xiaolan Zhong, Eloïse Devaux, Cyriaque Genet, James A. Hutchison, and Thomas W. Ebbesen. Ground-State Chemical Reactivity under Vibrational Coupling to the Vacuum Electromagnetic Field. *Angew. Chem. Int. Ed.*, 55(38):11462–11466, 2016.

[3] A. Thomas, L. Lethuillier-Karl, K. Nagarajan, R. M. A. Vergauwe, J. George, T. Chervy, A. Shalabney, E. Devaux, C. Genet, J. Moran, and T. W. Ebbesen. Tilting a ground-state reactivity landscape by vibrational strong coupling. *Science*, 363(6427):615–619, February 2019.

[4] K. S. Daskalakis, S. A. Maier, R. Murray, and S. Kéna-Cohen. Nonlinear interactions in an organic polariton condensate. *Nature Mater*, 13(3):271–278, March 2014.

[5] Hashem Zoubi and G. C. La Rocca. Polariton–polariton kinematic interaction modulation and kinematic bipolaritons in organic microcavities. *Solid State Communications*, 138(7):359–364, May 2006.

[6] Marina Litinskaya. Exciton polariton kinematic interaction in crystalline organic microcavities. *Phys. Rev. B*, 77(15):155325, April 2008.

[7] Eric R. Bittner and Carlos Silva. Estimating the conditions for polariton condensation in organic thin-film microcavities. *J. Chem. Phys.*, 136(3):034510, January 2012.

[8] Timur Yagafarov, Denis Sannikov, Anton Zasedatelev, Kyriacos Georgiou, Anton Baranikov, Oleksandr Kyriienko, Ivan Shelykh, Lizhi Gai, Zhen Shen, David Lidzey, and Pavlos Lagoudakis. Mechanisms of blueshifts in organic polariton condensates. *Commun Phys*, 3(1):1–10, January 2020.

[9] Adam D. Dunkelberger, Roderick B. Davidson, Wonmi Ahn, Blake S. Simpkins, and Jeffrey C. Owrutsky. Ultrafast Transmission Modulation and Recovery via Vibrational Strong Coupling. *J. Phys. Chem. A*, 122(4):965–971, February 2018.

[10] Adam D. Dunkelberger, Andrea B. Grafton, Igor Vurgaftman, Öney O. Soykal, Thomas L. Reinecke, Roderick B. Davidson, Blake S. Simpkins, and Jeffrey C. Owrutsky. Saturable Absorption in Solution-Phase and Cavity-Coupled Tungsten Hexacarbonyl. *ACS Photonics*, 6(11):2719–2725, November 2019.

[11] Justyna A. Ćwik, Sahinur Reja, Peter B. Littlewood, and Jonathan Keeling. Polariton condensation with saturable molecules dressed by vibrational modes. *EPL Europhys. Lett.*, 105(4):47009, February 2014.

[12] Felipe Herrera and Frank C. Spano. Cavity-Controlled Chemistry in Molecular Ensembles. *Phys. Rev. Lett.*, 116(23):238301, June 2016.

[13] Luigi Amico, Rosario Fazio, Andreas Osterloh, and Vlatko Vedral. Entanglement in many-body systems. *Rev. Mod. Phys.*, 80(2):517–576, May 2008.

[14] J. Eisert, M. Cramer, and M. B. Plenio. Colloquium: Area laws for the entanglement entropy. *Rev. Mod. Phys.*, 82(1):277–306, February 2010.

[15] T. Botzung, D. Hagenmüller, S. Schütz, J. Dubail, G. Pupillo, and J. Schachenmayer. Dark state semilocalization of quantum emitters in a cavity. *Phys. Rev. B*, 102(14):144202, October 2020.

[16] Nahum C. Chávez, Francesco Mattiotti, J. A. Méndez-Bermúdez, Fausto Borgonovi, and G. Luca Celardo. Disorder-Enhanced and Disorder-Independent Transport with Long-Range Hopping: Application to Molecular Chains in Optical Cavities. *Phys. Rev. Lett.*, 126(15):153201, April 2021.

[17] Felipe Herrera and Frank C. Spano. Theory of Nanoscale Organic Cavities: The Essential Role of Vibration-Photon Dressed States. *ACS Photonics*, 5(1):65–79, January 2018.

[18] Shaocong Hou, Mandeep Khatoniar, Kan Ding, Yue Qu, Alexander Napolov, Vinod M. Menon, and Stephen R. Forrest. Ultralong-Range Energy Transport in a Disordered Organic Semiconductor at Room Temperature Via Coherent Exciton-Polariton Propagation. *Adv. Mater.*, 32(28):2002127, 2020.

[19] V. M. Agranovich, M. Litinskaia, and D. G. Lidzey. Cavity polaritons in microcavities containing disordered organic semiconductors. *Phys. Rev. B*, 67(8), February 2003.

[20] Jérôme Dubail, Thomas Botzung, Johannes Schachenmayer, Guido Pupillo, and David Hagenmüller. Large Random Arrowhead Matrices: Multifractality, Semi-Localization, and Protected Transport in Disordered Quantum Spins Coupled to a Cavity. *ArXiv210508444 Quant-Ph*, May 2021.

[21] C. Sommer, M. Reitz, F. Mineo, and C. Genes. Molecular polaritonics in dense mesoscopic disordered ensembles. *Phys. Rev. Research*, 3(3):033141, August 2021.

[22] Michael L. Wall, Arghavan Safavi-Naini, and Ana Maria Rey. Simulating generic spin-boson models with matrix product states. *Phys. Rev. A*, 94(5):053637, November 2016.

[23] M. Ahsan Zeb, Peter G. Kirton, and Jonathan Keeling. Exact States and Spectra of Vibrationally Dressed Polaritons. *ACS Photonics*, 5(1):249–257, January 2018.

[24] Gerrit Groenhof, Clàudia Climent, Johannes Feist, Dmitry Morozov, and J. Jussi Toppari. Tracking Polariton Relaxation with Multiscale Molecular Dynamics Simulations. *J. Phys. Chem. Lett.*, 10(18):5476–5483, September 2019.

[25] Yu Zhang, Tammie Nelson, and Sergei Tretiak. Non-adiabatic molecular dynamics of molecules in the presence of strong light-matter interactions. *J. Chem. Phys.*, 151(15):154109, October 2019.

[26] Claude Cohen-Tannoudji, Jacques Dupont-Roc, and Gilbert Grynberg. *Atom-Photon Interactions: Basic Processes and Applications*. Wiley, New York, 1992.

[27] J. Doyle, B. Friedrich, R. V. Krems, and F. Masnou-Seeuws. Editorial: Quo vadis, cold molecules? *Eur. Phys. J. D*, 31(2):149–164, November 2004.

[28] Lincoln D. Carr, David DeMille, Roman V. Krems, and Jun Ye. Cold and ultracold molecules: Science, technology and applications. *New J. Phys.*, 11(5):055049, May 2009.

[29] Goulven Quéméner and Paul S. Julienne. Ultracold Molecules under Control! *Chem. Rev.*, 112(9):4949–5011, September 2012.

[30] Steven A. Moses, Jacob P. Covey, Matthew T. Miecnikowski, Deborah S. Jin, and Jun Ye. New frontiers for quantum gases of polar molecules. *Nature Phys*, 13(1):13–20, January 2017.

[31] John L. Bohn, Ana Maria Rey, and Jun Ye. Cold molecules: Progress in quantum engineering of chemistry and quantum matter. *Science*, 357(6355):1002–1010, September 2017.

# Part IV.

# Many-body Quantum Dynamics

# 11. Logarithmic Growth of Operator Entanglement under Dephasing

In Chapters 9 and 10, MPS methods were used to numerically study many-body dynamics in closed quantum systems. However, as emphasized throughout this thesis, most quantum systems are not closed, and environment interactions play a crucial role in the dynamics. This chapter discusses a recent project to numerically study open spin chains under dephasing using MPS methods [1].

This chapter is organized as follows: The model is introduced in Section 11.1. Then, operator entanglement is discussed as an open system alternative to entanglement entropy in Section 11.2. Section 11.3 contains the main numerical finding of logarithmic operator entanglement growth at long times, which is analytically explained in the classical (large dephasing) limit in Section 11.4. Finally, the implications of this finding are discussed in Section 11.5, which concludes this chapter.

## 11.1. Model

We analyze an spin-1/2 chain, where spins interact with their nearest neighbors and the environment, as schematically indicated in Figure 11.1. We assume a Markovian interaction with the environment, sucha that the time evolution is described by the Lindblad master equation ($\hbar \equiv 1$ throughout this chapter)

$$\partial_t \hat{\rho} = \mathcal{L}\hat{\rho} = -\mathrm{i}\Big[\hat{H}, \hat{\rho}\Big] - \sum_n \left(\hat{L}_n^\dagger \hat{L}_n \hat{\rho} + \hat{\rho}\hat{L}_n^\dagger \hat{L}_n - 2\hat{L}_n \hat{\rho} \hat{L}_n^\dagger\right). \tag{11.1}$$

Here, $\hat{H}$ is the system Hamiltonian, and $\hat{L}_n$ are local Lindblad operators acting on site $n$ (see Chapter 2).

We focus on three paradigmatic spin models: the XXZ model, the XYZ model, and the transverse field Ising model. Most of our analysis will be centered on the XXZ model with Hamiltonian

$$\hat{H}_{\mathrm{XXZ}} = \frac{1}{4}\sum_i \left(J\hat{\sigma}_i^x \hat{\sigma}_{i+1}^x + J\hat{\sigma}_i^y \hat{\sigma}_{i+1}^y + J_z \hat{\sigma}_i^z \hat{\sigma}_{i+1}^z\right). \tag{11.2}$$

Here, $\hat{\sigma}_i^{x,y,z}$ are the Pauli matrices, while $J$ and $J_z$ are the nearest neighbor interaction strengths. Alternatively, this model may be thought of as (distinguishable) hard core particles, such as atoms in an optical lattice. Then, $J$ is the tunneling rate and $J_z$ is nearest neighbor repulsion (or attraction for $J_z < 0$).

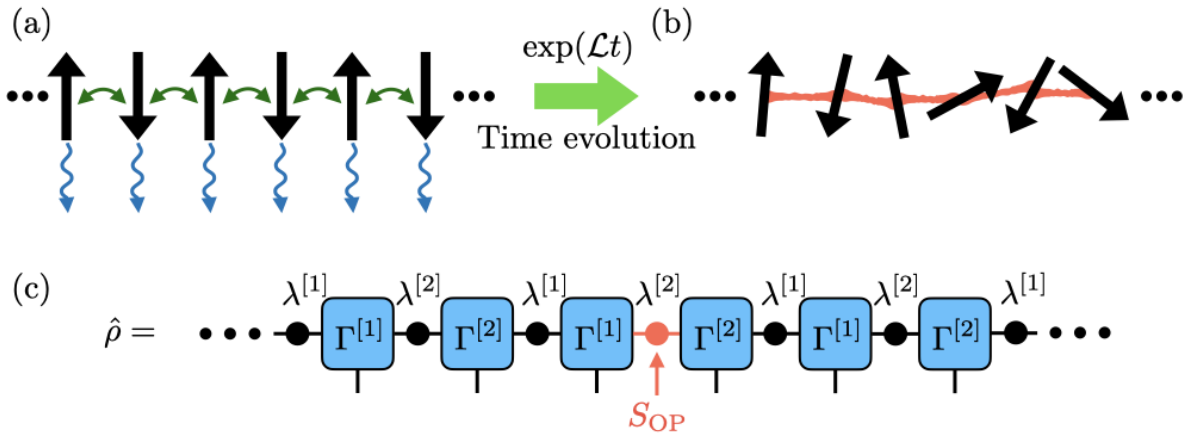


Figure 11.1. – Schematic model and simulation. (a) We consider an infinite spin chain with nearest neighbor interactions (green double arrows) and dephasing (blue arrows), which is initially in a Néel state. (b) After some time evolution, the system evolves from a pure state into a mixed states with correlations between the spins, indicated by the red connections. (c) The spin chain is simulated using an infinite MPS as described in Section 4.5. The operator entanglement is determined by the $\lambda$ tensors, as indicated in red.

In addition, we will also consider the more general XYZ model

$$\hat{H}_{\mathrm{XXZ}} = \frac{1}{4}\sum_i \left(J\hat{\sigma}_i^x\hat{\sigma}_{i+1}^x + J_y\hat{\sigma}_i^y\hat{\sigma}_{i+1}^y + J_z\hat{\sigma}_i^z\hat{\sigma}_{i+1}^z\right) , \tag{11.3}$$

and the transverse field Ising model

$$\hat{H}_{\mathrm{XXZ}} = \frac{1}{4}\sum_i \left(J\hat{\sigma}_i^x\hat{\sigma}_{i+1}^x\right) + \frac{h_z}{2}\sum_i \hat{\sigma}_i^z . \tag{11.4}$$

Here, $h_z$ is the field strength of a transverse field.

We consider an environment interaction that leads to dephasing, i.e.

$$\hat{L}_n = \sqrt{\frac{\gamma}{2}}\hat{\sigma}_n^z . \tag{11.5}$$

Dephasing generally arises when the environment coupling conserves magnetization. This is for example the case in optical lattices, where off-resonant scattering of lattice laser photons can localize atoms without leading to loss [2, 3].

We are interested in the non-equilibrium dynamics of highly excited states. In particular, we will focus on the Néel state in $z$ direction

$$\hat{\rho}(t=0) = \bigotimes_i \left(|\uparrow\rangle\langle\uparrow|_{2i} \otimes |\downarrow\rangle\langle\downarrow|_{2i+1}\right) . \tag{11.6}$$

For later comparison, we will further consider the Néel state in $x$ direction $\hat{\rho}(t=0) = \bigotimes_i |{\leftarrow}\rangle\langle{\leftarrow}|_{2i} \otimes |{\rightarrow}\rangle\langle{\rightarrow}|_{2i+1}$, with $|{\leftarrow}\rangle = (|{\uparrow}\rangle + |{\downarrow}\rangle)/\sqrt{2}$ and $|{\rightarrow}\rangle = (|{\uparrow}\rangle - |{\downarrow}\rangle)/\sqrt{2}$.

The time evolution of this state is simulated using an iTEBD method for density matrices with re-orthogonalization, as introduced in Chapter 4 [4]. In particular, we write the density matrix as

$$\hat{\rho} = \sum_{\{i_n\}} \sum_{\{\chi_n\}} \prod_n \lambda^{[n]}_{\chi_n\chi_n} \Gamma^{[n][i_n]}_{\chi_n\chi_{n+1}} \hat{\rho}_n^{[i_n]} . \tag{11.7}$$

Here, the $\hat{\rho}_n^{[i_n]}$ are a basis for the local density matrix of the $n$th spin given by the Choi isomorphism, and the $\lambda$ and $\Gamma$ tensors are the standard tensors for a canonical form [5]. The translation invariant tensor network structure is indicated in Figure 11.1(c).

To simulate the XXZ chain with initial Néel state in $z$ direction, we further take advantage of the conservation of the total magnetization $\hat{S}_z = (\sum_n \hat{\sigma}_n^z)/2$, that is $\mathcal{L}\hat{S}_z = 0$. This was discussed in Scection 4.3. In short, the density matrix is split into symmetry sectors according to the magnetization of the right half of the chain $\hat{S}_z^R = (\sum_{n>0} \hat{\sigma}_n^z)/2$, i.e. $\hat{\rho} = \sum_{M_R} \hat{\rho}_{M_R}$ with $\hat{S}_z^R \hat{\rho}_{M_R} = M_R \hat{\rho}_{M_R}$. This splitting leads to a block sparse form of the $\Gamma$ tensors, and an increased efficiency.

## 11.2. Operator Entanglement

For closed quantum systems, bi-partite entanglement entropies indicate whether the system can be efficiently simulated using MPS methods, as was done in Chapters 9 and 10 [6] (see Reference [7] for the limits of this interpretation). For open system simulation using (vectorized) Matrix Product Density matrices, the equivalent quantity is Operator Space Entanglement Entropy, or simply Operator Entanglement (OE) [8]. This quantity is computed analogous to the (von Neumann) entanglement entropy for states according to

$$S_{\mathrm{OP}} = -\sum_{\chi} \left(\lambda^{[n]}_{\chi\chi}\right)^2 \log_2 \left[\left(\lambda^{[n]}_{\chi\chi}\right)^2\right] , \tag{11.8}$$

where the $\lambda^{[n]}$ are the Schmidt values defined in Equation (11.7). Despite its name, OE does not measure quantum entanglement, but accounts for any correlation between the sub-systems.

## 11.3. Numerical Results

In the XXZ model, for not too large $\gamma$ and $J_z$, we find an initial fast growth of operator entanglement at short times. This initial growth is followed by a decay, and a long time logarithmic growth of entanglement [see Figure 11.2(a)]. For larger $\gamma$ and $J_z$, the initial peak is suppressed, but the logarithmic growth at long times persists.

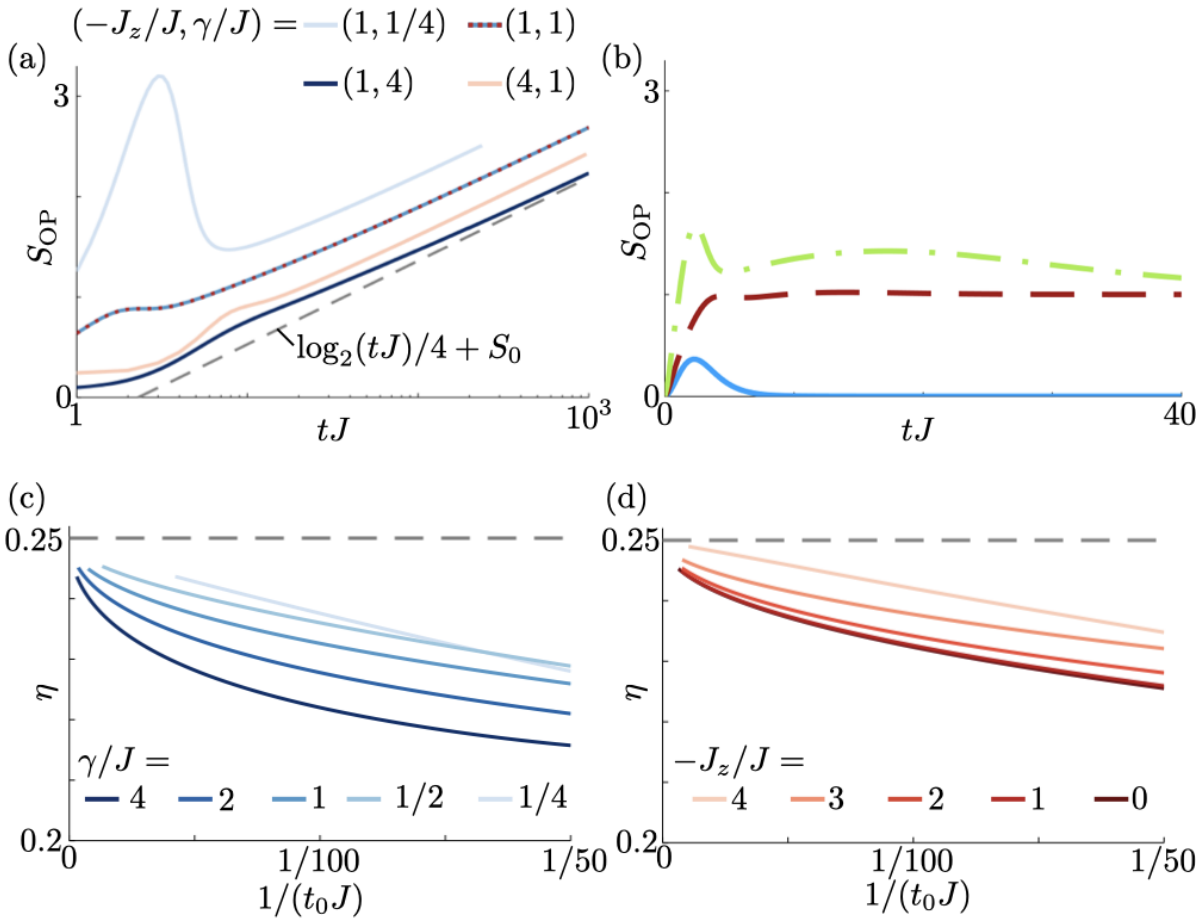


Figure 11.2. – Time evolution of operator entanglement $S_{\mathrm{OP}}$. (a) Time evolution for different parameter in the XXZ model starting in a Néel state in $z$ direction (logarithmic time axis). At long times, we find logarithmic growth with prefactor 1/4. (b) Operator Entanglement for different scenarios. Blue solid line: XXZ model with initial Néel state in $x$ direction ($J_z = -J/2$, $\gamma = J/2$); red dashed line: transverse field Ising model with initial Néel state in $z$ direction ($h_z = J$, $\gamma = J/2$); greed dash-dotted line: XYZ model with initial Néel state in $z$ direction ($J_y = 0.8J$, $J_z = -J/2$, $\gamma = J/2$). (c),(d) Prefactor of the logarithmic growth at long times. The tangents to the operator entanglement curves in panel (a) $\eta \log_2(tJ) + S_0$ at time $t_0$ are computed as a function of inverse time. In panel (c), $J_z = -J$ is fixed and $\gamma$ is varied, while in panel (d), $\gamma = J$ is fixed and $J_z$ is varied. The grey dashed lines are analytical estimates in the limit of large dephasing and long time.

This logarithmic growth is in contrast to different models and initial states, for which we find that the operator entanglement generally remains bounded [Figure 11.2(b)]. We further find that the logarithmic growth has an universal prefactor 1/4, independent of the dephasing strength or the an-isotropy [Figure 11.2 (c) and (d), respectively].

## 11.4. Analytical Explanation

In this section, we explain the logarithmic growth of operator entanglement in the limit of large dephasing. The crucial property for this explanation is that the total magnetization $\hat{S}_z$ is conserved, which is in contrast to the other models considered in Fig. 11.2(b). Using this conservation law, the total OE can be separated into one contribution within symmetry sectors with given $N_R$, and one due to the mixing of different symmetry sectors as [1]

$$S_{\mathrm{OP}} = \sum_{M_R} p_{M_R} S_{\mathrm{res}}(M_R) - p(M_R) \log_2[p(M_R)] \,. \tag{11.9}$$

Here $p(M_R) = \mathrm{Tr}(\hat{\rho}_{M_R})$ is the probability that the system is in the symmetry sector $M_R$, and $S_{\mathrm{res}}(M_R)$ is the symmetry resolved operator entanglement [9]. At long times, $S_{\mathrm{res}}(M_R)$ remains bounded and the operator entanglement is determined by the second term, only [1].

In the case of large dephasing $\gamma \gg J, J_z$, Cai and Barthel showed that the XXZ model reduces to a model with classical spin flips between two neighboring sites [10]. This model is equivalent to the simple symmetric exclusion process, which is known to exhibit anomalous spin diffusion. In particular, it was shown that at long times [11]

$$p(M_R; t) \sim \exp\left(-\frac{M_R^2}{\sqrt{t}}\right) . \tag{11.10}$$

This result straightforwardly yields

$$S_{\mathrm{OP}} \sim -\sum_{M_R} p(M_R) \log_2[p(M_R)] \sim \frac{1}{4} \log_2(t) \,. \tag{11.11}$$

## 11.5. Conclusion

We have shown that in a XXZ spin chain with dephasing, operator entanglement exhibits universal logarithmic growth with a prefactor of 1/4 at long times. In the classical limit, this finding is analytically explained by anomalous diffusion of particles on a line. We note again that the operator entanglement observed here is not genuine quantum entanglement, but instead describes classical correlations between the magnetization on both sides of the chain. This finding demonstrates the efficient classical simulability of quantum models under dephasing.

# Bibliography


[1] D. Wellnitz, G. Preisser, V. Alba, J. Dubail, and J. Schachenmayer, "The rise and fall, and slow rise again, of operator entanglement under dephasing," *in preparation*, 2021.

[2] H. Pichler, A. J. Daley, and P. Zoller, "Nonequilibrium dynamics of bosonic atoms in optical lattices: Decoherence of many-body states due to spontaneous emission," *Phys. Rev. A*, vol. 82, p. 063605, Dec. 2010.

[3] S. Sarkar, S. Langer, J. Schachenmayer, and A. J. Daley, "Light scattering and dissipative dynamics of many fermionic atoms in an optical lattice," *Phys. Rev. A*, vol. 90, p. 023618, Aug. 2014.

[4] R. Orús and G. Vidal, "Infinite time-evolving block decimation algorithm beyond unitary evolution," *Phys. Rev. B*, vol. 78, p. 155117, Oct. 2008.

[5] M. Zwolak and G. Vidal, "Mixed-State Dynamics in One-Dimensional Quantum Lattice Systems: A Time-Dependent Superoperator Renormalization Algorithm," *Phys. Rev. Lett.*, vol. 93, p. 207205, Nov. 2004.

[6] U. Schollwöck, "The density-matrix renormalization group in the age of matrix product states," *Annals of Physics*, vol. 326, pp. 96–192, Jan. 2011.

[7] N. Schuch, M. M. Wolf, F. Verstraete, and J. I. Cirac, "Entropy Scaling and Simulability by Matrix Product States," *Phys. Rev. Lett.*, vol. 100, p. 030504, Jan. 2008.

[8] J. Dubail, "Entanglement scaling of operators: a conformal field theory approach, with a glimpse of simulability of long-time dynamics in 1+1d," *J. Phys. A: Math. Theor.*, vol. 50, p. 234001, May 2017.

[9] M. Goldstein and E. Sela, "Symmetry-Resolved Entanglement in Many-Body Systems," *Phys. Rev. Lett.*, vol. 120, p. 200602, May 2018.

[10] Z. Cai and T. Barthel, "Algebraic versus Exponential Decoherence in Dissipative Many-Particle Systems," *Phys. Rev. Lett.*, vol. 111, p. 150403, Oct. 2013.

[11] B. Derrida and A. Gerschenfeld, "Current Fluctuations of the One Dimensional Symmetric Simple Exclusion Process with Step Initial Condition," *J Stat Phys*, vol. 136, pp. 1–15, July 2009.

# 12. Conclusion and Outlook

In this thesis, I have investigated the quantum many body dynamics of cavity coupled molecular ensembles. By investigating simple models, collective and dissipative effects were analyzed in detail, and it was shown how they can be utilized to steer chemical reactions, both inside and outside the ultra-cold regime. We have further analyzed entanglement dynamics to better understand the role of quantum effects and the computational complexity of these systems. I have focused on entanglement between vibrational and electro-photonic degrees of freedom, which is neglected in common mean-field approximations. We show that this entanglement can be enhanced by electronic disorder or large (but not too large) initial molecular excitation fractions. In the last project, we have analyzed the time evolution of operator entanglement in open spin chains subject to dephasing. There, after an initial rise and fall, the interplay of number conservation leads to a long-time logarithmic growth of operator entanglement.

Methodically, it was demonstrated how established methods from quantum optics can be adapted to tackle polaritonic chemistry problems. It was shown that these methods are particularly useful to analyze collective and dissipative effects, which play a crucial role in experimental setups.

Cold and ultra-cold molecules offer the potential to readily observe many of the predictions made in this thesis. We already proposed a scheme to create an ensemble of ultra-cold molecules coupled to a cavity. The resulting diatomic molecules have a single vibrational coordinate, so that the predictions made with the Holstein-Tavis-Cummings model may be directly observable. For these molecules, the vibrational coordinate is generally not harmonic. This anharmonicity may steer the vibration further out of a coherent (classical) state and it will be interesting to investigate this further in the future. In cold molecule experiments, entanglement of nuclear and electronic degrees of freedom can be measured [1], and disorder can be introduced in a controlled manor in optical lattice setups [2]. Such entanglement studies are not only fundamentally interesting, but also offer potential applications, such as quantum sensing [3]. For example, entanglement induced by a cavity has been used for enhanced measurement precision, breaking the standard quantum limit [4]. Such experiments combining cavities and ultra-cold molecules are being set up, providing the ultimate opportunity to verify theoretical methods [5].

Furthermore, the MPS simulations can be easily adapted to study the formation of ultra-cold molecules proposed in this thesis, investigating effects of noise in more detail. Two particularly interesting prospects would be the creation of molecules outside an optical lattice, simplifying the experimental requirements. A second prospect is to push beyond the adiabatic regime, investigating a potential speed-up of molecular formation

using high intensity laser pulses.

Concerning polaritonic chemistry, the finding of disorder enhanced vibrational entanglement is directly relevant for future numerical studies. For large scale simulations, vibrational entanglement is often neglected in mean-field simulations. Previously, it has been analytically argued that collective effects should suppress such entanglement [6]. It is an interesting prospect to numerically verify these approximations, and to analyze under which conditions entanglement becomes important. In this respect, it will be particularly insightful to combine the MPS tools for cavities (Chapters 9,10) and open systems (Chapter 11) to understand how the environment influences the predictions of this thesis.

From another perspective, entanglement is a resource for quantum technologies applications. Polaritonic setups are currently under investigation as potential candidates for quantum computation and quantum simulation [7, 8]. For example, Bose-Einstein condensation at room temperature has been demonstrated in organic polaritonic setups [9]. Demonstration of entanglement would be another big step towards the realization of room temperature quantum technologies. In these setups in particular, the investigation of the effects of environment interactions are very important, as those are generally the limiting component for quantum technologies.

A natural extension of the work presented in this thesis is an extension of the MPS simulations to more general models. This may include anharmonic vibrational degrees of freedom, different vibrational frequencies for ground and excited states, and multiple electronic states or vibrational coordinates, which can all be readily implemented. For example, by including excited singlet and triplet states, the simulations may be directly relevant to understand modified singlet-triplet transitions inside a cavity, that have been observed in different scenarios [10]. Another interesting extension would be to include multiple cavity modes, since there is never just a single coupled cavity mode, and multiple cavity modes have been shown to have inportant consequences for multi-level particles coupled to a cavity [11].

It will also be interesting to combine the simple reaction models analyzed in the first part of this thesis with vibrational degrees of freedom included in the second part. In such systems, adiabatic elimination could be used to eliminate the vibrations and compute effective reaction rates analytically, similar to the elimination of the excited states. Such analytical estimates could then be directly verified by MPS simulations, where dissipation can be readily implemented as discussed in the final part of this thesis, and may even make numerical simulations more efficient.

These type of noisy simulations may also be interesting for the simulation of vibrational strong coupling experiments. Here, the reactions are thermally induced, making thermal noise an integral part of the system. Ultimately this may even help to answer the question whether the observed effects are fundamentally quantum mechanical in nature, or can be explained classically.

# Bibliography


[1] Y. Lin, D. R. Leibrandt, D. Leibfried, and C.-w. Chou, "Quantum entanglement between an atom and a molecule," *Nature*, vol. 581, pp. 273–277, May 2020.

[2] M. Schreiber, S. S. Hodgman, P. Bordia, H. P. Lüschen, M. H. Fischer, R. Vosk, E. Altman, U. Schneider, and I. Bloch, "Observation of many-body localization of interacting fermions in a quasirandom optical lattice," *Science*, vol. 349, pp. 842–845, Aug. 2015.

[3] C. L. Degen, F. Reinhard, and P. Cappellaro, "Quantum sensing," *Rev. Mod. Phys.*, vol. 89, p. 035002, July 2017.

[4] G. P. Greve, C. Luo, B. Wu, and J. K. Thompson, "Entanglement-Enhanced Matter-Wave Interferometry in a High-Finesse Cavity," *ArXiv211014027 Phys. Physicsquant-Ph*, Oct. 2021.

[5] H. Konishi, K. Roux, V. Helson, and J.-P. Brantut, "Universal pair polaritons in a strongly interacting Fermi gas," *Nature*, vol. 596, pp. 509–513, Aug. 2021.

[6] F. Herrera and F. C. Spano, "Cavity-Controlled Chemistry in Molecular Ensembles," *Phys. Rev. Lett.*, vol. 116, p. 238301, June 2016.

[7] T. Boulier, M. J. Jacquet, A. Maître, G. Lerario, F. Claude, S. Pigeon, Q. Glorieux, A. Amo, J. Bloch, A. Bramati, and E. Giacobino, "Microcavity Polaritons for Quantum Simulation," *Adv. Quantum Technol.*, vol. 3, no. 11, p. 2000052, 2020.

[8] M. Dusel, S. Betzold, O. A. Egorov, S. Klembt, J. Ohmer, U. Fischer, S. Höfling, and C. Schneider, "Room temperature organic exciton–polariton condensate in a lattice," *Nat Commun*, vol. 11, p. 2863, June 2020.

[9] S. Kéna-Cohen and S. R. Forrest, "Room-temperature polariton lasing in an organic single-crystal microcavity," *Nat. Photonics*, vol. 4, pp. 371–375, June 2010.

[10] M. Hertzog, M. Wang, J. Mony, and K. Börjesson, "Strong light–matter interactions: A new direction within chemistry," *Chem. Soc. Rev.*, vol. 48, pp. 937–961, Feb. 2019.

[11] A. P. Orioli, J. K. Thompson, and A. M. Rey, "Emergent dark states from superradiant dynamics in multilevel atoms in a cavity," *ArXiv210600019 Cond-Mat Physicsquant-Ph*, May 2021.

Université de Strasbourg

David Wellnitz

# Collective Quantum Dynamics of Molecular Ensembles coupled to a Cavity

EDSC École Doctorale des Sciences Chimiques

**Résumé** L'objectif central de cette thèse est de développer une compréhension théorique plus approfondie de la dynamique quantique collective et dissipative d'ensembles moléculaires couplés à des cavités en trois parties : Dans la première partie, nous utilisons une cavité pour améliorer l'efficacité de formation de molécules ultra-froides dans leur état fondamental en exploitant la dissipation et les effets collectifs, et nous simulons efficacement la dynamique de jusqu'à $10^6$ molécules. Dans la deuxième partie, l'analyse est étendue à la température ambiante. Les régimes de dynamique de réaction modifiée sont identifiés dans le cas d'une réaction simple de transfert d'électrons photo-induite. En plus, nous démontrons que l'intrication entre les différents degrés de liberté peut être significativement augmentée en introduisant du désordre dans le système avec des simulations de réseaux de tenseurs. Dans la troisième partie, nous démontrons que le déphasage conduit à une croissance logarithmique de l'intrication des opérateurs dans une chaîne de spin ouverte.

**Mots clés**: QED en cavité, dynamique quantique à $N$ corps, chimie polaritonique, molécules ultra-froides, états de produits matriciels, systèmes quantiques ouverts, intrication.

**Abstract** This thesis aims to develop a deeper theoretical understanding of the collective, dissipative quantum dynamics of cavity-coupled molecular ensembles in three parts: First, a cavity is used in a novel scheme for dissipative formation of ultra-cold ground state molecules with collectively enhanced efficiency, which can be efficiently simulated for very large ($> 10^6$ molecules) ensembles. Secondly, the analysis is extended to room-temperature polaritonic chemistry. Here, regimes for modified reaction dynamics are identified for a simple photo-induced electron transfer reaction under incoherent pumping. Then, it is shown that entanglement between vibrational and electro-photonic degrees of freedom can be significantly enhanced by introducing disorder into the system using matrix product state simulations. For the disorder-less regime, further efficient approximations methods are developed. Thirdly, in a recent project, the build-up of operator entanglement is studied in an open spin-chain with dephasing, which is found to exhibit logarithmic growth.

**Keywords**: Cavity QED, Many-body Quantum Dynamics, Polaritonic Chemistry, Ultra-cold Molecules, Matrix Product States, Open Quantum Systems, Entanglement